Master thesis in Acoustics

Finite element modeling of ultrasound measurement systems for gas. Comparison with experiments in air.

Rune Hauge
June - 2013

Department of Physics and Technology

UNIVERSITY OF BERGEN

Preface

The experimental work and FE simulations performed as part of this thesis is the result of a close cooperation between Eivind Mosland and the author. As a results of this, Chapters 3, 4, 5, and 6 are present in both our master theses, but in slightly different forms.

- Chapter 3: Experimental setup and measurement methods, is mainly written by Mosland, except Section 3.7.
- Chapter 4: Finite element simulation setup, is mainly written by the Mosland, except Section 4.5.
- Chapter 5: Matching layer material characterization, is mainly written by the author.
- Chapter 6: Transducer construction, is co-written by Mosland and the author.

This master thesis was performed as part of the project "Ultrasonic instrumentation for gas characterisation" under The Michelsen Centre for Industrial Measurement Science and Technology (MIMT). Two other activities are carried out in the project, by Storheim [1], Mosland [2].

Thank you Eivind, for the fruitful corporation during the work of thesis and earlier exams. It has truly been a pleasure working with you!

I want to thank my supervisor Per Lunde, and co-supervisors Magne Vestrheim and Jan M. Kocbach. Your knowledge and inspiration through weekly supervising have been precious.

Espen Storheim, partially funded by MIMT, deserves a special thank you. Your time and patience through many questions, and willingness to help with the experimental setup, MATLAB , FEMP , and LaTeX has been precious.

I would like to thank Magne Aanes, for always being ready to answer questions, and for sharing his experience with transducer construction.

Per Heradstveit has been very helpful in the soldering process, and by supplying equipment needed for the experimental setup.

The engineering workshop at the Department of Physics and Technology deserves my expressions of gratitude for the further development of the measurement setup, and for always being helpful and welcoming.

I would like to say thank you to the rest of the Acoustics group at the University of Bergen, where the door has always been open, and questions are met with interest and devotion.

A heartfelt thank you goes to my loving wife, Karoline. Your love and support has been invaluable through the work of this thesis.

Rune Hauge, Bergen 10. June 2013

Contents

List of Figures

List of Tables

Chapter 1

Introduction

1.1 Background and motivation

A combination of an ultrasonic transmitter/receiver pair, with dedicated electronics for signal generation and recording (here referred to as a ”measurement system”), may be used for a range of applications, e.g. fiscal measurement of oil and gas [3–6], calorific value measurements and gas characterization [7, 8], accurate measurements of sound speed and absorption in gases and liquids [9–12], and non-destructive testing and evaluation [13–16].

For accurate use of a measurement system, understanding of the physical processes in the system is important. A transmitting transducer of finite dimensions radiating into air will not create a plane wave sound field. The resulting effects is termed diffraction, which is an important property of a real measurement system. Other processes include e.g. the electro-mechanical transfer functions for transmitting and receiving, the medium absorption, reflections and electrical loading of the transmit-receive system. The main focus of this work is accurate modeling of an experimental setup, where consideration of the aforementioned effects is needed.

A theoretical model designed to describe a measurement system, or characterize a specific part of a measurement system (here termed a ”system model”), is important for several purposes. The ability to accurately simulate the measurement system at hand might be very valuable for design and optimization of ultrasonic measurement instruments, quality assurance in construction of transducers, analysis of measurement data, etc. For these purposes, the system modeling tool provides means to improve the effectiveness of an experimental work with regard to time consumption and cost, and it contributes to a higher level of theoretical knowledge about the measurement system. The system model is usually divided into several ”modules”, e.g. signal generation, transmitting electronics, transmitter, medium, receiver, receiving electronics and termination [14, 17–22]. The modules can be modeled separately, or combined, making it possible to follow the signal through each module, and how the signal is transformed as it propagates in the system.

Some modules of special interest in most system models, are the transducer radiating into a medium, and the receiving transducer. Generation and reception of sound pressure waves by real transducers are complex, as several surfaces of the transducers are contributing to the transmission/reception. In addition, knowledge of the distance-dependent diffraction effect [23–27], and radiation modes, e.g. the thickness-extension (TE) and radial (R) modes, are important for describing the frequency and time response of a transducer. Transducers radiating in R mode is focused on in this work. A typical ultrasonic transducer consists of a piezoelectric ceramic disk, with one or several front and backing layers, and a transducer housing.

Modeling of such piezoelectric transducers in a measurement system, necessitates the use of a three-dimensional modeling tool, as the transducer structure is usually too complex to describe accurately using a one-dimensional model. One such modeling method is the finite element (FE) type model, which is a numerical model that enables modeling of e.g. TE and R modes. By use of a FE model, the potential for modeling of a transmit-receive pair at arbitrary distances, accounting for near-field effects, is enabled.

1.2 Previous work

System models for ultrasonic measurement systems in use today include models based on the Mason model (or similar one-dimensional descriptions) for the transmitting and receiving transducers, combined e.g. with uniform piston type of radiation models for the wave propagation in the medium [17–19, 28, 29];

simplified electrical transmission line descriptions [30]; an electroacoustic measurement model [14,20,21], to more advanced FE based descriptions [22].

A system model for an ultrasonic flowmeter was presented by Lygre et al. in [17]. The "FLOSIM" model for simulation of signal transmission for a single acoustic beam in an ultrasonic transit-time flowmeter was used to propagate a signal through the system. The FLOSIM model contains several modules, including signal generator, transmitting and receiving transducers, the flowing fluid, and transmitting and receiving electronics. For the transmit-medium-receive modules, a 1D model for simulation of thickness-vibrating piezoelectric transducers are used. The model allows for usage of one (or several) backing and front layers in the transducer. Simulation in both time and frequency domain are possible by use of Fourier synthesis.

Vervik utilized TRANSCAD, an one-dimensional TE mode model, and adapted it for use on transducers radiating in R mode [18,19] for description of the physical effects which influences on the flow-metering transit-times. The transducer model is implemented into a FLOSIM based system model, where the effect of receiving electronics and cables are measured and incorporated into the model.

A PSpice[1] approach for a pulse-echo setup for determination of the sound speed and attenuation in liquids and solids was presented by Deventer et al. [30], where simple transmitting electronics and no receiving electronics are used in the model. PSpice enables for TE mode description. The transmitting transducer, including the piezoelectric ceramic material PZT-5A and tungsten-epoxy backing layer, and signal propagation is modeled using a KLM type model.

Lunde et al. incorporated FE modeling for the piezoelectric transducers and fluid medium in the FLOSIM system model [22]. Comparisons were made between a FE and a Mason type 1D/piston model for a transmit-receive system. No transmitting or receiving electronics are used, except for a Thévenin equivalent circuit for signal generator, and termination of the system. Both the electrical and acoustical response functions showed a substantial difference between the FE and Mason model. When modeling the averaged sound pressure over the area of the receiver as a function of time, it was evident that the Mason 1D model did not describe the signal and its shape with the same accuracy as the FE model. Lunde et al. found that important effects of the transmitting and propagation of the signal is available by implementing FE based modeling into a system model.

Schmerr and Song presents a system model for an ultrasonic nondestructive evaluation (NDE) system [14]. The measurement system is divided into five main parts; the signal generator, cables, transmitting transducer, material specimen for evaluation and receiving transducer. Each system component, including the propagation and reception of the signal, is modeled using equivalent electrical circuits. Comparison between the system model and measurements are given for two different experimental setups for NDE application, showing a agreement between experiments and simulations of about 1 dB or less.

From the literature research conducted in this thesis, no published works have been found where a system model, using FE modeling of the transmit-medium-receive modules, is combined with transmitting and receiving electronics for description of an ultrasound measurement system. In addition, description of physical effects such as e.g. diffraction, near-field and absorption are necessary for an accurate modeling of the transmit-medium-receive system.

1.3 Objectives

The objective of this work is to develop and implement a finite element (FE) based linear system model for description of a measurement system for air at arbitrary measurement distances, and compare the system model to experiments in air.

The model will be expressed as several modules, describing signal generation, transmitting electronics, the transmitting transducer, medium, the receiving transducers, the receiving electronics, and termination of the measurement system. This enables for analysis of both single modules, and the combination of several modules.

In the medium module, physical effects such as e.g. medium absorption, diffraction and near-field effects are sought modeled. The system is based on a transmit-receive type of measurement system, and the transmit-medium-receive modules of the system model is calculated using an in-house developed FE model, FEMP 5.0, for 3D axisymmetric modeling of piezoelectric transducer structures and sound field.

The transmitting and receiving electronics will be modeled using transmission line theory for the cables, combined with the input and output impedances of the instruments. The effect of the cables will be investigated, to visualize the impact they have on the measurement system.

By use of the Fourier synthesis, the system model will be calculated in both frequency and time domain. This makes comparison between simulations and experiments possible, for both the frequency responses and time-traces.

---

[1] PSpice is a product of OrCAD, Inc., Beaverton, OR, homepage at `http://www.orcad.com`

The experimental measurement system described by the system model will be set up, and used to conduct experiments for comparison with the system model. The measurements will be done in air at room temperature, using both single circular piezoelectric ceramic disks, and more complex transducers structures with backing and matching layer in transducer housing. The transducer structures will be used to presumably increase the sensitivity and bandwidth of the system when transmitting into air. Fourier analysis will be used post process, for extraction of the measured signal from waveforms possibly affected by measurement noise.

The transducer structures for use in the measurement system will be developed and constructed in the present work, presumably improving the transducer sensitivity and bandwidth. FE simulation are conducted parallel to the construction process for optimization of material dimensions, and determination and ordering of materials. Insufficient material data provided by the manufacturer will be complemented by material characterization, including sound speed measurements. The transducers will be designed for usage in air at the R1 mode.

The frequency range of interest spans up to 300 kHz, which covers the important first radial (R1) mode of both the single piezoelectric ceramic disks and the constructed transducer structures.

1.4 Thesis outline

The outline of this thesis is as follows:

- Chapter 2
  The theoretical background for this thesis is given in Chapter 2, introducing system models describing the acoustical measurement system in Chapter 3.
- Chapter 3
  In Chapter 3, the present electrical and acoustical measurements setups are presented. A pistonphone calibration method of the pressure condenser microphones are given, and the post-process routines are
- Chapter 4
  This chapter presents the simulation and material parameters for the FE model used in this work. An overview of the various structures used in the FE model is given.
- Chapter 5
  Matching layers are introduced for improvement of the transducers characteristics in air. In this chapter, the matching layers are described by sound speed and density measurements. The measurement setup and theory utilized for the matching layer characterization, differs from the rest of the thesis, thus theory, measurement setup, signal processing and results for the sound speed and density measurements are given in this chapter.
- Chapter 6
  Piezoelectric transducer structures are developed to presumably improve the bandwidth and sensitivity compared to use of piezoelectric ceramic disk, for radiation in air. The transducer design and assembly process are presented.
- Chapter 7
  This chapter presents results for transfer functions describing different parts of the system model. The transfer functions for the transmit-medium-receive modules are compared to measurements, where the measurements are conducted using different combinations transmitting and receiving transducers.
- Chapter 8
  In Chapter 8, the system models, experimental setup and transducer construction are discussed.
- Chapter 9
  In thic chapter, conclusions of the current work is drawn, and the potential for further work is outlined.
- Appendix A
  In appendix A, the main MATLAB scripts used in the thesis are given.
- Appendix B
  The structure-files used for FE modeling is given in Appendix B.

- Appendix C
  Paper submitted for the proceedings of the 36$^{\text{th}}$ Scandinavian Symposium on Physical Acoustics, Geilo 3$^{\text{rd}}$ - 6$^{\text{th}}$ February 2013

Chapter 2

Theory

In this chapter, a system model designed to describe the present experimental setup (cf. Chapter 3) is introduced. A brief overview of system modeling is given, introducing a generic electroacoustical measurement system. The system variables are presented, and two theoretical models for expressing the diffraction correction are given; (1) a further developed Khimunin type of diffraction correction, and (2) a new type of relative diffraction correction. The relation between these expressions for the diffraction correction is given. The voltage-to-voltage transfer function for the transmit-medium-receive system is derived, including models for the diffraction correction and the absorption in the medium. The transmitting and receiving electronics of the current experimental setup is incorporated into the system model as voltage-to-voltage transfer functions.

The system model is introduced in Section 2.1, where the measurement system is divided into several modules, which are presented. The important transmit-medium-receive part of the system model is calculated in Section 2.2, by expressing the transfer function from the input voltage of the transmitter, to the output voltage of the receiver, using the two different expressions for the diffraction correction. A model for calculating the diffraction correction is given in Section 2.3. The medium absorption is included into the system model in Section 2.4, while use of the spherical reciprocity factor for representing the signal reception is given in Section 2.5. The cables connecting the transmitting and receiving electronics are represented by voltage-to-voltage transfer functions, and included into the system model in Section 2.6. FE modeling is used for calculating the radiation of the transmitting transducer and sound pressure field. A summary of the theory used in the current FE model, Femp, is given in Section 2.7. In Section 2.8, the use of Fourier transform for obtaining the system models time response functions is given. A method for calculating the transmitting voltage response from measurements is given in Section 2.9.

2.1 System model

In this section, a system model is developed in order to describe the measurement system used in the current work. The system model is able to both characterize parts of the measurement system, and to calculate the output voltage of the system, based on the input voltage. The measurement system is described by representing the key parts of the system as modules [17], see Fig. 2.1.

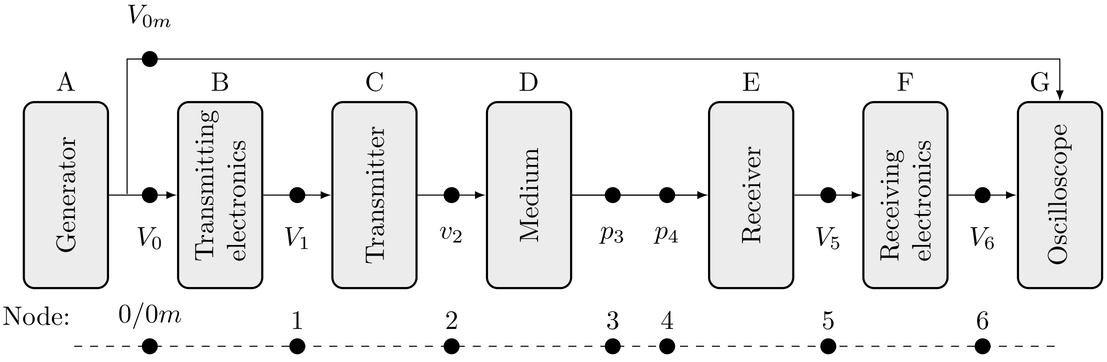

Figure 2.1: A system model with key parts represented by modules.

The variables subscripts in Fig. 2.1 denote the node number of the variable. No time dependent variables are used in this chapter, except for Section 2.8, thus, no extra notation (e.g. ("f")) is used for the frequency in this chapter. A time dependency of $e^{i\omega t}$ is assumed. Following is a description of the Modules A through G shown in Fig. 2.1.

- Module A: The generator is used to generate the excitation voltage to the system, which for the present measurement system is a single frequency sinusoidal signal with constant amplitude and a finite number of periods, currently referred to as a "burst". In the system model, the generator is represented by a Thévenin equivalent circuit, with electromotive force V_{gen} and output impedance Z_{gen}. The output voltage from the generator, in node 0, V_0, is the input voltage to Module B. Node $0m$ (node 0 "measured") is placed at the input terminals of the oscilloscope, and is connected to node 0 by a coaxial cable, hereafter named cable #2, see Module G.

- Module B: Generally transmitting electronics consists of e.g. power amplifiers, frequency filters and cables, however, the transmitting electronics for the present measurement system consists solely of the coaxial cable connecting the generator to the transmitter, henceforth referred to as cable #1. It is seen that the coaxial cables connecting the instruments in the measurement system is of importance for the propagating signal, cf. Section 7.1, and the cable is thus included as a module. The output voltage from the transmitting electronics is the driving voltage of the transmitter, V_1. Node 1 is placed at the input terminals of Module C.

- Module C: Is the transmitting transducer, converting the excitation signal from the transmitting electronics, V_1, to vibration of the active areas of the transducer. This represents the coupling to the medium, as sound energy is radiated from the transmitter to the medium. In the current work, the transmitting transducer and its radiation into the medium is described by FE modeling, cf. Section 2.7. In node 2, v_2 is the particle velocity at the center of the transmitting transducers front, used for propagation of the theoretical plane wave model, cf. Section 2.2.1. Node 2 is placed at the front face of Module C. Two types of transmitting transducers are used in the current work; piezoelectric ceramic disks (cf. Section 3.6) and transducer structures developed in the current work (cf. Chapter 6), both with circular fronts.

- Module D: This module contains the medium in the system model. The medium in the present measurement system is air at 1 atm. and room temperature [1]. In the system model, the diffraction and absorption effects are included. As an output of Module D, p_3 is the axial free-field sound pressure at reference distance d_0 from the transmitter, presently $d_0 = 1$ m, and p_4 is the axial free-field sound pressure at the center of the receiving transducers front. Thus node 3 is placed inside Module D, while node 4 is placed at the front of the receiving transducer in Module E.

- Module E: The receiving transducer converts the acoustic energy, propagated through the air, to the output voltage from the receiver, V_5. Node 5 is placed at the output terminals of Module E. The amount of acoustic energy converted depends on how much energy is reflected and refracted off the receiving transducer, and how much is propagated into the transducer and converted. The magnitude of V_5 depends on the ratio of impedances between the receiving electronics and the receiving transducer. Three types of receiving transducers are used in this work; a commercial pressure condenser microphone, and the piezoelectric ceramic disk and transducer structure, as used in Module C. The receiving transducer is coaxially aligned with the transmitting transducer. Node 5 is placed at the output terminals of Module E.

- Module F: The receiving electronics consist of a measurement amplifier, frequency filter and coaxial cables. The cable connecting the receiving transducer to the amplifier is named cable #3, while the cable connecting the amplifier output to the oscilloscope is named cable #4. The module modifies the received signal by amplifying and filtering, reducing unwanted frequency components/noise. However, the instruments used in Module F might also contribute to the measurement noise. The amplifier works in two stages, it has an input and output amplification. The external frequency filter is connected to the amplifier between the input and output channels. The frequency filter has two channels, one high-pass and one low-pass. In addition to the external filter, the amplifier has an internal high-pass filter. For a more complete overview of the receiving electronics, cf. Section 3.3.4. As in Module B, the coaxial cables connecting the instruments are seen to affect the signal, cf. Section 7.1. The output voltage from Module F is V_6, which is recorded by the oscilloscope in Module G. Node 6 is placed at the input terminals of Module G.

- Module G: The termination of the measurement system, which is an oscilloscope in the present measurement setup. The oscilloscope records the voltages V_6, and V_{0m}, see Fig. 2.1. In the system

---

[1] It is expressed as a vacuum for some simulations cases, greatly decreasing the calculation time.

model, V_{0m} is differed from V_0 to account for the effect of coaxial cable #2, connecting the generator and the oscilloscope. V_{0m} is the voltage at the input terminals to the oscilloscope, and V_0 is at the output terminals of the generator. The oscilloscope represents a termination impedance, which results in a small electrical load on the receiving electronics.

In calculation of the system model, the system in Fig. 2.1 is assumed to be linear. Each module is represented by a transfer function, relating the output to the input value [17]. The voltage-to-voltage transfer function from node i to node j is denoted H_{ij}^{VV}. Being expressed as transfer functions, the modules can readily be removed or added, to adapt the system model to other measurement systems. For the system model in Fig. 2.1, the transfer function expressing V_6 based on V_{0m}, H_{0m6}^{VV}, is given as

$$H_{0m6}^{VV} \equiv \frac{V_6}{V_{0m}} = \frac{V_0}{V_{0m}} \cdot \frac{V_1}{V_0} \cdot \frac{v_2}{V_1} \cdot \frac{p_3}{v_2} \cdot \frac{\langle p_4 \rangle}{p_3} \cdot \frac{V_5}{\langle p_4 \rangle} \cdot \frac{V_6}{V_5}. \tag{2.1}$$

The ratio expressed by H_{0m6}^{VV} corresponds to the two recorded voltages in the experimental setup. In the following section, the transfer function expressing the output voltage from Module E, based on the input voltage to Module C is calculated.

2.2 Calculation of $H_{15}^{VV,open}$

In this section, the transfer function $H_{15}^{VV,open}$, is calculated. $H_{15}^{VV,open}$ is defined as

$$H_{15}^{VV,open} \equiv \frac{V_5^{open}}{V_1}, \tag{2.2}$$

where V_5^{open} is the output voltage from the receiving transducer under open-circuit conditions, i.e. the receiving transducer is terminated with an infinite impedance, to simplify the calculation. $H_{15}^{VV,open}$ might also be expressed as

$$H_{15}^{VV,open} = \frac{v_2}{V_1} \cdot \frac{p_3}{v_2} \cdot \frac{\langle p_4 \rangle}{p_3} \cdot \frac{V_5^{open}}{\langle p_4 \rangle}, \tag{2.3}$$

thus H_{15}^{VV} is used to replace node 1 through 5 with open-circuit conditions in Eq. (2.1), and H_{0m6}^{VV} is then expressed as

$$H_{0m6}^{VV} = \frac{V_0}{V_{0m}} \cdot \frac{V_1}{V_0} \cdot H_{15}^{VV,open} \cdot \frac{V_5}{V_5^{open}} \cdot \frac{V_6}{V_5}, \tag{2.4}$$

where $V_0/V_{0m} \cdot V_1/V_0$ and $V_5/V_5^{open} \cdot V_6/V_5$ are calculated in Section 2.6. $H_{15}^{VV,open}$ is valid for a lossless medium, rendering H_{0m6}^{VV} in Eq. (2.4) impractical for an absolute comparison with experimental results. Hence $H_{15}^{VV,open}$ is modified in Section 2.4 to include the absorption inherent in air.

In Fig. 2.2, the system model with the Thévenin equivalent circuit used for Module A, and open-circuit conditions applied for Module E is shown.

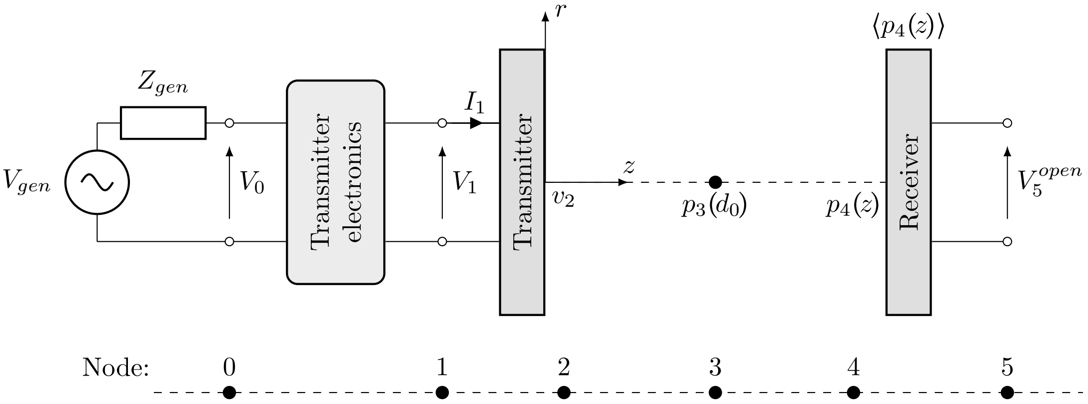

Figure 2.2: Modules A through E, with open-circuit conditions applied for Module D.

In Fig. 2.2, I_1 is the current input to the transmitter. The origin of the (r, z) coordinate system is at the center of the front face of the transmitting transducer, r is the radial distance and z is the axial distance to the receiving transducers front. In node 4, $\langle . \rangle$ denotes that $p_4(z)$ is averaged over the acoustically sensitive area of the receiving transducer, A, i.e.

$$\langle p_4(z) \rangle \equiv \frac{1}{A} \int_A p_4(r,z) dA. \tag{2.5}$$

Generally the area A is the complete surface of the transducer, but in the present work, A is the area of the front surface of the receiver, simplifying the derivation of $\langle p_4(z) \rangle$.

In the current section, Module D (cf. Fig. 2.1) is assumed to be homogeneous and lossless. The absorption effects of the air in Module D are covered in Section 2.4. The model utilizes a general pressure sound wave propagation model, which is normalized using two different theoretical models, in order to include the effect of the distance dependent acoustic diffraction at the transducers, termed diffraction correction. The two models are;

- *Model 1:* which was developed in [31], based on the concept and ideas presented in [32]. It is used e.g. in [11, 12, 33–35]. V_5^{open} is expressed using both a general sound propagation model, and a plane wave propagation model is used as normalization for the diffraction correction.
- *Model 2:* Developed by Lunde in [31]. V_5^{open} is expressed using a relatively general propagation model, as for *Model 1*. The far-field sound pressure $p_4(z_\infty)$ is used as normalization, expressing a relative diffraction correction.

Both *Model 1* and *Model 2* consider the diffraction correction in a sound field calculated using a full description of the transmitting transducer, with different normalizations of the diffraction correction. These models makes it possible to do comparisons between the traditional and well known, to the more advanced methods of calculating the diffraction correction. The diffraction correction methods are further discussed in Section 2.3.

In the following, *Model 1* and *Model 2* are presented in Sections 2.2.1 and 2.2.2, respectively.

2.2.1 *Model 1*: Using the plane wave propagation model as reference

The model presented in this section is derived in [31], from which the notation here is adopted. Two output voltages from the measurement system in Fig. 2.2 are defined, V_5^{open} and $V_{5,plane}^{open}$. V_5^{open} is the output voltage from the measurement system, using a relatively general sound propagation model, e.g. by use of FE modeling, giving

$$V_5^{open} = V_0 \cdot \frac{V_1}{V_0} \cdot \frac{v_2}{V_1} \cdot \frac{p_3(d_0)}{v_2} \cdot \frac{\langle p_4(z) \rangle}{p_3(d_0)} \cdot \frac{V_5^{open}}{\langle p_4(z) \rangle}. \tag{2.6}$$

$V_{5,plane}^{open}$ is similar to V_5^{open}, but with a plane wave propagation model utilized, i.e.

$$V_{5,plane}^{open} = V_0 \cdot \frac{V_1}{V_0} \cdot \frac{v_2}{V_1} \cdot \frac{p_3^{plane}(d_0)}{v_2} \cdot \frac{p_4^{plane}(z)}{p_3^{plane}(d_0)} \cdot \frac{V_{5,plane}^{open}}{p_4^{plane}(z)}, \tag{2.7}$$

where $p_4^{plane}(z)$ is the free-field plane wave sound pressure at distance z from the transmitter, with particle velocity v_2, i.e. [36]

$$p_4^{plane}(z) = v_2 \rho c e^{-ikz}. \tag{2.8}$$

$p_3^{plane}(d_0)$, is equivalent to $p_4^{plane}(z)$, but expressed at the reference distance d_0, i.e.

$$p_3^{plane}(d_0) = v_2 \rho c e^{-ikd_0}. \tag{2.9}$$

Next, a method for describing the diffraction correction, accounting for a non-uniformly vibrating transmitter is given. This method was first presented in [32]. The axial free-field sound pressure in the medium at the far-field distance z_∞, $p_4(z_\infty)$, is considered. The sound field at z_∞ is assumed to be spherical, hence $p_4(z_\infty)$ is extrapolated back to the front of the transmitting transducer, using the axial far-field expression for an uniformly vibrating circular piston source mounted in a rigid baffle of infinite extent (hereafter referred to as the "piston source"), resulting in an equivalent piston source velocity at the transmitters front, $v_2^{eq,pist}$, given as [34]

$$v_2^{eq,pist} = \frac{2 z_\infty e^{ikz_\infty}}{i \rho c k a^2} \cdot p_4(z_\infty), \tag{2.10}$$

where $k = \frac{\omega}{c}$ is the wave number and a is the radius of the transmitting transducer. ρ and c is the density and sound speed in Module D, respectively. The particle velocity $v_2^{eq,pist}$ is the required particle velocity of a piston source needed to generate the far-field pressure $p_4(z_\infty)$ [34]. The equivalent particle velocity $v_2^{eq,pist}$ is in turn used to calculate the equivalent free-field plane wave sound pressure in the medium at distance z, i.e.

$$p_4^{eq,plane}(z) = v_2^{eq,pist} \rho c e^{-ikz}. \tag{2.11}$$

$p_4^{eq,plane}(z)$ represents the pressure in a plane wave with particle velocity $v_2^{eq,pist}$ [34], and is used for normalization when defining the diffraction correction relative to plane waves.

Using the plane wave propagation model as normalization for the relatively general propagation model, the ratio of V_5^{open} to $V_{5,plane}^{open}$ is expressed from Eqs. (2.6) and (2.7) as

$$\frac{V_5^{open}}{V_{5,plane}^{open}} = \frac{\langle p_4(z) \rangle}{p_4^{plane}(z)} \cdot \frac{\dfrac{V_5^{open}}{\langle p_4(z) \rangle}}{\dfrac{V_{5,plane}^{open}}{p_4^{plane}(z)}}. \tag{2.12}$$

The expression is simplified further by defining the open-circuit free-field receiving voltage sensitivity, for normally incident pressure waves as [37][2]

$$M_V \equiv \frac{V_{5,\infty}^{open}}{p_4(z_\infty)}, \tag{2.13}$$

where $V_{5,\infty}^{open}$ and $p_4(z_\infty)$ are found in the far-field. To simplify Eq. (2.12), M_V is assumed to be independent of the axial distance between the transmitter and receiver, i.e.

$$\frac{V_5^{open}}{\langle p_4(z) \rangle} = \frac{V_{5,plane}^{open}}{p_4^{plane}(z)} = \frac{V_{5,\infty}^{open}}{p_4(z_\infty)} \equiv M_V. \tag{2.14}$$

M_V expressed in Eq. (2.14) is hence used to simplify Eq. (2.12),

$$\frac{V_5^{open}}{V_{5,plane}^{open}} = \frac{\langle p_4(z) \rangle}{p_4^{plane}(z)}. \tag{2.15}$$

The plane wave pressure $p_4^{plane}(z)$ is expressed by dividing Eq. (2.8) by Eq. (2.11),

$$\frac{p_4^{plane}(z)}{p_4^{eq,plane}(z)} = \frac{v_2 \rho c e^{-ikz}}{v_2^{eq,pist} \rho c e^{ikz}} = \frac{v_2}{v_2^{eq,pist}},$$
$$p_4^{plane}(z) = \frac{v_2}{v_2^{eq,pist}} \cdot p_4^{eq,plane}(z). \tag{2.16}$$

Inserting Eq. (2.16) into Eq. (2.15) yields

$$\frac{V_5^{open}}{V_{5,plane}^{open}} = \frac{v_2^{eq,pist}}{v_2} \cdot \frac{\langle p_4(z) \rangle}{p_4^{eq,plane}(z)} = \frac{v_2^{eq,pist}}{v_2} \cdot H^{dif}(z), \tag{2.17}$$

where $H^{dif}(z)$ is the diffraction correction, defined as [32]

$$H^{dif}(z) \equiv \frac{\langle p_4(z) \rangle}{p_4^{eq,plane}(z)}. \tag{2.18}$$

$H^{dif}(z)$ expressed using Eq. (2.18) corresponds to the Simplified Finite element Diffraction Correction (SFDC) method [31], where the sound field in which $\langle p_4(z) \rangle$ is expressed, is calculated using a full description of the transmitting transducer. In Section 2.3, the SFDC method is further discussed, and compared to a more traditional method of calculating the diffraction correction.

Using Eq. (2.17), V_5^{open} is written as

$$V_5^{open} = V_{5,plane}^{open} \cdot \frac{v_2^{eq,pist}}{v_2} \cdot H^{dif}(z). \tag{2.19}$$

---

[2] A different notation is used here.

By dividing Eq. (2.19) by the input voltage to the system, V_1, the voltage-to-voltage transfer function from node 1 to node 5 under open-circuit conditions, $H_{15}^{VV,open}$, is given as

$$H_{15}^{VV,open} \equiv \frac{V_5^{open}}{V_1} = H_{15,plane}^{VV,open} \cdot \frac{v_2^{eq,pist}}{v_2} \cdot H^{dif}(z), \tag{2.20}$$

where

$$H_{15,plane}^{VV,open} \equiv \frac{V_{5,plane}^{open}}{V_1} = \frac{p_4^{plane}(z)}{V_1} \cdot \frac{V_{5,plane}^{open}}{p_4^{plane}(z)} = \frac{v_2 \rho c e^{-ikz}}{V_1} \cdot M_V. \tag{2.21}$$

By inserting $H_{15,plane}^{VV,open}$ from Eq. (2.21), and $v_2^{eq,pist}$ from Eq. (2.10), into Eq. (2.20) the transfer function $H_{15}^{VV,open}$ is expressed as [31]

$$H_{15}^{VV,open} = \frac{c}{i\pi a^2 f V_1} p_4(z_\infty) z_\infty M_V H^{dif}(z) e^{ik(z_\infty - z)}. \tag{2.22}$$

Hereafter, $H_{15}^{VV,open}$ expressed using Eq. (2.22), is termed *Model 1* [31]. $H_{15}^{VV,open}$ is used in Eq. (2.4), and modified in Section 2.4 to include the absorption inherent in Module D. In Section 2.2.2, an alternative and equivalent model for calculating $H_{15}^{VV,open}$ is presented.

2.2.2 *Model 2*: Using far-field as reference

This model is developed by Lunde in [31], from which the notation and following derivation is adopted. As in Section 2.2.1, two voltages in node 5 are expressed, i.e. V_5^{open}, given in Eq. (2.6), for the relatively general propagation model, and $V_{5,\infty}^{open}$, which is the output voltage from the receiver, when the receiver is in the transmitters far-field, i.e. $z = z_\infty$. $V_{5,\infty}^{open}$ is given as [31]

$$V_{5,\infty}^{open} = V_0 \cdot \frac{V_1}{V_0} \cdot \frac{v_2}{V_1} \cdot \frac{p_3(d_0)}{v_2} \cdot \frac{\langle p_4(z_\infty)\rangle}{p_3(d_0)} \cdot \frac{V_{5,\infty}^{open}}{\langle p_4(z_\infty)\rangle}. \tag{2.23}$$

The ratio of V_5^{open}, defined in Eq. (2.6), to $V_{5,\infty}^{open}$ is expressed as

$$\frac{V_5^{open}}{V_{5,\infty}^{open}} = \frac{\langle p_4(z)\rangle}{\langle p_4(z_\infty)\rangle} \cdot \frac{\dfrac{V_5^{open}}{\langle p_4(z)\rangle}}{\dfrac{V_{5,\infty}^{open}}{\langle p_4(z_\infty)\rangle}}. \tag{2.24}$$

For far-field conditions the free-field sound pressure averaged over the sensitive surface of a finite receiver, $\langle p_4(z_\infty)\rangle$, is approximated by the axial free-field sound pressure in that position, $p_4(z_\infty)$ [31], i.e.

$$\langle p_4(z_\infty)\rangle \approx p_4(z_\infty). \tag{2.25}$$

The relative diffraction correction, $R^{dif}(z)$ is now introduced. The relative diffraction correction is defined as the ratio of the averaged free-field sound pressure over the sensitive area of the receiver at measurement distance z, $\langle p_4(z)\rangle$, to the averaged free-field sound pressure over a receiver in the farfield, $\langle p_4(z_\infty)\rangle$ [31], i.e.

$$R^{dif}(z) \equiv \frac{\langle p_4(z)\rangle}{\langle p_4(z_\infty)\rangle}. \tag{2.26}$$

M_V, defined in Eq. (2.13), is assumed to be independent of z and thus valid for both near-field and far-field distances, i.e.

$$\frac{V_5^{open}}{\langle p_4(z)\rangle} = \frac{V_{5,\infty}^{open}}{p_4(z_\infty)} = M_V. \tag{2.27}$$

Using Eqs. (2.26) and (2.27), along with the assumption in Eq. (2.25), the ratio of voltages in Eq. (2.24) is expressed as

$$\frac{V_5^{open}}{V_{5,\infty}^{open}} \approx \frac{\langle p_4(z)\rangle}{\langle p_4(z_\infty)\rangle} = R^{dif}(z). \tag{2.28}$$

The open-circuit output voltage from the receiver is then approximated as

$$V_5^{open} \approx R^{dif}(z) \cdot V_{5,\infty}^{open}. \tag{2.29}$$

An alternative, and equivalent, expression for the relative diffraction correction, is composed using $H^{dif}(z)$ at distances z and z_∞, expressing the relation between $R^{dif}(z)$ and $H^{dif}(z)$ [31].

$$\begin{aligned} R^{dif}(z) &\equiv \frac{\langle p_4(z)\rangle}{\langle p_4(z_\infty)\rangle} = \frac{\langle p_4(z)\rangle}{p_4^{eq,plane}(z)} \cdot \frac{p_4^{eq,plane}(z)}{p_4^{eq,plane}(z_\infty)} \cdot \frac{1}{\dfrac{\langle p_4(z_\infty)\rangle}{p_4^{eq,plane}(z_\infty)}}, \\ &= \frac{H^{dif}(z)}{H^{dif}(z_\infty)} \cdot \frac{p_4^{eq,plane}(z)}{p_4^{eq,plane}(z_\infty)} = \frac{H^{dif}(z)}{H^{dif}(z_\infty)} \cdot \frac{v_0^{eq,pist}\rho c e^{-ikz}}{v_0^{eq,pist}\rho c e^{-ikz_\infty}}, \\ &= \frac{H^{dif}(z)}{H^{dif}(z_\infty)} \cdot e^{-ik(z-z_\infty)}, \end{aligned} \tag{2.30}$$

where Eqs. (2.11) and (2.18) are used, and

$$H^{dif}(z_\infty) \equiv \frac{\langle p_4(z_\infty)\rangle}{p_4^{eq,plane}(z_\infty)} \approx \frac{p_4(z_\infty)}{p_4^{eq,plane}(z_\infty)}, \tag{2.31}$$

is the diffraction correction at far-field distance z_∞. $R^{dif}(z)$ is thus alternatively expressed as the ratio of the diffraction correction at distance z to the diffraction correction at the far-field distance z_∞, multiplied by the plane wave phase $e^{-ik(z-z_\infty)}$.

Hence the relative diffraction correction might be expressed using either the definition in Eq. (2.26) together with the approximation in Eq. (2.25), or using the ratio of diffraction correction as seen in Eq. (2.30). These alternatives are expressed respectively as *Model 2A* and *Model 2B* in Eq. (2.32) [31].

$$R^{dif}(z) \equiv \frac{\langle p_4(z)\rangle}{\langle p_4(z_\infty)\rangle} \approx \begin{cases} \dfrac{\langle p_4(z)\rangle}{p_4(z_\infty)} = \dfrac{V_5^{open}}{V_{5,\infty}^{open}}. & Formulation\ A \\ \dfrac{H^{dif}(z)}{H^{dif}(z_\infty)} \cdot e^{-ik(z-z_\infty)}. & Formulation\ B \end{cases} \tag{2.32}$$

For calculating $R^{dif}(z)$ using *formulation A*, $\langle p_4(z)\rangle$ and $p_4(z_\infty)$ are needed. These values are obtained using the finite element modeling program used in the current work, see Section 2.7. When $R^{dif}(z)$ is calculated using *formulation B*, the diffraction correction H^{dif} is needed for distances z and z_∞. Using *formulation A* and *B* for calculating $R^{dif}(z)$ makes it possible to compare e.g. FE simulations to simplified and traditional models for calculating $H^{dif}(z)$. A simplified model for calculating H^{dif} is presented in Section 2.3.

As in Section 2.2.1, the receiver output voltage, V_5^{open}, found in Eq. (2.29), is divided by the transmitters input voltage V_1, expressing the open circuit voltage-to-voltage transfer function, $H_{15}^{VV,open}$, as

$$H_{15}^{VV,open} \equiv \frac{V_5^{open}}{V_1} \approx H_{15,\infty}^{VV,open} \cdot R^{dif}(z), \tag{2.33}$$

where

$$H_{15,\infty}^{VV,open} \equiv \frac{V_{5,\infty}^{open}}{V_1}. \tag{2.34}$$

Alternatively, $H_{15,\infty}^{VV,open}$ is expressed using M_V, defined in Eq. (2.13), and the open-circuit free-field transmitting voltage response, S_V, defined as [37] [3]

$$S_V \equiv \frac{p_3(d_0)}{V_1}. \tag{2.35}$$

Hence

$$H_{15,\infty}^{VV,open} \equiv \frac{V_{5,\infty}^{open}}{V_1} \approx \frac{p_3(d_0)}{V_1} \cdot \frac{p_4(z_\infty)}{p_3(d_0)} \cdot \frac{V_{5,\infty}^{open}}{p_4(z_\infty)} = S_V \cdot M_V \cdot \frac{p_4(z_\infty)}{p_3(d_0)}. \tag{2.36}$$

Eq. (2.36) is inserted into Eq. (2.33), giving

$$H_{15}^{VV,open} \approx S_V \cdot M_V \cdot \frac{p_4(z_\infty)}{p_3(d_0)} \cdot R^{dif}(z). \tag{2.37}$$

---

[3] A different notation is used here.

Using *Formulation A* for $R^{dif}(z)$ gives [31]

$$H_{15}^{VV,open} \approx S_V \cdot M_V \cdot \frac{p_4(z_\infty)}{p_3(d_0)} \cdot \frac{\langle p_4(z)\rangle}{p_4(z_\infty)} = S_V \cdot M_V \cdot \frac{\langle p_4(z)\rangle}{p_3(d_0)}, \tag{2.38}$$

while using *Formulation B* for $R^{dif}(z)$ gives [31]

$$H_{15}^{VV,open} \approx S_V \cdot M_V \cdot \frac{p_4(z_\infty)}{p_3(d_0)} \cdot \frac{H^{dif}(z)}{H^{dif}(z_\infty)} \cdot e^{ik(z-z_\infty)}. \tag{2.39}$$

Hereafter, $H_{15}^{VV,open}$ expressed using Eqs. (2.38) and (2.39) are referred to as *Model 2A* and *Model 2B*, respectively [31]. H_{0m6}^{VV}, as expressed in Eq. (2.4) can now be calculated using Eqs. (2.22) and (2.38) - (2.39) to express $H_{15}^{VV,open}$.

2.3 Diffraction correction

The diffraction correction is defined in Eq. (2.18), where $\langle p_4(z)\rangle$ is the free-field sound pressure generated by a transducer, presently averaged over the front surface of the receiver, and $p_4^{eq,plane}$ is the equivalent plane sound pressure, cf. Section 2.2. Both these quantities are known; $\langle p_4(z)\rangle$ by FE simulations (cf. Section 2.7) and $p_4^{eq,plane}(z)$ by Eq. (2.11), where FE simulations also are applied.

Calculating $H^{dif}(z)$ directly using Eq. (2.18) corresponds to the SFDC method [32]. Both the theory in Section 2.2 and the FE modeling makes calculation of $H^{dif}(z)$ by use of SFDC available. However, the method is still being tested [1, 11], and usage and discussion of SFDC is thus not prioritized in the current work, as it is not part of the thesis scope. Instead, a traditional method for calculating $H^{dif}(z)$ is used here.

The simplified model, used for calculating the diffraction correction in this work, is Khimunin's diffraction correction for a piston source [38]. It is seen that $H^{dif}(z)$ is equivalent to Khimunin's diffraction correction, generalized to include the description of a full transmitter.

Khimunin's diffraction correction

Fig. 2.3 illustrates a piston source with radius a, and a circular "receiving area" with radius b, coaxially aligned with the transmitter, and separated from the transmitter with distance z. The "receiving area" is acoustically transparent and is in the position of the receiver.

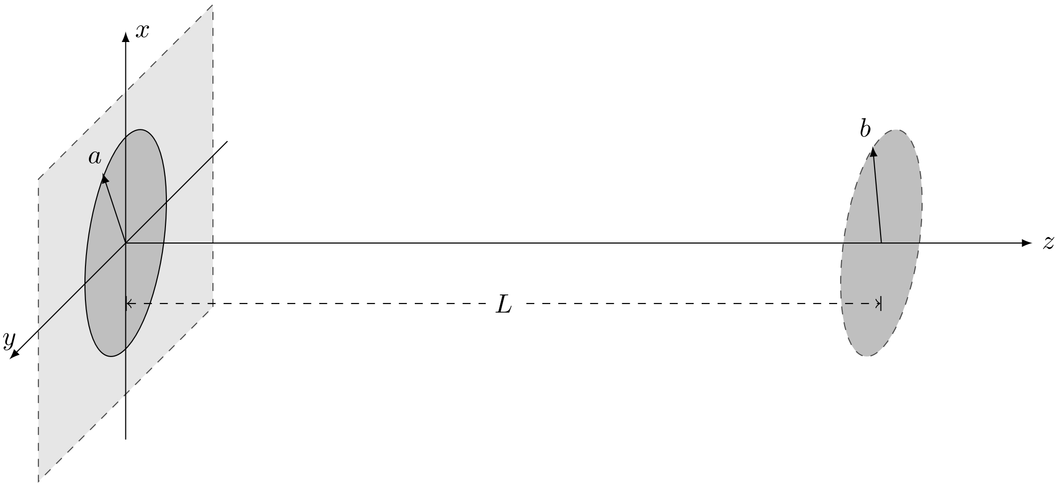

Figure 2.3: Illustration of a piston source (left) and a "receiving area" (right) at distance z from the source. The piston source and "receiving area" are coaxially aligned and have parallel faces.

The diffraction correction as defined by Khimunin is [38]

$$H_K^{dif}(z) \equiv \frac{\langle p(z)\rangle}{p^{plane}(z)}, \tag{2.40}$$

where $\langle p\rangle$ is the free-field sound pressure averaged over the "receiving area" at distance z. p^{plane} is the plane wave pressure at the same distance. Based on Williams' theory for a piston source [39], Khimunin formulated and calculated the diffraction correction for the magnitude [38] and phase [40], for $a = b$, see Fig. 2.3. The diffraction correction $H_K^{dif}(z)$ is given in [36] as

$$H_K^{dif}(ka,S) = 1 - \frac{4}{\pi}\int_0^{\pi/2} \exp\left[-i\frac{(ka)^2 S}{2\pi}\sqrt{1+\left(\frac{4\pi}{Ska}\right)^2\cos^2(\theta)}\right]\sin^2(\theta)\mathrm{d}\theta, \tag{2.41}$$

where θ is an integration variable, ka is a dimensionless quantity, and S is the frequently used normalization distance, defined by $S = z/(a^2/\lambda)$ [41]. Numerical methods must be used to calculate H_K^{dif}, as there is no analytical solution for the general case with arbitrary ka [11]. Eq. (2.41) is in this work calculated using numerical integration in the MATLAB script `Khimunin_diffractioncorrection.m`, see Appendix A.3.1.

When comparing Khimunins diffraction correction, $H_K^{dif}(z)$, to $H^{dif}(z)$ as defined in Eq. (2.18), it is seen that these definitions of the diffraction correction are analog.

$H^{dif}(z)$ is valid for a relatively generalized transmitting transducer, cf. Fig. 2.1 Module C, and reduces to $H_K^{dif}(z)$ when using a piston source. However, the SFDC method is still under testing, and thus Khimunin's method is used here as a simplified, but well known, traditional alternative for calculating the diffraction correction.

2.4 Propagation loss in air

In Section 2.2, $H_{15}^{VV,open}$ was expressed using two models, both for a lossless medium in Module D, cf. Fig. 2.1. In order to represent the experimental setup described in Chapter 3, knowledge about the loss of acoustical energy through the medium in which the sound propagates is needed. The medium in the experimental setup is air at 1 atm. and room temperature. The absorption in air is included in the system model by defining a complex wavenumber κ, i.e.

$$\kappa \equiv k - i\alpha, \tag{2.42}$$

where α is the absorption coefficient in air. The absorption coefficient for air is calculated using the model in [42], and implemented in the MATLAB script `absorbsjonluft.m`, cf. Appendix A.3.2.

The sound pressure in node 3 and 4, for a medium with propagation loss is defined as

$$p_{3,\alpha}(d_0) \equiv P_3(d_0)\cdot e^{-i\kappa d_0} = P_3(d_0)\cdot e^{-ikd_0}\cdot e^{-\alpha d_0}, \text{ and} \tag{2.43}$$

$$p_{4,\alpha}(z) \equiv P_4(z)\cdot e^{-i\kappa z} = P_4(z)\cdot e^{-ikz}\cdot e^{-\alpha z}, \tag{2.44}$$

where $P_3(d_0)$ and $P_4(z)$ is the lossless amplitude functions for node 3 and 4 respectively. A quantity calculated were the absorption in the medium is taken into account, is denoted "α". The lossless amplitude function multiplied with the propagation term yields the free-field axial sound pressure in the lossless medium as used in Section 2.2.

$$p_3(d_0) = P_3(d_0)\cdot e^{-ikd_0}, \tag{2.45}$$

$$p_4(z) = P_4(z)\cdot e^{-ikz}. \tag{2.46}$$

Hence $p_{3,\alpha}(d_0)$ and $p_{4,\alpha}(z)$ are written as

$$p_{3,\alpha}(d_0) = p_3(d_0)\cdot e^{-\alpha d_0}, \tag{2.47}$$

$$p_{4,\alpha}(z) = p_4(z)\cdot e^{-\alpha z}. \tag{2.48}$$

The expression $p_{4,\alpha}(z) = p_4(z)e^{-\alpha z}$ is also assumed to be valid in the far-field at axial distance z_∞ and for the averaged sound pressure over the receiver, $\langle p_4(z)\rangle$,

$$p_{4,\alpha}(z_\infty) = p_4(z_\infty)\cdot e^{-\alpha z_\infty}, \tag{2.49}$$

$$\langle p_{4,\alpha}(z)\rangle = \langle p_4(z)\rangle\cdot e^{-\alpha z}. \tag{2.50}$$

where it is assumed in Eq. (2.50) that the absorption is equal over the sensitive area of the receiver. Using Eq. (2.47), the transmitting voltage response with propagation loss, $S_{V,\alpha}$, is defined as

$$S_{V,\alpha} \equiv \frac{p_{3,\alpha}(d_0)}{V_1} = \frac{p_3(d_0)}{V_1}\cdot e^{-\alpha d_0} = S_V\cdot e^{-\alpha d_0}. \tag{2.51}$$

The expressions for the free-field axial plane wave sound pressure in position d_0 and z, $p_3^{plane}(d_0)$ and $p_4^{plane}(z)$, as well as the equivalent plane wave axial sound pressure, $p_4^{eq,plane}(z)$, are found with losses included by letting $k \to \kappa$ in Eqs. (2.8) - (2.11), giving

$$p_{4,\alpha}^{plane}(z) = v_2 \rho c e^{-i\kappa z} = v_2 \rho c e^{-ikz} \cdot e^{-\alpha z}, \tag{2.52}$$

$$p_{3,\alpha}^{plane}(d_0) = v_2 \rho c e^{-i\kappa d_0} = v_2 \rho c e^{-ikd_0} \cdot e^{-\alpha d_0}, \tag{2.53}$$

$$p_{4,\alpha}^{eq,plane}(z) = v_{2,\alpha}^{eq,pist} \rho c e^{-i\kappa z} = v_{2,\alpha}^{eq,pist} \rho c e^{-ikz} \cdot e^{-\alpha z}. \tag{2.54}$$

The particle velocity on the front of the transmitter, v_2, is here assumed to be independent of the absorption in air. The equivalent piston source particle velocity with absorption loss, $v_{2,\alpha}^{eq,pist}$, is found by letting $k \to \kappa$ in Eq. (2.10), i.e.

$$v_{2,\alpha}^{eq,pist} = \frac{2z_\infty}{i\rho\pi f a^2} \cdot p_{4,\alpha}(z_\infty) \cdot e^{i\kappa z_\infty} = \frac{2z_\infty}{i\rho\pi f a^2} \cdot p_4(z_\infty) \cdot e^{ikz_\infty}. \tag{2.55}$$

Using Eqs. (2.47) - (2.55), $H_{15}^{VV,open}$ for a lossy medium, $H_{15,\alpha}^{VV,open}$, are expressed as:

Model 1:

$$H_{15,\alpha}^{VV,open} = \frac{z_\infty c}{i\pi a^2 f V_1} \cdot p_4(z_\infty) \cdot M_V \cdot H^{dif}(z) \cdot e^{-ik(z-z_\infty)} \cdot e^{-\alpha z} \tag{2.56}$$

Model 2A:

$$H_{15,\alpha}^{VV,open} \approx S_V \cdot M_V \cdot \frac{\langle p_4(z) \rangle}{p_3(d_0)} \cdot e^{-\alpha z} \tag{2.57}$$

Model 2B:

$$H_{15,\alpha}^{VV,open} \approx S_V \cdot M_V \cdot \frac{p_4(z_\infty)}{p_3(d_0)} \cdot \frac{H^{dif}(z)}{H^{dif}(z_\infty)} \cdot e^{-ik(z-z_\infty)} \cdot e^{-\alpha z} \tag{2.58}$$

The fluid medium in the simulation tool used in this work, FEMP , is implemented without losses. The sound pressures used in the models for calculating $H_{15}^{VV,open}$ are thus calculated in FEMP and implemented as the lossless quantities $p_3(d_0)$, $p_4(z)$ and $\langle p_4(z) \rangle$. The quantities calculated by FEMP are then implemented in the above system models using Eqs. (2.56) - (2.58). $H_{15,\alpha}^{VV,open}$ is inserted into Eq. (2.4), giving H_{0m6}^{VV} for a lossy medium in Module D as

$$H_{0m6,\alpha}^{VV} = \frac{V_0}{V_{0m}} \cdot \frac{V_1}{V_0} \cdot H_{15,\alpha}^{VV,open} \cdot \frac{V_5}{V_5^{open}} \cdot \frac{V_6}{V_5}. \tag{2.59}$$

2.5 Use of spherical wave reciprocity

In each expression for $H_{15,\alpha}^{VV,open}$ found above, Eqs. (2.56) - (2.58), the open-circuit receiving voltage sensitivity, M_V, is required. In order to represent the experimental setup used in this work, presented in Chapter 3, M_V for different receivers are needed. Three types of receivers are utilized in the present measurement system, cf. Module E in Section 2.1. For the piezoelectric ceramic disks and the presently constructed transducers, cf. Chapter 6, M_V is not yet known, but this is part of on-going work [2]. As for the condenser microphone, frequency response data provided by the manufacturer combined with a calibration conducted in this work, yields information about $|M_V|$ up to 200 kHz, cf. Section 3.5.1. Hence when the microphone is used as the receiver, the system model transfer function is calculated using the calibrated $|M_V|$ for the microphone. But for the piezoelectric ceramic disk and transducer receiver, M_V is calculated using the complex spherical wave reciprocity.

The transmitting and receiving transducers are assumed to be; equal, linear, passive and reversible [43]. In addition they are assumed to fulfill certain reciprocity relations [43]. Under these assumptions, the relationship between M_V and the transmitting current response S_I, is given as [37,43]

$$J = \frac{M_V}{S_I}, \tag{2.60}$$

where J is the lossless complex spherical wave reciprocity factor, defined as [43]

$$J \equiv \frac{2d_0\lambda}{i\rho c} \cdot e^{ikd_0}. \tag{2.61}$$

The transmitting current response, S_I, is defined as [37][4]

$$S_I \equiv \frac{p_3(d_0)}{I_1}. \tag{2.62}$$

---

[4] A different notation is used here.

The relationship between S_I and S_V is expressed as

$$S_I = \frac{p_3(d_0)}{I_1} = \frac{p_3(d_0)}{\frac{V_1}{Z_T}} = Z_T \cdot \frac{p_3(d_0)}{V_1} = Z_T \cdot S_V, \tag{2.63}$$

where Z_T is the electrical input impedance to the transmitting transducer.

For a medium with propagation loss, J is expressed using the complex wavenumber, κ, defined in Section 2.4, i.e. [31,37]

$$J_\alpha = \frac{2d_0\lambda}{i\rho c} \cdot e^{ikd_0} \cdot e^{\alpha d_0}. \tag{2.64}$$

Thus, in Eqs. (2.56) - (2.58), M_V is expressed as

$$M_V = J_\alpha \cdot Z_T \cdot S_{V,\alpha} = J \cdot e^{\alpha d_0} \cdot Z_T \cdot S_V \cdot e^{-\alpha d_0} = J \cdot Z_T \cdot S_V. \tag{2.65}$$

2.6 Electronics

In the experimental setup used in this work, cf. Chapter 3, both transmitting and receiving electronics are used, cf. Modules B and F in Fig. 2.1. These modules affect both the transmitted and the received signal. Each cable connecting two instruments in the measurement system is expressed using a transfer function. A model for representing the cables is presented, and used to calculate the output voltage from a cable, terminated in one instruments input impedance, based on the input voltage to the cable, connected to another instruments output impedance. The objective of this section is to find V_1/V_{0m} and V_6/V_5^{open}, see Eqs. (2.4) and (2.59). In addition, the transfer function V_1/V_{gen} is found, for use in Section 2.8.

2.6.1 Cables

In the present measurement system, coaxial cables are used in both Module B and F. The cables might influence several important aspects, such as [44]; the measured impedance, the design of the electrical matching network, interference and noise, resonance frequencies, sensitivity changes and transfer functions and impulse responses.

In the current experimental setup, RG-58 coaxial cables with BNC-connectors are used to interconnect the instruments, cf. Section 3. The characteristic impedance of the RG-58 cable is 50 Ω. An overview of the cables used in the experimental setup is given in Table 3.4. In the current work, the cables are described using the distributed element model.

Distributed element model

Let the cable be represented as a lossless transmission line. The distributed element model assumes that the attributes of the transmission line is continuously distributed throughout the material. From [45][5] we have that for a lossless transmission line terminated in an impedance Z_L, the input impedance to the terminated transmission line, Z_{in}, is expressed as

$$Z_{in} = Z_0 \frac{Z_0 + iZ_L \tan(k_{em} l_x)}{Z_L + iZ_0 \tan(k_{em} l_x)}, \tag{2.66}$$

where Z_0 is the characteristic impedance of the cable, which for a lossless transmission line is expressed as [45]

$$Z_0 = \sqrt{\frac{L}{C}}, \tag{2.67}$$

where L and C are the inductance and capacitance per meter for the cable respectively. For the experimental setup used here, typical values for L and C are given in Table 3.3. In Eq. (2.66) k_{em} is the electromagnetic wavenumber expressed as:

$$k_{em} = \frac{\omega}{c_{em}} = \omega\sqrt{LC}, \tag{2.68}$$

where c_{em} is the electrical propagation speed in the cable. l_x is the length of the cable, the length of the cables used in the present measurement system is given in Table 3.4. Fig. 2.4 shows the equivalent circuit for the transmission line terminated in Z_L, with input impedance given in Eq. (2.66) [44].

---

[5] A different notation is used here.

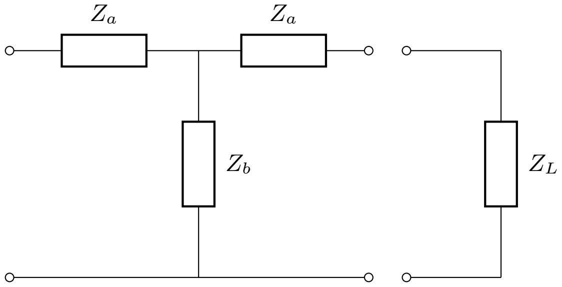

Figure 2.4: An equivalent circuit for a lossless transmission line terminated in Z_L, modeled using a distributed element model.

The impedances in Fig. 2.4, Z_a and Z_b, are expressed as [44]:

$$Z_a = iZ_0 \tan\left(k_{em}\frac{l_x}{2}\right), \tag{2.69}$$

$$Z_b = \frac{Z_0}{i\sin(k_{em}l_x)}. \tag{2.70}$$

The equivalent circuit in Fig. 2.4 together with the impedances Z_a and Z_b are used to model the cables in the experimental setup used in this work.

2.6.2 Transmitting electronics

In Fig. 2.5, the cables connecting nodes 0, $0m$ and 1 (cf. Fig. 2.1) and the generator in Module A is shown. The cables are represented by equivalent circuits as seen in Fig. 2.4, and the subscript numbering of the cable impedances denotes cable number.

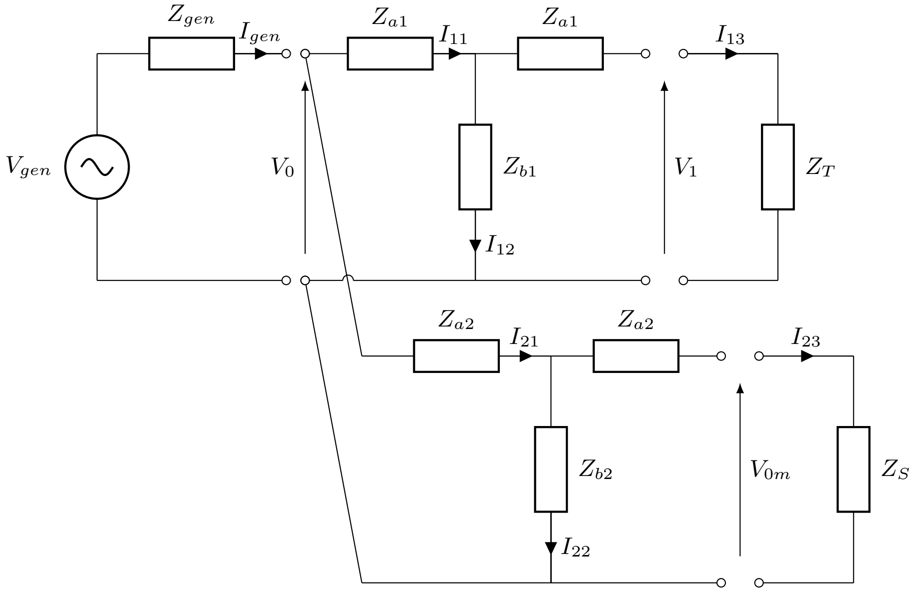

Figure 2.5: Equivalent circuit for the signal generator and the cables connecting it to the transmitting transducer, and oscilloscope.

In Fig. 2.5, Z_{a1}, Z_{b1}, Z_{a2} and Z_{b2} is the different impedances of cable #1 and #2, given by Eqs. (2.69) - (2.70) by inserting $l_x = l_1$ and $l_x = l_2$, respectively. l_1 is the length of cable #1 and l_2 is the length of cable #2, see Table 3.4. Z_T is the electrical input impedance of the transmitting transducer, and Z_S is the input impedance of the oscilloscope, see Table 3.2. I with the different subscripts denotes currents.

In the following, two transfer functions are expressed; $H_{0m1}^{VV} = V_1/V_{0m}$ which is used for expressing H_{0m6}^{VV} (cf. Eq. 2.4), and $H_{gen1}^{VV} = V_1/V_{gen}$ which is used in Section 2.8.

Calculation of H_{0m1}^{VV}

H_{0m1}^{VV} is calculated in two steps, for convenience, by expressing H_{0m1}^{VV} as

$$H_{0m1}^{VV} = \frac{V_1/V_0}{V_{0m}/V_0}, \tag{2.71}$$

and calculating V_1/V_0 and V_{0m}/V_0 separately. First, cable #1 connecting node 0 to node 1, terminated in Z_T is regarded. In Fig. 2.6, the respective part circuit of the circuit in Fig. 2.5 is shown.

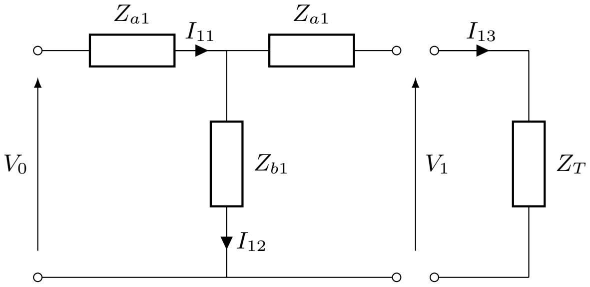

Figure 2.6: Equivalent circuit of the coaxial cable from node 0 to node 1, terminated in the transmitter.

By using Kirchoff's second law on the circuit displayed in Fig. 2.6 the following three equations are derived:

$$V_0 - I_{11}Z_{a1} - I_{13}Z_{a1} - V_1 = 0, \tag{2.72}$$

$$V_1 + I_{13}Z_{a1} - I_{12}Z_{b1} = 0, \tag{2.73}$$

$$V_1 - I_{13}Z_T = 0. \tag{2.74}$$

By using Kirchoff's first law on the currents in the circuit, I_{11} is expressed as

$$I_{11} = I_{12} + I_{13}. \tag{2.75}$$

By using Eq. (2.74), I_{13} is expressed as $I_{13} = V_1/Z_T$. Eq. (2.73) is modified to express I_{12}

$$I_{12} = \frac{V_1 + I_{13}Z_{a1}}{Z_{b1}}. \tag{2.76}$$

By inserting the expression found for I_{13}, I_{12} is expressed as

$$I_{12} = \frac{V_1 + \frac{V_1}{Z_T}Z_{a1}}{Z_{b1}} = V_1\left(\frac{\frac{Z_{a1}}{Z_T} + 1}{Z_{b1}}\right). \tag{2.77}$$

Then, by combining the terms which contains Z_{a1} in Eq. (2.72) and inserting for I_{11} from Eq. (2.75), it is expressed as

$$V_0 - Z_{a1}(I_{12} + 2I_{13}) - V_1 = 0. \tag{2.78}$$

By inserting the expression found for I_{12} and I_{13} above

$$V_0 - Z_{a1}\left(V_1\frac{\frac{Z_{a1}}{Z_T} + 1}{Z_{b1}} + 2\frac{V_1}{Z_T}\right) - V_1 = 0. \tag{2.79}$$

All the terms containing V_1 are collected and moved to the right side of the equation

$$V_0 = V_1\left(\frac{\frac{Z_{a1}^2}{Z_T} + 1}{Z_{b1}} + 2\frac{Z_{a1}}{Z_T} + 1\right). \tag{2.80}$$

By dividing both sides of Eq. 2.80 by V_1, and multiplying the right side by Z_TZ_{b1}, the transfer function $H_{01}^{VV} = V_1/V_0$ is expressed as:

$$H_{01}^{VV} = \frac{V_1}{V_0} = \frac{Z_TZ_{b1}}{Z_{a1}^2 + Z_TZ_{a1} + 2Z_{a1}Z_{b1} + Z_TZ_{b1}}. \tag{2.81}$$

In Fig. 2.7, the section of the circuit in Fig. 2.5 which shows the cable connecting node 0 to $0m$, terminated in Z_S, is shown.

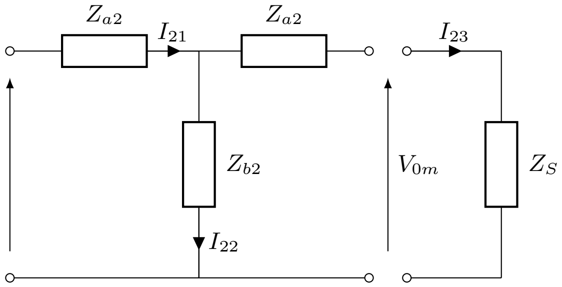

Figure 2.7: Equivalent circuit of the coaxial cable from node 0 to node $0m$, terminated in the oscilloscope.

It is seen that the circuit in Fig. 2.7 is equivalent to Fig. 2.6, hence a similar procedure as for deriving Eq. (2.81) is done for the transfer function $H^{VV}_{00m} = V_{0m}/V_0$, yielding

$$H^{VV}_{00m} = \frac{V_{0m}}{V_0} = \frac{Z_S Z_{b2}}{Z^2_{a2} + Z_S Z_{a2} + 2Z_{a2}Z_{b2} + Z_S Z_{b2}}. \tag{2.82}$$

By inserting Eqs. (2.81) and (2.82) into Eq. (2.71), H^{VV}_{0m1} is expressed as:

$$H^{VV}_{0m1} = \frac{V_1}{V_{0m}} = \frac{H^{VV}_{01}}{H^{VV}_{00m}}. \tag{2.83}$$

H^{VV}_{0m1} is inserted into Eq. (2.59), and $H^{VV}_{0m6,\alpha}$ is thus expressed as

$$H^{VV}_{0m6,\alpha} = H^{VV}_{0m1} \cdot H^{VV,open}_{15,\alpha} \cdot \frac{V_5}{V^{open}_5} \cdot \frac{V_6}{V_5}. \tag{2.84}$$

Calculation of H^{VV}_{gen1}

An alternative representation of the circuit in Fig. 2.5 is shown in Fig. 2.8. As the transfer function H^{VV}_{gen1} is derived, the lower branch of the circuit in Fig. 2.5 is represented by its input impedance, $Z_{in,2}$, given by Eq. (2.66) as

$$Z_{in,2} = Z_0 \frac{Z_0 + iZ_S \tan(k_{em} l_2)}{Z_S + iZ_0 \tan(k_{em} l_2)}, \tag{2.85}$$

where l_2 is the length of cable #2.

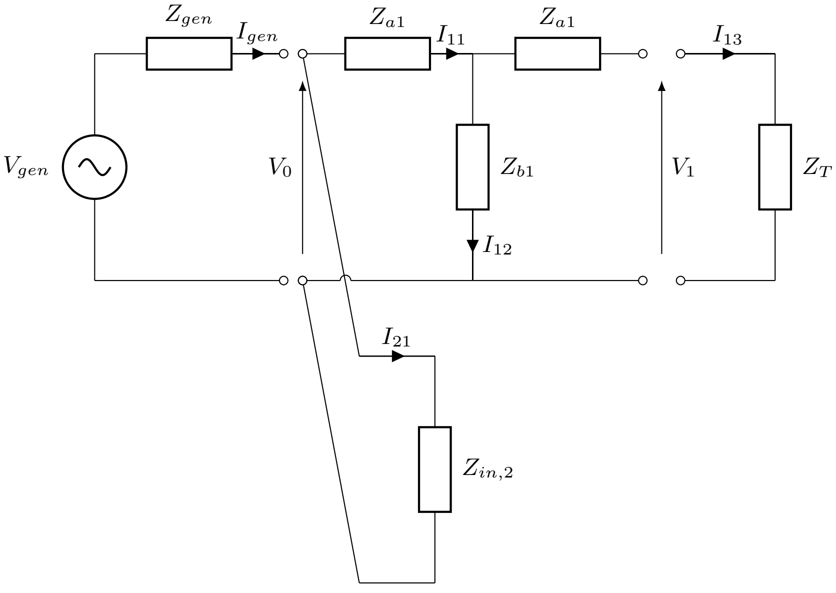

Figure 2.8: As Fig. 2.5, but with the coaxial cable terminated in the oscilloscope expressed with its input impedance.

Using Kirchoffs second law on several loops in the circuit in Fig. 2.8 yields

$$V_{gen} - I_{gen}Z_{gen} - I_{11}Z_{a1} - I_{13}Z_{a1} - V_1 = 0, \tag{2.86}$$

$$V_0 - I_{11}Z_{a1} - I_{21}Z_{b1} = 0, \tag{2.87}$$

$$V_0 - I_{21}Z_{in,2} = 0, \tag{2.88}$$

$$V_1 + I_{13}Z_{a1} - I_{12}Z_{b1} = 0, \tag{2.89}$$

$$V_1 - I_{13}Z_T = 0. \tag{2.90}$$

Using Kirchoffs first law gives the following current relations

$$I_{11} = I_{12} + I_{13}, \tag{2.91}$$

$$I_{gen} = I_{11} + I_{21} = I_{12} + I_{13} + I_{21}. \tag{2.92}$$

Using Eqs. (2.87) , (2.88) and (2.91), I_{21} is expressed as

$$I_{21} = \frac{(I_{12} + I_{13})Z_{a1} + I_{12}Z_{b1}}{Z_{in,2}} \tag{2.93}$$

which is inserted into Eq. (2.92), yielding

$$I_{gen} = I_{12} + I_{13} + \frac{(I_{12} + I_{13})Z_{a1} + I_{12}Z_{b1}}{Z_{in,2}}. \tag{2.94}$$

Using Eqs. (2.89) - (2.90), I_{31} and I_{12} are expressed as

$$I_{13} = \frac{V_1}{Z_T}, \tag{2.95}$$

$$I_{12} = \frac{V_1 + I_{13}Z_{a1}}{Z_{b1}} = V_1 \cdot \frac{1 + \frac{Z_{a1}}{Z_T}}{Z_{b1}}. \tag{2.96}$$

The Eqs. (2.91) and (2.94) - (2.96) is inserted into Eq. (2.86), giving

$$V_{gen} - V_1 \frac{1 + \frac{Z_{a1}}{Z_T}}{Z_{b1}} \left(Z_{gen} \left(1 + \frac{Z_{a1} + Z_{b1}}{Z_{in,2}} \right) + Z_{a1} \right) - \frac{V_1}{Z_T} \left(Z_{gen} \left(1 + \frac{Z_{a1}}{Z_{in,2}} \right) + 2Z_{a1} \right) - V_1 = 0. \tag{2.97}$$

By collecting the terms containing V_1, H^{VV}_{gen1} is expressed as

$$H^{VV}_{gen1} = \frac{Z_{b1}Z_T}{Z_T + Z_{a1}\left(Z_{gen}\left(1 + \frac{Z_{a1}+Z_{b1}}{Z_{in,2}}\right) + Z_{a1}\right) + Z_{b1}\left(Z_{gen}\left(1 + \frac{Z_{a1}}{Z_{in,2}}\right) + 2Z_{a1}\right) + Z_{b1}Z_T}. \tag{2.98}$$

H^{VV}_{gen1} is used in Section 2.8 for propagating V_{gen} to V_1 in node 1.

2.6.3 Receiving electronics

The transfer function for the receiving electronics is $H^{VV}_{5open6} = V_6/V_{5open}$. This function gives the voltage in node 6, terminated in Module G, based on the open-circuit node 5 voltage, connected to Module D, see Fig. 2.1. As explained in Section 2.1 for Module G, the amplifier is connected to the frequency filter in several stages. Hence, electrical modeling of the amplifier and frequency filter are complex, and thus not prioritized in this work. It is assumed that the frequency filter, and the cables connecting it to the amplifier, does not affect the magnitude of the signal at the measurement frequency. The signal amplification is corrected for in the measurement post-process (cf. Section 3.7), giving the measured voltage signal in node 6 without the amplification. The amplification is thus not corrected for in the system model.

In the present measurement setup, three types of transducers are used for Module E, including a pressure condenser microphone made by Brüel & Kjær (B&K). The microphone is connected to the amplifier, also made by B&K, using the cables and connectors supplied by the manufacturer. Modeling of this receiver system is complex due to the structure, and the lack of product data available. Thus, when the microphone is used as receiver, the effect of open-circuit conditions are assumed to be small, and in the frequency range were the microphone is calibrated, cf. Section 3.5.1, it is assumed that $V_6 = V_5^{open}$.

For the other receivers used, the transfer function from node 5 under open-circuit conditions to node 6, H^{VV}_{5open6} is calculated in two steps, by expressing H^{VV}_{5open6} as

$$H_{5open6} = \frac{V_5'}{V_5^{open}} \cdot \frac{V_6}{V_5'}, \tag{2.99}$$

where V_5' is defined as the voltage both over the input and output terminals of the amplifier. In the following V_5'/V_5^{open} and V_6/V_5' is calculated separately.

The receiving transducer is connected to a signal amplifier through coaxial cable #3. The equivalent circuit for this connection is represented in Fig. 2.9.

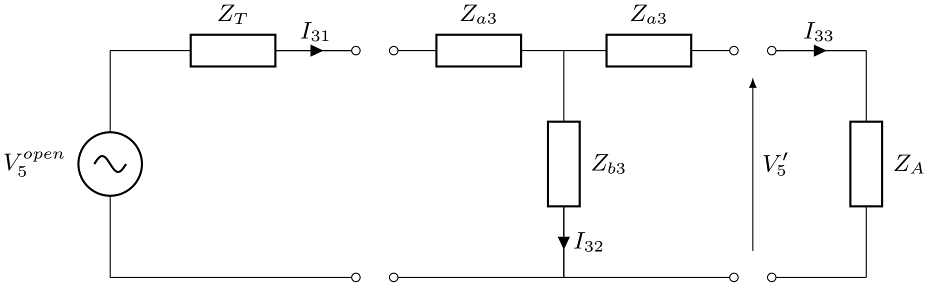

Figure 2.9: Equivalent circuit of the receiving transducer terminated in the amplifier, through a coaxial cable.

In Fig. 2.9, V_5^{open} is the open-circuit output voltage from the receiving transducer. Z_T is the output impedance of the receiving transducer, where it is assumed that the receiving and transmitting transducers are equal (cf. Section 2.5). Z_A is the input impedance of the amplifier, given as 1 MΩ || 90 pF. The impedances Z_{a3} and Z_{b3} are given in Eqs. (2.69) - (2.70) with $l_x = l_3$, where l_3 is the length of cable #3, given in Table 3.4. A set of equations are set up using Kirchoff's second law on Fig. 2.9, i.e.

$$V_5^{open} - I_{31}Z_T - I_{31}Z_{a3} - I_{33}Z_{a3} - V_5' = 0, \tag{2.100}$$

$$V_5' + I_{33}Z_{a3} - I_{32}Z_{b3} = 0, \tag{2.101}$$

$$V_5' - I_{33}Z_A = 0. \tag{2.102}$$

From Eq. (2.102), the current I_{33} is expressed as

$$I_{33} = \frac{V_5'}{Z_A}. \tag{2.103}$$

Using Eq. (2.101), I_{32} is written as

$$I_{32} = \frac{V_5' + I_{33}Z_{a3}}{Z_{b3}} = \frac{V_5' + \frac{V_5}{Z_A}Z_{a3}}{Z_{b3}}, \tag{2.104}$$

where Eq. (2.103) has been used to insert for I_{33}. The relationship between the currents I_{31}, I_{32} and I_{33}, is given by Kirchoff's first law as

$$I_{31} = I_{32} + I_{33}. \tag{2.105}$$

Inserting for I_{31} in Eq. (2.100), using Eq. (2.105), yields

$$V_5^{open} - (I_{32} + I_{33})\,Z_T - (I_{32} + 2I_{33})\,Z_{a3} - V_5' = 0, \tag{2.106}$$

into where I_{32} and I_{33} is inserted using Eqs. (2.103) and (2.104), i.e.

$$V_5^{open} - Z_T\left(\frac{V_5'}{Z_A} + V_5'\frac{1 + \frac{Z_{a3}}{Z_A}}{Z_{b3}}\right) - Z_{a3}\left(V_5'\frac{1 + \frac{Z_{a3}}{Z_A}}{Z_{b3}} + 2\frac{V_5'}{Z_A}\right) - V_5' = 0. \tag{2.107}$$

By collecting the terms including V_5 and isolating V_5^{open}, the ratio V_5/V_5^{open} is expressed as

$$\frac{V_5'}{V_5^{open}} = \frac{1}{Z_T\left(\frac{1}{Z_A} + \frac{1 + \frac{Z_{a3}}{Z_A}}{Z_{b3}}\right) - Z_{a3}\left(\frac{1 + \frac{Z_{a3}}{Z_A}}{Z_{b3}} + \frac{2}{Z_A}\right) - 1} \tag{2.108}$$

which is defined as the voltage-to-voltage transfer function from V_5^{open} to V_5', $H_{5open5'}^{VV}$. For readability, the right side of Eq. (2.108) is multiplied by Z_AZ_{b3}, and $H_{5open5'}^{VV}$ is written as

$$H_{5open5'}^{VV} \equiv \frac{V_5'}{V_5^{open}} = \frac{Z_AZ_{b3}}{Z_TZ_{b3} + Z_TZ_A + Z_TZ_{a3} + Z_AZ_{a3} + Z_{a3}^2 + 2Z_{a3}Z_{b3} + Z_AZ_{b3}}. \tag{2.109}$$

The amplifier is connected to the oscilloscope which records the received signal, through coaxial cable #4. The equivalent circuit for this connection is represented in Fig. 2.10.

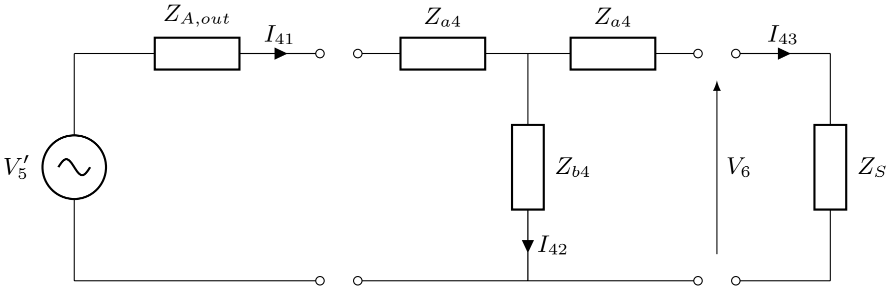

Figure 2.10: Equivalent circuit of the amplifier terminated in the oscilloscope, through a coaxial cable.

In Fig. 2.10, $Z_{A,out}$ is the output impedance of the amplifier, given as 100 Ω. Calculation of the transfer function from V_5' to V_6, $H_{5'6}^{VV}$, corresponds to the calculation of $H_{5open5'}^{VV}$, but with different variables, i.e.

$$H_{5'6}^{VV} = \frac{V_6}{V_5'} = \frac{Z_{A,out}Z_{b4}}{Z_{A,out}Z_{b4} + Z_{A,out}Z_S + Z_{A,out}Z_{a4} + Z_S Z_{a4} + Z_{a4}^2 + 2Z_{a4}Z_{b4} + Z_S Z_{b4}}. \tag{2.110}$$

Using Eqs. (2.109) and (2.110) the transfer function from the output voltage of the receiver, V_5^{open}, to the recorded voltage by the oscilloscope, V_6, is expressed as:

$$H_{5open6}^{VV} = \frac{V_6}{V_5^{open}} = \frac{V_5'}{V_5^{open}}\frac{V_6}{V_5'} = H_{5open5'}^{VV}H_{5'6}^{VV}. \tag{2.111}$$

H_{5open6}^{VV} is inserted into Eq. 2.59, expressing $H_{0m6,\alpha}^{VV}$ as

$$H_{0m6,\alpha}^{VV} = H_{0m1}^{VV} \cdot H_{15,\alpha}^{VV,open} \cdot H_{5open6}^{VV}. \tag{2.112}$$

$H_{0m6,\alpha}^{VV}$ is then expressed using transfer functions from node 0m to node 6. In Section 3.7 $H_{0m6,\alpha}^{VV}$ is related to the measurements done with the experimental setup.

2.7 Finite element model

In the system model, the transmitting transducer (Module C) and fluid medium (Module D) are modeled using FE modeling, while the signal reception (in Module E) is calculated by use of the spherical reciprocity factor (cf. Section 2.5). FE modeling of Module C and D are used to describe all modes of radiation of a (relatively) complex transducer structure, e.g. a piezoelectric disk (cf. Section 3.6) or an encapsulated transducer with matching and backing layer (cf. Chapter 6), radiating into a fluid/vacuum medium.

The simulation tool used is the FE model *Finite Element Modeling of Piezoelectric structures* 5.0 (FEMP 5.0) [46,47]. A summary of the FE theory is given here, stating the equations used for calculating the transducers admittance Y, and the sound pressure radiated from the transducer, p. In the system model, Y is used to calculate Z_T, and p is used to calculate $p_3(d_0)$, $p_4(z)$, $\langle p_4(z)\rangle$ and $p_4(z_\infty)$.

The studied problem is a piezoelectric body, e.g. a piezoelectric disk, polarized in the thickness direction, radiating into a fluid. The symmetry in the disk is utilized, making the problem axisymmetric. The region of interest is approximated by a finite number of smaller volumes, i.e. the elements in the FE method [46]. The elements are separated between finite and infinite elements, the distance from the center of the structure studied to the beginning of the infinite elements is R_{inf} [46]. A number of nodes are defined in each element, where the unknown quantities are to be determined [46]. The FE equations for a piezoelectric disk immersed in an infinite fluid medium is given as [46]

$$-\omega^2\begin{bmatrix} M_{uu} & 0 & 0 \\ 0 & 0 & 0 \\ 0 & 0 & -M_{\psi\psi}\end{bmatrix}\begin{Bmatrix}\hat{u}\\ \hat{\phi}\\ \hat{\psi}\end{Bmatrix} + i\omega\begin{bmatrix} 0 & 0 & C_{u\psi} \\ 0 & 0 & 0 \\ C_{\psi u} & 0 & 0\end{bmatrix}\begin{Bmatrix}\hat{u}\\ \hat{\phi}\\ \hat{\psi}\end{Bmatrix} + \begin{bmatrix} K_{uu} & K_{u\phi} & 0 \\ K_{\phi u} & K_{\phi\phi} & 0 \\ 0 & 0 & -K_{\psi\psi}\end{bmatrix}\begin{Bmatrix}\hat{u}\\ \hat{\phi}\\ \hat{\psi}\end{Bmatrix} = \begin{Bmatrix}0\\ -Q\\ 0\end{Bmatrix}. \tag{2.113}$$

A description of the variables used in Eq. (2.113) is listed in Table 2.1. Definitions of the variables are found in [46].

Table 2.1: Description of variables in Eq. (2.113), and reference to the respective equation number they are define at in [46]

Variable	Description	Eq. number in [46]
$[M_{uu}]$	Global mass matrix	(3.51)
$[M_{\psi\psi}]$	Global fluid mass matrix	(3.129)
$[C_{u\psi}]$	Global fluid/structure coupling matrix	(3.139)
$[C_{\psi u}]$	Global fluid/structure coupling matrix	(3.139)
$[K_{uu}]$	Global stiffness matrix	(3.76)
$[K_{u\phi}]$	Global piezoelectric stiffness matrix	(3.76)
$[K_{\phi u}]$	Global piezoelectric stiffness matrix	(3.76)
$[K_{\phi\phi}]$	Global dielectric stiffness matrix	(3.76)
$[K_{\psi\psi}]$	Global fluid stiffness matrix	(3.132)
$\{Q\}$	Global charge vector	(3.76)
$\{\hat{u}\}$	Global displacement vector	(3.47)
$\{\hat{\phi}\}$	Global electric potential vector	(3.57)
$\{\hat{\psi}\}$	Global fluid velocity potential vector	(3.119)
ω	Angular frequency	-

The FE equations in Eq. (2.113) are transformed to H-form, which simplifies the calculation of the response functions of the piezoelectric disk [46]. To transform the equations to H-form, the potential in the nodes of the elements are condensed out of the FE equations, and the potential difference between two electrodes of the piezoelectric disk, V, and current going through the non-grounded electrode, $I = dQ/dt = i\omega Q$, are introduced. Eq. (2.113) is then rewritten as [46]

$$-\omega^2\begin{bmatrix} M_{uu} & 0 & 0 \\ 0 & 0 & 0 \\ 0 & 0 & -M_{\psi\psi} \end{bmatrix}\begin{Bmatrix} \hat{u} \\ V \\ \hat{\psi} \end{Bmatrix}+i\omega\begin{bmatrix} 0 & 0 & C_{u\psi} \\ 0 & 0 & 0 \\ C_{\psi u} & 0 & 0 \end{bmatrix}\begin{Bmatrix} \hat{u} \\ V \\ \hat{\psi} \end{Bmatrix}+\begin{bmatrix} H_{uu} & H_{u\phi} & 0 \\ H_{\phi u} & H_{\phi\phi} & 0 \\ 0 & 0 & -K_{\psi\psi} \end{bmatrix}\begin{Bmatrix} \hat{u} \\ V \\ \hat{\psi} \end{Bmatrix}=\begin{Bmatrix} 0 \\ -I/(i\omega) \\ 0 \end{Bmatrix}, \tag{2.114}$$

where H_{uu}, $H_{u\phi}$, $H_{\phi u} = H_{u\phi}^T$ and $H_{\phi\phi}$ are given in Eqs. (3.190) - (3.192) in [46], respectively. The response functions of a piezoelectric transducer are calculated directly from Eq. (2.114) by using matrix manipulation [46]. The third equation in Eq. (2.114) is rewritten as

$$\omega^2[M_{\psi\psi}]\{\hat{\psi}\} + i\omega[C_{\psi u}]\{\hat{u}\} - [K_{\psi\psi}]\{\hat{\psi}\} = 0, \tag{2.115}$$

from which the global fluid velocity potential vector is expressed as

$$\{\hat{\psi}\} = -i\omega\left(-[K_{\psi\psi}] + \omega^2[M_{\psi\psi}]\right)^{-1}[C_{\psi u}]\{\hat{u}\}. \tag{2.116}$$

The electrical admittance for the fluid case is expressed as [46]

$$Y = i\omega\left[\{H_{u\phi}\}^T[D]^{-1}\{H_{u\phi}\} - H_{\phi\phi}\right], \tag{2.117}$$

where the matrix $[D]$ is expressed as [46]

$$[D] = [H_{uu}] - \omega^2[M_{uu}] + \omega^2[C_{u\psi}]\left(-[K_{\psi\psi}] + \omega^2[M_{\psi\psi}]\right)^{-1}[C_{\psi u}]. \tag{2.118}$$

Assuming a time harmonic case with a time dependency of $e^{i\omega t}$, the relationship between the velocity potential ψ, and the acoustic pressure in the fluid is given as:

$$p = -i\omega\rho_f\psi, \tag{2.119}$$

where ρ_f is the density of the fluid. The admittance Y, expressed in Eq. (2.117), is used to express Z_T by the relation

$$Z_T = \frac{1}{Y}. \tag{2.120}$$

The axial pressures in the system model, $p_3(d_0)$, $p_4(z)$ and $p_4(z_\infty)$, are expressed by calculating p in FEMP at axial distances d_0, z and z_∞, respectively. FEMP also has a built-in function which calculates p averaged over a "receiving area", which is an acoustical transparent area with radius a parallel to the transmitter, thus expressing $\langle p_4(z)\rangle$.

To decrease the calculation time of memory-intensive problems, some of the FE simulations are performed without fluid elements, i.e. ignoring the fluid load of air. An approximate solution for the transmitting voltage response is then found using the hybrid FE/Rayleigh integral method, which calculates the Rayleigh integral based on the displacement over the front of the transducer found in the FE simulation [46]. An error is introduced when using the Rayleigh integral, as it assumes that the transmitter is mounted in a rigid baffle of infinite extent [46].

2.8 Time domain response

Description of the present measurement system, cf. Chapter 3, in both time and frequency domain, is a key objective of the current work. Only frequency response functions are calculated in the current implementation of FEMP, hence description of the systems time response is obtain through Fourier transformation.

In the experimental setup, the time-trace signals read by the oscilloscope corresponds to node $0m$ and 6 voltages, see Fig. 2.1, i.e. $V_{0m}(t)$ and $V_{6,\alpha}(t)$. In the current system model, $V_{0m}(t)$ and $V_{6,\alpha}(t)$ are obtained by inverse Fourier transforming $V_{0m}(f)$ and $V_{6,\alpha}(f)$. In this section, a response or transfer function X is termed $X(t)$ for the time domain, and $X(f)$ for the frequency domain, for clarity. In the system model, $V_{0m}(f)$ and $V_{6,\alpha}(f)$ are found by exciting the system with the electromotive force of the signal generator, $V_{gen}(t)$. $V_{gen}(t)$ is given as a burst which is propagated through nodes 0-6, using the transfer functions H_{gen1}, $H_{15,\alpha}^{VV,open}$ and H_{5open6}^{VV}.

For the current application, both time and frequency response signal are discrete, and thus computable using MATLAB . The MATLAB algorithm for Fast Fourier transformation (FFT), `fft`, is used for calculating the direct Fourier transformation and `ifft` for the inverse. Usage of the `fft` algorithm in MATLAB is discussed in Section 3.7.

$V_{gen}(t)$ has a signal frequency f_{sig}, amplitude A, sample frequency F_s and a whole number of periods N_p, i.e.

$$V_{gen}(t) = A \cdot \sin\left(2\pi f_{sig} t\right), \tag{2.121}$$

where t is a discrete time vector, starting at t =0 and ending at $t = N_p/f_{sig}$, with sample time $T_s = 1/F_s$. Different values are used for f_{sig}, A, F_s and N_p, as they represent the signal generator settings. The values used are given in Chapter 7. The frequency response $V_{gen}(f)$, is obtained by FFT of $V_{gen}(t)$, i.e.

$$V_{gen}(t) \xrightarrow{FFT} V_{gen}(f). \tag{2.122}$$

$V_{gen}(f)$ is propagated to node 1, i.e.

$$V_1(f) = H_{gen1}(f) \cdot V_{gen}(f), \tag{2.123}$$

where $H_{gen1}(f)$ is given in Eq. (2.98). The signal is propagated from node 1 to node 5 under open-circuit conditions, cf. Fig 2.2, using $H_{15,\alpha}^{VV,open}(f)$,

$$V_{5,\alpha}^{open}(f) = H_{15,\alpha}^{VV,open}(f) \cdot V_1(f), \tag{2.124}$$

where $H_{15,\alpha}^{VV,open}(f)$ is defined in Eqs. (2.56) - (2.58) for Model 1, 2A and 2B, respectively. $V_{5,\alpha}^{open}(f)$ is propagated from node 5 to node 6, using $H_{5open6}^{VV}(f)$, i.e.

$$V_{6,\alpha}(f) = H_{5open6}^{VV}(f) \cdot V_{5,\alpha}(f), \tag{2.125}$$

where $H_{5open6}^{VV}(f)$ is defined in Eq. (2.111). IFFT is used to calculate the time domain voltage in node 6, $V_{6,\alpha}(t)$, i.e.

$$V_{6,\alpha}(t) \xleftarrow{IFFT} V_{6,\alpha}(f). \tag{2.126}$$

$V_{6,\alpha}(t)$ corresponds to the received voltage recorded by the oscilloscope in the experimental setup. The frequency response voltage in node $0m$, $V_{0m}(f)$, is calculated by propagating $V_1(f)$ from node 1 to node $0m$, i.e.

$$V_{0m}(f) = H_{10m}^{VV}(f) \cdot V_1(f), \tag{2.127}$$

where $H_{10m}^{VV}(f)$ is defined in Eq. (2.83). $V_{0m}(t)$ is calculated by IFFT of $V_{0m}(f)$, i.e.

$$V_{0m}(t) \xleftarrow{IFFT} V_{0m}(f). \tag{2.128}$$

The measured and calculated $V_{0m}(t)$ and $V_{6,\alpha}(t)$ are compared for different frequencies, cf. Chapter 7.

2.9 Measured transmitting voltage response

In measurements using the calibrated pressure condenser microphone as receiver, the transmitting voltage response $S_{V;\alpha}$, is readily measured. Module F is not modeled during the microphone measurements, cf. 2.6. In addition, it is assumed that Module B does not affect the measurements.

From its definition in Eq. (2.35), S_V is written as

$$S_{V,\alpha} = \frac{p_{3,\alpha}(d_0)}{V_1} = \frac{V_{5,\infty\alpha}^{open}}{V_1} \cdot \frac{1}{\frac{V_{5,\infty\alpha}^{open}}{p_{4,\alpha}(z_\infty)}} \cdot \frac{p_{3,\alpha}(d_0)}{p_{4,\alpha}(z_\infty)}, \tag{2.129}$$

which, by using one of Eqs. (2.56) - (2.58) for H_{15}^{VV} and Eq. (2.14), is expressed as

$$S_{V,\alpha} = \frac{H_{15,\infty\alpha}^{VV,open}}{M_V} \cdot \frac{p_3(d_0)}{p_4(z_\infty)} \cdot e^{-\alpha(d_0 - z_\infty)}, \tag{2.130}$$

where it is assumed that M_V is not affected by the medium absorption, i.e.

$$M_V = \frac{V_{5,\infty}}{p_4(z_\infty)} = \frac{V_{5,\infty\alpha}}{p_{4,\alpha}(z_\infty)}. \tag{2.131}$$

By definition [48], d_0 is in the transmitters far-field. The axial far-field pressures $p_3(d_0)$ and $p_4(z_\infty)$ are written as [36]

$$p_3(d_0) = v_2 \rho\omega \frac{a^2}{2d_0} e^{-i(kd_0 - \frac{\pi}{2})} \quad \text{and} \tag{2.132}$$

$$p_4(z_\infty) = v_2 \rho\omega \frac{a^2}{2z_\infty} e^{-i(kz_\infty - \frac{\pi}{2})}, \tag{2.133}$$

respectively. Inserting Eqs. (2.132) - (2.133) into Eq. (2.130) yields

$$S_{V,\alpha} = \frac{H_{15,\infty\alpha}^{VV,open}}{M_V} \cdot \frac{z_\infty}{d_0} \cdot e^{-\alpha(d_0 - z_\infty)} \cdot e^{-ik(d_0 - z_\infty)}. \tag{2.134}$$

For the measurements using the microphone as receiver, it is assumed that it is placed in the transmitters far-field, i.e. $z_\infty = z$, giving

$$S_{V,\alpha} = \frac{H_{15,\alpha}^{VV,open}}{M_V} \cdot \frac{z}{d_0} \cdot e^{-\alpha(d_0 - z)} \cdot e^{-ik(d_0 - z)}. \tag{2.135}$$

Using Eq. (2.135), $S_{V,\alpha}$ of the transmitter is measured, assuming that $V_{0m} = V_1$ and $V_{5,\alpha}^{open} = V_{6,\alpha}$, hence $H_{15,\alpha}^{VV} = H_{0m6,\alpha}^{VV}$. Results are presented in Chapter 7.

Chapter 3

Experimental setup and measurement methods

In this chapter, the measurement setup, modeled by the system model in Chapter 2, and measurement methods are described.

The experiments include both electric and acoustic measurements, in addition to physical measurements. The system model in Chapter 2 is designed to describe the acoustical measurements. An overview of the equipment is given in Section 3.1, the dimension and weight measurements are described in Section 3.4, and the electrical measurement setup is covered in Section 3.2. The acoustical measurement setup and methods are described in Section 3.3, covering transmitting electronics, transducers and positioning, receiving electronics, environmental parameters, and data acquisition. The Brüel & Kjær microphones and the piezoelectric ceramic disks used in the acoustic measurements are presented in Sections 3.5 and 3.6, respectively. Finally the digital signal processing of the recorded data is described in Section 3.7. The piezoelectric transducers developed during the present work and used in the measurements are not covered here, but in Chapter 6.

3.1 Equipment

An overview of the equipment used in the measurements is given in Table 3.1.

Table 3.1: Equipment used in the measurements

Brand/name	Type of equipment	Serial number
	Physical measurements	
Biltema 19-1444	Digital caliper	-
TESA DIGIT-CAL SI	Digital caliper	4J09704
Mitutoyo MDH-25M	Digimatic micrometer	15229628
A&D GF-3000-EC	Precision balance	P1826763
	Electrical measurements	
HP 4192A	Impedance analyzer	23423
Vaisala HMI41	Humidity and temperature indicator	S4030049
	Acoustical measurements - instrumentation	
Agilent 33220A	Waveform generator	MY44023589
Brüel & Kjær 2636	Measurement amplifier	1615638
Krohn-Hite 3940A	Digital filter	AM2626
Tektronix DPO3012	Digital oscilloscope	195539
Vaisala HMT313	Temperature and relative humidity sensor	F4850018
	Acoustical measurements - positioning	
Physik Instrumente M-037	Compact precision rotation stage	0912 A
Physik Instrumente M-535	Linear positioning stage	-
Physik Instrumente M-531	Linear positioning stage	1460497
	Acoustical measurements - transducers	
Brüel & Kjær 4138	1/8-inch pressure-field microphone	1832479
Brüel & Kjær UA-0160	Adaptor - microphone to preamplifier	-
Brüel & Kjær 2633	Preamplifier	-
Brüel & Kjær 4138-A-015	Microphone system	2795107
- Brüel & Kjær 4138	1/8-inch pressure-field microphone	2784915
- Brüel & Kjær 2670	Preamplifier	2799662
Element #6	Piezoelectric ceramic Pz27 disk	-
Element #10	Piezoelectric ceramic Pz27 disk	-
Element #16	Piezoelectric ceramic Pz27 disk	-
Transducer No. 1	In-house constructed transducer[1]	-
Transducer No. 2	In-house constructed transducer[1]	-
Transducer No. 3	In-house constructed transducer[1]	-
	Acoustic measurements - microphone calibration	
Brüel & Kjær 4228	Pistonphone	1918465
Brüel & Kjær UZ0004	Correction barometer	1918465

3.2 Electrical measurement setup

The electric properties of the piezoelectric ceramic disks and piezoelectric transducers developed during the present work are determined using an HP 4192A impedance analyzer [49], shown in Fig. 3.1. The conductance, G_T, and susceptance, B_T, are measured and the admittance found by

$$Y_T = G_T + iB_T = \frac{1}{Z_T}. \tag{3.1}$$

---

[1] Piezoelectric transducers developed during the present work.

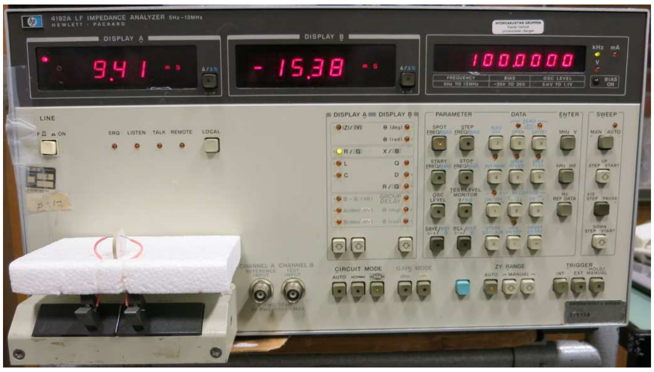

Figure 3.1: HP 4192A impedance analyzer used in the electrical measurements.

The impedance analyzer is allowed a warmup time of at least 30 minutes, and to account for the wires used in the measurements, a zero offset adjustment of the impedance analyzer (described at page 3-50 in [49]) is performed for the maximum frequency in the measurement series, before measurements are performed. A drive voltage, referred to a oscillation level in [49], of $V_{rms} = 0.3$ V is used in the presented results.. Measurements using different drive voltages, performed on a Pz27 piezoelectric disk of approximate dimensions 20 mm × 2 mm, are shown in Figs. 3.2 and 3.3, for the first and second radial modes of the disk, respectively. The non-linear effects is seen to cause a downward frequency shift of the resonances and a level reduction of the maximum conductance. $V_{rms} = 0.3$ V is chosen to minimize the non-linear distortion, while avoiding the resolution limitations observed for the lowest voltage in Fig. 3.3.

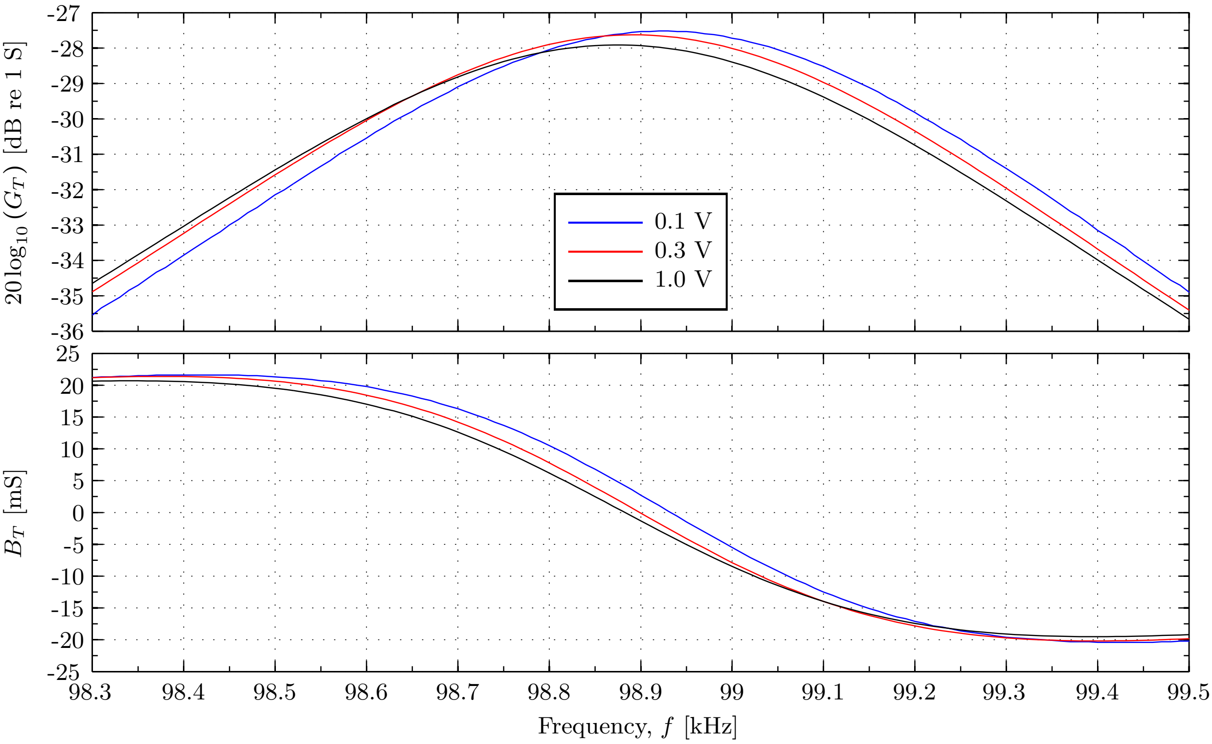

Figure 3.2: Conductance and susceptance of a Pz27 piezoelectric ceramic disk of approximate dimensions 20 mm × 2 mm. Comparison of measurement with different drive voltages. For the frequency range around the first radial mode (R1) of the disk.

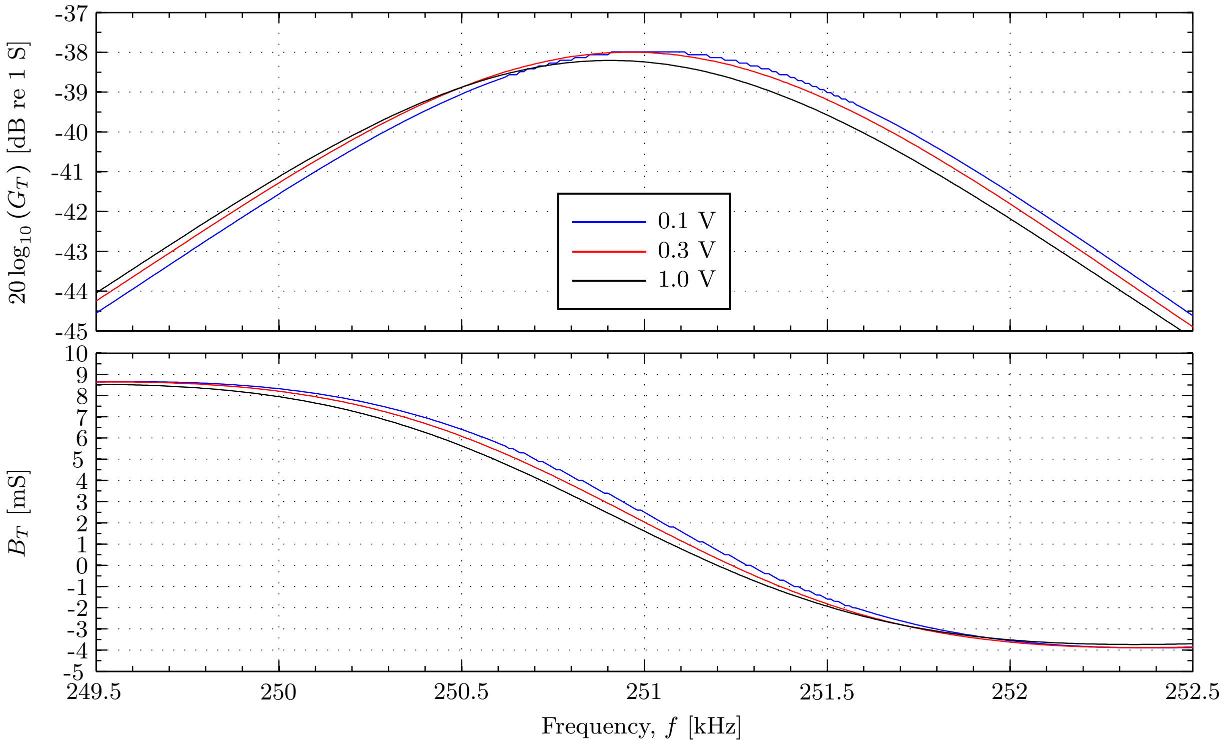

Figure 3.3: As Fig. 3.2, but for the frequency range around the second radial mode (R2) of the disk.

Different wires are used when measuring the admittance, depending on the device measured. Measurements on piezoelectric ceramic disks are performed with the disk placed loosely in a wide groove in a polystyrene holder and held upright by two thin wires connected to the impedance analyzer, as seen in Fig. 3.4.

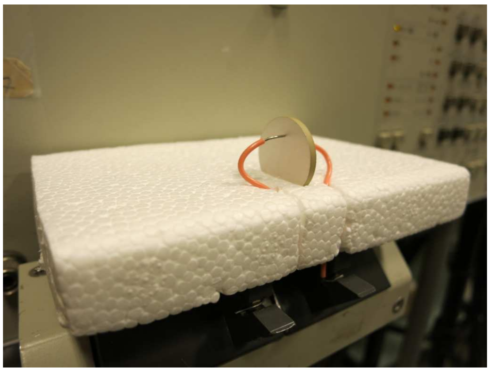

Figure 3.4: A polystyrene holder is used when measuring the admittance of single piezoelectric ceramic disks, with the disk placed loosely in a wide groove in the polystyrene.

This setup is intended to minimize the mechanical load, which is important for comparison with FE simulations. Some repeatability issues are observed at the resonances, as shown for the conductance in Figs. 3.5 and 3.6, with a slight change in the magnitude and a shift of the series resonance between any two measurements. This is possibly due to the fact that the exact placement of the disk and the wires varies for each measurement. Between each measurement in Figs. 3.5 and 3.6, the disk is removed from the holder and then put back, with the rest of the parameters kept unchanged. A small adjustment of the spring in the wires was performed between measurement #2 and measurement #3, increasing the repeatability issues.

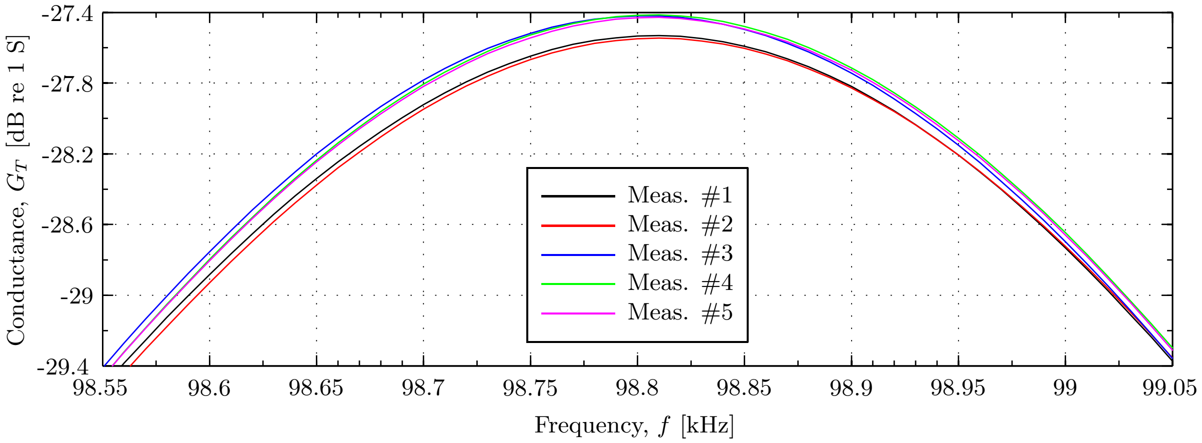

Figure 3.5: Conductance of a Pz27 piezoelectric ceramic disk of approximate dimensions 20 mm × 2 mm. Repeatability measurements. For a frequency range around the first radial mode series resonance.

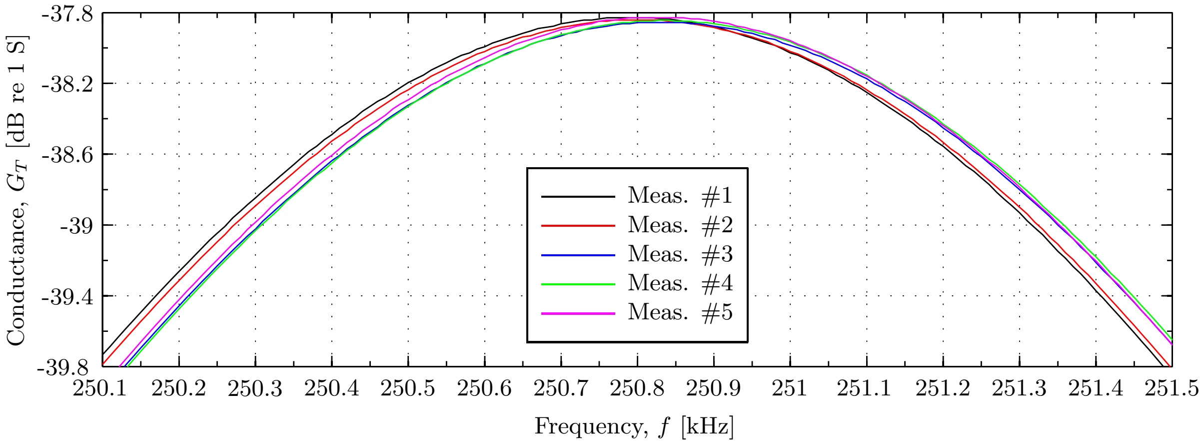

Figure 3.6: As Fig. 3.5, but for a frequency range around the second radial mode series resonance.

When electrical measurements are performed on piezoelectric disks with matching layer, a different holder constructed of polystyrene and wires is used. The matching layer is wider than the element, which is attached to the matching layer using conductive epoxy, with the conductive epoxy layer extending out to cover remaining rim of the matching layer. A wire is soldered onto the rear electrode on the element. The measurements are performed with the rim of the matching layer, covered in conductive epoxy, resting on a wire tripod. One of the wires in the tripod is connected to the impedance analyzer, as well as the soldered-on wire. Electrical measurements on the piezoelectric transducers, constructed during this work, are performed as shown in Fig. 3.7.

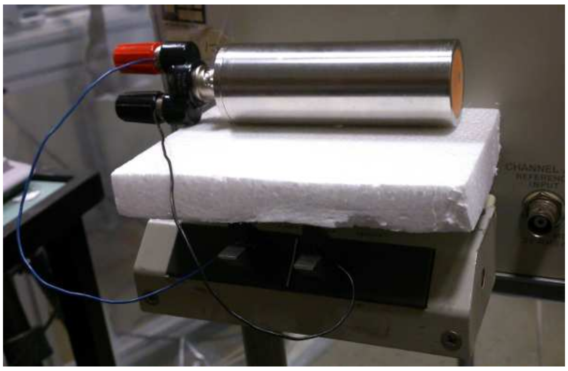

Figure 3.7: Electrical measurement setup for the piezoelectric transducers constructed during this work.

Environmental parameters are recorded for each measurement series. The temperature and relative humidity are measured with a Vaisala HMP46 probe connected to a Vaisala HMI41 indicator. The measurement uncertainty is ± 2.5 % RH and ± 0.3 °C for the measurement ranges of interest [50]. The ambient pressure is measured using a Brüel & Kjær UZ0004 analog barometer [51].

The measurements are performed by a computer running the MATLAB-script `impanal.m`, given in Appendix A.1.1, connected to the impedance analyzer using a GPIB-to-USB adaptor. The measured temperature, relative humidity and pressure, as well as the oscillation level and the measurement frequencies in kHz are specified in the script. The resolution chosen is best around regions of interest, i.e. the resonances, ranging from 10 Hz to 1 kHz. The script is set to pause 250 ms between each query to the impedance analyzer, which is sufficient as one measurement takes approximately 150 ms for frequencies above 400 Hz [49]. The vectors containing conductance, susceptance and frequency (in kHz) are saved to file.

3.3 Acoustical measurement setup

An overview of the acoustical experimental setup is given in Fig. 3.8. The acoustical measurement setup is based on the measurement setup developed by Storheim [1] and used in [52]. A pulse is generated by a waveform generator (1) and propagates through air from a transmitting transducer (2) to a receiving transducer (3), where is is amplified by a measurement amplifier (4) with an external filter (5) and recorded by an oscilloscope (6). The oscilloscope also measures the output voltage from the waveform generator. Temperature and relative humidity are recorded. The transmitter and receiver are mounted on carriages on a metal frame inside a plastic measurement chamber, and connected to positioning equipment.

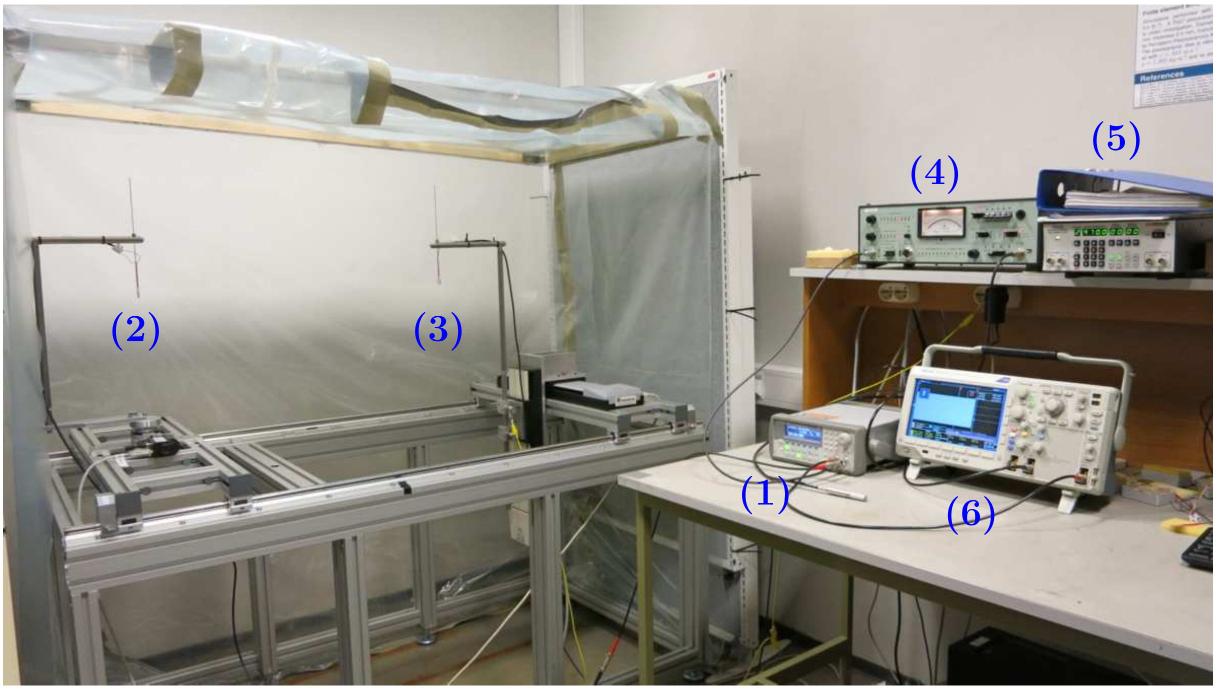

Figure 3.8: An overview of the acoustical measurement setup.

A schematic diagram of the measurement setup is shown in Fig. 3.9. The different parts are described in more detail in the appropriate sections. The input and output impedance of the equipment are needed to account for the instrumentation in the measurements and are given in Table 3.2. The impedance of the instruments are either treated as an ideal resistor, or as an ideal resistor in parallel with an ideal capacitor. The latter is denoted by the symbol "∥".

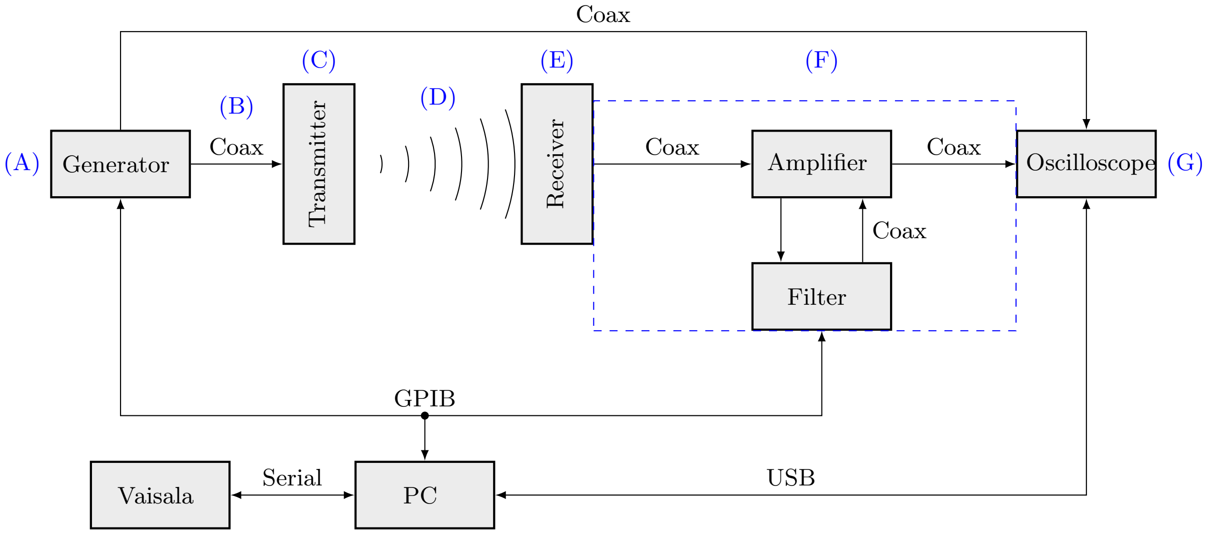

Figure 3.9: Schematic diagram of the measurement setup used in the acoustical measurements. The different parts of the measurement setup is associated with its respective module (blue), cf. Fig. 2.1.

The different modules of the system model in Chapter 2 is depicted in Fig. 3.9. In the following, the acoustical measurement system is correlated with the modules.

Table 3.2: Output and input impedance of some of the equipment used in the acoustical measurements

Brand/name	Type of equipment	Input impedance[2]	Output impedance[3]
Brüel & Kjær 2636	Measurement amplifier	1 MΩ ‖ 90 pF	~100 Ω
Tektronix DPO3012	Digital oscilloscope	1 MΩ ‖ 11.5 pF	-
Agilent 33220A	Waveform generator	-	50 Ω
Krohn-Hite 3940A	Digital filter	1 MΩ ‖ 100 pF	50 Ω

3.3.1 Modules A and B

A sinusoidal electric burst is generated by an Agilent 33220A waveform generator [53]. The signal is transmitted to the transmitting transducer and to a Textronix DPO3012 digital oscilloscope [54]. A BNC T-connector at the generator output enables parallel connection of the oscilloscope and the transmitting transducer. Coaxial cables with a characteristic impedance of 50 Ω are used to connect the instruments. The oscilloscope is connected to the waveform generator to measure the input voltage to the transmitting transducer, as this varies significantly with the frequency due to impedance changes. The waveform generator and digital oscilloscope are seen in Fig. 3.10

---

[2] The input impedance of the B&K 2636 measurement amplifier is given for the direct input, not when using a B&K preamplifier.

[3] The output impedance of the B&K 2636 measurement amplifier is the output impedance of the port connected to the Tektronix DPO3012 oscilloscope.

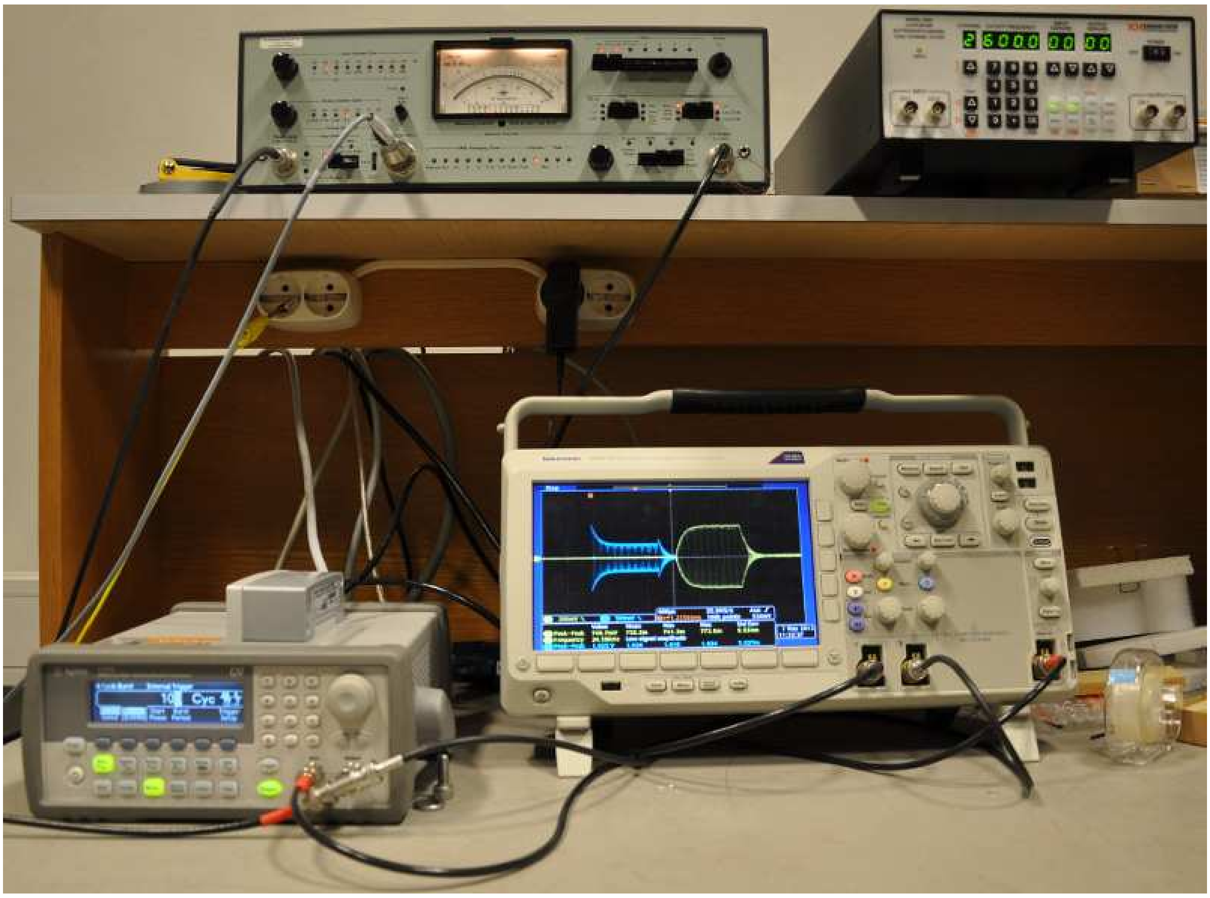

Figure 3.10: Instruments used in the acoustic measurements. The oscilloscope, waveform generator, amplifier and filter, in clockwise order, starting from the bottom right.

The burst period of the generated signal is set to 40 ms, which corresponds to a burst repetition rate of 25 Hz. A lower burst period is seen to be insufficient for the reverberations to die off between each burst. The amplitude of the sine wave is usually set to either V_{pp} = 1 V or V_{pp} = 10 V, but can be adjusted from V_{pp} = 1 mV to V_{pp} = 10 V. The stated voltage is the voltage generated into a 50 Ω load, and it is doubled at open-circuit conditions [53]. Outside resonance the impedance of a single piezoelectric disk is much larger than 50 Ω, and thus the voltage approaches V_{pp} = 20 V instead of the specified V_{pp} = 10 V. An open-circuit notation is adopted for convenience, e.g. denoting a measurement with a specified voltage of V_{pp} = 1 V at 50 Ω load conditions as a V_{pp} = 2 V measurement. All voltages used in the calculations are measured voltages and do therefore not necessarily correspond to either V_{pp} = 1 V or V_{pp} = 2 V.

The burst length is held constant for each measurement series by adjusting the number of cycles to the current measurement frequency. A burst length of 1.4 ms at a measurement frequency of 100 kHz corresponds to 140 cycles. Burst lengths of 1 ms (~34 cm), 1.4 ms (~48 cm) and 1.6 ms (~55 cm) are used in measurements, depending on the transmitter, receiver and separation distance. The burst length and separation distance for a given setup is chosen to minimize the effect of electric crosstalk and acoustic reflection from the walls and other nearby protrusions. Separation distances of z = 44 cm, 55 cm, 66 cm and 77 cm are used.

3.3.2 Cables

Coaxial cables of type RG58 with a characteristic impedance of approximately 50 Ω are used in this work. Module B consists entirely of the coaxial cable connecting the Module A to Module C, and several cables are used in Module F (cf. Fig 3.9), however the two cables connecting the frequency filter to the amplifier are not modeled in this work (cf. Section 2.6.3). In Section 2.6, the cables are modeled with the typical values of inductance and capacitance shown in Table 3.3.

Table 3.3: Coaxial cable type RG58, typical specifications [44]

Typical specifications.	
Inductance per metre:	$L = 250$ nH/m
Capacitance per metre:	$C = 100$ pF/m

The different cable lengths used in the measurements are specified in Table 3.4. Note that a proprietary cable (not RG58) of 2 m is used when a B&K microphone is connected to the measurement amplifier.

Table 3.4: Overview of the approximate lengths of the RG58 coaxial cables used in the different transducer configurations, see Table 3.5.

Name	From	To	Length
Cable # 1	Waveform generator	Transmitting piezoelectric disk	4.0 m
	Waveform generator	Transmitting piezoelectric transducer	3.0 m
Cable # 2	Waveform generator	Oscilloscope	1.0 m
Cable # 3	Receiving piezoelectric disk	Measurement amplifier	3.4 m
	Receiving piezoelectric transducer	Measurement amplifier	2.2 m
Cable # 4	Measurement amplifier	Oscilloscope	1.0 m

3.3.3 Modules C and E

In Module C, piezoelectric ceramic disks and piezoelectric transducers developed during the present work are used as transmitting transducers. These transducers are also used as receiving transducer in Module E, in addition to two 1/8-inch Brüel & Kjær 4138 condenser microphones [55], one of them with a Brüel & Kjær 2633 preamplifier [56], the other with a Brüel & Kjær 2670 preamplifier [57]. The transducer configurations used in this work are given in Table 3.5.

Table 3.5: Transducer configurations used in measurements.

Transmitting transducer type	Receiving transducer type	Separation distance	Burst length
Piezoelectric ceramic disk	B&K 4138	44 cm	1 ms (~34 cm)
Piezoelectric ceramic disk	Piezoelectric ceramic disk	77 cm	1.4 ms (~48 cm)
Piezoelectric transducer	B&K 4138	55 cm	1.4 ms (~48 cm)
Piezoelectric transducer	Piezoelectric transducer	66 cm	1.6 ms (~55 cm)

The transmitting transducer and the receiving transducer are mounted on separate carriages to enable adjustment of the separation distance. The carriages are placed on top of a metal frame, with a surrounding plastic measurement chamber to minimize air flow and temperature fluctuations affecting the measurements, see Fig. 3.11.

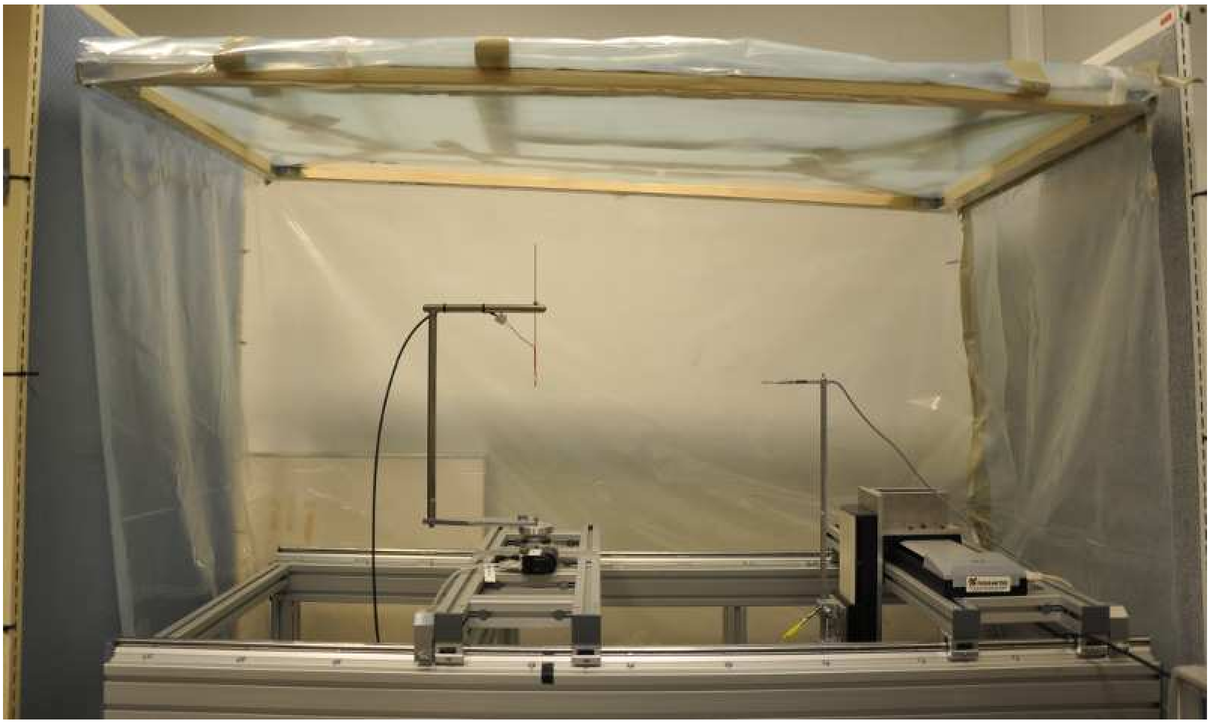

Figure 3.11: The acoustical measurement setup, with a piezoelectric ceramic disk as the transmitting transducer and a Brüel & Kjær 4138 microphone as the receiving transducer. Placed inside the plastic measurement cage with the front flap open.

The transmitter and receiver are first aligned coaxially by visual inspection and a self levelling laser cross level, and then acoustic measurements are performed while the position of the receiver is adjusted in the plane orthogonal to the acoustic axis. The transmitter and receiver are assumed to be coaxial, with respect to the acoustic axis, when the maximum output voltage is measured. Two computer-controlled [58,59] linear positioning stages, PI M-531 [60] and PI M-535 [61], are used in the positioning. The transmitting transducer is connected to a PI M-037 rotation stage [62], included in the setup for future use. The separation distance is measured manually with a folding rule, with an estimated total uncertainty of ± 2 mm.

The different types of transducers are mounted in different ways. The Brüel & Kjær microphones are inserted in a hole in an aluminium rod and fastened by a screw at the back, as shown in Fig. 3.12.

Figure 3.12: A Brüel & Kjær 4138-A-015 microphone system mounted on an aluminium rod.

The suspension of the piezoelectric ceramic disks is shown in Fig. 3.13, and the suspension for the piezoelectric transducers developed during the present work is shown in Fig. 3.14. Both types are suspended from a stainless steel structure shaped like an inverted 'L'. Wires are soldered on to the piezoelectric ceramic disk (see Section 3.6) and fastened to a vertical thin metal rod by heat shrink tubing, see Fig. 3.13. The rod is in turn suspended from the horizontal stainless steel rod.

The piezoelectric ceramic disks and the piezoelectric transducers are connected to the instruments using coaxial cables and BNC-connectors. The Brüel & Kjær microphones are connected by a Brüel &

Kjær cable and a 7 pin connector. The suspension of the receiving transducer is connected to electric ground to reduce the electromagnetic noise.

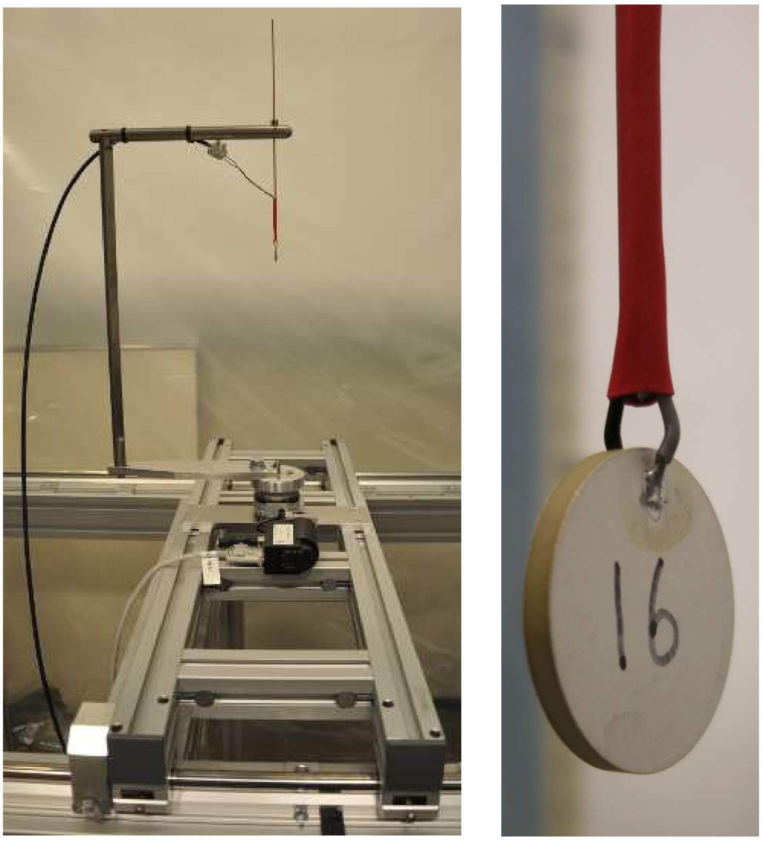
(a) (b)

Figure 3.13: A piezoelectric ceramic disk acting as a transmitting transducer.

Figure 3.14: Two piezoelectric transducers developed during the present work with a separation distance of 66 cm.

3.3.4 Module F

The receiving transducer is connected to a Brüel & Kjær 2636 measurement amplifier [63] with an external Krohn-Hite 3940A digital filter [64]. The measurement amplifier is in turn connected to the Textronix

DPO3012 digital oscilloscope where the signal is terminated and recorded.

A maximum total amplification of 100 dB in 10 dB ± 0.05 dB steps is available in the amplifier. A total gain of 60 dB is used in the results presented in this work; amplifying the signal by 40 dB at the input, prior to the external filter, and 20 dB at the output. The measurement amplifier has an internal high-pass filter turned on with a cutoff frequency at 22.4 Hz and 30 dB per octave attenuation. The linear frequency range of the amplifier is 1 Hz to 200 kHz, and a correction must therefore be introduced when measuring at frequencies above 200 kHz. A typical frequency response of the B&K 2636 measurement amplifier is given in [63] and shown in Fig. 3.15.

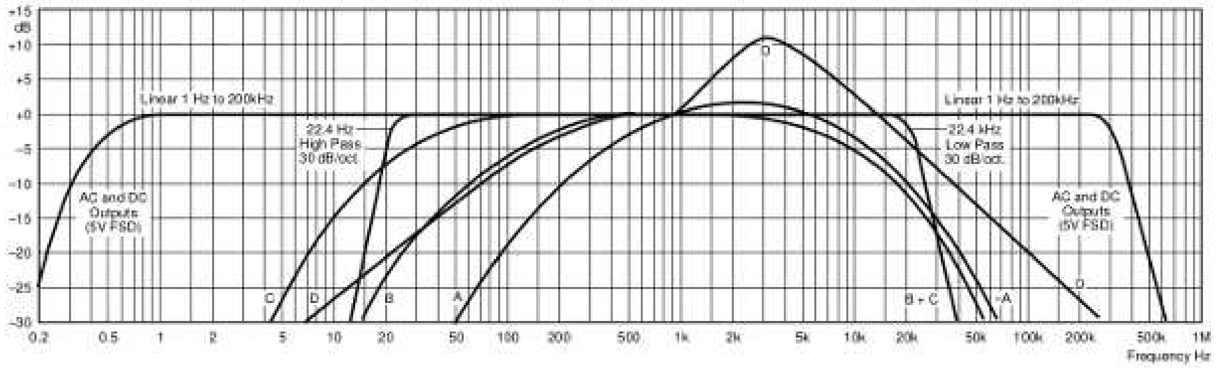

Figure 3.15: The typical frequency response of a B&K 2636 measurement amplifier. The curve to the far right apply to the measurements in this work.

Instead of using the supplied typical values, the behaviour of the amplifier used in this work is determined by measuring the output voltage of a sinusoidal wave generated by the waveform generator and amplified by the measurement amplifier. The ratio of the voltage at the lowest frequency to the voltage at higher frequencies is shown in Fig. 3.16 and used to correct the measurements.

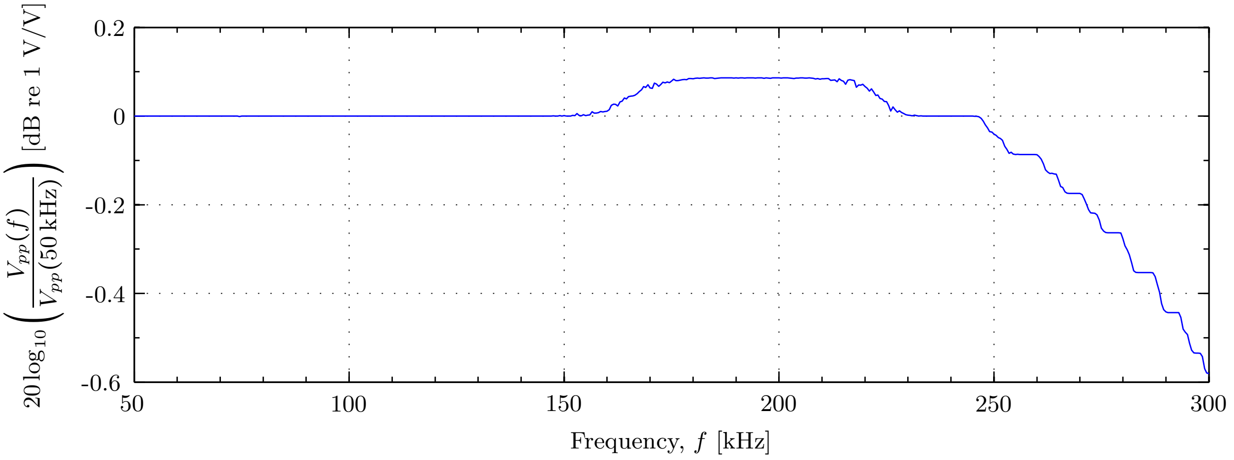

Figure 3.16: The measured peak to peak voltage for the frequency range 50 kHz to 300 kHz, normalized to the measured peak to peak voltage at 50 kHz. Used to correct the acoustic measurements.

The external digital filter has two separate channels, each with a 24 dB per octave attenuation outside the passband. A bandpass filter is achieved by using one channel as a high-pass filter and the other as a low-pass filter. A computer-controlled moving bandpass filter is implemented, where the cutoff frequency of the low-pass filter is set to twice the measurement frequency and the cutoff frequency of the high-pass filter is set to half the measurement frequency. Thus maximal filtering is achieved without dampening at the measurement frequency. Note that in the results shown in this work, only the low-pass filter cutoff frequency is adjusted as the measurement frequency changes. The cutoff frequency of the high-pass filter is set once at the start of the measurement series. This is due to a previously unnoticed error in the MATLAB -script.

3.3.5 Module G

The Textronix DPO3012 digital oscilloscope is used to record both the input voltage to the transmitting transducer and the output voltage from the receiving transducer. The acquisition is triggered by the waveform generator.

An input resistance of 1 MΩ in parallel with a capacitance of 11.5 pF is used. To reduce the random noise in the system, a number of signal bursts are averaged before the received voltage signal is recorded by a computer. Averaging of 128 bursts are used in the measurements presented.

A lowest possible V/div should be chosen when the signal is recorded to get the most out of the 8-bit resolution of the oscilloscope. It is however important not to use a lower V/div than 10 mV/div. This is because a unwanted reduction in the recorded voltage is observed for lower settings due to averaging of the random noise. Fig. 3.18 shows a recorded output voltage waveform with 10 mV/div, both with averaging over 128 bursts and for a single burst. The amplitude of the averaged signal is well within the window frame, and a lower V/div would increase the voltage resolution. The recording of a single burst shows significant amounts of white noise, which is cancelled by averaging multiple bursts. Note that the 8 voltage divisions are visible in the window, but two additional divisions extending above and below the visible view are also recorded by the oscilloscope. Thus the visible window height is 80 mV, while the recorded height is 100 mV.

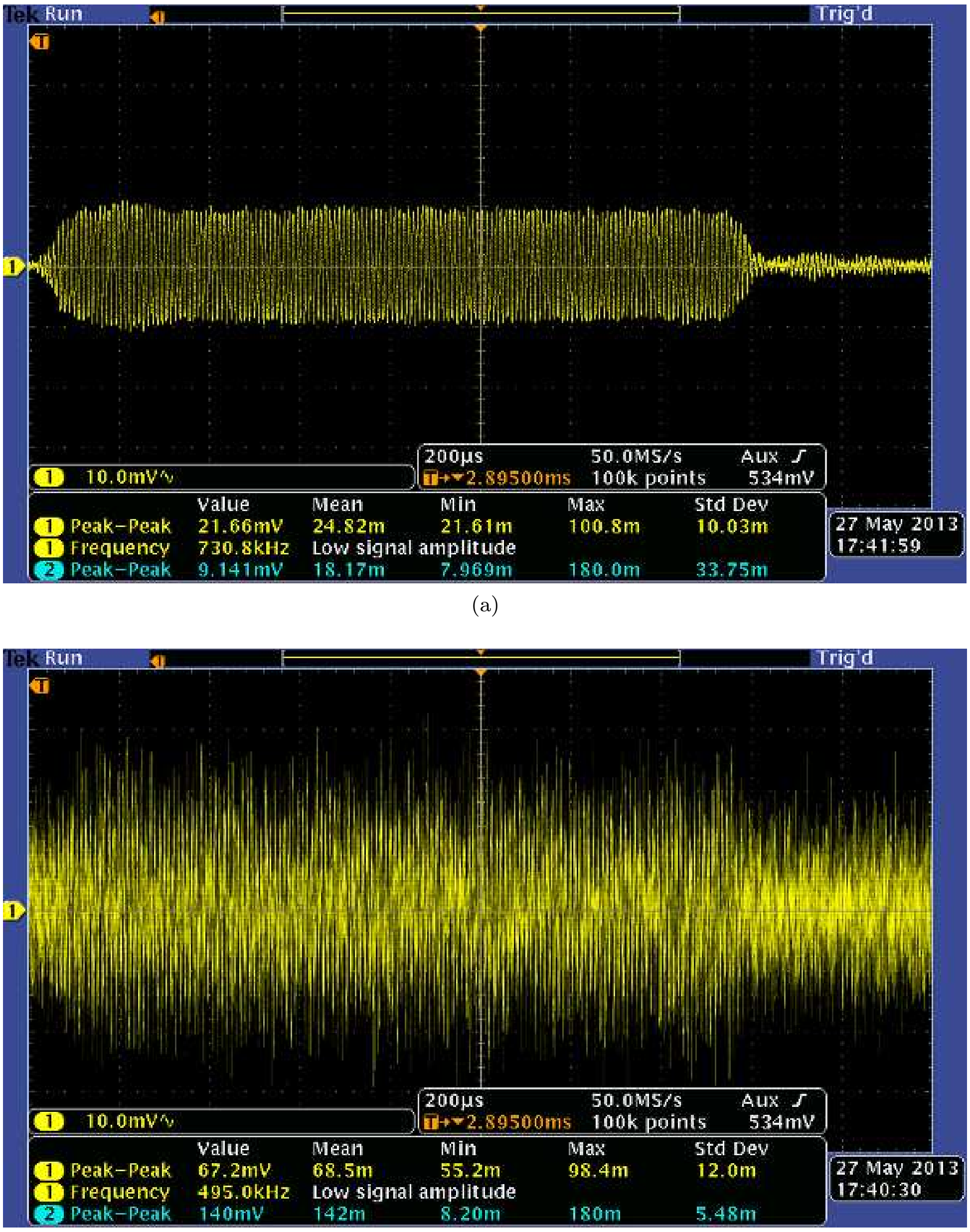

```
Tek Run                                                   Trig'd
 1  10.0mV∿                    200μs       50.0MS/s     Aux ⨍
                               T→▾2.89500ms 100k points  534mV
               Value      Mean       Min        Max        Std Dev
 1 Peak-Peak   21.66mV    24.82m     21.61m     100.8m     10.03m    27 May 2013
 1 Frequency   730.8kHz   Low signal amplitude                       17:41:59
 2 Peak-Peak   9.141mV    18.17m     7.969m     180.0m     33.75m
```

(a)

```
Tek Run                                                   Trig'd
 1  10.0mV∿                    200μs       50.0MS/s     Aux ⨍
                               T→▾2.89500ms 100k points  534mV
               Value      Mean       Min        Max        Std Dev
 1 Peak-Peak   67.2mV     68.5m      55.2m      98.4m      12.0m     27 May 2013
 1 Frequency   495.0kHz   Low signal amplitude                       17:40:30
 2 Peak-Peak   140mV      142m       8.20m      180m       5.48m
```

(b)

Figure 3.17: Example measured output voltage with 10 mV/div vertical scaling. (a) averaged over 128 bursts and (b) for a single burst. Transducer No. 2 is used as transmitter and Transducer No. 3 is used as receiver, with a separation distance of 66 cm.

Fig. 3.18 shows the same signals as in Fig. 3.17, but with 2 mV/div. The peak to peak voltage of the averaged signal now appears to be reduced to under 16 mV, which is the range of the visible window, compared to the 20 mV seen in 3.17. The reason for this discrepancy is seen in Fig. 3.18b, where clipping of the white noise is observed, thus causing the averaging not to fully cancel out noise components. A minimum of 10 mV/div is deemed sufficient to include the vast majority of the white noise in the current measurement setup.

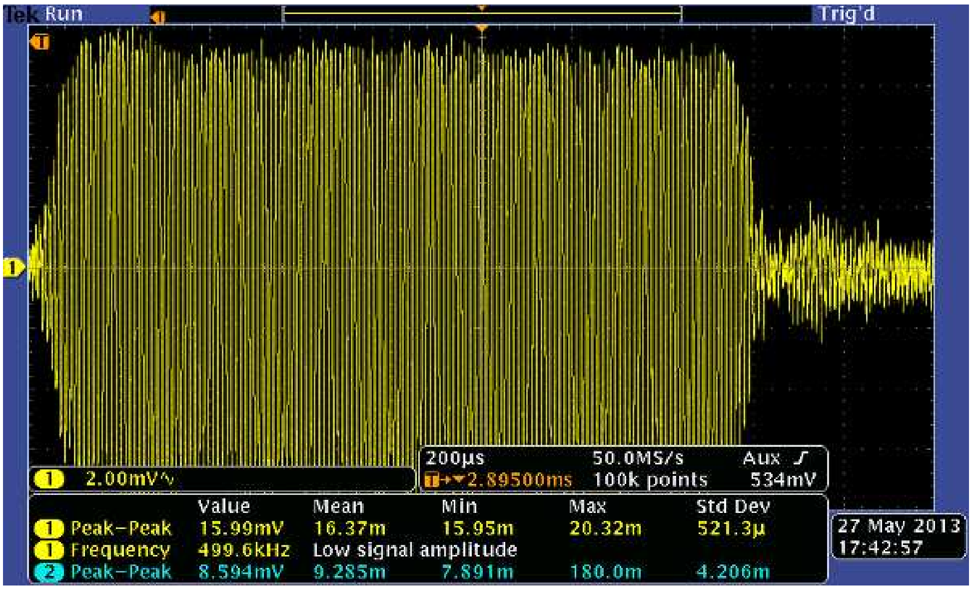

1 2.00mV∿

200µs 50.0MS/s Aux ⨍
T→▾2.89500ms 100k points 534mV

	Value	Mean	Min	Max	Std Dev
1 Peak–Peak	15.99mV	16.37m	15.95m	20.32m	521.3µ
1 Frequency	499.6kHz	Low signal amplitude			
2 Peak–Peak	8.594mV	9.285m	7.891m	180.0m	4.206m

27 May 2013
17:42:57

(a)

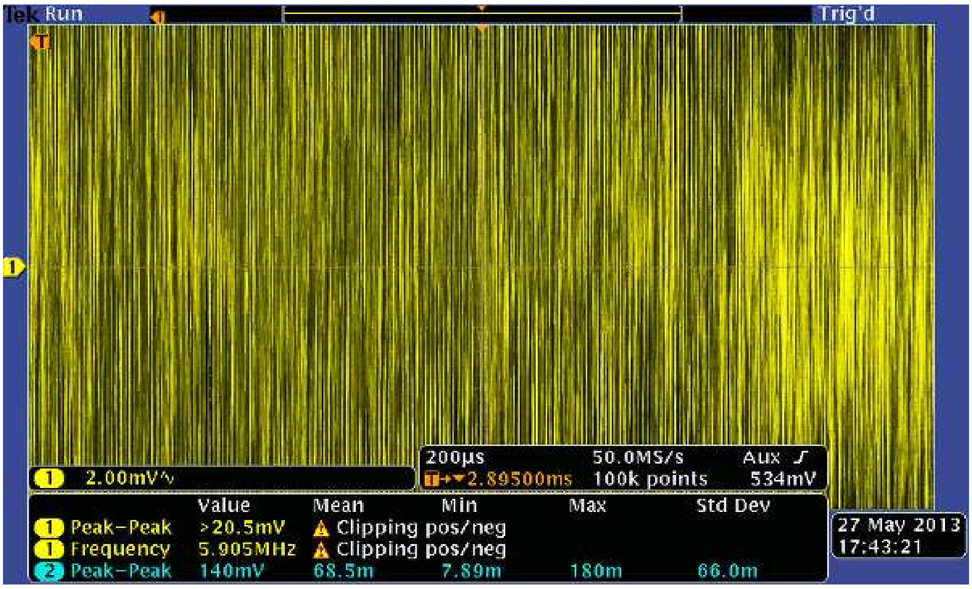

1 2.00mV∿

200µs 50.0MS/s Aux ⨍
T→▾2.89500ms 100k points 534mV

	Value	Mean	Min	Max	Std Dev
1 Peak–Peak	>20.5mV	⚠ Clipping pos/neg			
1 Frequency	5.905MHz	⚠ Clipping pos/neg			
2 Peak–Peak	140mV	68.5m	7.89m	180m	66.0m

27 May 2013
17:43:21

(b)

Figure 3.18: As Fig. 3.17, but with 2 mV/div vertical scaling.

The temporal settings are adjusted so that there are 100 000 samples in the windows, which results in a sample rate of 50 MHz for 200 μs/div (2 ms window length).

3.3.6 Environmental parameters

Relative humidity and temperature are recorded in order to account for absorption in the medium. The relative humidity (RH) and temperature are measured using a Vaisala HMT313 sensor [65]. This instrument is not included in the system model. The sensor has an uncertainty of ± 0.6 % RH below 40 % RH and an uncertainty of 1.0 % RH above 40 % RH. The uncertainty in the temperature measurements is ± 0.10 °C [66].

3.3.7 Noise measurements

The noise in a specific acoustical measurement configuration is determined by an additional measurement series, where the noise is recorded just prior to the arrival of the signal burst, in a time window with a total length of 400 μs (40 μs/div) and with 10 mV/div vertical scaling. Only the output voltage from the receiver is recorded. The recorded noise is used to calculate the signal to noise ratio (SNR).

3.3.8 Data acquisition

A computer running Windows 7 communicates with the instruments MATLAB-scripts and different communication interfaces: the Tektronix DPO3012 oscilloscope via USB, the Agilent 33220A waveform generator and the Krohn-Hite 3940A filter via a GPIB-to-USB adaptor, and the Vaisala HMT313 temperature and relative humidity sensor via an RS-232-to-USB adaptor (see Fig. 3.9). The scripts are given in Appendix A. Measurements are initiated by the script `main.m`, which calls several subscripts, and performed for a measurement series consisting of electric and acoustic measurements for specified frequencies.

- Settings used in the measurements are specified in `measurement_parameters.m`. Important settings used to control the instruments are the frequency vector, input voltage to the transmitting transducer, burst repetition rate, number of averaged bursts and filename. The frequency vector specifies for which frequencies measurements shall be performed. An input voltage of V$_{pp}$ = 10 V corresponds to a V_{pp} = 20 V open-circuit voltage (see Section 3.3.1). Additional information, such as the separation distance, amplifier gain and the transmitter and receiver used, are entered for use in the post-processing.
- The instruments are initialized by `calibration_parameters.m`.
- Electric measurements
    - In the electric measurements the appropriate V/div is assigned to the oscilloscope. Then measurements are performed for each specified frequency.
    - The number of cycles in the signal burst is adjusted for each frequency to keep the temporal signal length constant.
    - The time window is adjusted using `adjustTime.m`.
    - The data acquisition of the scope is turned off, and turned on again after a one second pause. This is done to reset the acquisition mode between each frequency, as problems with the averaging have been observed when this routine is omitted.
    - The signal is recorded using `DPO_les.m`, along with the timescale, voltage scale and termination impedance.
- Acoustic measurements
    - The acoustic measurements are performed following the same routine as the electrical measurements, with some alterations.
    - The cutoff frequencies for high- and low-pass filter is set to half and twice the measurement frequency, respectively, thus implementing a moving bandpass filter. Note that an error in the script caused only the low-pass filter cutoff frequency to be adjusted. The high-pass filter cutoff frequency is kept at the initial value.
    - The appropriate voltage scaling are determined automatically for each measurement frequency using `adjustAmplitude.m`, to ensure maximum resolution. The minimum chosen V/div is 10 mV.
    - The script used for recording the signal, `DPO_les.m`, is called from `adjustAmplitude.m` for use in the automatic scaling, and hence an additional calling of `DPO_les.m` is not necessary.
- Everything is saved to a timestamped file.
- The instruments are shut down. Some problems have been observed with the instrument shutdown, and it is therefore recommended to manually run the commands `delete(instrfindall)` and `clear all` between each measurement series.

3.4 Measurements of dimension and mass

Accurate measurements of physical dimensions of the piezoelectric ceramic disks and the piezoelectric transducers developed as part of this work are needed in order to perform accurate FE simulations. Different measurement devices are used to perform the measurements, depending on the dimensions of the sample.

Physical dimensions are measured by: a Mitutoyo MDH-25 digimatic micrometer [67] with a measurement range of 0 to 25 mm, a resolution of 0.1 μm and an accuracy of ±0.5 μm, a TESA DIGIT-CAL SI digital caliper [68] with a measurement range of 0 to 150 mm, a resolution of 0.01 mm and an accuracy of

± 0.03 mm, and a Biltema 19-1444 digital caliper with a measurement range of 0 to 150 mm, a resolution of 0.01 mm and an accuracy of ± 0.03 mm.

For each dimension, a measurement series consisting of 10 measurements are performed and the mean, $\bar{x}$, and the standard deviation, σ_x, are calculated. The measured points are distributed across the measured surface. The total measurement uncertainty is calculated by [69]

$$\sigma_{tot} = \sqrt{\sigma_x^2 + (\sigma_{instr})^2}, \tag{3.2}$$

where σ_{instr} is the uncertainty of the measurement device used.

The mass is measured using a A&D GF-3000 precision balance [70] with a stated repeatability (standard deviation) of 0.01 g and linearity of ± 0.02 g.

3.5 Brüel & Kjær 4138 microphone systems

Two different Brüel & Kjær microphone systems are used in the measurements. Both consists of a B&K 4138 1/8-inch microphone [55] and a B&K preamplifier, including a proprietary cable of 2 m, where a B&K UA-160 1/8-inch to 1/4-inch adaptor is used connect the microphone to the preamplifier. A preamplifier is used since the microphone requires a 200 V external polarization voltage. Details on the microphone systems is given in Table 3.6. Microphone system No. 1 is assembled in-house and includes a B&K 2633 preamplifier [56]. Microphone system No. 2 is assembled and sealed in a clean environment by B&K [71] and includes a BK2670 preamplifier [57]. Both preamplifiers are stated to have a flat frequency response [56, 57].

Table 3.6: Microphone systems used in the measurements

Brand/name	Type of equipment	Serial number
	Microphone system No. 1	
Brüel & Kjær 4138	1/8-inch pressure-field microphone	1832479
Brüel & Kjær UA-160	Adaptor - microphone to preamplifier	-
Brüel & Kjær 2633	Preamplifier	-
	Microphone system No. 2	
Brüel & Kjær 4138-A-015	Microphone system	2795107
- Brüel & Kjær 4138	1/8-inch pressure-field microphone	2784915
- Brüel & Kjær UA-160	Adaptor - microphone to preamplifier	-
- Brüel & Kjær 2670	Preamplifier	2799662

The Brüel & Kjær 4138 1/8-inch pressure-field microphone is designed for "high-level and very high-frequency measurements and measurements in confined spaces" according to the manufacturer [55], with a stated frequency range of 6.5 Hz to 140 kHz. However, the supplied calibration charts of the open-circuit pressure frequency response cover the frequency range from 20 Hz to 200 kHz [72, 73], where The frequency response is measured with an electrostatic actuator and expressed relative to response at 250 Hz. The calibration charts for the microphones in Microphone system No. 1 and Microphone system No. 2 are shown in Figs. 3.19 and 3.20, respectively.

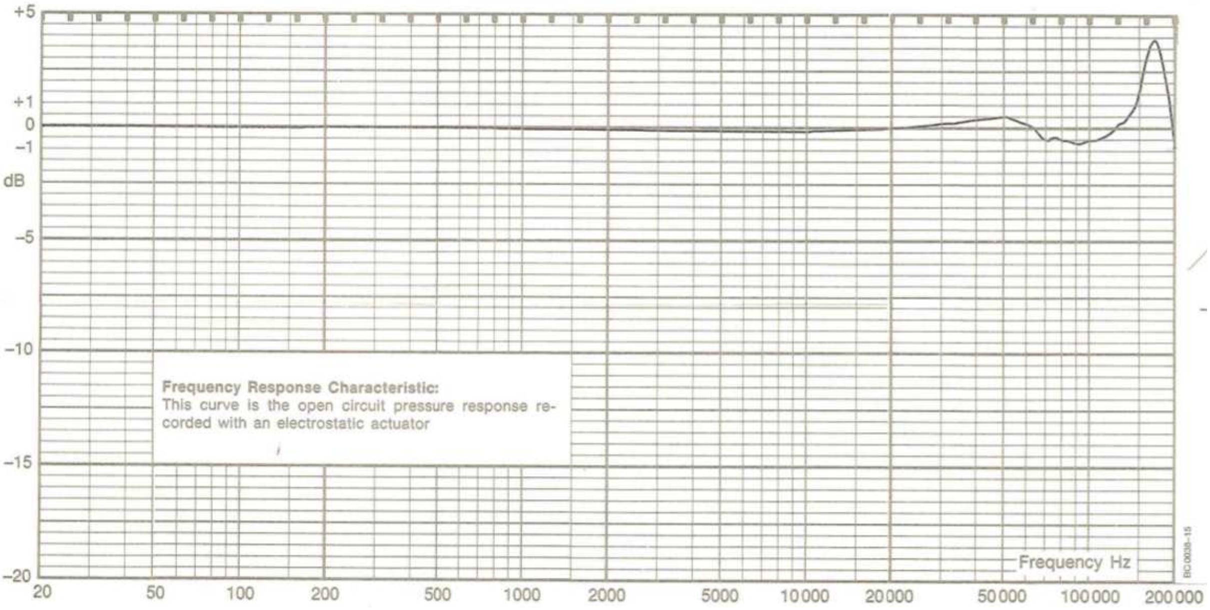

Figure 3.19: Calibration chart of the open-circuit pressure frequency response, relative to 250 Hz, of the Brüel & Kjær 4138 pressure-field microphone [72], serial no. 1832479, as used in Microphone system 1. Measured with an electrostatic actuator.

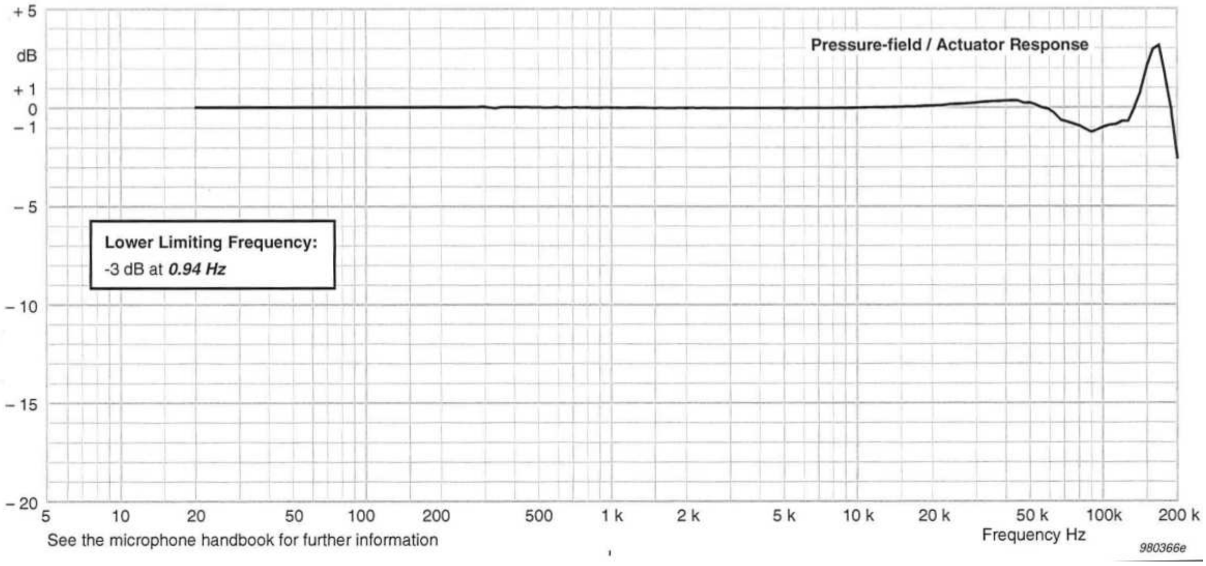

Figure 3.20: As Fig. 3.19, but for Brüel & Kjær 4138 pressure-field microphone [73], serial no. 2784915, as used in Microphone system No. 2.

An additional calibration of Microphone system No. 2, B&K 4138-A-015, is performed by Brüel & Kjær for frequencies up to 100 kHz [74], yielding the open-circuit pressure frequency response, relative to 250 Hz. In Fig.3.21 this calibration of Microphone system No. 2 is compared to the calibration of the microphone as shown in Fig. 3.20. These calibrations should agree, since the preamplifier frequency response is flat [57]. A maximum difference between the two calibrations of about 0.5 dB is observed at 100 kHz, where the uncertainty in the calibration of the system is 0.4 dB [74]. It is seen that the two calibrations agree within the given uncertainties. The calibration of the microphone (Fig. 3.20) is used in this work, as this provides the largest frequency range and it is assumed that the frequency response of the microphone and of the microphone system agree. This assumption is also applied to Microphone system No. 1.

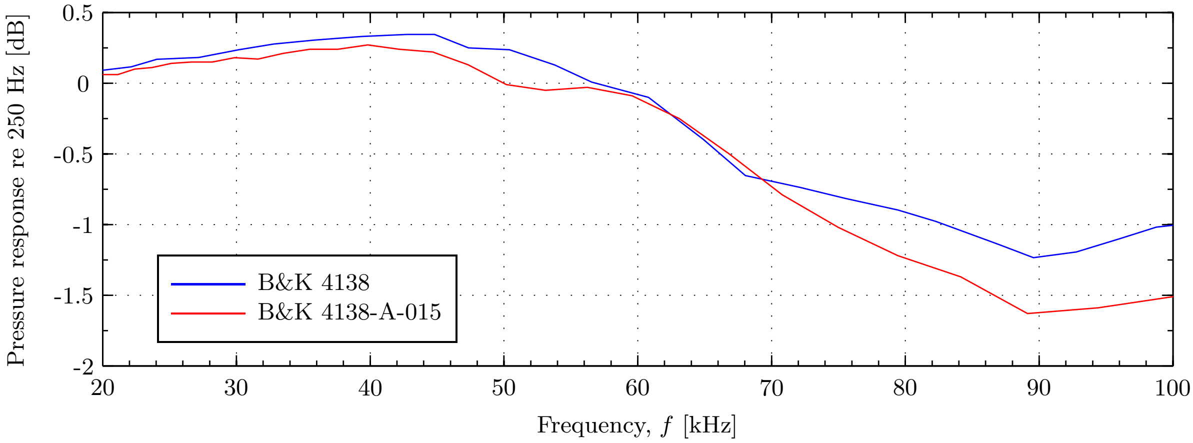

Figure 3.21: Comparison of the calibrated open-circuit pressure frequency responses, relative to 250 Hz, of the B&K 4138 microphone [73] (serial no. 2784915) in Microphone system No. 2 and the complete Microphone system No. 2 [74] (B&K 4138-A-015, serial no. 2795107).

The free-field open-circuit receiving voltage response of the microphone system, relative to 250 Hz, is determined by including a free-field correction to Fig. 3.19 and Fig. 3.20. The typical free-field correction for B&K 4138 microphones with protection grid [75] is given in Fig. 3.22. The curve for 0° incidence is used. It is assumed that the transition to dashed lines after 100 kHz indicates greater uncertainties for these frequencies. The curve for normal incidence is digitalized, as well as the calibration curves in Figs. 3.19 and 3.20, and used to determine $|M_V|$ relative to 250 Hz, shown for both microphone systems in Fig. 3.23.

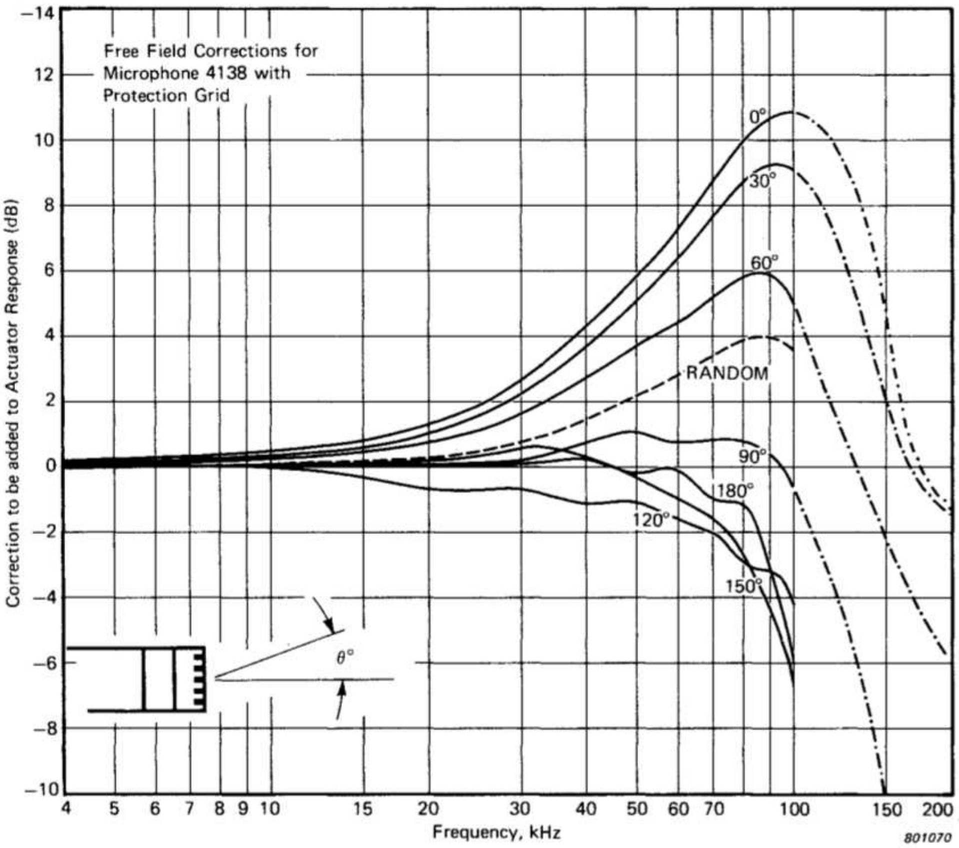

Figure 3.22: "Free-field correction curves for eighth-inch Condenser Microphone Type 4138 fitted with normal protection grid" [75]. Typical values only. The curve for normal incidence is used in the calculations.

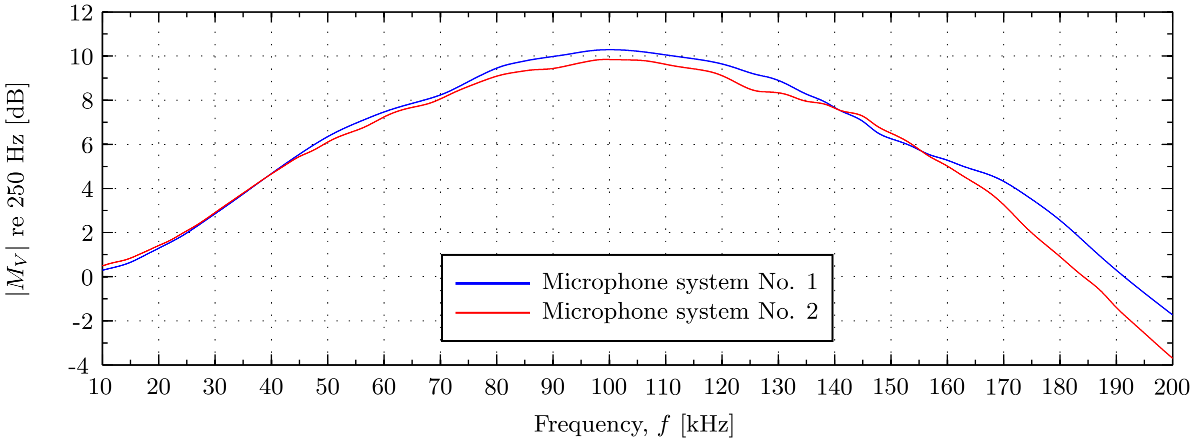

Figure 3.23: $|M_V|$ relative to 250 Hz for the two microphone systems used in this work.

3.5.1 Calibration of the microphones using a pistonphone

The magnitude of the free-field open-circuit receiving voltage response of each of the microphone systems is determined by combining the relative $|M_V|$ (shown in Fig. 3.23) with the free-field open-circuit receiving voltage response at 250 Hz. The latter is found by calibration with a Brüel & Kjær 4228 pistonphone [51] with a DP-0774 adaptor, as no free-field correction is needed at 250 Hz [75].

In the calibration, the microphone system, consisting of a microphone and a preamplifier, is connected to the B&K 2636 measurement amplifier with 20 dB gain, and without filters, and recorded by the Tektronix DPO3012 oscilloscope. $|M_V|$ is given by effective quantities as [37]

$$|M_V| = \frac{V_e}{p_e}, \tag{3.3}$$

where p_e is the effective free-field pressure at the position of the receiving transducer, assuming normal incidence and plane wavefronts at the transducer surface [37], and V_e is the effective open-circuit output voltage from the receiving transducer.

The pistonphone generates a known sound pressure level, SPL, which is defined as [48]

$$SPL \equiv 20\log_{10}\left(\frac{p_e}{p_{ref}}\right), \tag{3.4}$$

where p_{ref} is the reference level, usually set to 20 μPa in air. The given SPL for the pistonphone is 124.11 ± 0.09 dB re 20 μ at 251.2 Hz ± 0.1% [76]. The SPL is valid at 1013 hPa, 20°C and a relative humidity (RH) of 65 %. If the calibration of the microphone system is performed under different conditions the sound pressure level is found by [76]

$$\text{Actual } SPL = \text{Stated } SPL + \Delta L_p + \Delta L_V, \tag{3.5}$$

where ΔL_V is the correction for the load volume, and ΔL_p is the correction for the ambient pressure, which can be read directly from the supplied correction barometer UZ0004 or calculated using a correction of 0.2 dB per 23 hPa. ΔL_V is zero for a 1/8-inch microphone with protection grid [76].

Combining Eqs. (3.3), (3.4) and (3.5) and inserting known values yield

$$|M_V(251.2\,\mathrm{Hz})| = \frac{V_e}{10^{\frac{SPL+\Delta L_p}{20}}\, p_{ref}} = \frac{V_e}{10^{\frac{124.11+\Delta L_p}{20}}\, 20\times10^{-6}}, \tag{3.6}$$

which is $|M_V|$ at 251.2 Hz.

The effective output voltage is found from the measured peak-to-peak voltage, V_{pp}^{rec}, by

$$V_e = \frac{V_{pp}^{rec}}{20\sqrt{2}}, \tag{3.7}$$

where it is assumed that the input voltage to the measurement amplifier equals the recorded voltage, when the 20 dB gain in the measurement amplifier is corrected for by dividing the voltage by $10^{20/20} = 10$.

The microphone system with a Brüel & Kjær 4138 microphone, serial no. 1832479, and a Brüel & Kjær 2633 preamplifier, was calibrated at an ambient pressure of 1005 hPa, resulting in a correction factor $\Delta L_p = -0.07$ dB. The measured voltage was $V_{pp}^{rec} = 443.8$ mV, giving

$$|M_V(251.2\,\mathrm{Hz})| = \frac{V_e}{p_e} = \frac{15.6907\,\mathrm{mV}}{31.844\,\mathrm{Pa}} = 0.493\,\mathrm{mV/Pa}. \tag{3.8}$$

The given sensitivity of the microphone is 0.822 mV/Pa [72]. It is stated in [72] that the use of a Brüel & Kjær 2633 preamplifier typically reduces the sensitivity by approximately 6 dB, which corresponds to a total sensitivity of approximately 0.411 mV/Pa for the given configuration. The sensitivity of this microphone system was also calculated in [77] and [52]. The former has calculated it to be 0.3157 mV/Pa, the latter to 0.535 mV/Pa. This discrepancy has not been investigated further.

The Brüel & Kjær 4138-A-015 microphone system, serial no. 2795107, was also calibrated at an ambient pressure of 1005 hPa, resulting in a correction factor $\Delta L_p = -0.07$ dB. The measured voltage was $V_{pp}^{rec} = 470.5$ mV, giving

$$|M_V(251.2\,\mathrm{Hz})| = \frac{V_e}{p_e} = \frac{16.6347\,\mathrm{mV}}{31.844\,\mathrm{Pa}} = 0.522\,\mathrm{mV/Pa}. \tag{3.9}$$

The given sensitivity of the Brüel & Kjær 4138 is 0.925 mV/Pa [73], while it is 0.524 mV/Pa for the microphone system [71]. The sensitivity of the microphone system found by calibration with a pistonphone agrees well within the ± 0.2 dB (approx. 2.3 %) uncertainty of the value stated in [71]

3.6 Piezoelectric ceramic disks

Piezoelectric ceramic disks of the material Pz27, manufactured by Ferroperm [78], are used as transmitters and receivers, and as part of the piezoelectric transducers developed during the present work. Pz27 is a soft lead zirconate titanate with a relatively high Curie temperature, exceeding 350 °C, and high electromechanical coupling factors [78].

Disks with stated diameter, D, of 20 mm and a stated thickness, T, of 2 mm are used. The standard tolerance given by Ferroperm for either of the dimensions is ± 3 %. A batch of 20 disks were ordered and physical and electrical measurements were performed in order to choose which disks to use in the acoustic measurements. The measured dimensions are given in Table 3.7, and some of the electrical results are shown in Sections 6.1.1 and 7.4. It is desirable to use similar disks in the measurements, primarily determined based on the frequency of the first radial resonance peak found in the electrical measurements. The Element #10 and Element #16 were chosen for acoustical measurements and the Element #5, Element #15 and Element #20 were chosen to be used in the transducer construction.

Table 3.7: Dimensions of Pz27 piezoelectric ceramic disks with stated dimensions 20 mm × 2 mm and a tolerance of ± 3 %, measured with a Mitutoyo MDH-25M digimatic micrometer.

Disk No.	D [mm]	T [mm]
#1	20.24 ± 0.01	2.038 ± 0.001
#2	20.229 ± 0.006	2.020 ± 0.002
#3	20.241 ± 0.007	2.025 ± 0.003
#4	20.236 ± 0.005	2.0241 ± 0.0008
#5	20.24 ± 0.01	2.012 ± 0.003
#6	20.25 ± 0.01	2.031 ± 0.001
#7	20.24 ± 0.01	2.041 ± 0.004
#8	20.23 ± 0.01	2.036 ± 0.002
#9	20.206 ± 0.006	2.002 ± 0.002
#10	20.234 ± 0.008	2.035 ± 0.002
#11	20.23 ± 0.01	2.0244 ± 0.0008
#12	20.246 ± 0.007	2.040 ± 0.002
#13	20.242 ± 0.008	2.031 ± 0.002
#14	20.24 ± 0.01	2.040 ± 0.002
#15	20.23 ± 0.01	2.003 ± 0.001
#16	20.24 ± 0.01	2.035 ± 0.001
#17	20.23 ± 0.02	2.018 ± 0.001
#18	20.24 ± 0.01	2.037 ± 0.001
#19	20.26 ± 0.01	2.027 ± 0.001
#20	20.25 ± 0.01	2.033 ± 0.002

In order to perform the acoustic measurements, the piezoelectric ceramic disks need to be suspended from a horizontal steel bar, as described in Section 3.3.3. This is made possible by soldering wires to the disks, one wire on each of the electrodes, close to the edge. The disks were preheated to 175 °C and then soldered with 250 °C at the tip of the soldering iron, well below the Curie temperature. The soldering was performed by staff engineer Per Heradstveit. Fig. 3.24 shows a piezoelectric ceramic disk with and without wires connected.

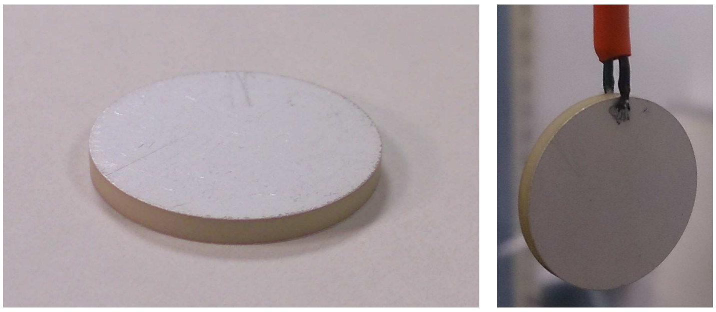
(a) (b)

Figure 3.24: Pz27 piezoelectric ceramic disk of approximate dimensions 20 mm × 2 mm. (a) Without wires. (b) With wires attached.

3.7 Signal processing

The measured voltage-to-voltage transfer function, corresponding to $H^{VV}_{0m6,\alpha}$, is expressed by extracting a voltage value from the measured waveforms in node $0m$ and 6, see Fig. 2.1. The measured waveforms in these nodes corresponds to V_{0m} and $V_{6,\alpha}$. The value representing each recorded waveform is the steady-state peak-to-peak voltage, V^{rec}_{pp}. V^{rec}_{pp} is calculated post-process, for an interval of samples in the recorded waveform, chosen as the steady-state.

3.7.1 The steady-state interval

The steady-state of a measured waveform is selected by visual inspection. The steady-state is selected as a sample interval, e.g. all samples between sample n_{start} and n_{stop}. The measured $V_{6,\alpha}$ is used for determining the steady-state area used for both $V_{6,\alpha}$ and V_{0m}, as the $V_{6,\alpha}$ waveform is the more complex waveform, due to a number of factors inherent in the physical processes of sound wave propagation and reception. The steady-state interval is held constant for all frequencies in one measurement series. A recorded waveform example, using piezoelectric elements as transmitter/receiver, is shown in Fig. 3.25.

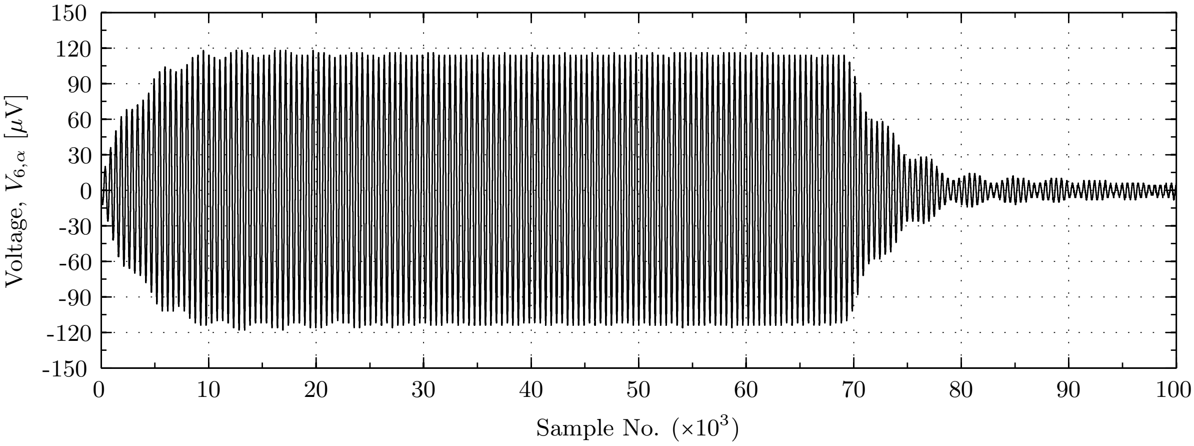

Figure 3.25: An example waveform.

A visual inspection of the waveform in Fig. 3.25 suggests that steady-state is reached somewhere between n_{start} = 20000 and 30000. A waveform from the same measurement, but at another frequency of interest, is shown in Fig. 3.26.

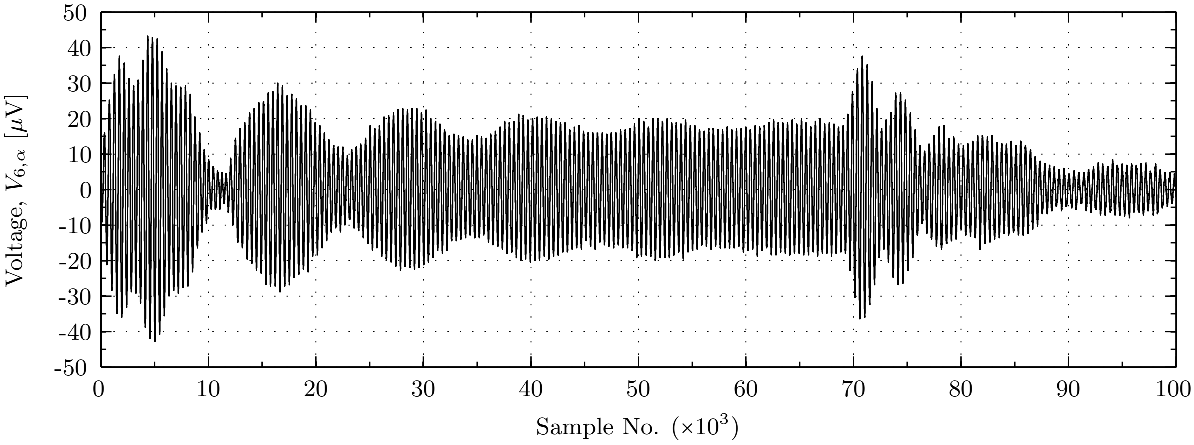

Figure 3.26: An example waveform.

In Fig. 3.26, steady-state is not reached within the applied burst length. An apparent way to reach steady-state for the Fig. 3.26 waveform is to increase the number of cycles in the applied burst. But increasing the burst length, while maintaining a constant separation distance between the transmitter and receiver, might cause effects such as (a) standing waves between the transmitter and receiver, and (b) cause sound waves reflected of other surfaces in the measurement cage to be recorded. To compensate, the measurement distance could also be increased, but that would decrease the SNR. Furthermore, the measurement series for Figs. 3.25 and 3.26 is done with maximum separation distance between the transmitter and receiver possible in the current measurement setup. Thus, the choice of the sample interval where V_{pp}^{rec} is calculated, is a compromise between the number of cycles wanted in the V_{pp}^{rec} calculation for statistical integrity, and whether or not steady-state has been reached. Henceforth, "calculation interval" is used to express the sample interval where V_{pp}^{rec} is calculated.

Calculation of V_{pp}^{rec} for a recorded waveform, either V_{0m} or $V_{6,\alpha}$, is done either by Fourier transform of the calculation intervals, cf. Section 3.7.2, or by direct calculation on the measured waveform, cf. Section 3.7.3.

The calculation intervals used in the signal processing performed in this work are shown in Table. 3.8.

Table 3.8: Calculation intervals used in the signal processing.

Transmit/receive combination	Calculation interval [10^3 samples]
Element to microphone	50 - 95
Element to element	45 - 65
Transducer to microphone	45 - 68
Transducer to transducer	50 - 78

3.7.2 Calculation of V_{pp}^{rec} - Fourier transform method

The MATLAB script `findPeakToPeak_FFT.m` calculates V_{pp}^{rec} for a given sample interval of a recorded waveform, cf. Appendix A.2.11. Let $V_{sig}(t)$ be the discrete voltage signal in the calculation interval of either V_{0m} or $V_{6,\alpha}$, recorded at the measurement frequency f_{sig}. The number of samples in $V_{sig}(t)$ is N_{sig}. The Fourier transform of $V_{sig}(t)$ is calculated using the `fft` algorithm in MATLAB , i.e.

$$V_{sig}(t) \xrightarrow{FFT} V_{sig}(f), \tag{3.10}$$

where $V_{sig}(t)$ has been zero-padded to a total length of 200000 samples in the `fft` function. The peak-to-peak voltage is found as

$$V_{pp}^{rec}(f_{sig}) = 2 \cdot 2 \cdot \frac{V_{sig}(f_{sig})}{N_{sig}}. \tag{3.11}$$

The frequency spectrum output of the function `fft` is two-sided, i.e. a spectrum is displayed for both negative and positive frequencies. For a real time response, the two spectra are symmetrical around the DC-component [79]. Parseval's theorem [80], states that the energy of the time and frequency domain must be equal. Hence only half the energy of the time domain is contained in the positive frequencies of the frequency spectra. The frequency spectra is multiplied by 2 to correct for this, as V_{pp}^{rec} is found at the (positive) measurement frequency f_{sig}. The peak-to-peak voltage is twice the size of the amplitude, thus $V_{sig}(f_{sig})$ is multiplied by 2 a second time. The frequency spectrum amplitude is dependent of the discrete time domain signal length. For instance, given a discrete sine wave with a whole number of cycles with amplitude A, the frequency spectrum amplitude for the sine waves frequency is $|A|/m$ [79], where m is the number of samples in the sine wave[4]. Thus, $V_{sig}(f_{sig})$ is divided by N_{sig}, in order to obtain the voltage amplitude of the measured waveform at frequency f_{sig}.

As an example, the calculation interval selected for the measurement series from which the waveforms in Figs. 3.25 and 3.26 are extracted, is sample $n_{start} = 40000$ through $n_{stop} = 65000$. Fig. 3.27 shows $V_{sig}(f)$ calculated using Eq. (3.10), for the waveform in Fig. 3.25.

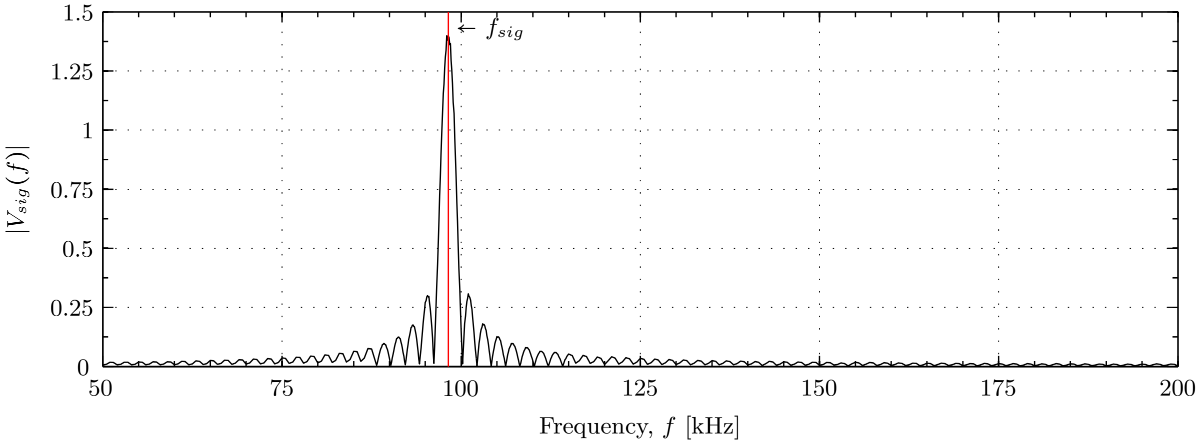

Figure 3.27: The frequency spectra of the waveform in Fig. 3.25. The calculation interval is $n_{start} = 40000$ through $n_{stop} = 65000$. The measurement frequency is marked with a red line.

---

[4] Zero-padding of the time-domain sine wave does not affect this expression [81].

The value of $|V_{sig}(f_{sig})|$ in Fig. 3.27 is 1.397. The number of samples in the calculation interval is $N_{sig} = n_{stop} - n_{start} = 25000$ samples. Using Eq. (3.11), V_{pp}^{rec} is found as

$$V_{pp}^{rec}(f_{sig}) = 2 \cdot 2 \cdot \frac{1.379}{25000} \approx 220\,\mu\text{V}, \tag{3.12}$$

which is seen to be close to the peak-to-peak voltage of the calculation interval in Fig. 3.25.

3.7.3 Calculation of V_{pp}^{rec} - direct method

An alternative, and more straight-forward method for extracting V_{pp}^{rec} from a measured waveform is implemented in the MATLAB script `findpeakToPeak.m`, cf. Appendix A.2.10. The calculation interval zero-crossings are found, equivalent to in Section 5.3.1. The sample length of one period at the measurement frequency is calculated. The V_{pp}^{rec} value is then calculated for each whole periode in the calculation interval, and the output value of the function is the averaged peak-to-peak voltage of each period.

This method is more sensitive to noise than the Fourier transform method described in Section 3.7.2. While the Fourier method filters out the signal frequency from the calculation interval spectrum, the direct method includes the overlaying noise in the calculation. This effect is visualized in Chapter 7, where the two methods for finding V_{pp}^{rec} are compared.

3.7.4 Calculation of SNR

The recorded noise (see Section 3.3.7) is used to determine the noise level. A calculation interval with $n_{start} = 50000$ and $n_{stop} = 90000$ is used. The RMS of the noise, with the DC-component subtracted, is calculated by [82]

$$V_{rms}^{noise} = \sqrt{\frac{1}{N}\sum_{i=1}^{N}(V_i - \bar{V})^2}, \tag{3.13}$$

where N is the number of samples in the calculation interval, V_i is the voltage of sample i and $\bar{V}$ is the mean of the noise. The SNR is determined by [82]

$$SNR = 20\log_{10}\left(\frac{V_{rms}^{rec}}{V_{rms}^{noise}}\right), \tag{3.14}$$

where $V_{rms}^{rec} = V_{pp}^{rec}/(2\sqrt{2})$ is the RMS of the recorded signal in the corresponding acoustic measurement.

Chapter 4

Finite element simulation setup

FE modeling is used to model the transmitting transducer and sound field in this thesis. In this chapter a brief description of the FE simulation tool used in this work, FEMP 5.0, is given in Section 4.1. Section 4.2 covers some important simulation parameters that need to be specified, and the corresponding values used in this work. The different commands that are used to set up and mesh the modelled piezoelectric structures are described in Section 4.3, and examples of the resulting meshes are shown. An overview of the material parameters needed to define piezoelectric materials, elastic (non-piezoelectric) materials and fluids are given in Section 4.4, as well as all material parameters used in the simulations in this work.

4.1 FEMP 5.0

The FE modelling is performed using the latest version of the simulation tool Finite element modelling of piezoelectric transducers, FEMP 5.0 [46,47]. A brief description of the theory can be found in Section 2.7. FEMP 5.0 is written in MATLAB . The input parameters to FEMP 5.0 are specified in a text file with the file extension `.inn`. The `.inn`-file may contain multiple values assigned to a single variable, allowing parametric simulations. A set of predefined transducer structures are available to specify the geometry of the current problem. Additional structures can be defined by use of the files `read_inn_project.m` and `init_const_project.m` where input parameters, points, areas and boundary conditions for a transducer structure are specified [46,47].

4.2 Simulation parameters

A number of simulation parameters must be given for each FE simulation. Only the simulation parameters used in this work are covered here.

- The dimensions of the transducer and the fluid domain are specified. When infinite fluid elements are used, the meshing angle in radians is set to 1.3 rad [83].
- A mesh is the spatial distribution of the finite and infinite elements in the FE simulation. The mesh is set up using 5 elements per wavelength, chosen as a compromise between calculation time and accuracy [46], which determines the element size in each material. In the fluid the wavelength for longitudinal waves are used, while the wavelength for shear waves are used in both piezoelectric and non-piezoelectric elastic materials [46].
- 8 node, corresponding to 2nd order, isoparametric finite elements and 12th order infinite elements are used in the simulations. Note that only finite elements are used if the transducer structure is modelled vibrating in vacuum [46].
- The infinite elements must be set up by defining R_{inf}, which is the radial distance from the origin of the mesh to the interface between the finite and infinite fluid elements. The accuracy of the solution are influenced by the choice of R_{inf}. For 12th order infinite elements, a minimum distance of $R_{inf} = 0.25a^2/\lambda$ is recommended in [46], where λ is the wavelength in the fluid and a is the radius of the front surface of the structure. The radius of the matching layer is used when calculating R_{inf} for the piezoelectric transducer, developed during this work.

Direct time-harmonic analysis is used in this work to solve the FE problem for a given set of frequencies [46]. It can be quite memory-intensive as the full set of calculations are performed for each frequency. In this work the losses are included as described in Section 4.4. Note that the air is modelled without loss.

When the FE problem is solved using the direct time-harmonic method, several quantities can be computed and saved [83]. The electrical admittance, Z_T, and the transmitting voltage response, S_V, of the transducer are always calculated in the simulations performed in this work. Other quantities that are saved in certain simulations are the axial pressure and the averaged pressure at a plane parallel to the transducer front surface of a specified size and at a specified axial distance.

The transmitting voltage response of the transducer is calculated at a specified axial reference distance from the front of the transducer structure. In this work the transmitting voltage response is calculated at 1000 m in the FE simulation, and then extrapolated back to $d_0 = 1$ m by spherical extrapolation, i.e $|S_V(d_0 = 1\,\mathrm{m})| = 1000\,|S_V(1000\,\mathrm{m})|$ since only the magnitude is considered when comparing to the present measurements. This is done to ensure that the transmitting voltage response is determined at far-field conditions.

4.3 Transducer meshing structures

A number of different piezoelectric structures are used in this work. Some of the structures used that are not included in FEMP 5.0 can be found in Appendix B.

- `piezodisk` models a piezoelectric ceramic disk vibrating in vacuum. This structure is included in FEMP 5.0.
- `piezodiskfluid` is used to model a piezoelectric ceramic disk vibrating in air. This structure is included in FEMP 5.0.
- `piezodiskwidefrontfluid` models a piezoelectric ceramic disk with a matching layer of greater radius than the disk, vibrating in air. Square fluid finite element at the front and back of the transducer are used to enhance the accuracy. Note that this means that R_{inf} must be greater than $\sqrt{2}a$, where a is the radius of the matching layer. A decimated mesh is shown in Fig. 4.1b. Implemented by Storheim [84].
- `piezodiskwidefrontglue` is used to model a piezoelectric ceramic disk with a matching layer attached to the disk with a layer of glue, vibrating in vacuum.
- `transducerfluid` is used to model the piezoelectric transducer developed during this work, radiating in air (see Chapter 6). The silver conductive epoxy layers are omitted[1]. The complete transducer, i.e. the full length of the backing layer and stainless steel housing, cannot be modelled in the current simulation setup due to insufficient computing power to handle the amount of elements required. A length of approximately 20 mm instead of approximately 80 mm is therefore used as the total length of the transducer. A decimated mesh of `transducerfluid` is shown in Fig. 4.1a. Based on a structure implemented by Storheim [84].
- `transducervacuum` models the piezoelectric transducer vibrating in vacuum, i.e the piezoelectric disk, matching layer, silver conductive epoxy layers, backing layer and housing cylinder. The housing rear lid is omitted. The full length of the stainless steel casing is used, and the short calculation times simplifies multiple simulations to investigate different material parameters. An example mesh is shown in Fig. 4.2, with a short housing for convenience.

In the structures where a backing layer is included, a solid cylinder is modelled, thus omitting the cylindrical hole in the middle of the backing layer, and the coned rear end of the backing layer (see Fig. 6.2.

---

[1] The structure is based on a structure implemented by Storheim [84]. Some adjustments have been made, but the more time consuming inclusion of the silver conductive epoxy layers has not been given priority.

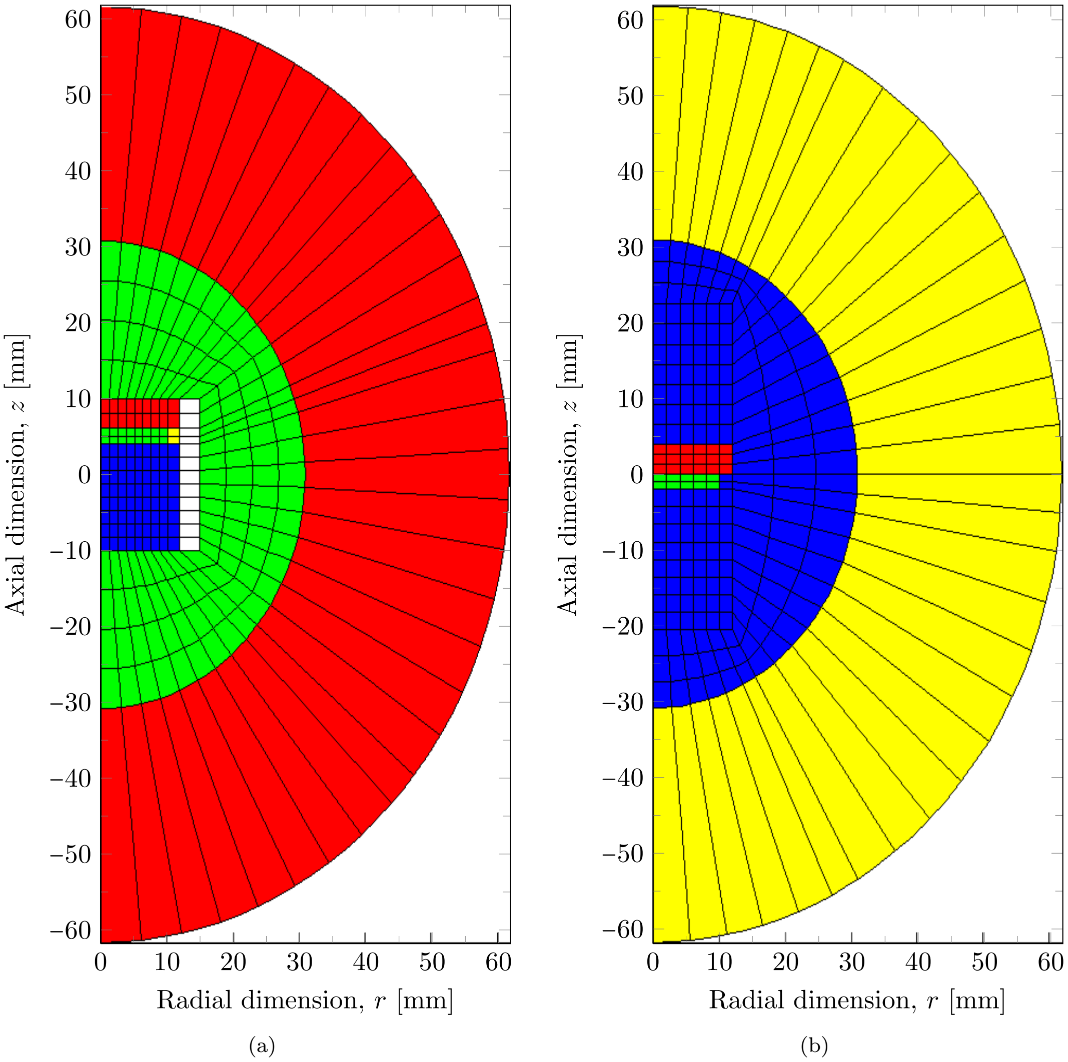

Figure 4.1: Decimated meshes, with 5 elements per wavelength at 10 kHz and R_{inf} = 30.9 mm, corresponding to a meshing frequency of 300 kHz. Silver conductive epoxy are omitted in both models. (a) shows a decimated mesh from `transducerfluid`, where the backing and housing are shorter than for the constructed transducer due to calculation limitations. (b) shows a decimated mesh from `piezodiskwidefrontfluid`.

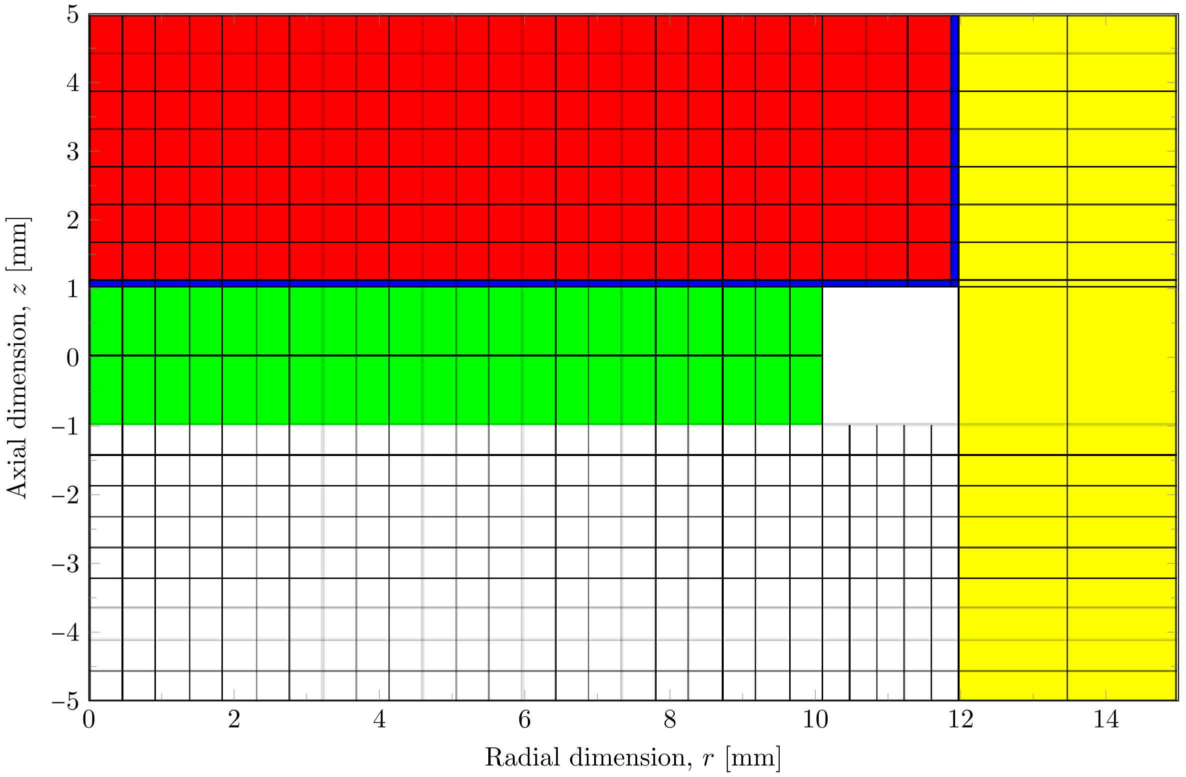

Figure 4.2: An example mesh from `transducervacuum`. The red area is the matching layer, the blue area is the silver epoxy, the green area is the piezoelectric ceramic disk, the yellow area is the stainless steel housing, and the white grid is the backing layer. Note that the length of the housing cylinder is set to 10 mm here to better show the mesh, as opposed to the real length of approximately 80 mm. Meshed with 5 elements per wavelength at 300 kHz.

4.4 Material parameters

It is often challenging to obtain accurate material parameters, either due to the incomplete material data supplied by the manufacturer or because of uncertainties in the supplied data, and also batch to batch variations in the materials. In FEMP the material data are stored in a `material.dat`-file. Three different types of materials can be defined: piezoelectric materials, elastic (non-piezoelectric) materials and fluids.

Piezoelectric material are described by mechanical, electromechanical and electrical material parameters, and the density, ρ. FEMP uses the elastic stiffness constants at constant electric field, c_{11}^E, c_{12}^E, c_{13}^E, c_{33}^E, c_{44}^E and c_{66}^E, the piezoelectric stress constants, e_{31}, e_{33} and e_{15}, and the permittivity at constant strain, ε_{11}^S and ε_{33}^S. The losses are described by a full set of complex material constants in the simulations performed in this work, accounting for dielectric, elastic, and piezoelectric losses. A simplified loss model may alternatively be used, where the elastic losses are described by the mechanical quality factor Q_m and the dielectric losses are described by the loss tangent δ_e [46].

To describe elastic materials with no piezoelectric properties, the density, ρ, mechanical quality factor, Q_m, sound speed for longitudinal waves, c_l, and the sound speed for shear waves, c_s, must be given. Poisson's ratio, σ, may be given instead of c_s [46].

The fluid is modelled without losses and described by its sound speed, c, and density, ρ [46].

4.4.1 The piezoelectric ceramic, Pz27

The piezoelectric material used in this work is Pz27 from Ferroperm [78]. The material data provided by the manufacturer are specified with an uncertainty of ± 10 % for the dielectric properties, ± 5 % for the electromechanical properties and ± 2.5 % for the mechanical properties. Previous work has shown that a better agreement between measurements and FE simulations is achieved if an adjusted data set is used to model Pz27 [85,86]. The adjusted material data set found in [85] is used here. This was determined based on the work in [86] and [87], and the material data set was adjusted to improve the agreement between the simulations and measurements at the first radial mode resonances. The measurements in [85] were conducted with piezoelectric elements with similar dimensions as those used in this work. It is however emphasized that the adjusted material parameters may not represent the actual material parameters of the piezoelectric ceramic, and will therefore not necessarily fit equally well when used to model different batches or elements of different dimensions [85]. Both the material data from Ferroperm and the adjusted data set from [85] are given in Table. 4.1.

Table 4.1: Material data for the piezoelectric material type Pz27. The adjusted data set is used in the FE simulations.

Parameter	Unit	Ferroperm data [78]	Adjusted data set [85]
c_{11}^E	[10^{10} Pa]	14.70	$11.875\left(1+i\frac{1}{95.75}\right)$
c_{12}^E	[10^{10} Pa]	10.50	$7.430\left(1+i\frac{1}{71.24}\right)$
c_{13}^E	[10^{10} Pa]	9.37	$7.425\left(1+i\frac{1}{120.19}\right)$
c_{33}^E	[10^{10} Pa]	11.30	$11.205\left(1+i\frac{1}{120.19}\right)$
c_{44}^E	[10^{10} Pa]	2.30	$2.110\left(1+i\frac{1}{120.19}\right)$
e_{31}	[C·m^{-2}]	-3.09	$-5.40\left(1-i\frac{1}{166}\right)$
e_{33}	[C·m^{-2}]	16.00	$16.0389\left(1-i\frac{1}{323.177}\right)$
e_{15}	[C·m^{-2}]	11.60	$11.20\left(1-i\frac{1}{200}\right)$
ϵ_{11}^S	[10^{-p} F/m]	10.0005	$8.110044\left(1-i\frac{1}{50}\right)$
ϵ_{33}^S	[10^{-p} F/m]	8.0927	$8.14585\left(1-i\frac{1}{86.28}\right)$
ρ	[kg·m^{-3}]	7700	7700
Q_m	-	80	-
$\tan\delta$	-	0.017	-

4.4.2 Air

The air is modelled without losses, using the material parameters given in Table 4.2, corresponding to approximately 20 °C and 1 atm.

Table 4.2: Material data used to model the fluid medium, air.

Name	Parameter	Unit	Value
Density	ρ	[kg/m^3]	1.21
Sound speed	c	[m/s]	343

4.4.3 Matching layer

A matching layer is used, when the piezoelectric transducers are constructed (see Chapter 6), to improve the acoustic coupling between the piezoelectric ceramic disk and the fluid medium, i.e. air. Two materials were assessed in detail when the matching layer material was chosen. Both were Aptflex syntactic foam from Precision Acoustics, R3 and R7, which is a composite material made of glass spheres with epoxy resin as the polymeric binder [88, 89]. According to the manufacturer it is a tough non-conducting material with a low specific gravity, high hydrostatic compressive strength, and excellent chemical resistance [89]. The microbubbles in the syntactic foam have a diameter size distribution between approximately 10 and 90 μm [88].

The longitudinal sound speed ($c_l = 2034 \pm 30$ m/s), density ($\rho = 570 \pm 20$ kg/m^3) and Poisson's ratio ($\sigma = 0.375 \pm 0.05$) are specified for Aptflex R3. The attenuation coefficient, α, is given for frequencies from 1 MHz to 7 MHz [88]. As this is well above the frequencies of interest in this work, a curve fit must be performed to find extrapolated values. The supplied attenuation coefficient is used to calculate the mechanical quality factor, Q_m, by [44]

$$Q_m = \frac{k}{2\alpha_{Np/m}}, \tag{4.1}$$

where $\alpha_{Np/m}$ is the attenuation coefficient in Neper per meter, found by $\alpha_{Np/m} = 100\alpha_{dB/cm}/20\log_{10}(e)$. The curve fitting $\alpha_{dB/cm} = 0.42+3.84(f[\text{MHz}])^{1.27}$, supplied by PA [88], does not give physically plausible values at low frequencies, as is seen in Fig. 4.3. A new curve fitting is therefore performed in this work, giving $\alpha_{dB/cm} = 4.069(f[\mathrm{MHz}])^{1.24}$. Both the curve of the measured absorption coefficients, the supplied curve fit and the new curve fit are shown in Fig. 4.3, along with the corresponding quality factors. A plot of Q_m resulting from the new curve fit for the frequency range 50 kHz to 300 kHz is shown in Fig. 4.4. From this curve a Q_m of 55 is chosen for use in the simulations, for convenience, as Q_m varies between 44 and 68 in the plotted frequency range. It is important to keep in mind that Q_m is found based on measurements at higher frequencies and that a different curve fit may give a more appropriate value.

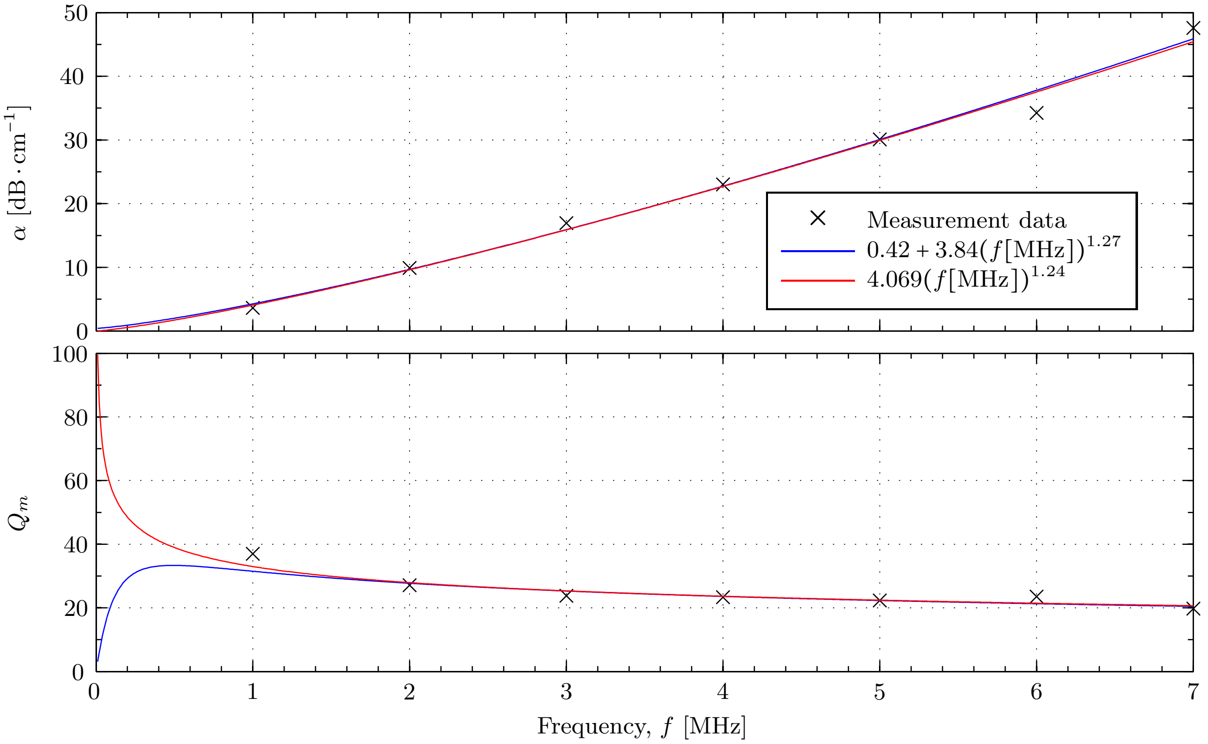

Figure 4.3: Attenuation coefficient, $\alpha_{dB/cm}$, and corresponding mechanical quality factor, Q_m, for Aptflex R3. It shows sample values measured by Precision Acoustics [88], curve fit performed by Precision Acoustics, $\alpha_{dB/cm} = 0.42 + 3.84(f[\mathrm{MHz}])^{1.27}$ [88], and curve fit performed in this work, $\alpha_{dB/cm} = 4.069(f[\mathrm{MHz}])^{1.24}$. Plotted for frequencies up to 7 MHz.

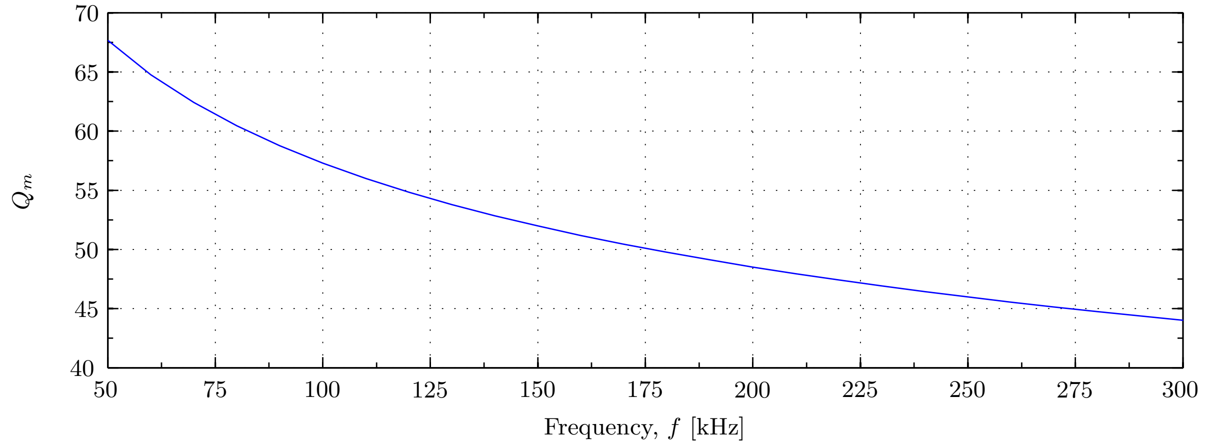

Figure 4.4: Mechanical quality factor, Q_m, of Aptflex R3 for the frequency range 50 kHz to 300 kHz. Found by curve fit of measured values, performed in this work, $\alpha_{dB/cm} = 4.069(f[\mathrm{MHz}])^{1.24}$.

Material data for Aptflex R7 are not available from the manufacturer as it is a quite new material. A density of approximately 450 kg/m^3 is indicated, as well as a longitudinal sound speed below that of

Aptflex R3 [88]. In the simulations the Poisson's ratio for R7 is assumed to be the same as for the rest of the Aptflex syntactic foams available, $\sigma = 0.375 \pm 0.05$ [89]. It is also assumed that Q_m is similar for R3 and R7.

The density and longitudinal sound speed are measured (see Chapter 5), as the material data for Aptflex R7 are uncertain at best. Measurements are also conducted on Aptflex R3, and values exceeding the uncertainties supplied by PA [89] are found.

The different material data for R3 and R7 used in the FE simulations are given in Table 4.3.

Table 4.3: Material data used when modelling Aptflex R3 and Aptflex R7.

Name	Parameter	Unit	R3[2]	R3[3]	R3[4]	R7[5]
Density	ρ	[kg/m^3]	570	598	598	420
Longitudinal sound speed	c_l	[m/s]	2034	2100	2100	2266
Poisson's ratio	σ	-	0.375	0.375	0.35	0.375
Mechanical Q-factor	Q_m	-	55	55	40	55

4.4.4 Glue

A two-component silver conductive epoxy from MG Chemicals [?] is used to glue the matching layer to the piezoelectric ceramic disk and to the metal housing. According to the manufacturer it forms high strength conductive bonds and can be used in place of traditional solder [?]. The stated volume resistivity is 0.38 Ω·cm and the hardness is 65 Shore D [?]. No additional data of interest here is given in the package. The data sheet currently available from the manufacturer contains different values than stated on the packaging of the silver conductive epoxy [?, 90]. There the volume resistivity is stated to be 0.0174 Ω·cm and the hardness to be between 70D and 75D. The density is also included, and it is given as 2440 kg/m^3 [90]. This density is used to model the silver conductive epoxy used in the transducer construction.

The longitudinal sound speed and Poisson's ratio are not supplied from the manufacturer. Estimated values must therefore be used in the FE simulations, based on material data for similar materials.

Material parameters for a silver epoxy are found in [91], with a longitudinal sound speed of 1900 m/s, shear sound speed of 980 m/s, density of 2710 kg/m^3 and a mechanical quality factor of $Q_m = 18$ at 2 MHz. These material data are used in the simulations, but with the density as given in [90] and an estimated mechanical quality factor of $Q_m = 25$, as it is assumed that the losses will decreased with the frequency.

The material data used in the FE simulation to model the two component silver epoxy from MG Chemicals are given in Table 4.4.

Table 4.4: Material data used when modelling the silver conductive epoxy.

Name	Parameter	Unit	Estimated values
Density [90]	ρ	[kg/m^3]	2440
Longitudinal sound speed	c_l	[m/s]	1900
Shear sound speed	c_s	[m/s]	980
Mechanical Q-factor	Q_m	-	25

4.4.5 Housing

The housing is made of grade 316 stainless steel. The necessary material parameters needed to model stainless steel are not readily available, but the density of a grade 316 stainless steel is given in [92], $\rho = 8000$ kg/m^3, and in [93] Young's modulus and Poisson's ratio at 25 °C are given as $Y = 198.6$ GPa and $\sigma = 0.263$, respectively.

---

[2] Material data supplied by PA [88, 89]

[3] Measured c_l and ρ (see Chapter 5). σ and Q_m as stated by PA [88, 89].

[4] Measured c_l and ρ (see Chapter 5). Adjusted σ and Q_m (see Chapter 6)

[5] Measured c_l and ρ (see Chapter 5). σ and Q_m as stated by PA for R3 [88, 89].

These parameters are used to determine c_l by [44]

$$c_l = \sqrt{\frac{\lambda + 2\mu}{\rho}}, \tag{4.2}$$

and c_s by

$$c_s = \sqrt{\frac{\mu}{\rho}}, \tag{4.3}$$

where ρ is the density and λ and μ are the Lamé parameters, given as

$$\lambda = \frac{\sigma Y}{(1+\sigma)(1-2\sigma)} \qquad \text{and} \qquad \mu = \frac{Y}{2(1+\sigma)}, \tag{4.4}$$

where it is assumed that the material is isotropic.

Q_m is assumed to be the same as for the steel used in [94], $Q_m = 100$. The material parameters used in the simulations are given in Table 4.5.

Table 4.5: Material data used when modelling the stainless steel, grade 316, housing.

Name	Parameter	Unit	Estimated values
Density [92]	ρ	[kg/m^3]	8000
Longitudinal sound speed	c_l	[m/s]	5528
Shear sound speed	c_s	[m/s]	3135
Mechanical *Q*-factor	Q_m	-	100

4.4.6 Backing

Divinycell H130 [95] is used as backing in the transducer. The longitudinal sound speed is found from the values of Young's modulus, Poisson's ratio ($\sigma = 0.4 \pm 0.045$) and the density ($\rho = 130$ kg/m^3 ± 10 %) given in [95], using Eqs. (4.3) and (4.4). Both a nominal and minimum value for Young's modulus are given in [95], 175 MPa and 135 MPa, respectively. The nominal value is used in the calculations. No data is available on the mechanical loss in Divinycell H130. In [85] $Q_m = 25$ is used for Divinycell H200 and HCP70. An estimated $Q_m = 25$ is used when the full length of backing layer is used in `transducervacuum`, while $Q_m = 5$ is used when simulations are performed with `transducerfluid` to compensate for the reduced backing layer length. The material data used in the simulations are given in Table 4.6.

Table 4.6: Material data used when modelling the Divinycell H130 backing.

Name	Parameter	Unit	H130	H130
Density [95]	ρ	[kg/m^3]	130	130
Longitudinal sound speed	c_l	[m/s]	1698	1698
Poisson's ratio [95]	σ	-	0.4	0.4
Mechanical *Q*-factor	Q_m	-	5	25

4.5 Calculation of system model quantities

FE modeling is used in combination with transmission-line modeling for calculating the system model quantities derived in Chapter 2. In this section, the calculation approach for several of the system model quantities which are compared to measurements in Chapter 7, are presented.

4.5.1 Calculating $H_{15,\alpha}^{VV,open}$

The transfer function for Modules C-E, with open-circuit conditions and medium absorption, $H_{15,\alpha}^{VV,open}$, is presented as three expressions. *Model 1* is given in Eq. (2.56), where z_∞ is set to $z_\infty = 1000$ m, V_1 is set to V_1 = 1 V (an inherent), a is the radius of the piezoelectric ceramic disk, or the matching layer, if a matching layer is used in the structure modeled. The absorption coefficient α, is calculated using the MATLAB script `absorbsjonluft.m` (cf. Appendix A.3.2). The environmental parameters relative humidity and temperature, are measured for each frequency in a measurement series, and used in the calculation of α for comparison with measurements. The ambient pressure is not measured, and set to 1013 hPa. These values are used for all measurement comparisons, for convenience. The far-field pressure $p_4(z_\infty)$ is calculated from S_V found under far-field conditions in FEMP , i.e.

$$S_V(d_0 = 1000\,\mathrm{m}) = \frac{p_3(d_0 = z_\infty = 1000\,\mathrm{m})}{V_1} = \frac{p_4(z_\infty)}{V_1} = \frac{p_4(z_\infty)}{1\,\mathrm{V}} \tag{4.5}$$

where it has been used that V_1 = 1 V, and that $p_3(d_0) = p_4(z_\infty)$ for $d_0 = z_\infty$, i.e. node 3 and node 4 is placed at the same point.

The receiving sensitivity M_V is calculated using Eq. (2.65), where Z_T is the electrical impedance of the transmitting transducer, calculated in FEMP by $Z_T = 1/Y$ (cf. Section 2.7). While S_V is calculated as described in Section 4.2. The air density, ρ, is given in Table 4.2.

In this work, $H^{dif}(z)$ is calculated by assuming $H^{dif}(z) \approx H_K^{dif}(z)$, as discussed in Section 2.3, where $H_K^{dif}(z)$ is Khimunin's diffraction correction, defined in Eq. (2.40). $H_K^{dif}(z)$ is calculated using Eq. (2.41), which is implemented in the MATLAB script `Khimunin_diffractioncorrection.m`.

In the calculation of $H_{15,\alpha}^{VV,open}$ (cf. Eq. (2.57)), termed *Model 2A*, $\langle p_4(z)\rangle$ is calculated using a FEMP function, which averages the free-field axial sound pressure at distance z from the transmitter over an acoustically transparent area with radius a. The area is placed in the area of the front surface of the receiving transducer, without the receiving transducer present.

$p_3(d_0)$ is found using a FEMP function that calculates the free-field axial sound pressure at distance d_0 from the transmitter.

$H_{15,\alpha}^{VV,open}$ calculated using Eq. (2.58), termed *Model 2B*, uses the same quantities as above, in addition to $H_K^{dif}(z_\infty)$, which is calculated equivalent to the calculation for distance $H_K^{dif}(z)$.

4.5.2 Calculation of $R^{dif}(z)$

Two formulations are derived for $R^{dif}(z)$, and given in Eq. (2.32). The free-field sound pressures, $\langle p_4(z)\rangle$ and $p_4(z_\infty)$ are used when calculating *formulation A*. $\langle p_4(z)\rangle$ and $p_4(z_\infty)$ are calculated in the same manner as in the section above.

Formulation B is calculated using $H_K^{dif}(z)$ and $H_K^{dif}(z_\infty)$, where the same assumption as above has been made.

4.5.3 Calculation of transfer functions for electronics and cables

For the cases of piezoelectric ceramic disks, or the constructed transducers, used both as transmitters and receivers, the transfer functions for the transmitting and receiving electronics are calculated using Eqs. (2.81) and (2.109). Z_T in the transfer functions are calculated in FEMP by $Z_T = 1/Y$, as above.

When the microphone is used as the receiving transducer, no modeling of the receiving electronics are conducted. In this case it is assumed that $V_6 = V_5^{open}$. However, the effect of the receiving electronics are included in the calibrated receiving sensitivity of the microphone, $|M_{B\&K}|$, see Section 3.5.1. Thus, the effect of the receiving electronics is measured, and included in the measured $H_{0m6,\alpha}^{VV}$, when using a microphone receiver.

Chapter 5

Matching layer characterization

Matching layers are used to presumably increase the bandwidth and sensitivity of e.g. a piezoelectric ceramic disk radiating into air. In order to characterize the matching layers, sound speed measurements are conducted in the measurement cell made by Fosså [96]. The density of the matching layers are also determined, by volume and weight measurements. Knowing the longitudinal sound speed and density, the characteristic impedance of each matching layer is calculated.

Section 5.1 covers the theory used to find the sound speed and characteristic impedance of a matching layer. The measurement setup is presented in Section 5.2 and the signal processing used to extract the results from the measurements is described in Section 5.3. Then the results are shown in Section 5.4 and briefly discussed in 5.5. Theory, measurement methods and results are all presented in this chapter, because the measurement setup used here differs from the setup used elsewhere in this work.

The theory is used on measurements to calculate the sound speed in the materials Aptflex R3 and R7 from Precision Acoustics (PA). PA provides the longitudinal sound speed and density for R3, given as $c_{l,R3} = 2034 \pm 30$ m/s and $\rho_{R3} = 570 \pm 20$ kg/m^3 [88], respectively. These values are compared with the values found experimentally in this chapter. Since no sound speed value is given by PA for the material R7, it is determined here for use in simulations. A density of $\rho_{R7} = 450$ kg/m^3 for Aptflex R7, and a sound speed lower than for R3, is indicated by PA [88], and compared to the value measured here.

5.1 Theory

In the following, the theory needed for calculating the sound velocity in a material sample placed in water is presented. The theory covered in this work is a simplified version of the theory presented in [96], neglecting the effect of diffraction, and the transit times through the transmitting and receiving transducer and electronics.

5.1.1 Calculating the sound speed

In Fig. 5.1 the sound speed measurement cell used for the sound speed measurements is illustrated.

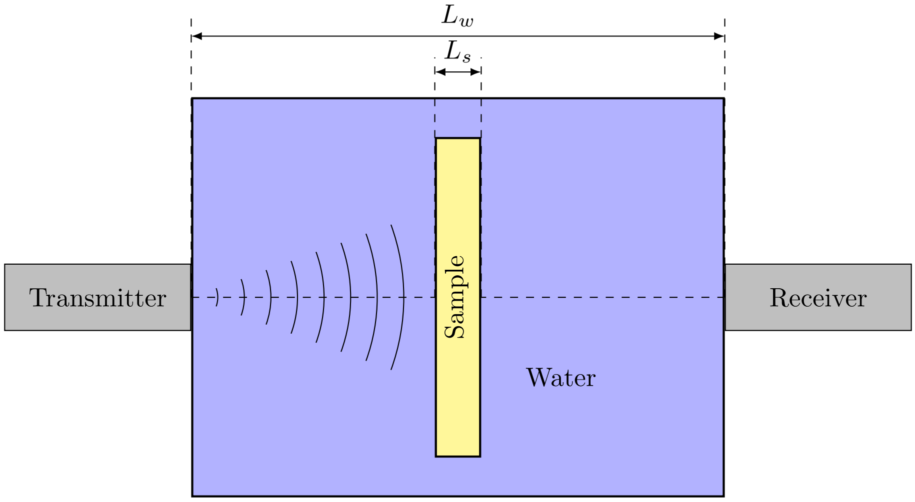

Figure 5.1: Illustration of the sound speed measurement cell. A sample of thickness L_s is immersed in water between a transmitting and a receiving transducer. The sample is orthogonally aligned with the axis of which the two transducers are coaxially aligned. The distance between the front of the transmitter and the front of the receiver is L_w.

To calculate the sound speed in the sample, two cases are considered; (1) the sample is not present in the tank, and (2) the sample is present in the tank. The plane wave transit time[1] for case (1), denoted $t^{(1)}$, is expressed as

$$t^{(1)} = \frac{L_w}{c_w^{(1)}}, \tag{5.1}$$

where L_w is the distance between the front of the transmitter and receiver, as seen in Fig. 5.1, and $c_w^{(1)}$ is the sound speed in water for case (1)[2]. The plane wave transit time for case (2), denoted $t^{(2)}$, is expressed as

$$t^{(2)} = \frac{L_w - L_s}{c_w^{(2)}} + \frac{L_s}{c_l}, \tag{5.2}$$

where L_s is the sample thickness, as seen in Fig. 5.1, $c_w^{(2)}$ is the sound speed in water for case (2), and c_l is the longitudinal sound speed in the sample. The difference in transit times between case (1) and (2) is expressed as

$$\Delta t = t_w^{(1)} - t_w^{(2)}. \tag{5.3}$$

By inserting Eqs. (5.1) and (5.2) into Eq. (5.3), the longitudinal speed in the sample, c_l, is expressed as

$$c_l = \left[\frac{L_w}{L_s} \left(\frac{1}{c_w^{(1)}} - \frac{1}{c_w^{(2)}} \right) + \frac{1}{c_w^{(2)}} - \frac{\Delta t}{L_s} \right]^{-1}. \tag{5.4}$$

In Eq. (5.4), , and L_s is measured using a digital caliper, cf. Section 5.2. $c_w^{(1)}$ and $c_w^{(2)}$ are calculated using Bilaniuk and Wong's 148 point equation for the sound speed in water as a function of temperature [97,98]. The water temperature is measured for each measurement, cf. Section 5.2.

The transit times $t_w^{(1)}$ and $t_w^{(2)}$ are measured by recording the input voltage to the transmitter, V_{el}, and the output voltage from the receiver, V_{ac}. By calculating the time difference between corresponding zero crossing pairs in the steady-state of the recorded waveforms, the transit time is measured.

5.1.2 Characteristic impedance

The characteristic impedance of a medium is for plane waves defined as [48]

$$z = \rho c, \tag{5.5}$$

where ρ is the density of the medium and c is the longitudinal sound speed in the medium.

---

[1] The time between the first transmitting wave onset to the first receiving wave onset.

[2] The sound speed in water for case (1) and (2) are considered separately because different water temperatures in the measurements for case (1) and (2), resulted in different sound speeds for the water. The change in the sound speed for the sample with temperature is not considered here.

5.2 Measurement setup and methods

A block diagram of the measurement setup is given in Fig. 5.2. The measurement setup closely resembles the setup used in [96].

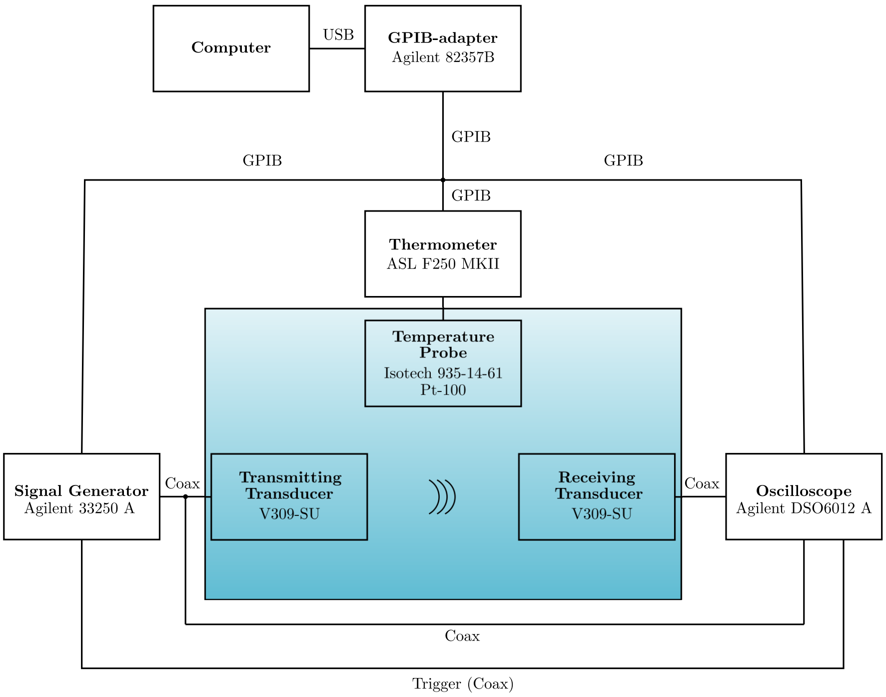

Figure 5.2: Block diagram of the measurement setup used in the sound speed measurements. Borrowed from [96]. Note that the thermometer and temperature probe depicted in this figure was not used during the present work.

An Agilent 33250A signal generator is generating the input voltage to an Olympus V309-SU transmitting transducer [99], which transmits sound into water. The signal is then received by an Olympus V309-SU receiving transducer, and recorded by an Agilent DSO6012A oscilloscope, with vertical resolution of 8 bits. In the oscilloscope, 16 averages are performed for each recorded waveform. The oscilloscope also records the input signal to the transmitting transducer. The measurement cell is filled with Biltema 361769 demineralized water, which is left to stabilize for 48 hours after pouring to minimize the occurrence of air bubbles interfering with the sound field. The temperature in the water during the acoustical measurements is measured using a Hanna Checktemp-1 handheld thermometer [100]. Hanna Checktemp-1 with a resolution of 0.1 °C and an accuracy of ±0.3°C in the temperature range of interest.

An input voltage of 5 Vpp, burst period of 10 ms and 12 cycles were used, as in [96]. Although the Olympus V309-SU transducers used have center frequencies at 4.69 and 5.39 MHz [96], the frequency used for the sound speed measurements is 3.0 MHz. High dampening in Aptflex R7 were observed for frequencies above 3.5 MHz, which resulted in a very low amplitude of the received voltage, V_{ac}, rendering post processing futile for the current input voltage.

The measured voltages are shown in Figs. 5.3 - 5.10, along with illustrations of the post process routine.

The volume of the samples are determined by measuring the thickness using a Mitutoyo MDH-25M digimatic micrometer [67], with a resolution of 0.1 μm and an accuracy of ±0.5 μm, and the width and length using a Biltema 191444 digital caliper, with a resolution of 0.01 mm and an accuracy of ±0.03 mm. In addition to contribute to determining the volume, the thickness measurement is used to express L_s, used in Eq. (5.4). 10 measurement points, evenly distributed over the sample, are collected for each sample's thickness, width and length measurement. See Table 5.3 for the measured dimensions of the two samples used in this work. The values listed in Table 5.3 are the average value of the 10 measurement points on each sample. L_w is measured by hand using a measuring tape.

The mass of the samples were measured using an A&D GF-3000-EC precision balance [70] with a stated repeatability (standard deviation) of 0.01 g and linearity of ± 0.02 g.

The instruments used in the measurements are listed in Table 5.1.

Table 5.1: The instruments used for the sound speed measurements.

Brand/name	Type of equipment	Serial number
Agilent 33250A	Signal generator	MY40014887
Agilent DSO6012A	Oscilloscope	MY45007479
Agilent 82357B	USB/GPIB Interface	2007/11 (internal ID)
Olympus V309SU	Transducer	725192
Olympus V309SU	Transducer	721067
Biltema 361769	Deminearlized water	-
Hanna CheckTemp-1	Handheld thermometer	-
Measurement cell	-	-
Standa 7R129	Rotary stage	-
Mitutoyo MDH-25M	Digimatic micrometer	15229628
Biltema 191444	Digital caliper	-
A&D GF-3000-EC	Precision balance	P1826763

5.3 Signal processing

MATLAB is used to calculate the transit time of the acoustical signal from the transmitter to the receiver. It is assumed that the acoustical signal propagates as a plane wave through both the water and sample material. The transit time is calculated by taking the time difference between a zero crossing pair in the V_{el} and V_{ac} waveforms. A zero crossing pair are e.g. the a zero crossing of a period in V_{el} and of the corresponding period in V_{ac}.

5.3.1 Zero crossing detection

This section covers the method for finding the zero crossings in the measured voltage waveforms V_{el} and V_{ac}. In the following, both V_{el} and V_{ac} are treated in the same way, and termed V.

The signal is interpolated with 100 points linearly distributed between each point of the original waveform. Then the mean value of the waveform is calculated. The mean value of the voltage waveform V is given as

$$\bar{V} = \frac{1}{N} \cdot \sum_{i=1}^{N} y_i, \tag{5.6}$$

where y_i is the value of sample number i in V, consisting of N samples. The sample y_i is regarded as a zero crossing if $\bar{V}$ is between y_i and y_{i+1}. In order to detect zero crossings, a new function C is defined as

$$C(y_i) = sgn\left(\bar{V} - y_{i+1}\right) - sgn\left(\bar{V} - y_i\right), \tag{5.7}$$

where $sgn(x)$ is the "sign function", defined as

$$sgn(x) = \begin{cases} -1 & \text{if } x < 0, \\ 0 & \text{if } x = 0, \\ 1 & \text{if } x > 0. \end{cases} \tag{5.8}$$

If y_i is below $\bar{V}$ and y_{i+1} is above, then $C(y_i) = 2$. If y_i is above $\bar{V}$ and y_{i+1} is below, then $C(y_i) = -2$. Zero crossing n is thus found as

$$n = i \,\text{if} : \begin{cases} C(y_i) = 2, \\ C(y_i) = -2. \end{cases} \tag{5.9}$$

The time of zero crossing n is t_i, where t_i is the time-value corresponding to y_i, i.e. $V(t_i) = y_i$. Only the zero crossings found in the steady state part of the signal is used for calculating the transit time. The time difference for the zero crossings in the steady state is averaged to express the time difference between the transmitted and received signal.

5.3.2 Measured waveforms, R3

In Figs. 5.3 - 5.6 the transmitted and received voltage signals for the case without and with a sample present are shown, respectively. The measurement frequency is 3.0 MHz. The figures display the zero crossings used for calculating the transit times for case (1) and (2). The zero crossings are represented by a "×".

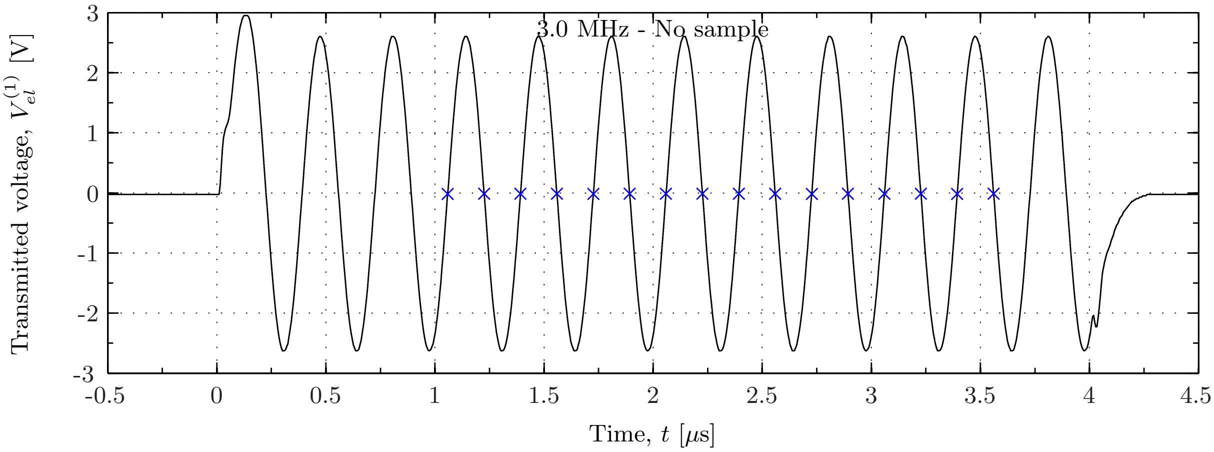

Figure 5.3: Transmitted voltage for case (1), $V_{el}^{(1)}$. Zero crossing marked with ×.

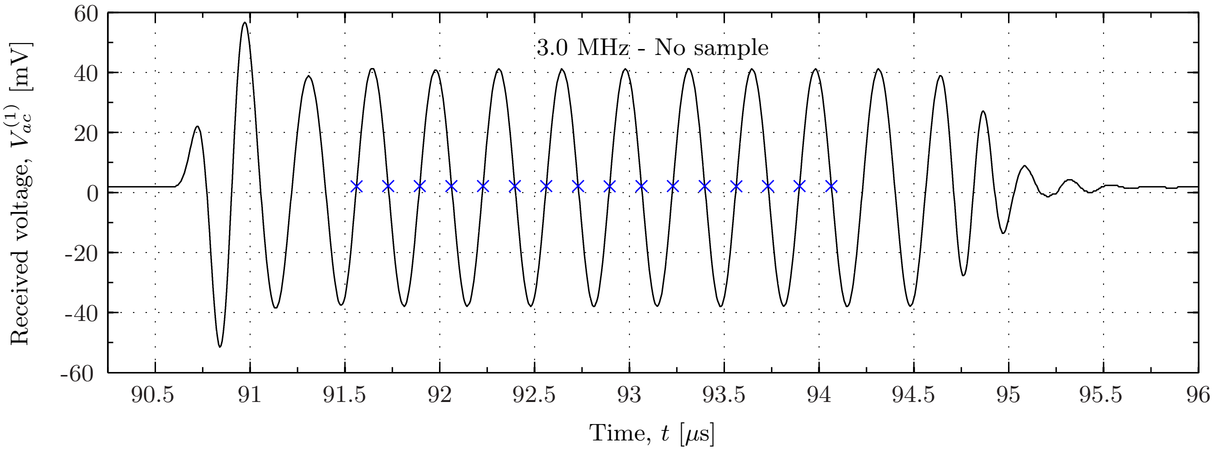

Figure 5.4: Received voltage for case (1), $V_{ac}^{(1)}$. Zero crossing marked with ×.

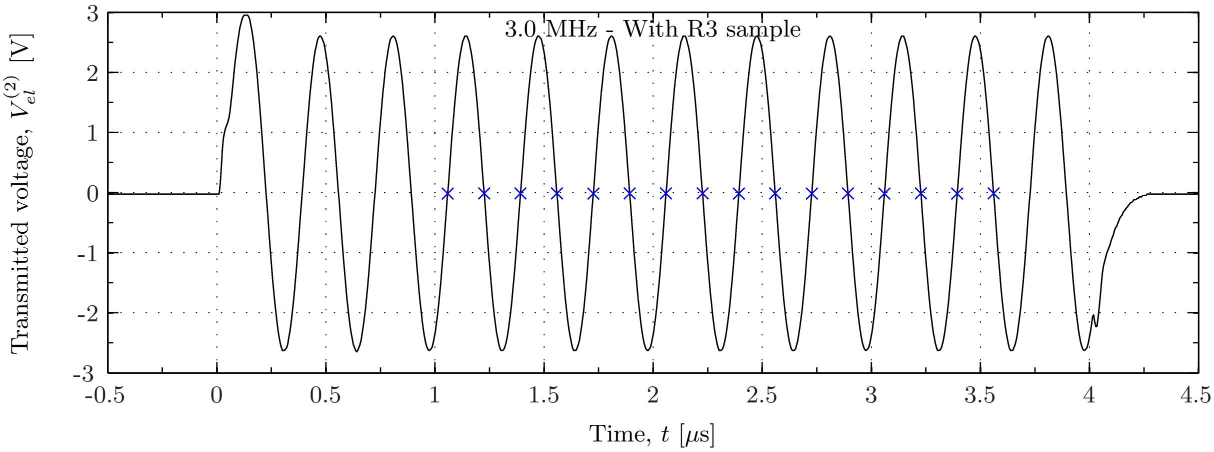

Figure 5.5: Transmitted voltage for case (2), $V_{el}^{(2)}$. Zero crossing marked with ×.

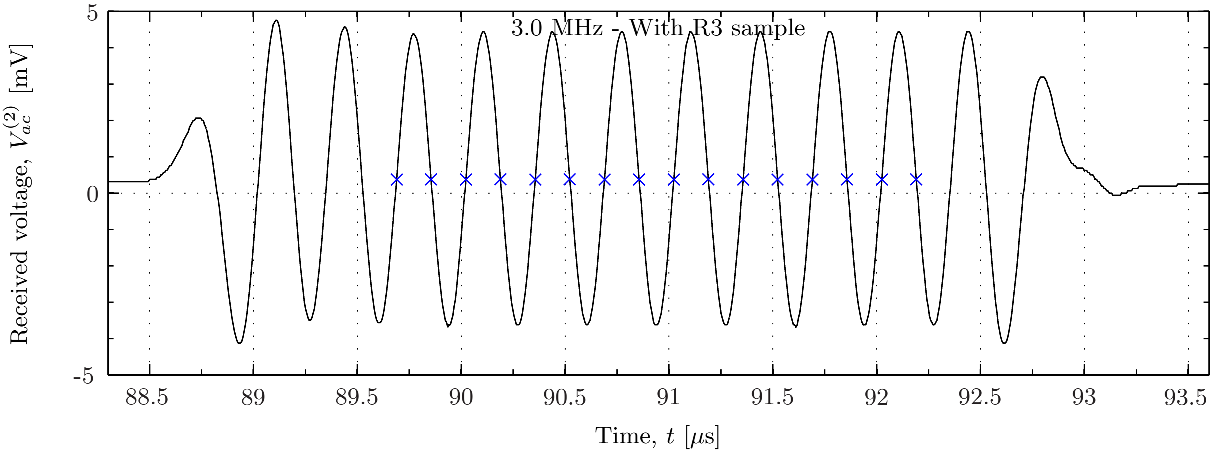

Figure 5.6: Received voltage for case (2), $V_{ac}^{(2)}$. Zero crossing marked with ×.

From Figs. 5.4 - 5.6 it is seen that the onset of the received signal when R3 is present is earlier than when the sound waves only propagates through water. This indicates that the longitudinal sound speed in R3, $c_{l,R3}$, is higher than the sound speed in water, c_w. This is as expected based on the material data given by PA.

5.3.3 Measured waveforms, R7

As for R3, the Figs. 5.7 - 5.10 show the recorded waveforms of $V_{el}^{(1)}$, $V_{ac}^{(1)}$, $V_{el}^{(2)}$ and $V_{ac}^{(2)}$ when R7 is used as the sample material. The measurement frequency is 3.0 MHz.

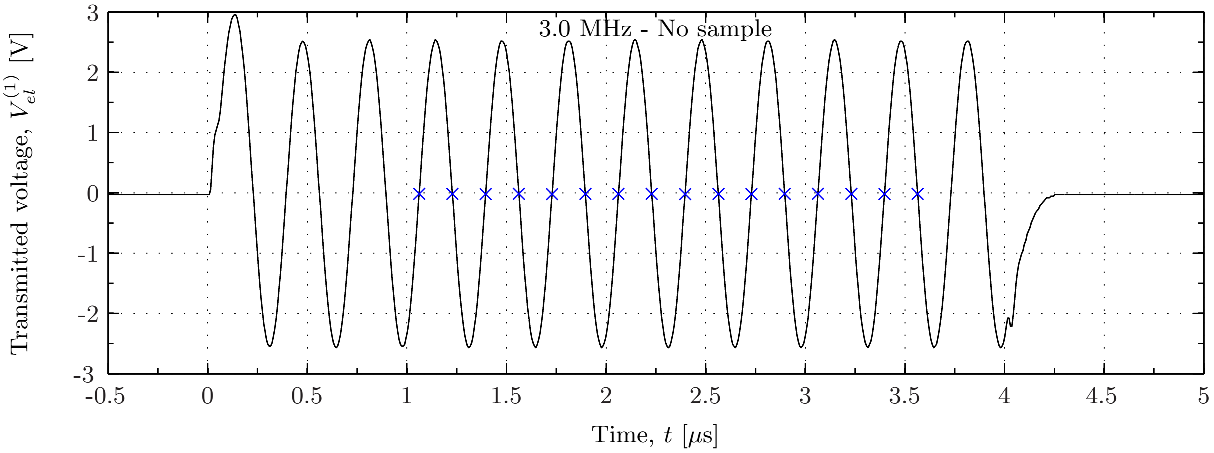

Figure 5.7: Transmitted voltage, V_{el}, for case (1). Zero crossing marked with ×.

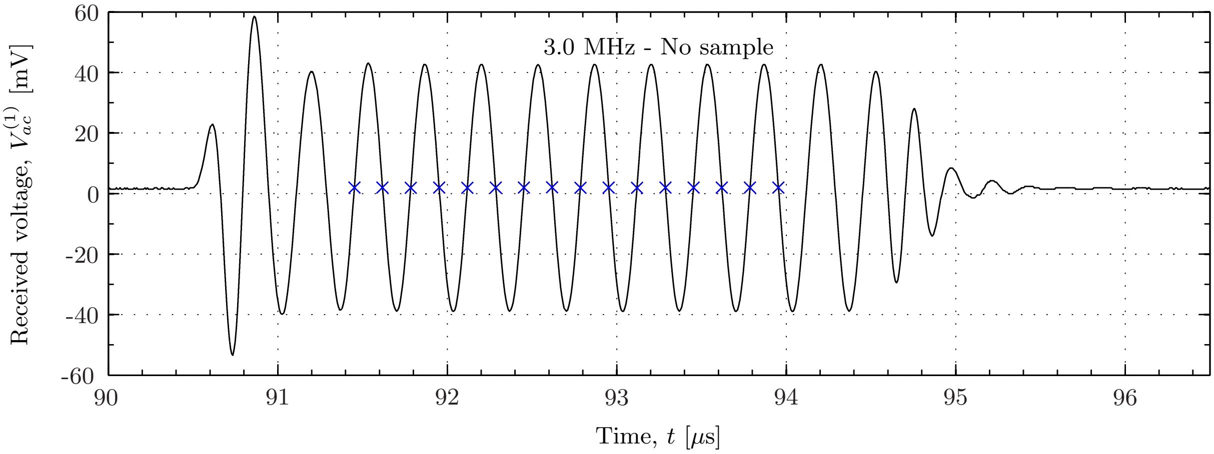

Figure 5.8: Received voltage, V_{ac}, for case (1). Zero crossing marked with ×.

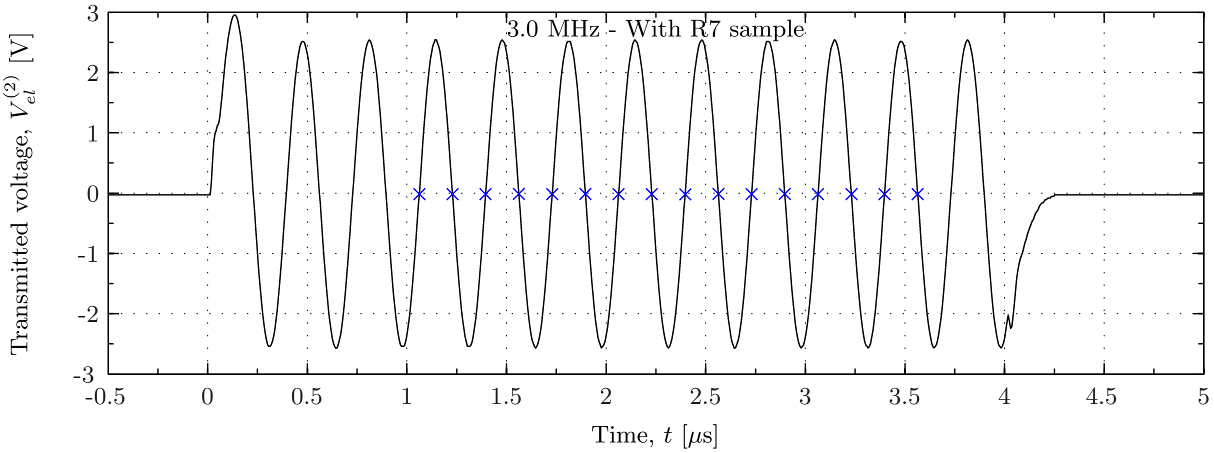

Figure 5.9: Transmitted voltage, V_{el}, for case (2). Zero crossing marked with ×.

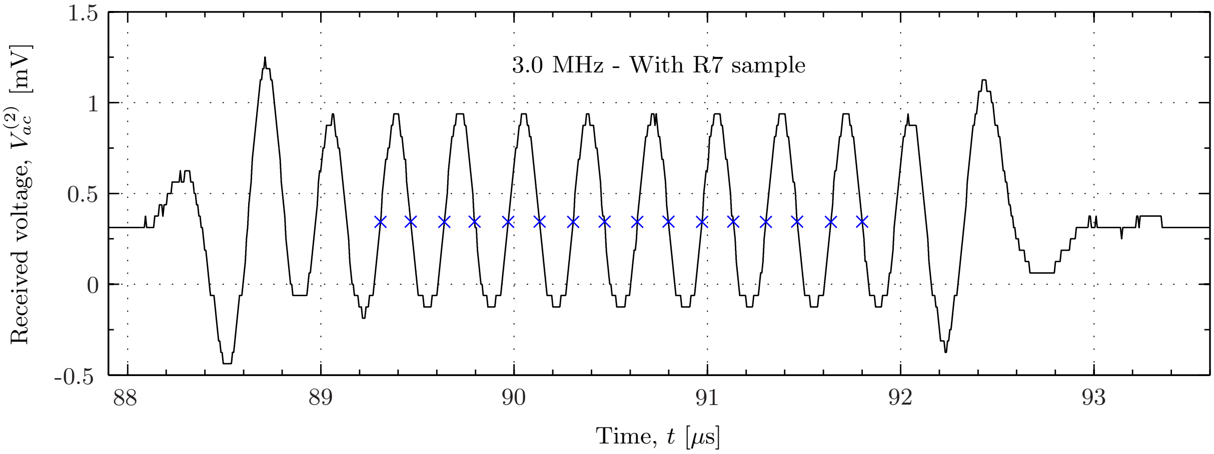

Figure 5.10: Received voltage, V_{ac}, for case (2). Zero crossing marked with ×.

It can be seen from Fig. 5.10 that the received signal with a sample present has a onset before the received signal with no sample present, seen in Fig. 5.8. This indicates that the sound speed in the sample is higher than the sound speed in water. It can also be seen that there is a significant decrease in magnitude for $V_{ac}^{(2)}$ compared to $V_{ac}^{(1)}$. This might be a result of the difference in impedance between the sample and water.

5.4 Results

In this section the results for sound speed, dimension and weight measurements is presented. The dimension and weight measurements are used to express the density of the matching layers, which together with the measured sound speed are used to calculate the characteristic impedance of the matching layers.

5.4.1 Sound speed

In Figs. 5.11 and 5.12 sound speed of Aptflex R3 and R7 are calculated using Eq. (5.4). A measurement is conducted without the sample present in the measurement cell, acting as a reference for 7 subsequent measurements carried out with the sample present.

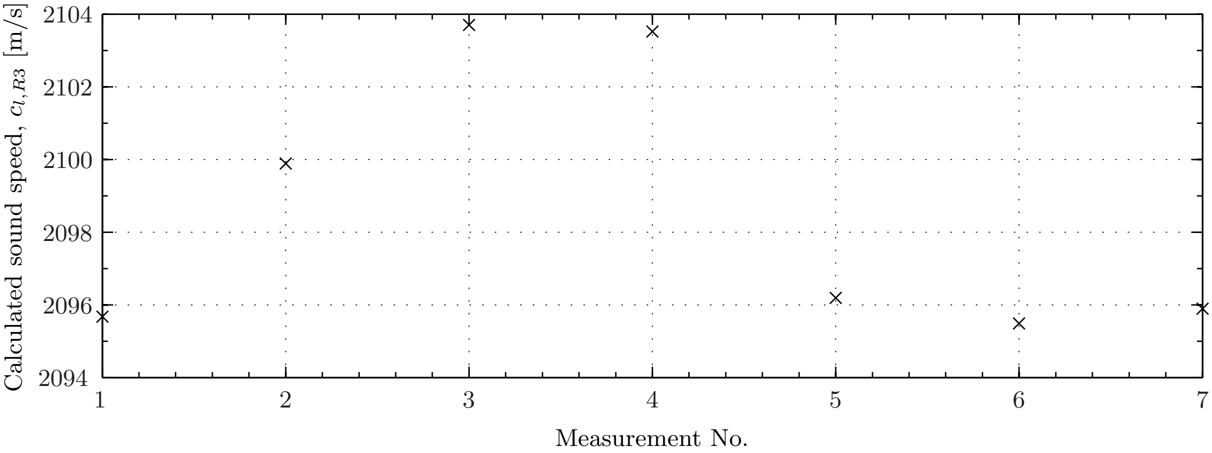

Figure 5.11: The calculated sound speed for R3, $c_{l,R3}$. Measurements done subsequently to each other over a span of 1.5 hours.

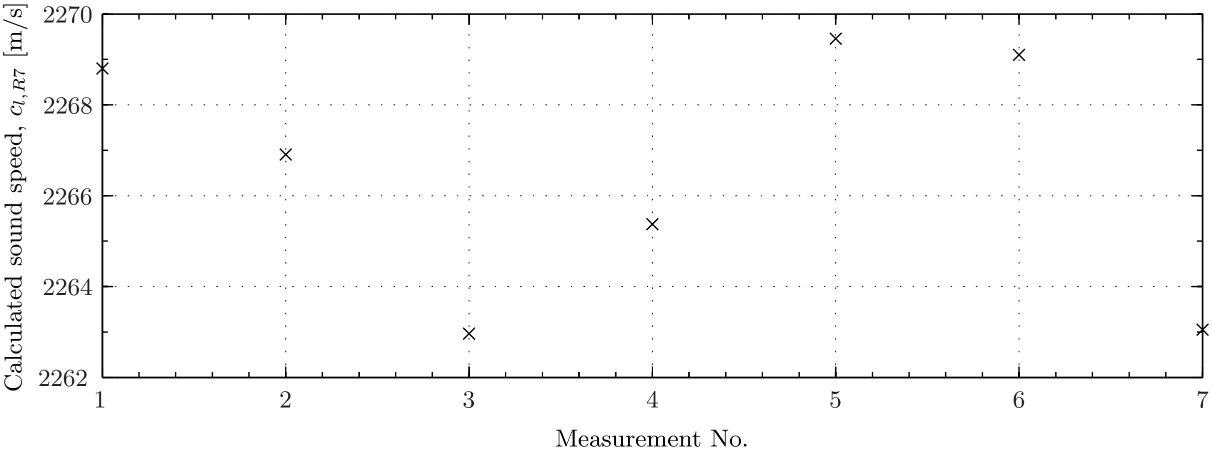

Figure 5.12: The calculated sound speed for R7, $c_{l,R7}$. Measurements done subsequently to each other over a span of 4.5 hours.

The mean sound speeds based on the measurements in Figs. 5.11 and 5.12 are given in Table 5.2 for both R3 and R7. The standard deviation of the 7 measurements for $c_{l,R3}$ is 3.7 m/s, and 2.8 m/s for $c_{l,R7}$.

Table 5.2: Averaged sound speed results.[3]

Material	Sound speed [m/s]
R3	2099
R7	2267

5.4.2 Density - characteristic impedance

The averaged results of the dimension measurements, and the mass, of R3 and R7 are given in Table 5.3. The measurements are conducted as described in Section 3.4.

Table 5.3: The dimensions of the samples investigated in this work.

Name	Thickness [mm]	Width [mm]	Length [mm]	Mass [g]
PA Aptflex R3	9.97 ± 0.03	72.34 ± 0.02	71.47 ± 0.04	30.64
PA Aptflex R7	9.43 ± 0.02	70.52 ± 0.03	70.61 ± 0.04	19.77

The measured values in Table 5.3 translates to densities for Aptflex R3 and R7 of ρ_{R3} = 595 kg/m^3 and ρ_{R7} = 420 kg/m^3, respectively. Using Eq. (5.5), the characteristic impedance of Aptflex R3 and R7 are calculated as z_{R3} = 1.25 Mrayl and z_{R7} = 0.95 Mrayl, respectively.

5.5 Discussion

The given sound speed and density of Aptflex R3 by PA are 2034 ± 30 m/s and 570 ± 20 kg/m^3, respectively. These values are both lower than the values measured here, the sound speed given by PA is approximately 65 m/s lower than the measured, and the density is approximately 30 kg/m^3 lower.

A density of 450 kg/m^3 is indicated by PA for Aptflex R7. The value measured here is approximately 30 kg/m^3 lower. The measured sound speed for R7 is approximately 160 m/s higher than the sound speed measured for R3, which is contrary to the predictions by PA, which suggested a lower sound speed for R7 than for R3.

---

[3] The standard deviation of the values averaged is given, but not used further, as investigation of uncertainties not are prioritized in this work.

Chapter 6

Transducer construction

Piezoelectric transducer structures with backing and matching layers in a transducer housing will presumably have better sensitivity and bandwidth compared to use of a single piezoelectric element. This chapter covers the construction of the piezoelectric transducers used in the present work. The transducers are made for use in air, utilizing the first radial mode of a piezoelectric ceramic disk. The piezoelectric ceramic disk has approximate dimensions 20 mm × 2 mm. The transducers are built with the goal of obtaining a higher magnitude level of the transmitting voltage response, S_V, and the voltage-to-voltage transfer function from node 1 to node 5, $H_{15}^{VV,open}$, and to increase the bandwidth compared to a single piezoelectric ceramic disk radiating into air.

Section 6.1 covers the transducer design, with the subsections covering the piezoelectric element, matching layer, backing layer and housing. The assembly process is described in Section 6.2.

Three piezoelectric transducers are constructed, named Transducer No. 1, Transducer No. 2 and Transducer No. 3.

6.1 Transducer design

The fundamental principle for the construction of the transducers in this work originates from the transducers examined in [18,94]. Figs. 6.1a and 6.1b show a solid and a transparent drawing of the transducer construction, respectively. The main components of the transducers are a piezoelectric element with a matching- and backing layer, encapsulated in a metal cylinder (transducer housing). The front electrode of the element is grounded into the metal housing by use of a conductive epoxy. The back electrode has a wire soldered onto it, which is connected to a BNC connector. The BNC connector is attached to the back plate of the housing. The metal back plate of the housing is attached to the housing by screws.

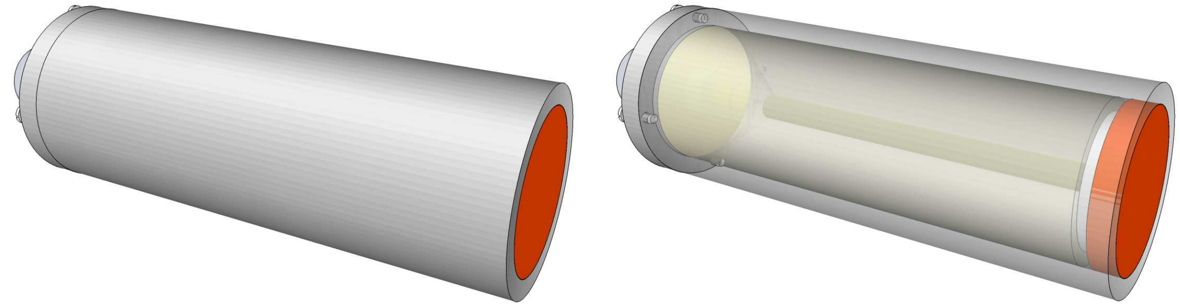

(a) (b)

Figure 6.1: Sketch of (a) the assembled transducer and (b) transparent view of the assembled transducer.

A schematic drawing of the designed transducer is shown in Fig. 6.2, with nominal dimensions given. Three transducers are constructed. The dimensions of each transducer may deviate from the nominal values due to inaccuracies in the manufacturing process.

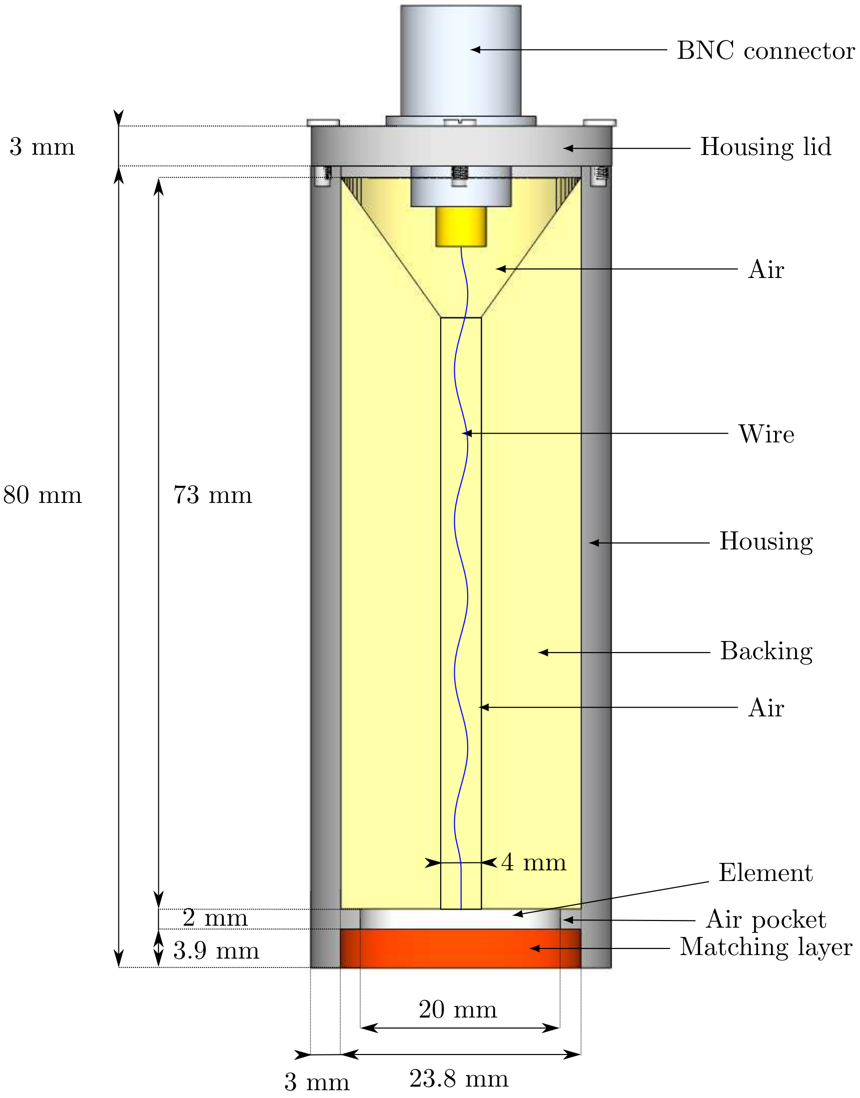

Figure 6.2: Sketch of the assembled transducer. Side view cross section. Showing the piezoelectric disk, matching layer, housing cylinder, backing layer, screwed on housing lid, wire, and BNC connector. The silver conductive epoxy between the piezoelectric disk and the matching layer and between the matching layer and housing wall is not shown.

6.1.1 Piezoelectric ceramic disk

The piezoelectric ceramic elements used in the transducer construction are circular disks of the material Pz27 from Ferroperm [78] with approximate[1] dimensions 20 mm × 2 mm (see Section 3.6). The piezoelectric disks are taken from the same batch as the single elements used in the acoustic measurements. Electrical measurements are conducted on all piezoelectric elements of this batch, comparing the magnitude of the conductance and the series resonance frequency of the first radial mode (R1), f_{R1}. Elements with similar f_{R1} and maximum conductance are chosen for the transducers: Element #3, Element #15 and Element #20 The measured and simulated conductance of these elements are shown in Fig. 6.3. The simulations are performed with the piezoelectric element vibrating in vacuum, to reduce calculation time (cf. Section [?]). It is observed in simulations that the effects of air loading are negligible compared to the difference between simulations and measurements. A frequency difference of approximately 0.6 kHz is observed between the simulated and measured values of f_{R1}, and approximately 1 kHz for f_{R2}, which is the series resonance frequency of the second radial mode (R2).

---

[1] See Table 6.1 for accurate dimensions of the elements used.

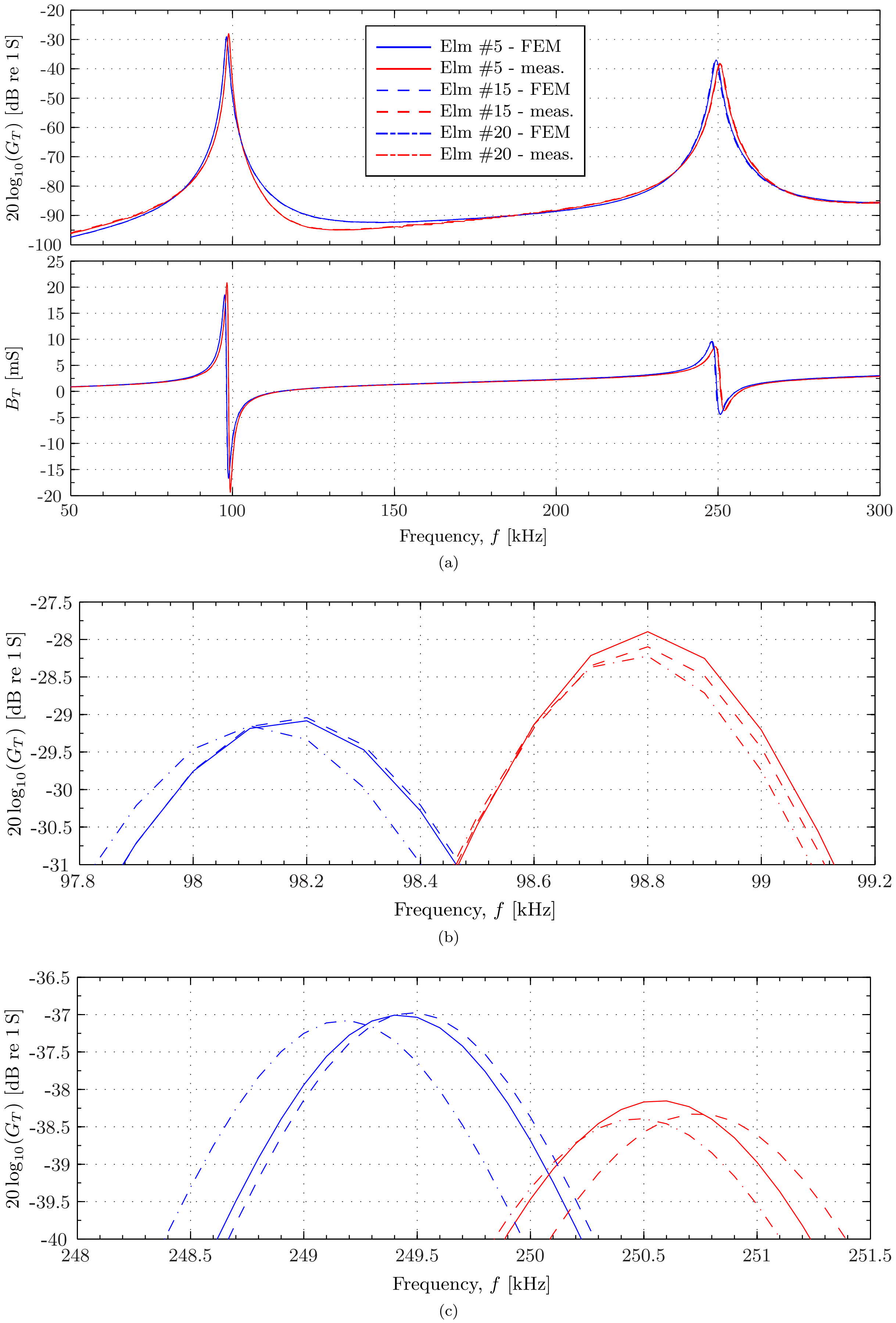

(a)

(b)

(c)

Figure 6.3: Measured and FE simulated conductance of Element #5, Element #15 and Element #20. Plotted for the frequency range 50 kHz to 300 kHz in (a), and centred around R1 in (b) and R2 in (c). (a) includes the measured and simulated conductance. The simulations are performed with the piezoelectric elements vibrating in vacuum, using `piezodisk` (see Section 4.3).

6.1.2 Matching layer

A matching layer is introduced in order to improve the improve the acoustic coupling to air and increase the bandwidth of the transducer. Transmission theory states that there is total transmission of acoustic power if the thickness of the matching layer is $T = \lambda/4$ and the characteristic impedance of the matching layer is the geometric mean of the characteristic impedances of air and Pz27, termed "quarter wavelength matching", [48]. λ is the wavelength in the matching layer. The of the characteristic impedance of Pz27, z_{Pz27}, is approximately 30 Mrayl[2] and that of air at room temperature the characteristic impedance is approximately $z_{air} = 415$ rayl [48]. This gives an ideal matching layer characteristic impedance of

$$z_m = \sqrt{z_{Pz27} z_{air}} \approx 0.11\,\text{Mrayl}. \tag{6.1}$$

Two materials are considered for this purpose, the Aptflex syntactic foams R3 and R7 manufactured by Precision Acoustics (PA) [88,89]. Two material samples are shown in Fig. 6.4. These materials have a higher characteristic impedance than the the one found in Eq. (6.1) and than materials used in previous work, e.g. in [85], but they are preferred because they are more mechanically robust.

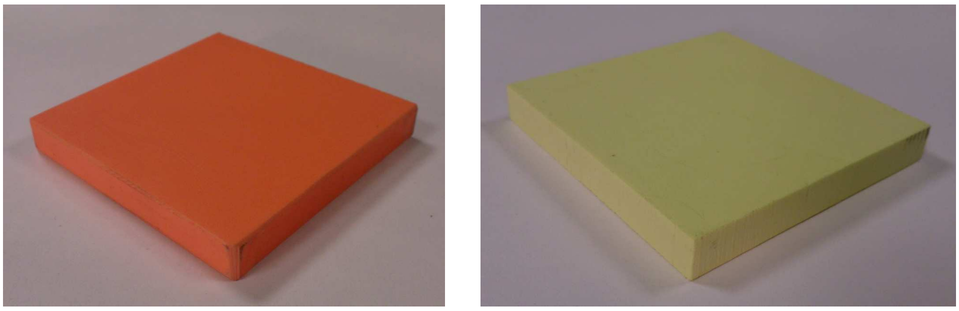
(a) (b)

Figure 6.4: Matching layer alternatives. Aptflex R3 is shown in (a) and Aptflex R7 is shown in (b).

The characteristic impedance of R3, using the material parameters supplied by PA [89], is[3] 1.16 Mrayl. Only indicated material parameters are available for R7, and measurements of c_l and ρ are therefore performed as part of this work (see Chapter 5). These measured values give a characteristic impedance of 0.95 Mrayl for R7. Based on the characteristic impedances, R7 is the better choice for matching layer, but accurate material parameters are of great importance in the FE simulations. The use of Aptflex R7 in simulations depends on assumptions based on similar materials, in addition to the quantities measured in-house (see Chapters 5 and 4).

In order to compare the behaviour of the two possible matching layers, the quarter wavelength thickness is calculated. Simulation of a piezoelectric element with dimensions[4] 20 mm × 2 mm give $f_{R1} = 99.3$ kHz. The longitudinal sound speed supplied by PA for R3, $c_{l,R3} = 2034$ m/s, and the measured longitudinal sound speed of R7, $c_{l,R7} = 2266$ m/s, are used to calculate the thicknesses

$$T_{R3} = \frac{c_{l,R3}}{4 f_{R1}} \approx 5.12\,\text{mm} \qquad \text{and} \qquad T_{R7} = \frac{c_{l,R7}}{4 f_{R1}} \approx 5.71\,\text{mm}. \tag{6.2}$$

To investigate if R7 or R3 offers better coupling to air and higher bandwidth the quantities[5] $H_{15}^{VV,open}$ and S_V are determined from simulations, using both Aptflex R3 and R7 as matching layer with quarter wavelength thicknesses. The simulations are performed using `piezodiskwidefrontfluid` (cf. Section 4.3), since the radius of the matching layer exceeds the radius of the piezoelectric disk in the chosen transducer design. A diameter of 22 mm is used for the matching layer in the simulations, and the quarter wavelength thickness found in Eq. (6.2). Results from simulations of H_{15}^{VV} and S_V for the frequency range 70 to 150 kHz for a Pz27 element with matching layer are given in Fig. 6.5. This frequency range covers the first radial mode of the piezoelectric element.

---

[2] From adjusted material data set, see Section 4.4

[3] The comparison was made prior to the measurements of c_l and ρ were performed on R3 (cf. Chapter 5).

[4] The choice of matching layer was done prior to determining which elements to use, and nominal dimensions are therefore used in the simulations.

[5] S_V is determined from the FE simulations as described in Section 4.2, and $H_{15}^{VV,open}$ is here calculated without correcting for diffraction [2].

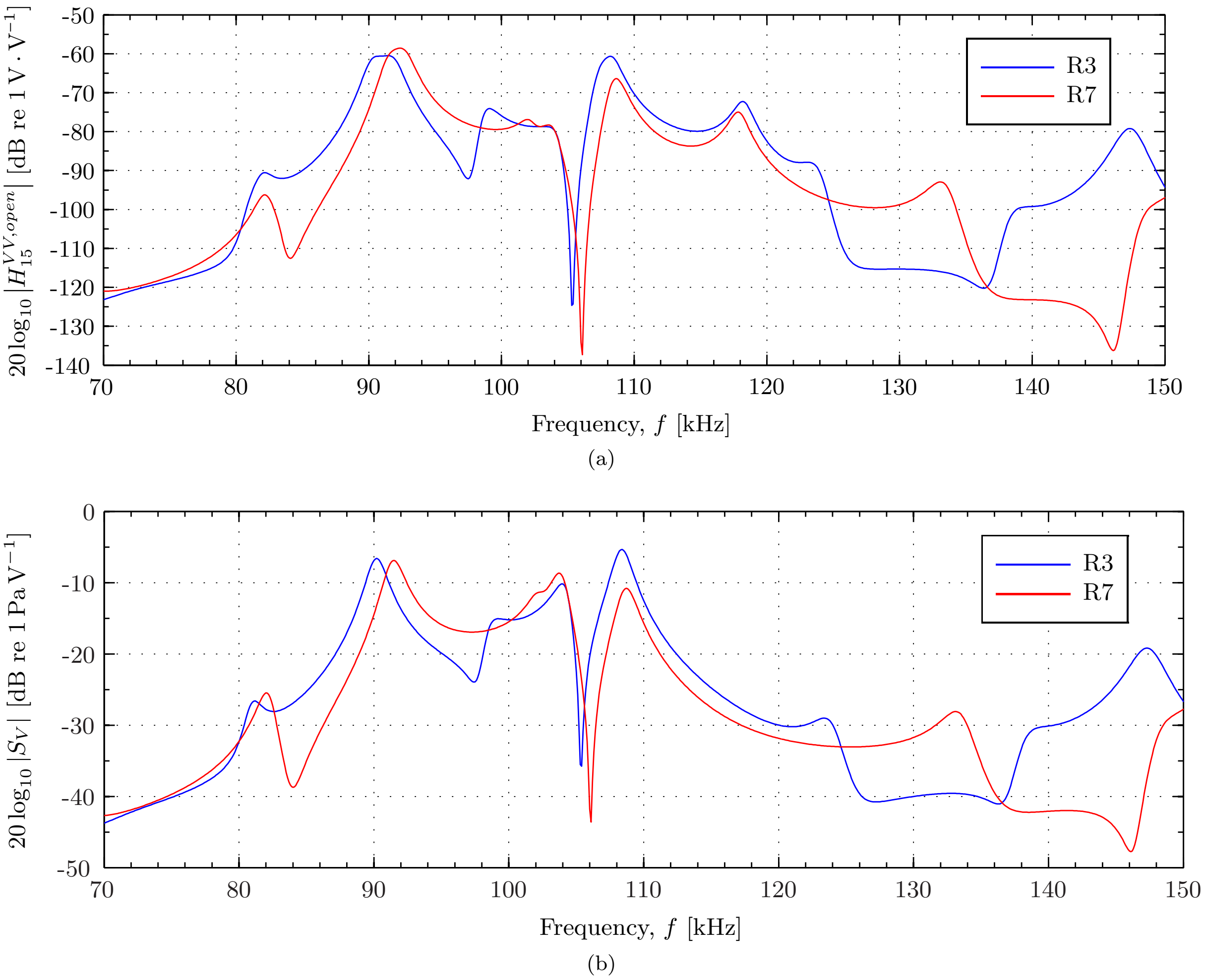

Figure 6.5: Simulated magnitude of (a) $H_{15}^{VV,open}$ and (b) S_V for the frequency range 70 to 150 kHz for a piezoelectric ceramic disk of the material Pz27 and dimensions 20 mm × 2 mm with an Aptflex matching layer. The dimensions are 22 mm × 5.1 mm for the R3 matching layer, 22 mm × 5.7 mm for the R7 matching layer. $H_{15}^{VV,open}$ are calculated for a separation distance of 1 m and for two identical reciprocal transducers. The simulations are performed with the structures vibrating in air, using `piezodiskwidefrontfluid` (see Section 4.3).

As seen in Fig. 6.5, using Aptflex R7 as matching layer does not significantly improve the magnitude of neither the $H_{15}^{VV,open}$ nor S_V, compared to R3. Neither R3 or R7 increases the −3 dB bandwidth significantly for the frequency area, since there are several peaks taller than 3 dB for both $H_{15}^{VV,open}$ and S_V.

Since there is no major improvement of the transmitting voltage response when using R7 compared to R3, the latter is chosen as the matching layer to use in the piezoelectric transducers. This is because material data needed to perform FE simulations of R3 are readily available from PA [89], while this is not the case for R7 (see Chapter 4).

A sensitivity analysis with multiple matching layer thicknesses and radiuses have been performed to determine the final dimensions of the Aptflex R3 matching layer, as a the quarter wavelength matching thickness might not be ideal. A relatively flat frequency response and magnitude improvement of S_V are sought. The material data for R3 provided by the manufacturer are used[6], and the piezoelectric disk is simulated with dimensions of 20 mm × 2 mm. The dimensions of the front layer are adjusted with increments of 0.1 mm.

A radius of 11 mm and thickness of 5.1 mm was used as starting points. The thickness was then varied between 3.5 mm and 6.0 mm. A thickness of 3.9 mm was chosen and FE simulations were performed with radiuses varying from 11.0 mm to 12.5 mm. From these simulations the most preferable combination of radius and thickness was seen to be 11.9 mm and 3.9 mm, respectively. In Fig. 6.6 S_V and $H_{15}^{VV,open}$ are compared for a piezoelectric disk without a matching layer, with an R3 matching layer of 22.0 mm × 5.1

---

[6] The matching layer characterization for R3 had not been performed at this point in the process.

mm (as in Fig. 6.5), and with an R3 matching layer of the chosen dimensions 23.8 mm × 3.9 mm.

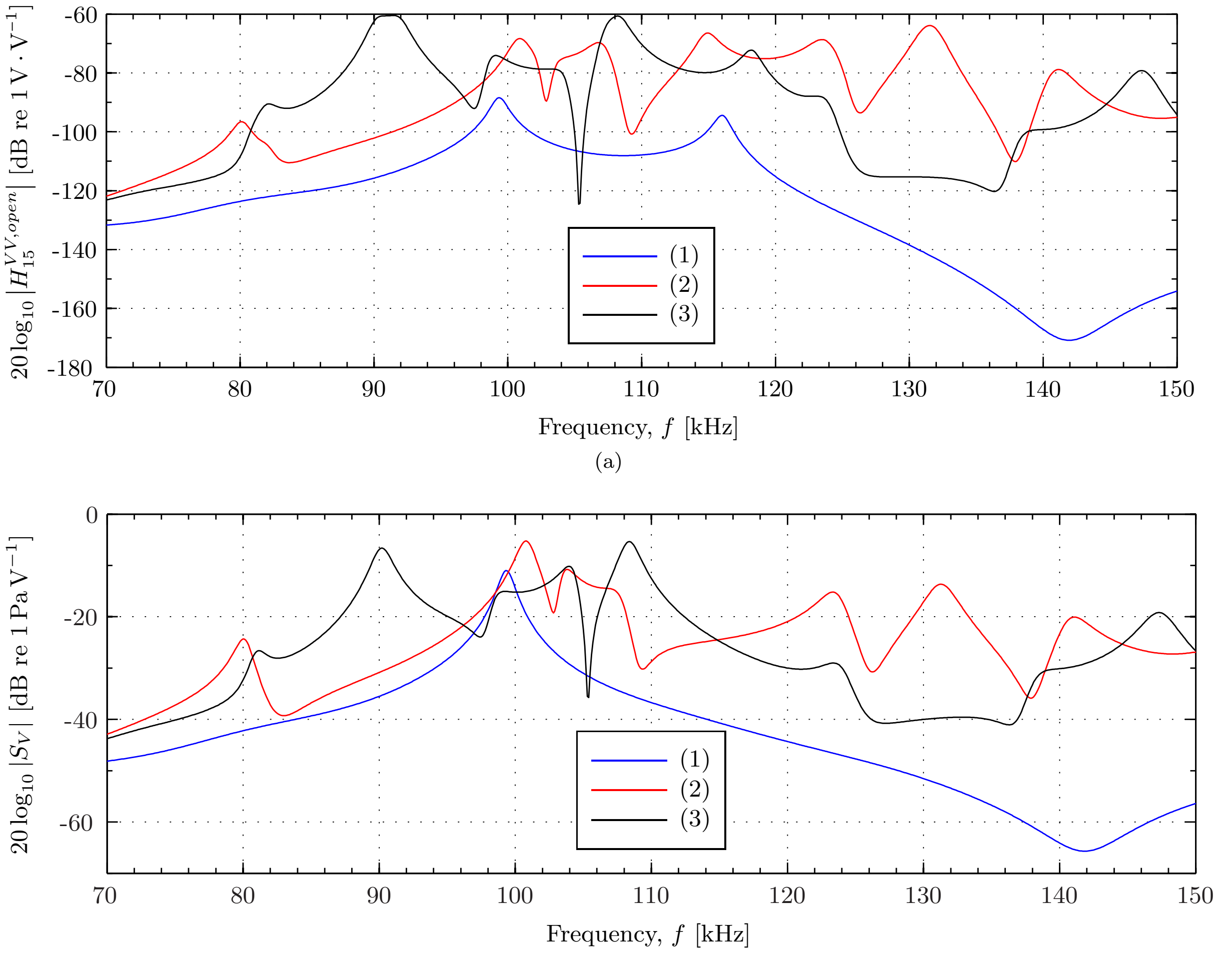

(a)

(b)

Figure 6.6: Comparison of the magnitude of (a) $H_{15}^{VV,open}$ and (b) S_V for a Pz27 piezoelectric ceramic disk of 20 mm × 2 mm. (1) is without a matching layer, (2) is with an R3 matching layer of 23.8 mm × 3.9 mm, and (3) is with an R3 matching layer of 22.0 mm × 5.1 mm. All simulations are performed with the structure vibrating in air, using `piezodiskwidefrontfluid` for (1) and (2), and `piezodiskfluid` for (3) (see Section 4.3).

Three R3 circular matching layers with nominal dimensions 11.9 mm x 3.9 mm were machined out by the in-house workshop and attached to the piezoelectric ceramic disks using silver conductive epoxy (see Sections 6.2 and 4.4.4). The measured dimensions of the piezoelectric ceramic disks and the matching layers are given in Table 6.1.

Table 6.1: Dimensions of the constructed transducers. Measured with a Mitutoyo MDH-25M digimatic micrometer (see Section 3.4).

Name	Transducer No. 1	Transducer No. 2	Transducer No. 3
Pz27 - Piezoelectric element	#5	#15	#20
- radius	10.12 ± 0.01 mm	10.12 ± 0.01 mm	10.125 ± 0.005 mm
- thickness	2.012 ± 0.003 mm	2.003 ± 0.001 mm	2.033 ± 0.002 mm
Aptflex R3 - Matching layer			
- radius	11.895 ± 0.005 mm	11.895 ± 0.001 mm	11.904 ± 0.002 mm
- thickness	3.86 ± 0.01 mm	3.85 ± 0.01 mm	3.816 ± 0.007 mm

Electrical measurements were performed at this stage for comparison with FE simulations, i.e. a piezoelectric disk, silver conductive epoxy, a matching layer, and a wire soldered to the rear electrode on the piezoelectric disk. The simulations are performed with the structure vibrating in vacuum for computational reasons, and the wire is neglected. The layer of silver conductive epoxy is assumed to be 0.1 mm and of equal width as the respective matching layer. Fig. 6.7, covering the frequency range 70 kHz to 160 kHz, shows that a frequency shift is observed in some of the resonances when simulations of the structure vibrating in air are compared to simulations of the structure vibrating in vacuum.

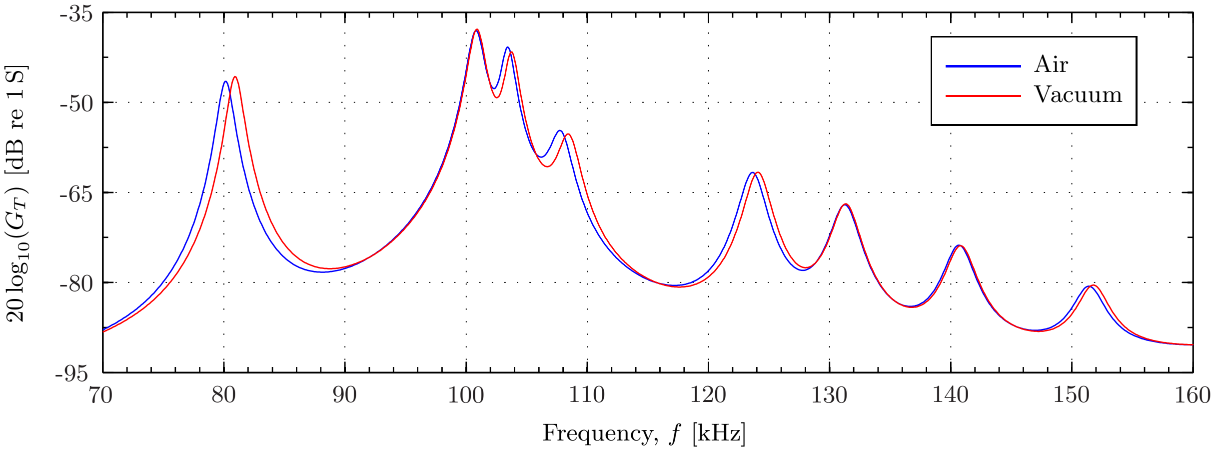

Figure 6.7: Comparison of of the simulated conductance of a Pz27 piezoelectric ceramic disk of dimensions 20 mm × 2 mm with an Aptflex R3 matching layer of dimensions 23.8 mm × 3.9 mm. Simulated with the structure vibrating in air and in vacuum. No silver conductive epoxy layer. `piezodiskwidefrontfluid` and `piezodiskwidefrontglue` is used (see Section 4.3).

Two measurements of the conductance and susceptance of a piezoelectric disk with a matching layer are shown in Fig. 6.8. Some repeatability issues are observed, with a deviation especially for higher frequencies and outside the peaks. There is also a small peak at approximately 70 kHz in the second measurement that does not appear in the first measurement. This may be due to small changes in the electrical measurement setup between each measurement (see Section 3.2 for a description of the setup).

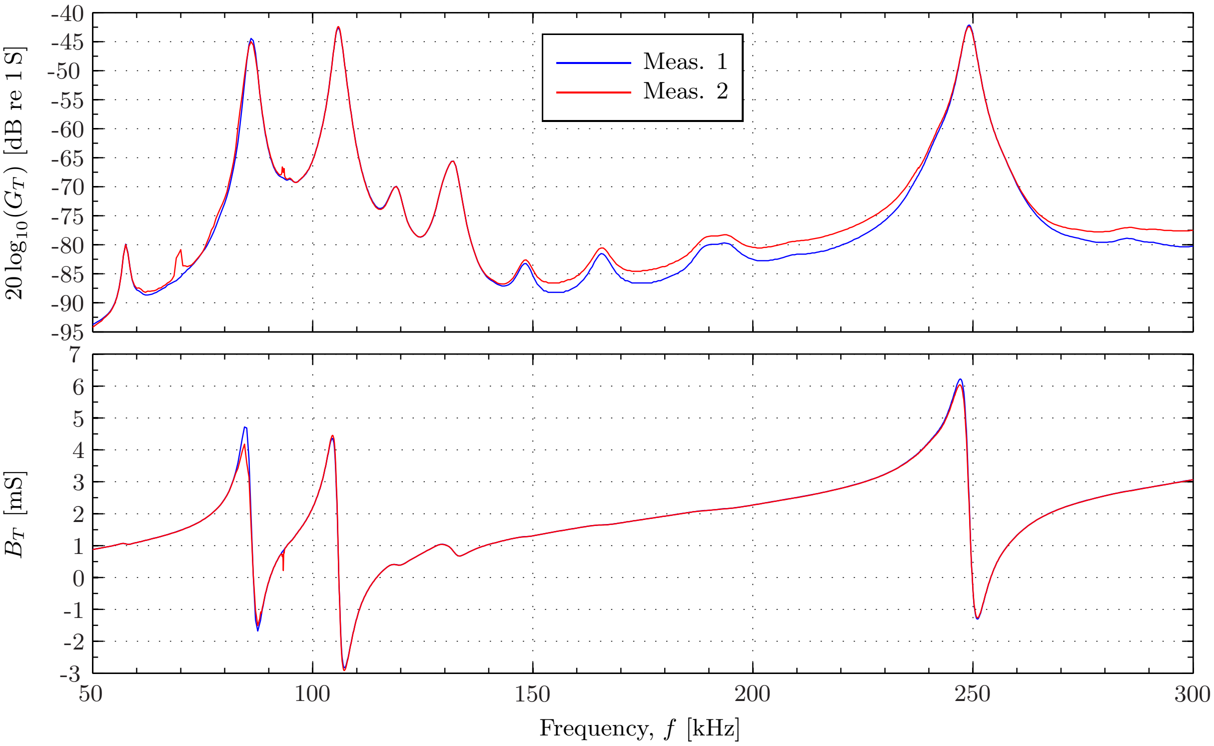

Figure 6.8: Measured conductance and susceptance of the piezoelectric disk with attached front layer of Transducer No. 2. Check of repeatability.

Comparison of measured and simulated conductance and susceptance are shown in Fig. 6.9 for the piezoelectric disk and matching layer used in Transducer No. 2. Better correspondence between the measured and simulated values are found by adjusting the nominal material data for the R3 matching layer. Measured values are used for the longitudinal sound speed and the density, while both Poisson's ratio and the mechanical quality factor are reduced. The former from 0.375 to 0.35 and the latter from 55 to 40. Figs. 6.10 and 6.11 show measurements and simulations, performed with the adjusted material data set for R3, for the piezoelectric disk and matching layer used in Transducer No. 1 and Transducer No. 3, respectively.

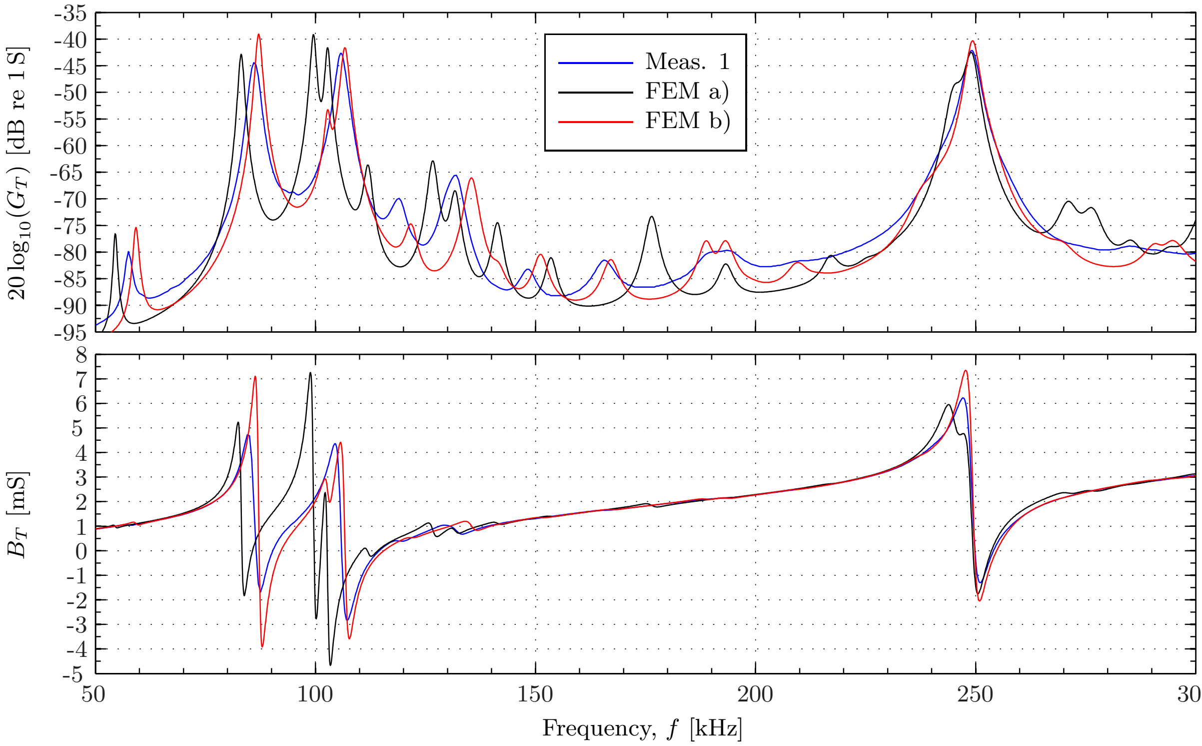

Figure 6.9: Measured conductance and susceptance of the piezoelectric disk with attached front layer of Transducer No. 2 compared to FE simulations with the structure vibrating in vacuum, with a layer of silver conductive epoxy. The material data for Aptflex R3 supplied by PA [89] are used in FEM a), and adjusted material data for R3 are used in FEM b). Using `piezodiskwidefrontglue` in the simulations (see Section 4.3).

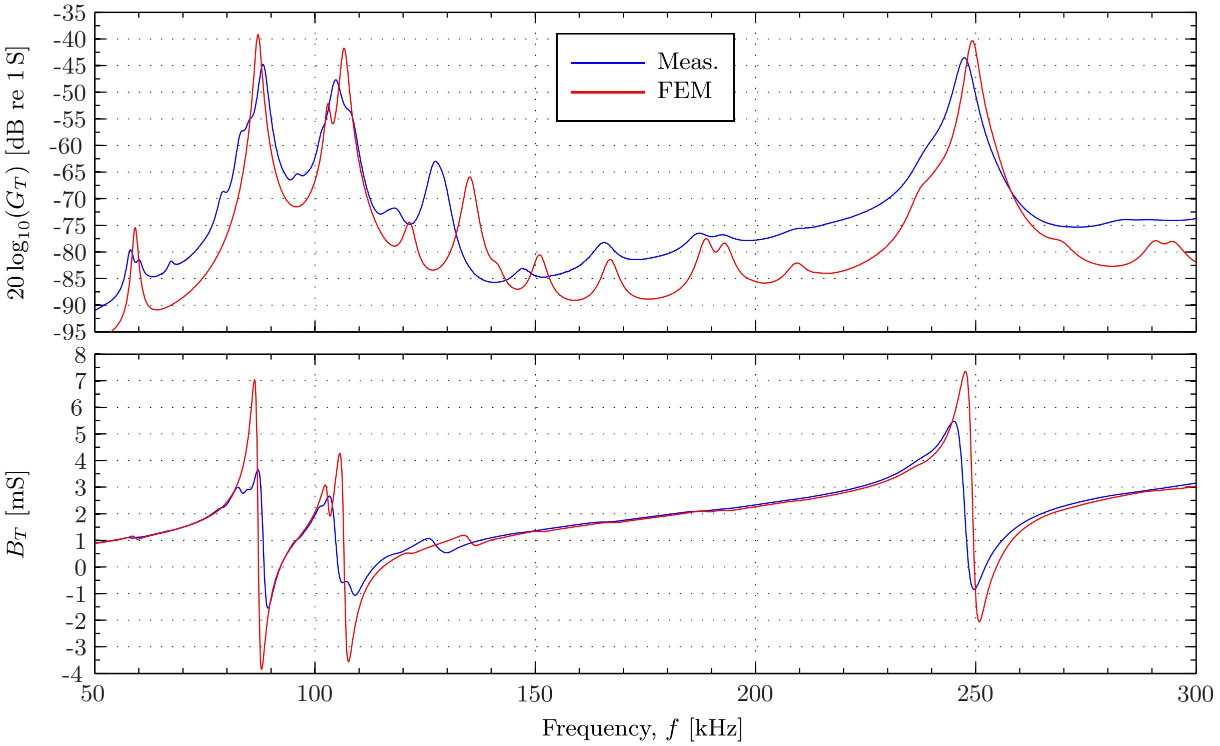

Figure 6.10: As Fig. 6.9, but for the element and matching layer of Transducer No. 1 and only simulations with the adjusted material data.

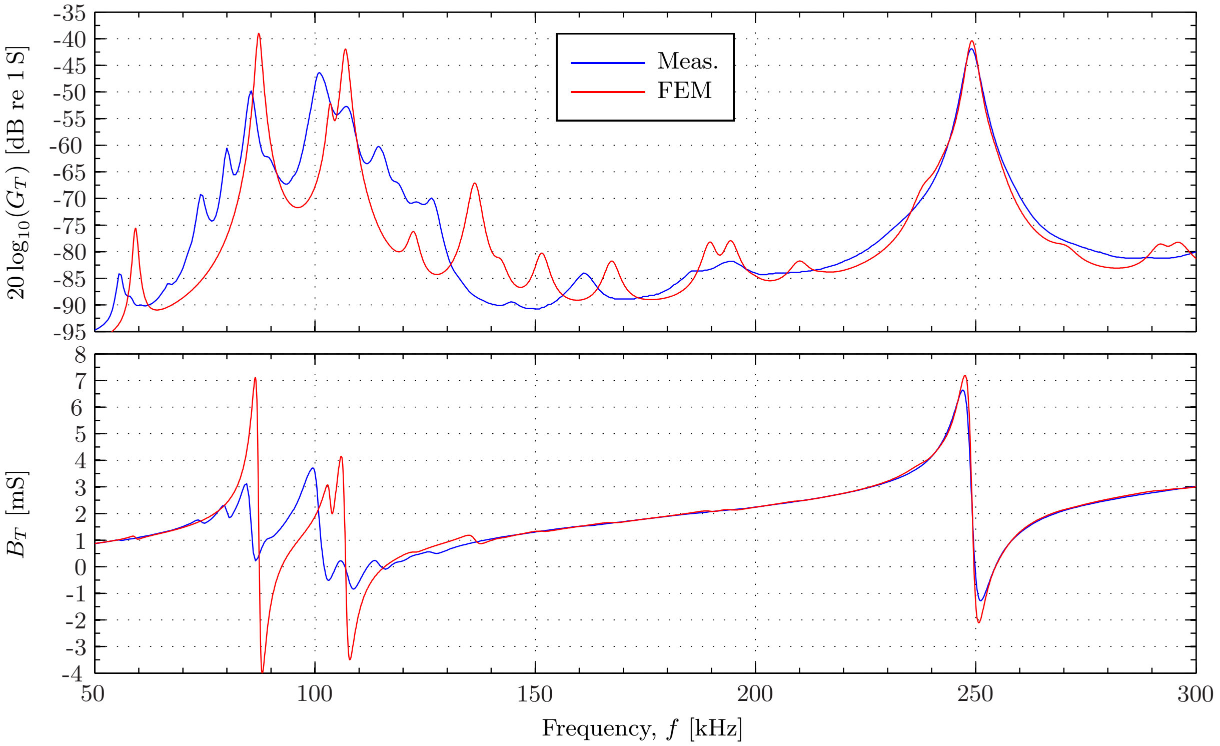

Figure 6.11: As Fig. 6.10, but for the element and matching layer of Transducer No. 3.

Qualitative agreement is observed between measurements and FE simulations in Figs. 6.9, 6.10 and 6.11. Fig. 6.12 compares the measured conductance and susceptance of the three different combinations of element and matching layer.

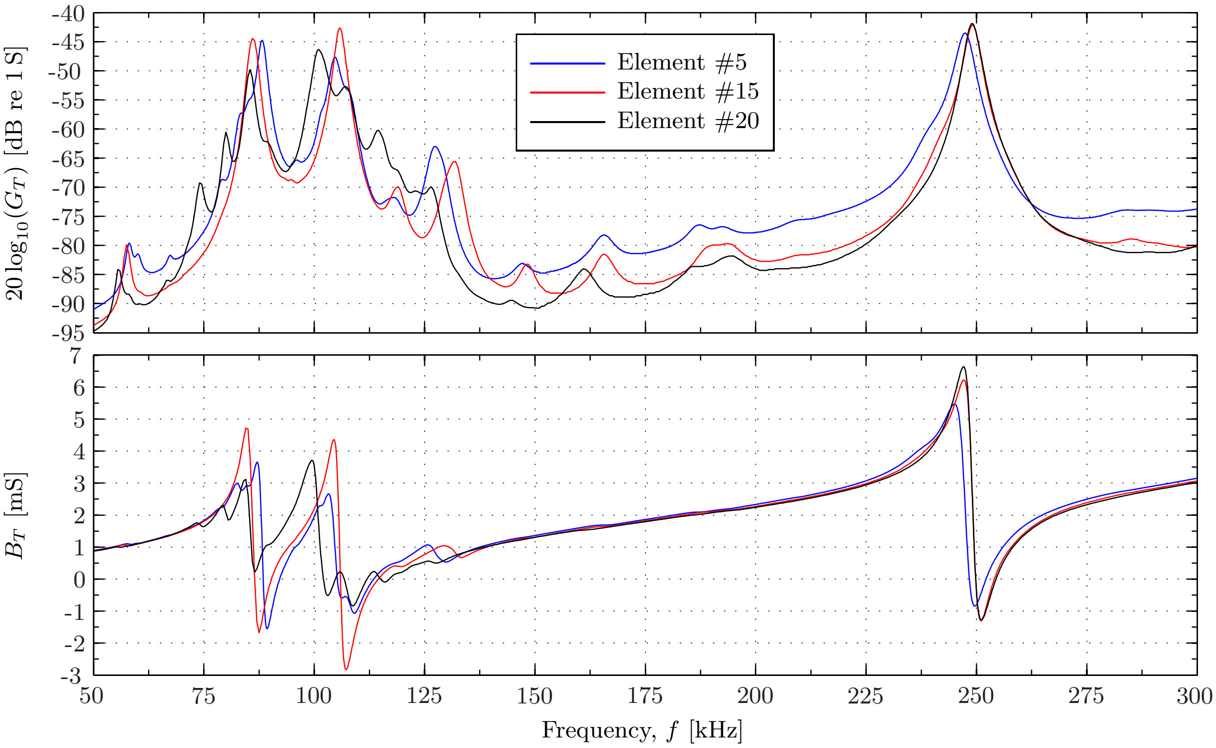

Figure 6.12: Comparison of measured conductance and susceptance of the Element #5 with matching layer (used in Transducer No. 1), Element #15 with matching layer (used in Transducer No. 2) and Element #20 with matching layer (used in Transducer No. 3).

It is seen that the measured conductance of the three sets of piezoelectric disks and matching layers varies more than the repeatability in the measurements and the dimension difference can account for. Possibly a more carefully controlled assembly process can reduce deviations. Better agreement between measurements and simulations may be achieved by further investigation and adjustment of material parameters, but the discrepancies in the measurements limit the attainable accuracy.

6.1.3 Backing layer and transducer housing

The material Dinvinycell H130 is used as backing layer [95]. The purpose of the backing layer is to flatten the frequency response of the transducer and to prevent standing waves inside the transducer housing. The backing layer has an equal radius as the matching layer, and a nominal depth of 73 mm. The rearmost side of the backing layer is coned inwards to scatter the backwards propagated soundwave from the element, thus reducing the forming of standing waves inside the backing layer. The depth of the cone is 14 mm, which makes room for the BNC connector fastened in the stainless steel lid. A 4 mm wide hole is made through the length of the backing layer, allowing the wire attached to the element to be extended back and connected to the BNC connector.

The transducer housing is made of grade 316 stainless steel. The stainless steel housing connects the front electrode of the piezoelectric element, through the silver conductive epoxy, to electric ground in the BNC connector. The inner diameter of the housing is 24 mm and the diameter of the matching layer is 23.8 mm, leaving room for the silver conductive epoxy. The housing walls has a thickness of 3 mm. A thinner wall might decrease the resonances in the stainless steel, but the current thickness allows for the housing lid to be fastened mechanically using screws into the housing wall, see Fig. 6.2. The inner length of the housing is 80 mm, which is chosen to have a deep enough backing layer that standing waves inside the housing are sufficiently dampened.

The measured conductance of the constructed transducers are shown in Figs. 6.13, 6.14 and 6.15 for Transducer No. 2, No. 1 and No. 3, respectively. The simulations are performed in with the transducer vibrating vacuum without backing layer and housing lid. The layer of silver conductive epoxy is assumed to be 0.1 mm between the piezoelectric disk and the matching layer and between the matching layer and the stainless steel housing cylinder. The adjusted material data set for the matching layer is used.

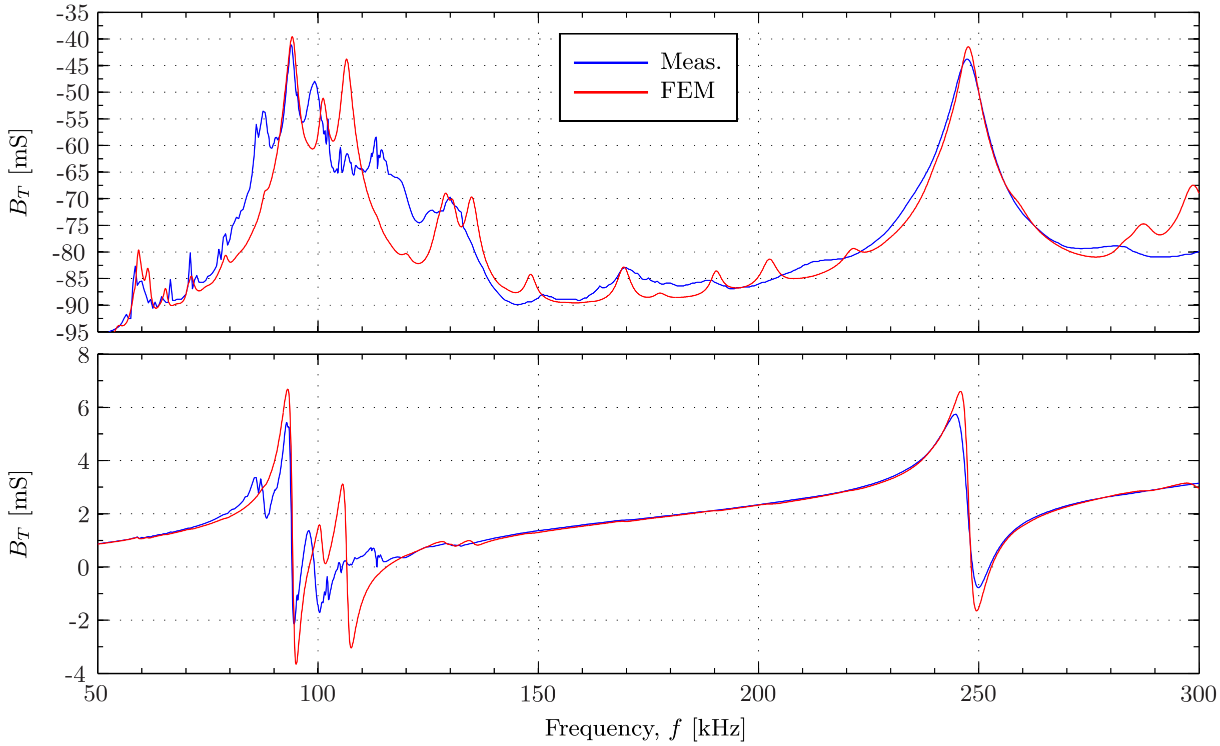

Figure 6.13: Measured conductance of Transducer No. 1 compared to FE simulations of the transducer vibrating in vacuum. The simulations are performed for a simplified transducer, without the backing layer and the stainless steel lid. The adjusted material data for the Aptflex R3 matching layer and `transducervacuum` are used in the simulation (see Section 4.3.

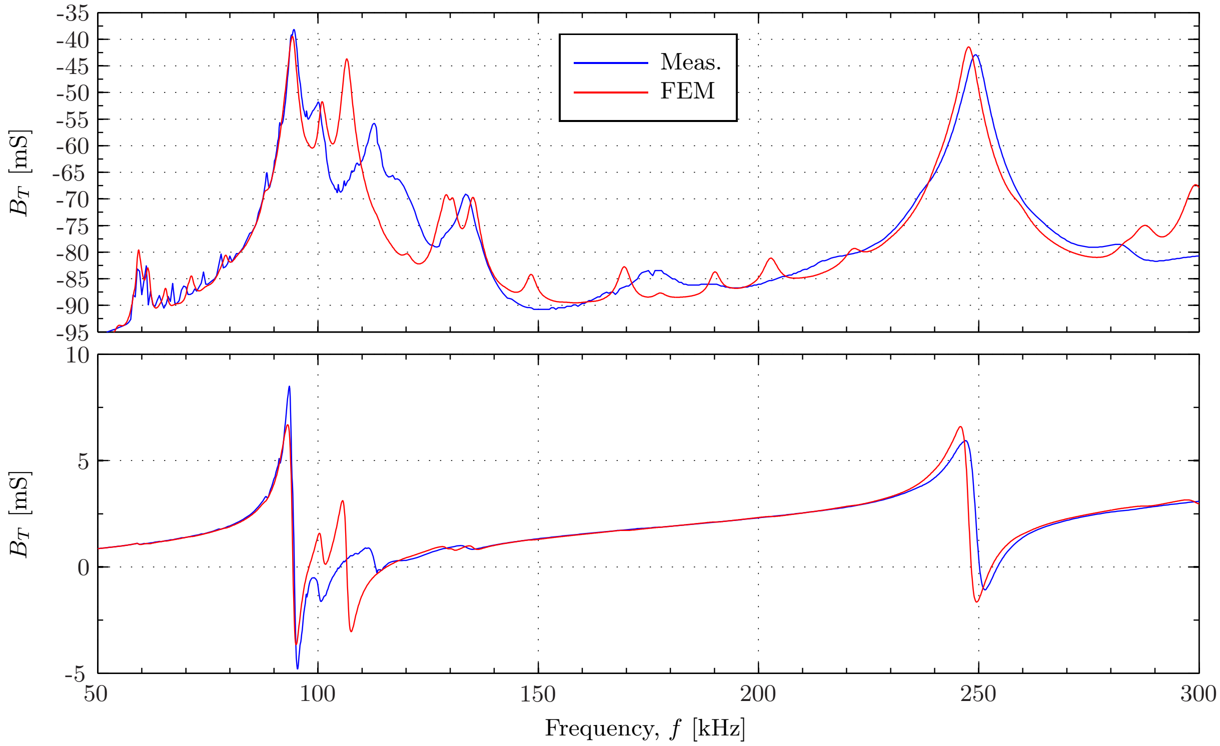

Figure 6.14: As in Fig. 6.13, but for Transducer No. 2.

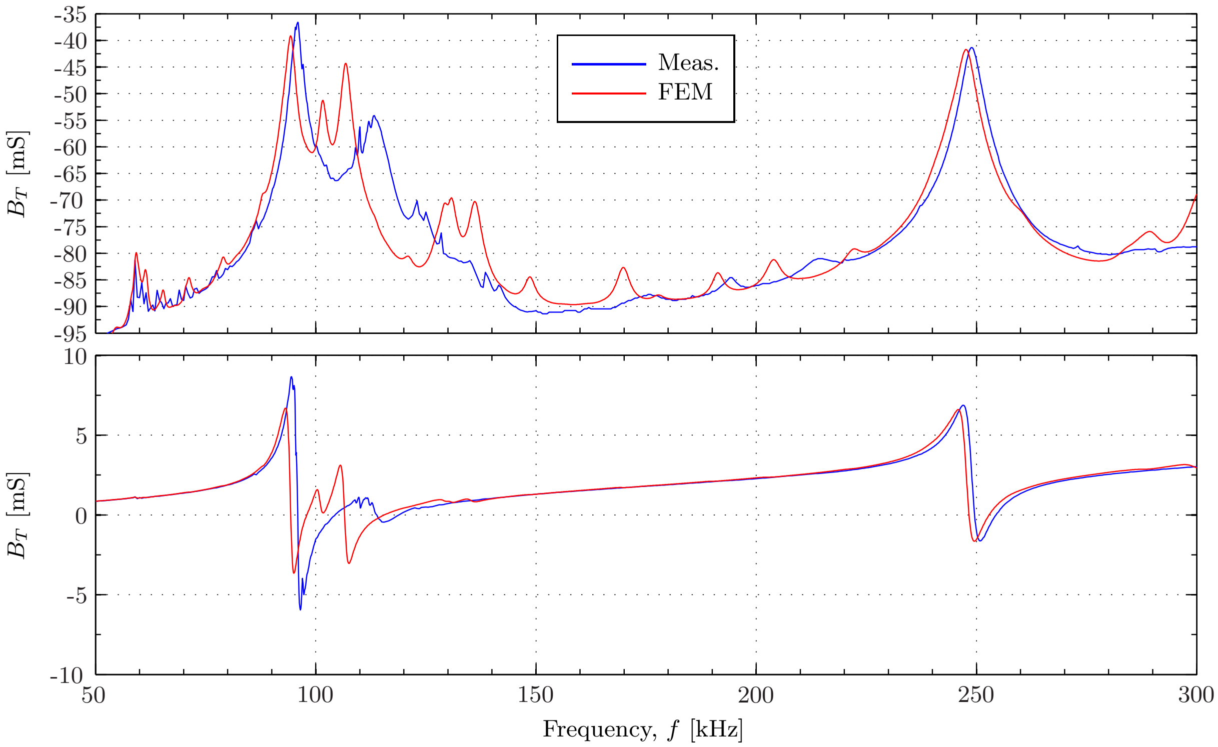

Figure 6.15: As in Fig. 6.13, but for Transducer No. 3.

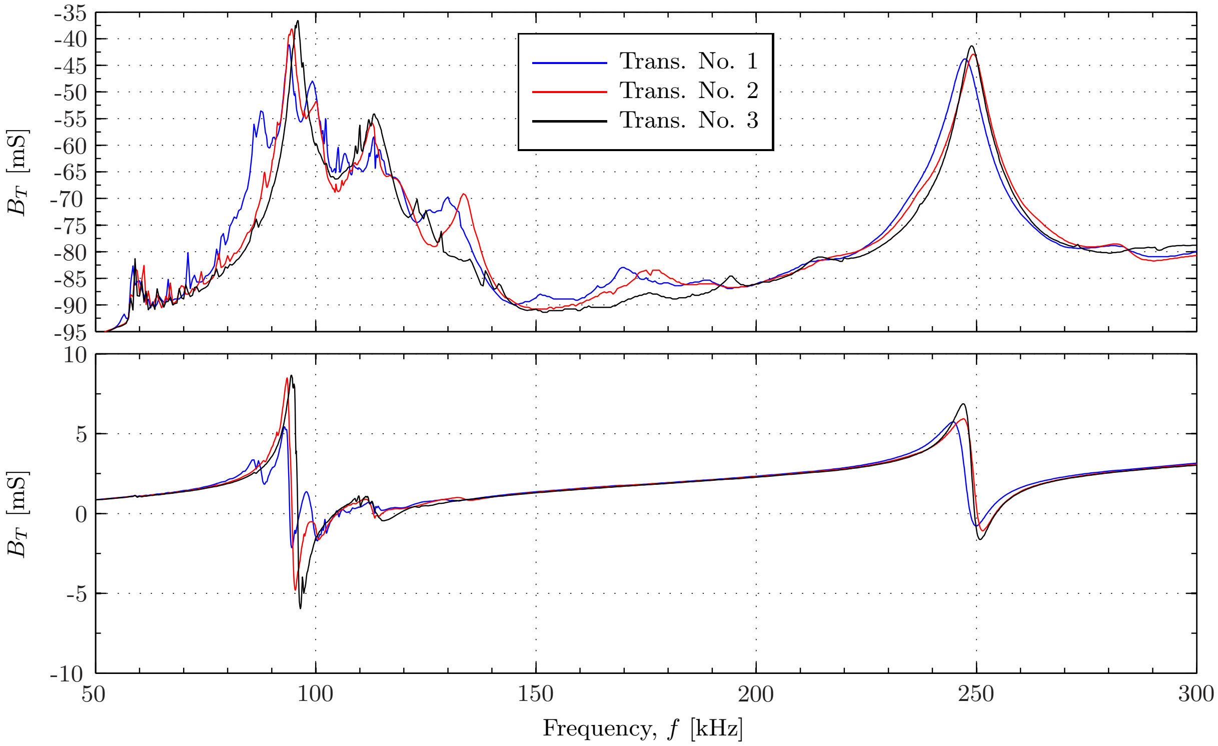

Figure 6.16: Comparison of measured conductance and susceptance of Transducer No. 1, Transducer No. 2, and Transducer No. 3.

Best agreement around the two main resonances are seen for Transducer No. 3 in Fig. 6.15, but the measured conductance lacks a resonance peak at approximately 140 kHz that appears in the simulations and in the measurements in Figs. 6.13 and 6.14.

Possible reasons for the deviations between measurements and simulations are found both in the construction and in the simulations. The simulations are performed with the transducer vibrating in vacuum, using nominal dimensions for the housing and assumed dimensions of the silver conductive epoxy. A simplified structure, `transducervacuum` (see Section 4.3), without the soldered-on wire, the backing layer, and the housing lid, is used in the simulations. Material data for the silver conductive epoxy and stainless steel are not supplied, and material data for similar materials are therefore used (see Section 4.4).

Results of acoustic measurements and comparison with FE simulations are shown in Chapter 7.

6.2 The assembly process

Three transducers are built, in order to conduct the three-transducer reciprocity calibration in [2]. The first step in the building process is to solder the signal wire onto the piezoelectric element. The soldering requires pre-heating of the element to 175 °C, so that the temperature of the solder iron can be reduced, thus allowing the element to keep a low enough temperature to prevent the polarization of the element being altered through the soldering process. The solder iron temperature is 250 °C. The soldering process is conducted by staff engineer Per Heradstveit, Dept. of Physics and Technology, UiB. The wire used is a multi core electrical wire recommended by staff engineer Heradstveit for its flexibility and mechanical strength.

The PA Aptflex R3 matching layer with nominal dimensions[7] 23.8 mm × 3.9 mm is attached to the front electrode of the piezoelectric element. The matching layer is machined out from a larger sample by the in-house workshop.

The matching layer is attached to the element using a two-component MG Chemicals silver conductive epoxy 8331 [**?**]. The conductive epoxy has a electrical resistivity of 0.017 Ω·cm. After the two components are mixed with a ratio of 1:1, the working time is 10 min. Eccocoat CC 2 conductive surface coating silver lacquer is applied to the edge of the matching layer, to enhance the electrical coupling to the side of the matching layer, which is attached to the steel wall of the housing later in the process. Conductive epoxy is then applied to the front electrode of the element, and to the backside of the matching layer. The conductive epoxy surfaces is pressed against a smooth PVC surface, and excess conductive epoxy is removed to obtain a thin layer of conductive epoxy on both surfaces. The element is placed on top of the matching layer and centred using a PVC cylindrical mould. A picture of the mould is given in Fig. 6.17a.

The mould is carefully removed and the element and matching layer are cured 12 hours or more before further use. After the conductive epoxy has cured, the electrical resistivity of the conductive epoxy from the edge of the element to the outer edge of the matching layer is measured using a multimeter. A resistance of approximately 10 Ω is measured on the parts used in transducer No. 1, while approximately 2 Ω is measured for transducer No. 2. In Fig. 6.17b, an element with wire soldered at the back electrode and matching layer attached at the front electrode using silver conductive epoxy is shown.

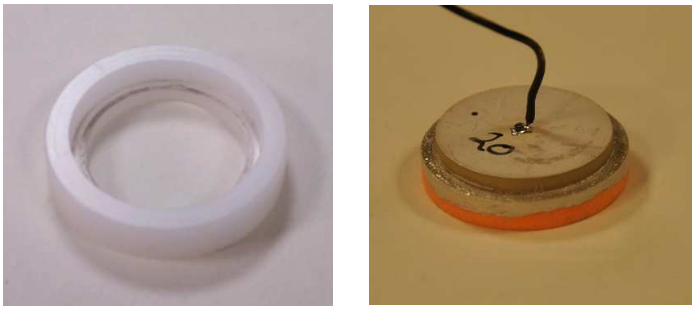

(a) (b)

Figure 6.17: Picture of (a) the PVC mould used for centering the piezoelectric element on the matching layer and (b) the piezoelectric element with the soldered wire on one electrode and the matching layer fastened on the other electrode.

A sandwich construction of the the Divinycell H130 backing layer is made using double-sided tape. A cylinder is then machined by the mechanical workshop to fit inside the housing, with a diameter of 24 mm and a length of 73 mm. The interfaces are aligned parallel to the wall of the housing to reduce the number of reflections. A hole is drilled through the length of the backing layer, allowing the wire attached to the element to be extended back and connected to the BNC connector. The diameter of the hole is 4 mm. Pictures of the backing layer from two different angles can be seen in Fig. 6.18.

---

[7] See Table 6.1 for accurate dimensions of the elements used.

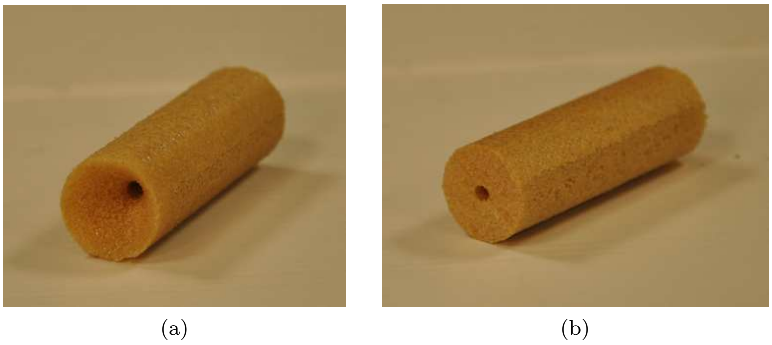
(a) (b)

Figure 6.18: Picture of the Divinycell H130 backing layer. Machined out to be assembled into the steel casing. Figure (a) shows the rearmost side of the backing layer, with the cone visible. (b) shows the face of the backing layer which is connected to the piezoelectric element.

The conductive epoxy used for attaching the element to the matching layer is applied around the edge of the matching layer. The matching layer is then inserted into the front of the housing, aligning the front of the matching layer with the front of the cylinder. The silver conductive epoxy connects the front electrode of the piezoelectric element to the steel housing, which in turn is connected to electric ground in the BNC connector.

The backing layer is inserted into the housing, with the wire soldered onto the element extended through the hole in the middle. No glue is used to attach the backing layer to the piezoelectric element, but it is held in place due to the tight fit of the backing layer in the housing cylinder.

The final step in the assembly of the transducers is installment of the steel lid which contains the BNC connector. To avoid any rotation of the BNC connector when the transducers are in use, the connector is locked in place by a screw from the side of the steel lid, see Fig. 6.19b. If the BNC connector were to rotate, it could cause the wire inside the transducer to break off from either the connector or the element. The signal wire extended back from the element is soldered onto the BNC connector, and the lid is fastened using screws into the steel housing.

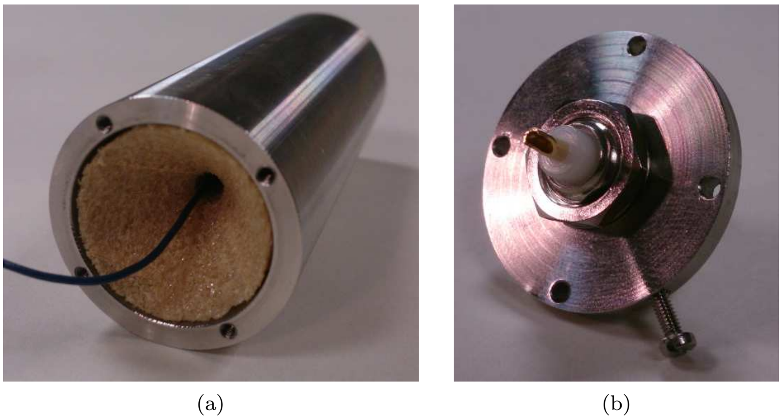
(a) (b)

Figure 6.19: Picture showing the rear of the housing, with the H130 backing material inserted. The wire from the piezoelectric element is seen extended through the middle of the backing. Picture showing the steel lid containing the BNC connector. The connector is hindered from rotating by use of a screw.

The finished transducer is seen in Fig. 6.20. The transducer shown is Transducer No. 1, suspended in the measurement chamber with the coaxial cable from the waveform generator connected.

(a) (b)

Figure 6.20: Picture of the assembled Transducer No. 1 suspended in the measurement setup. (a) shows the front of the transducer, while (b) shows the back of the transducer, with the coaxial cable connected to the BNC connector.

Chapter 7

Results

In this chapter, experimental and simulated results are presented. Simulations and measurements characterizing Modules A, B, D, G and F (cf. Figs. 2.1 and 3.9) are presented in Sections 7.1 - 7.4. The system models derived in Chapter 2 are presented in Section 7.5, and compared to acoustical measurements using different transmitter/receiver configurations in Sections 7.6 - 7.9.

The simulated effect of the coaxial cables are presented in Section 7.1, measurements of SNR are presented in Section 7.2, while the calculated diffraction correction is given in Section 7.3. Electrical measurements of G_T and B_T for the piezoelectric elements are compared to simulations in Section 7.4.

The three system models derived in Section 2.2 describe the transmit-receive system under open-circuit conditions. They are compare in Section 7.5, as functions of both frequency f and distance z, in order to highlight possible differences between them.

To gradually introduce the full complexity of effects for the transducers built in Chapter 6, Section 7.6 presents results for a piezoelectric element acting as transmitter and the microphone as receiver (referred to as ”element to microphone”), Section 7.7 gives results for a piezoelectric element acting both as transmitter and receiver (referred to as ”element to element”), Section 7.8 presents results for the constructed piezoelectric transducers acting as transmitter, and the microphone as receiver (referred to as ”transducer to microphone”), and Section 7.9 gives results for the piezoelectric constructed transducers acting both as transmitter and receiver (referred to as ”transducer to transducer”). Time domain waveforms of the simulated and measured V_{0m} and $V_{6,\alpha}$ are given for some frequencies of interest.

Presentation of results are given in this chapter, while main discussion of the results are given in Chapter 8.

7.1 Cable simulations

In Figs. 7.1 - 7.4, the transfer functions used for expressing the cables connecting the instruments in the measurement setup, $|H^{VV}_{0m1}|$, $|H^{VV}_{5open5'}|$, $|H^{VV}_{5'6}|$ and $|H^{VV}_{gen1}|$ are calculated, respectively. This shows the expected effect of the cables on the modeled measurement system. The calculation of the aforementioned functions is explained in Section 4.5.3.

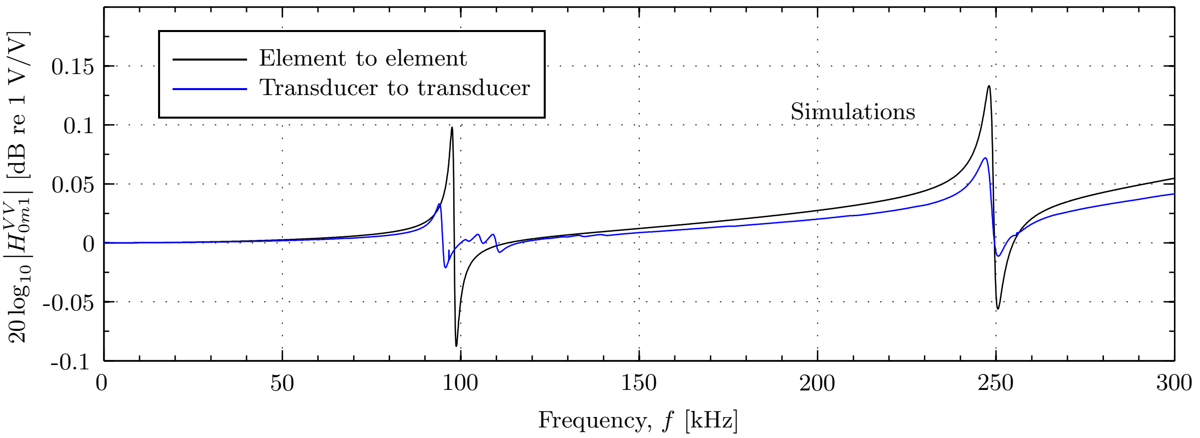

Figure 7.1: Comparison between simulated $|H_{0m1}^{VV}|$ for the element to element, and the transducer to transducer configuration.

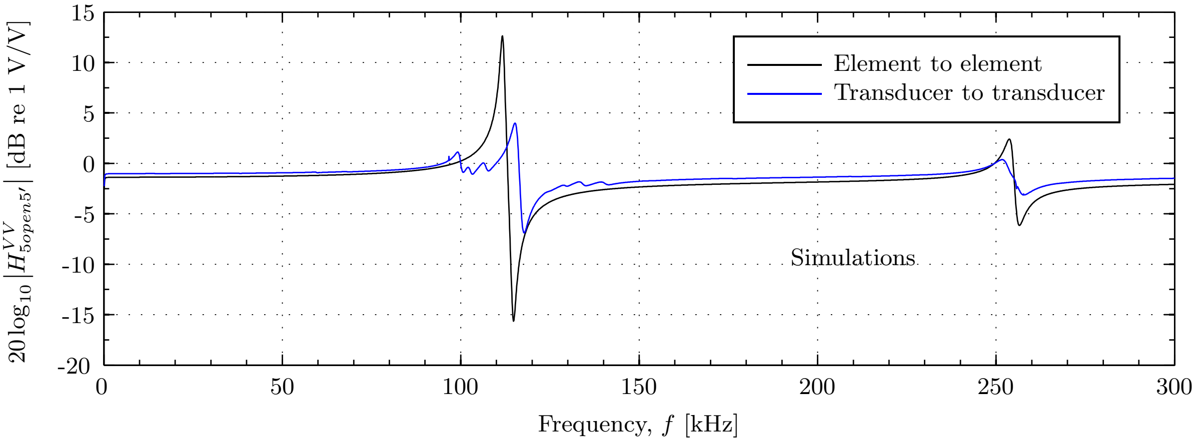

Figure 7.2: As Fig. 7.1, but for $|H_{5open5'}^{VV}|$.

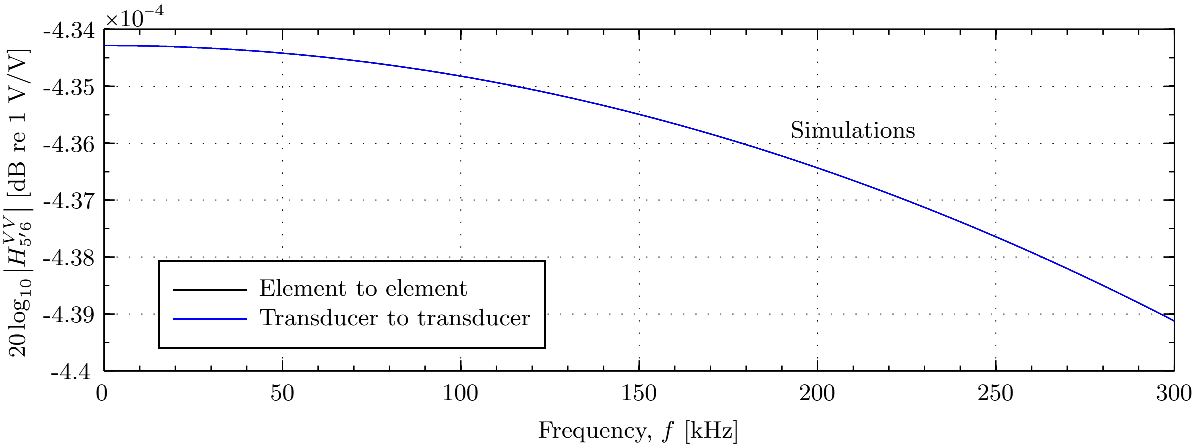

Figure 7.3: As Fig. 7.1, but for $|H_{5'6}^{VV}|$.

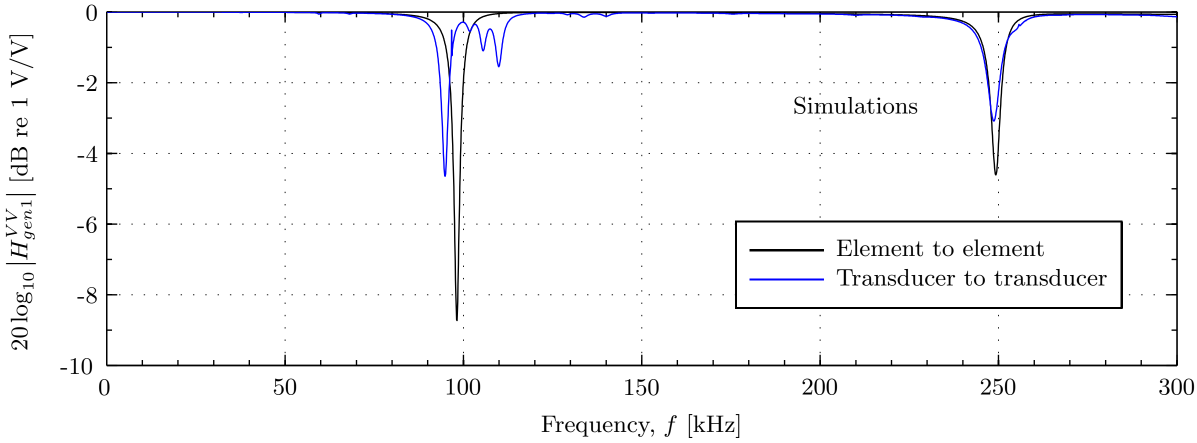

Figure 7.4: As Fig. 7.1, but for $|H_{gen1}^{VV}|$.

Fig. 7.1 shows a dampening of the resonance peaks/dips when using transducers in the transmit-receive system, compared to elements. At the resonance frequency of about 100 kHz, the transducers has several small peaks. The calculated $|H_{gen1}^{VV}|$ as shown in Fig. 7.4, is used for propagation of the time domain waveforms, shown later in this chapter, from the signal generator the node 1, cf. Section 2.8.

Similar behavior is seen in Fig. 7.2, but for both the elements and transducers, the magnitude of $|H_{5open5'}^{VV}|$ is approximately an order of 100 larger than for $|H_{0m1}^{VV}|$, as depicted in Fig. 7.1.

Fig. 7.3 shows a decrease over the whole frequency range, and both the elements and transducer case are equal, as expected, since the receiving transducers output impedance does not affect $|H_{5'6}^{VV}|$, cf. Section 2.6. The order of magnitude of $|H_{5'6}^{VV}|$ is 10^{-4} dB.

7.2 Measurement noise

The noise in the experimental setup is measured, expressing SNR (cf. Eq. (3.14)). The noise measurements method is given in Section 3.3.7. The noise is measured for the different transmitter/receiver combinations; element to microphone (see. Fig. 7.5), element to element (see. Fig. 7.6), transducer to microphone (see. Fig. 7.7) and transducer to transducer (see. Fig. 7.8).

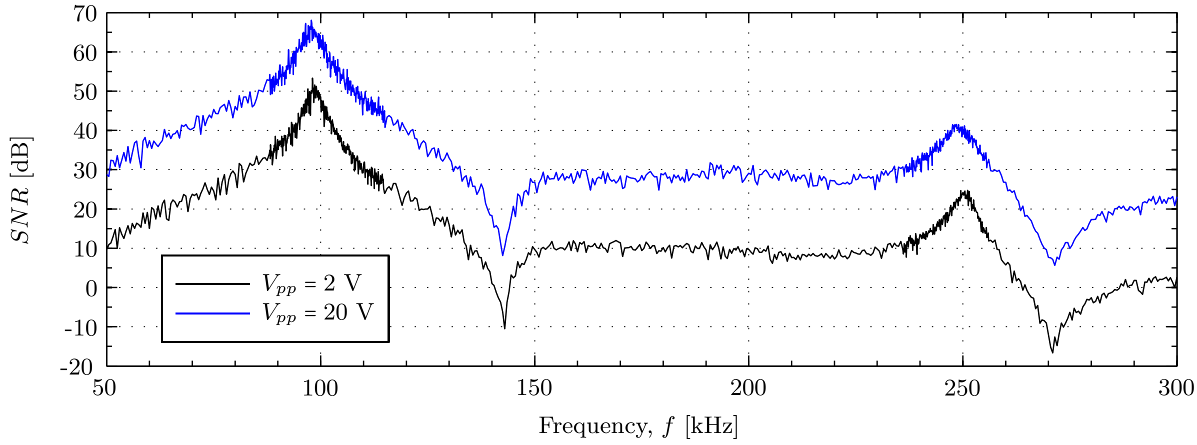

Figure 7.5: The measured SNR for a piezoelectric ceramic disk transmitter with a microphone receiver.

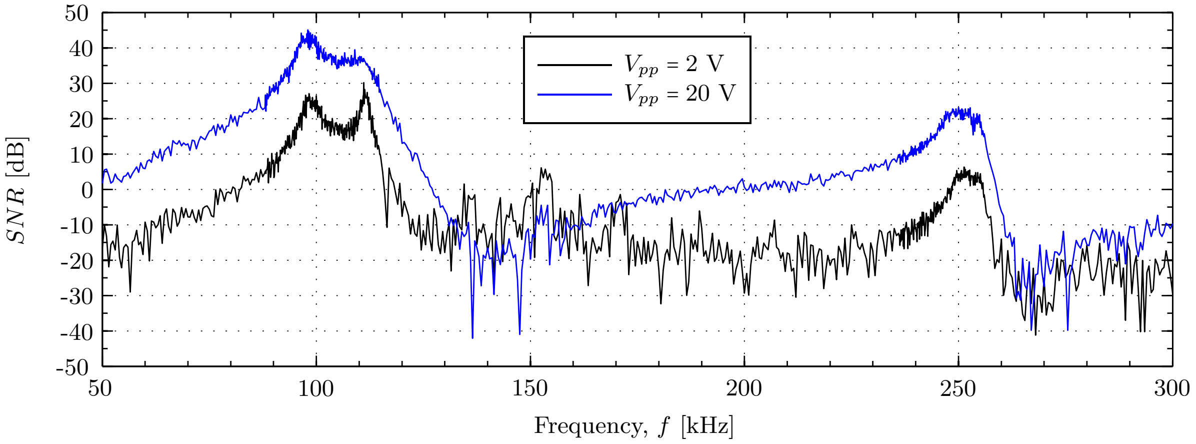

Figure 7.6: As Fig. 7.5, with a piezoelectric ceramic disk receiver.

In Figs. 7.5 - 7.6, it is seen that for element to microphone, the SNR at R1 is approximately 30 dB higher than for element to element, while it is approximately 20 dB higher at R2. In Fig. 7.5, the SNR gain when increasing V_{pp} from 2 to 20 V is approximately 15 dB for all frequencies. The equivalent increase in SNR in Fig. 7.6 is approximately 20 dB at the first resonance peak in R1, while it is approximately 15 dB at R2.

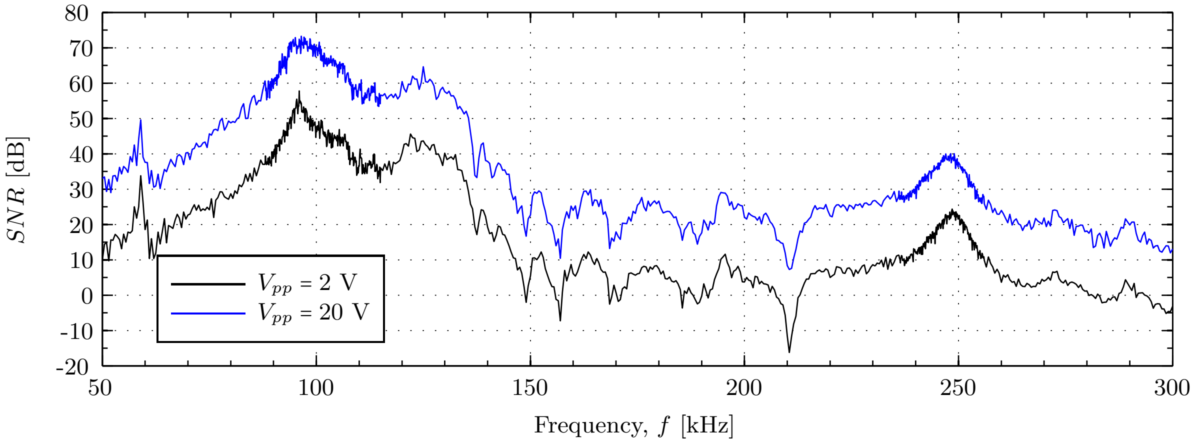

Figure 7.7: As Fig. 7.5, with a constructed transducer as transmitter.

Fig. 7.7, measured using transducer to microphone, shows a higher SNR at R1 compared to both element to microphone, and element to element. Increasing V_{pp} from 2 to 20 V increases SNR by almost 20 dB, for all measured frequencies.

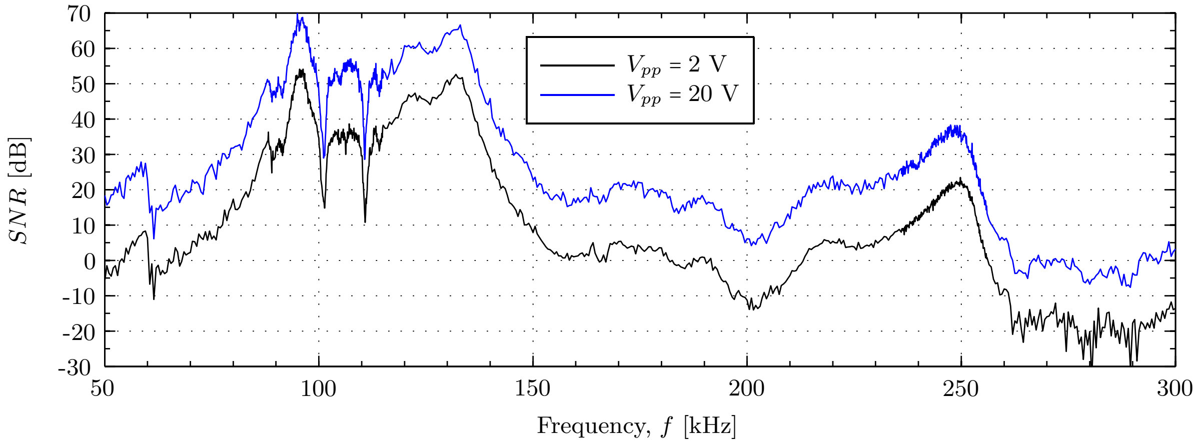

Figure 7.8: The measured SNR for constructed transducers used as transmitter and receiver.

In Fig. 7.8, it is seen that around R1, an increase in V_{pp} for the transducer to transducer case yields an approximately 15 dB increase for SNR. The high SNR values around R1 are interrupted by two narrow dips.

Comparison between V_{pp} = 20 V in Figs. 7.5 and 7.7 are shown in Fig. 7.9 and comparison between V_{pp} = 20 V in Figs. 7.6 and 7.8 are shown in Fig. 7.10.

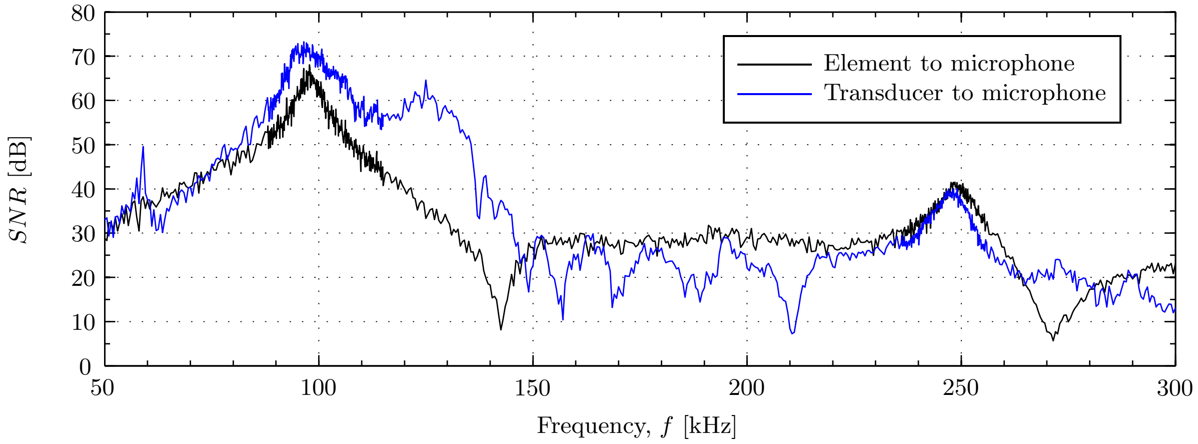

Figure 7.9: The measured SNR for a piezoelectric ceramic disk transmitter with a microphone receiver, compared to measured SNR for a constructed transducer transmitter with a microphone receiver.

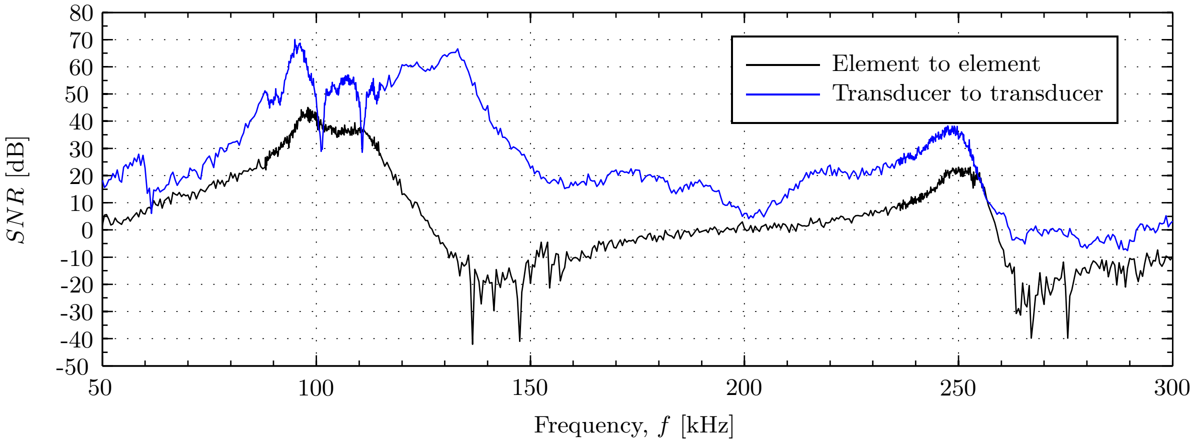

Figure 7.10: The measured SNR for constructed transducers used as transmitter and receiver, compared to measured SNR for piezoelectric ceramic disks used as transmitter and receiver.

From Fig. 7.9 it is seen that above 150 kHz, the element to microphone has a more uniform, and even slightly higher SNR, than the transducer to microphone. In Fig. 7.10 it is seen that by using a constructed transducer as transmitter, SNR is increased around R1. It appears that the R1 mode for the transducer to transducer case covers a larger frequency area than for element to element. Up to 70 dB increase is observed at the transducers second resonance frequency in R1, at approx. 130 kHz.

7.3 Diffraction correction

In Fig. 7.11, Khimunins diffraction correction $|H_K^{dif}|$ (cf. Eq. (2.41)), is plotted. Two radii are used in calculation of the curves in Fig. 7.11; 10 mm, corresponding to the approximate radius of the piezoelectric elements used, and 11.9 mm, which is the approximate radius of the matching layer used in the transducer structures. Thus the calculated diffraction correction in the measurement system when using either a piezoelectric element or constructed transducer as transmitter/receiver is shown.

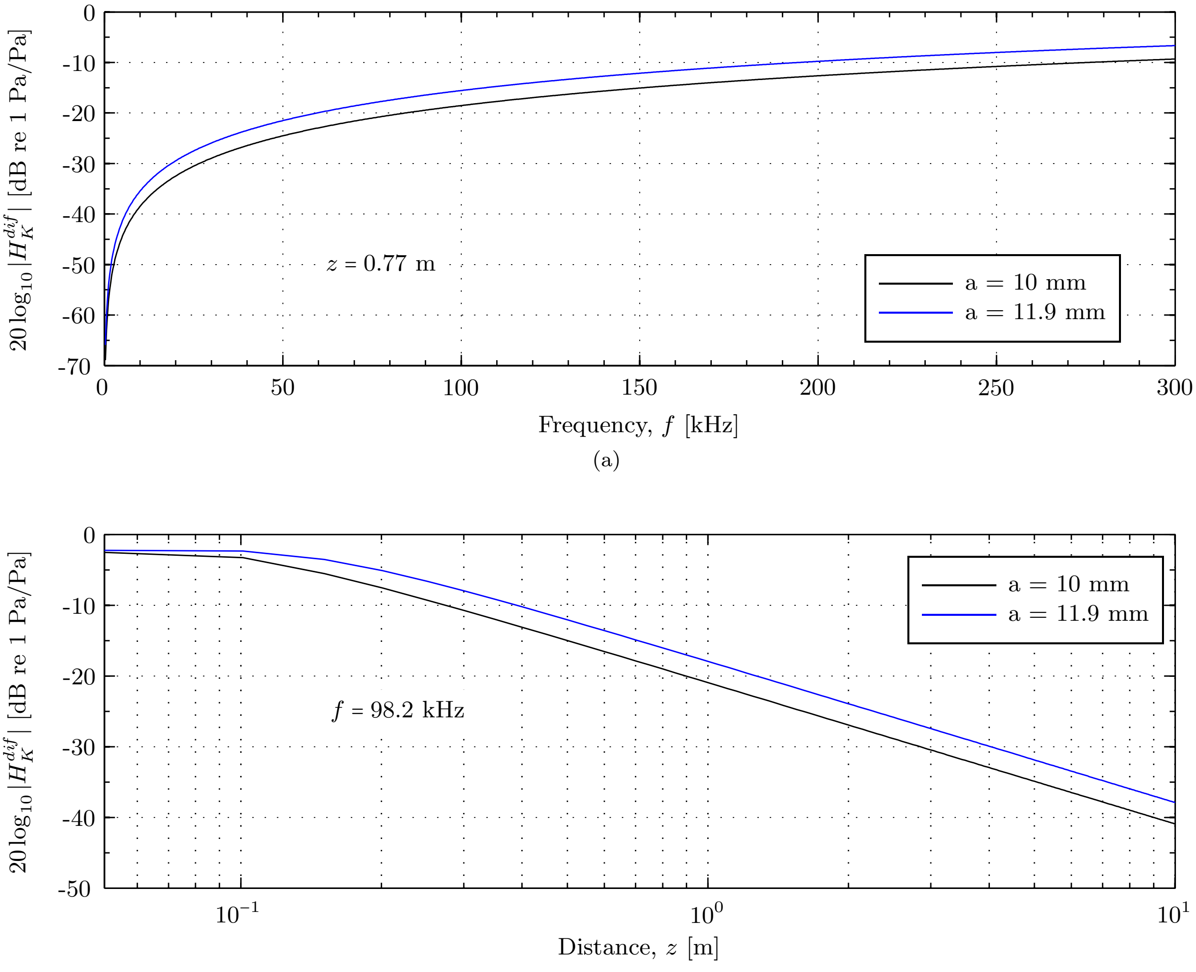

(a)

(b)

Figure 7.11: Comparison between $|H_K^{dif}|$ plotted vs. (a) frequency f, and (b) distance z.

Fig. 7.11a shows a logarithmic incline in $|H_K^{dif}|$, for both radii, where a = 11.9 mm has higher magnitude. In Fig. 7.11b, it is seen that a = 11.9 has higher magnitude for all distances between 0.05 and 10 m. For small z the difference is small, and a near constant difference is observed between 1 and 10 m.

The relative diffraction correction $R^{dif}(z)$ is shown in Fig. 7.12, calculated as described in Section 4.5.2. *Formulation A* is calculated by use of FEMP modeling of a piezoelectric ceramic disk, using the `piezodiskfluid` structure.

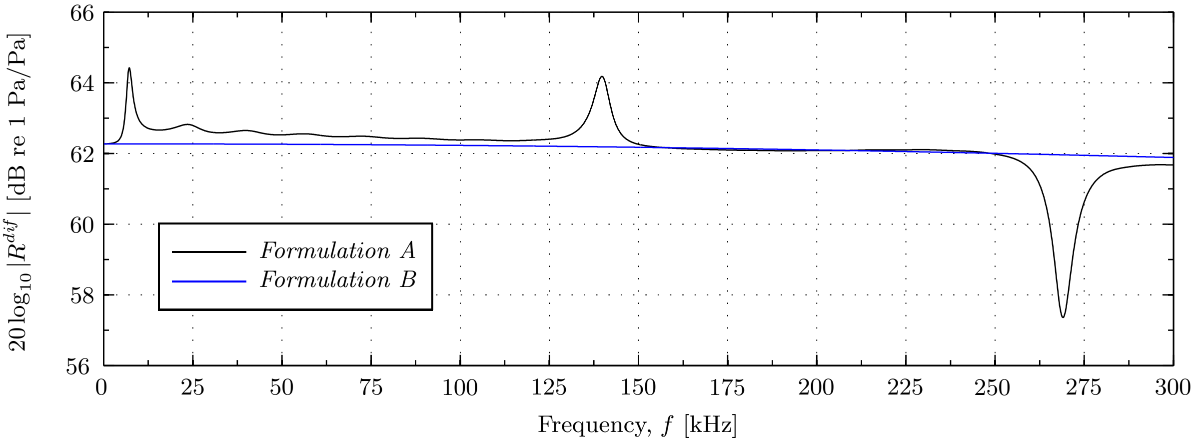

Figure 7.12: Comparison between $R^{dif}(z)$ expressed using *formulation A* and *formulation B*.

In Fig. 7.12 it is seen that *formulation B* has a much flatter response than *formulation A*. *Formulation A* has a peak at approximately 140 kHz, and a dip at approximately 270 kHz.

7.4 Electrical measurements and simulations

Electrical measurements are conducted both (a) in order to compare the elements between each other to determine a suitable pair for use in measurements (cf. Section 3.6), and (b) to compare the electrical measurements to simulations. Simulations and measurements for the elements used in the transducer construction are shown in Section 6.1.1. In this section, the two elements used in the acoustical measurements, Element #16 and Element #10, are shown. The electrical measurements are descried in Section 3.2, whereas calculation of the simulated electrical quantities are given in Section 2.7. The simulations are conducted using the structure `piezodiskfluid`, see Section 4.3.

Element #16

Figs. 7.13 - 7.15 shows the simulated conductance, G_T, and susceptance, B_T, for Element #16, compared to measurements conducted before and after the wires are soldered onto the element (cf. Section 3.6).

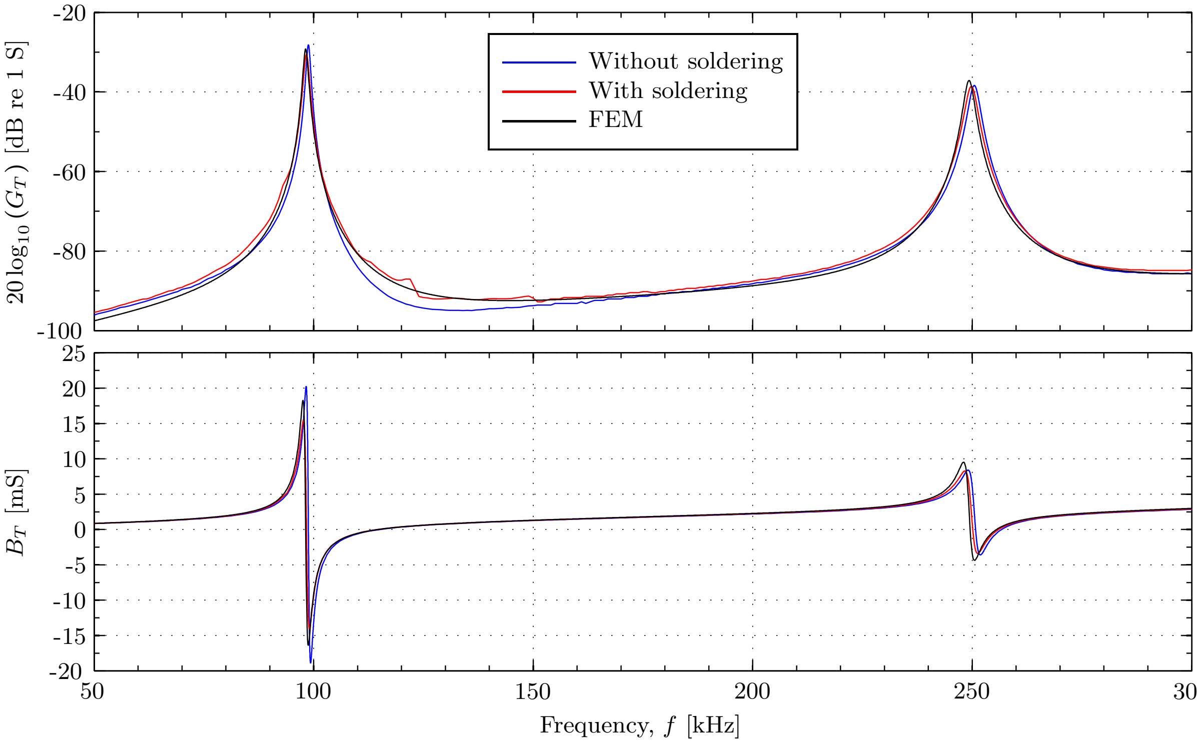

Figure 7.13: Conductance and susceptance of Element #16 for the frequency range 50 kHz to 300 kHz. Measured before and after the wires are soldered onto the element. Compared with FE simulations of the element vibrating in air.

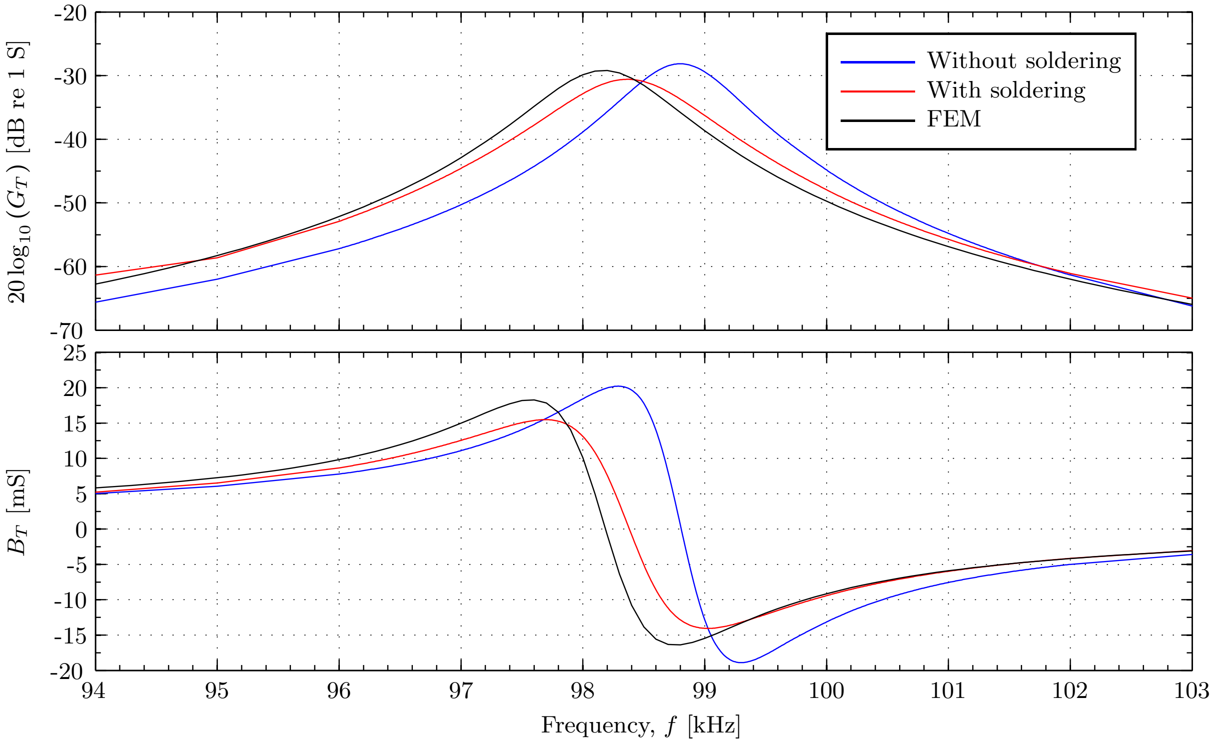

Figure 7.14: As Fig. 7.13, but for the frequency range 94 kHz to 103 kHz, around R1.

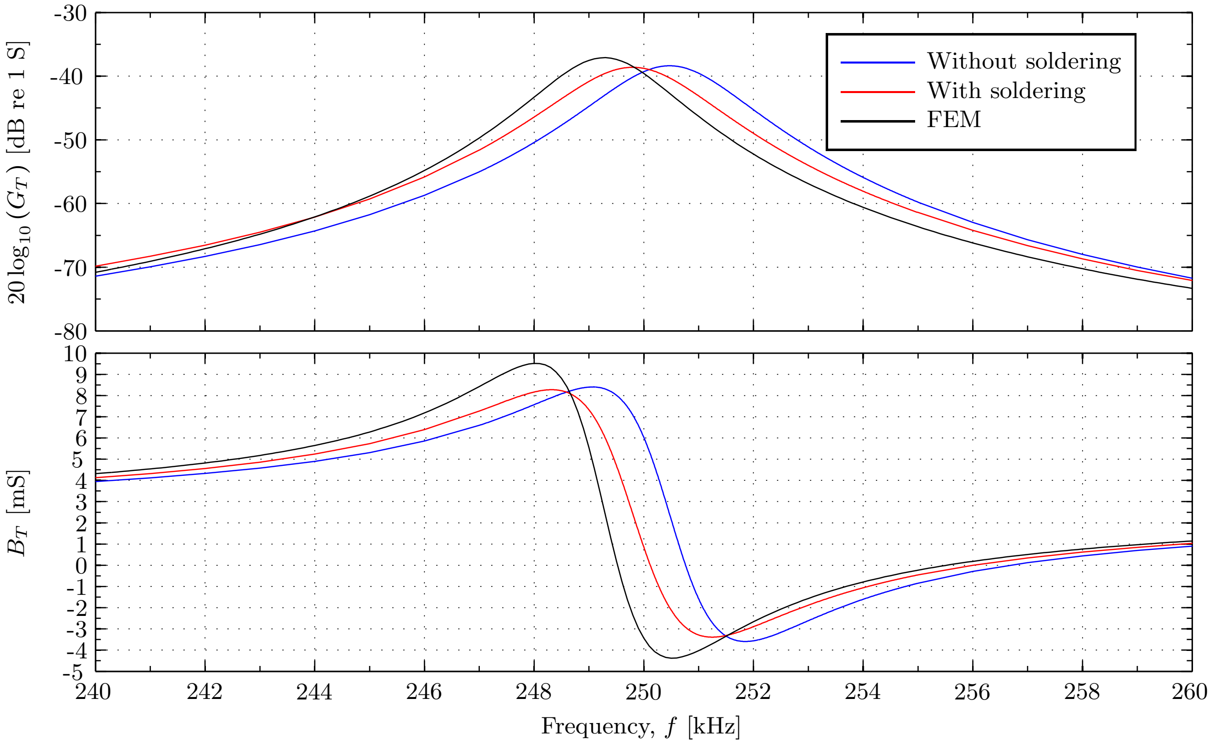

Figure 7.15: As Fig. 7.13, but for the frequency range 240 kHz to 260 kHz, around R2.

From Figs. 7.13 - 7.15, a fair agreement between the simulations and measurements are seen. It appears that the agreement between the simulations and measurements is better for the element with the wire soldered onto it.

Element #10

Figs. 7.16 - 7.18 shows the simulated conductance, G_T, and susceptance, B_T, for Element #10, compared to measurements conducted before and after the wires are soldered unto the element (cf. Section 3.6).

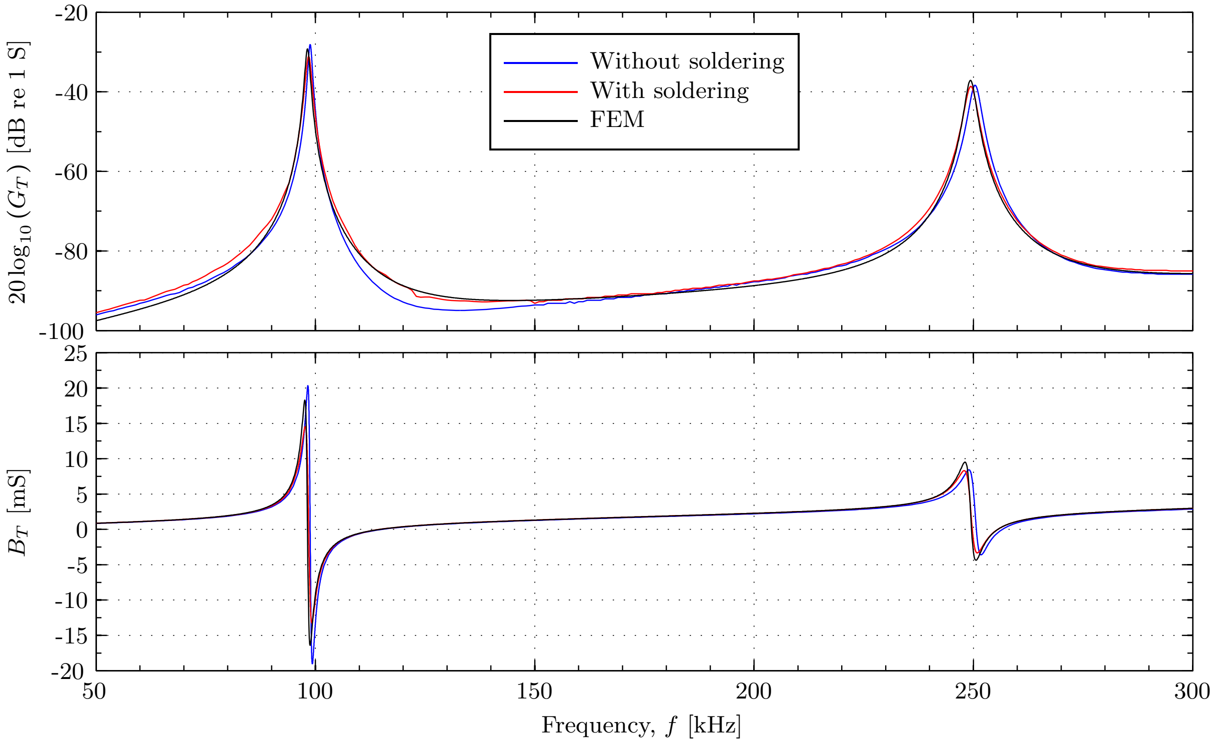

Figure 7.16: Conductance and susceptance of Element #10 for the frequency range 50 kHz to 300 kHz. Measured before and after the wires are soldered onto the element. Compared with FE simulations of the element vibrating in air.

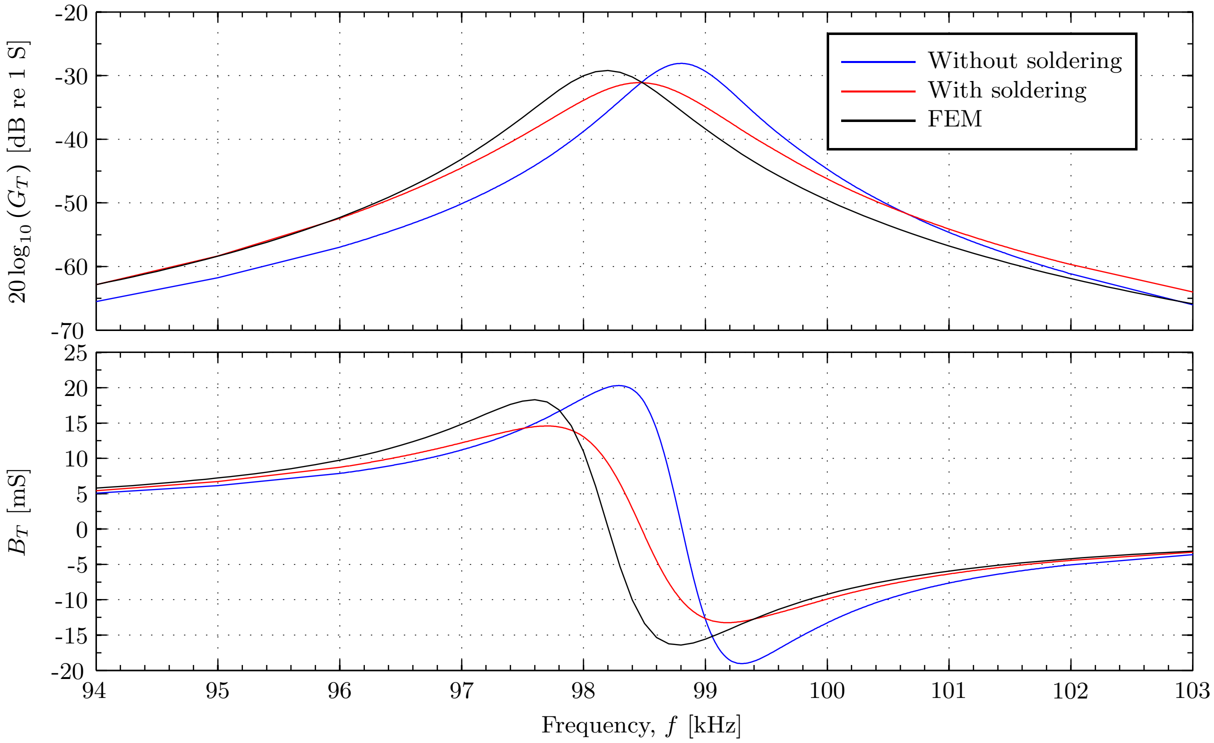

Figure 7.17: As Fig. 7.16, but for the frequency range 94 kHz to 103 kHz, around R1.

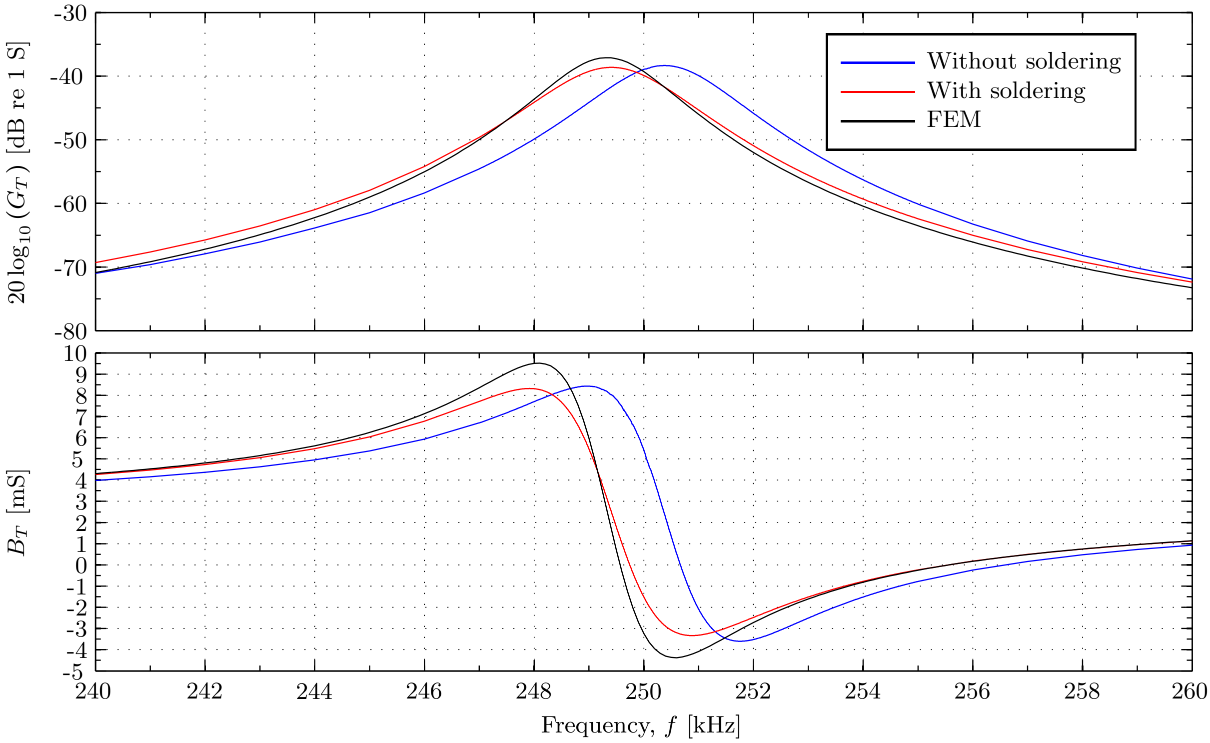

Figure 7.18: As Fig. 7.16, but for the frequency range 240 kHz to 260 kHz, around R2.

As for Element #16, a fair agreement between the simulations and measurements are seen in Figs. 7.16 - 7.18. Also here, it appears that the agreement between the simulations and measurements is better for the element with the wire soldered onto it.

7.5 System model comparison

Two models are derived for description of the signal propagating from node 1 to node 5 under open-circuit conditions, see Fig. 2.2. These are Model 1 and 2, with the alternative formulations 2A and 2B, defined in Eqs. (2.22), (2.38) and (2.39), respectively, for a lossless medium. A comparison of $|H_{15}^{VV}|$ calculated using the aforementioned equations is shown in Fig. 7.19. Simulations are done using the `piezodiskfluid` structure, cf. Section 4.3.

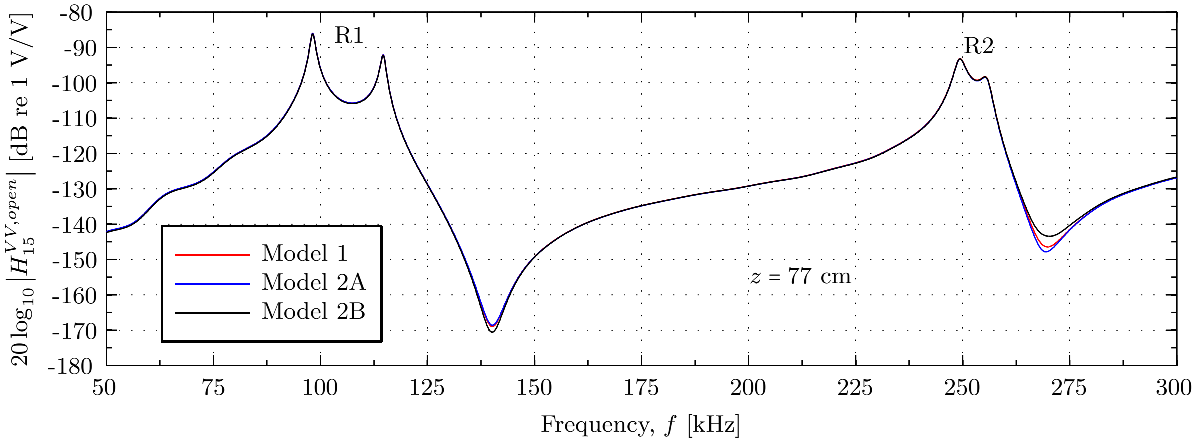

Figure 7.19: Comparison between $|H_{15}^{VV,open}|$ plotted against frequency for Model 1, 2A and 2B.

Fig. 7.19 shows that the largest deviation between the different models are found in the dips at approximately 140 kHz and 270 kHz. At the dip following R1, the largest deviation is 2 dB, while it is 5 dB in the dip following R2. For the rest of the frequency range, the deviation is less than 0.3 dB.

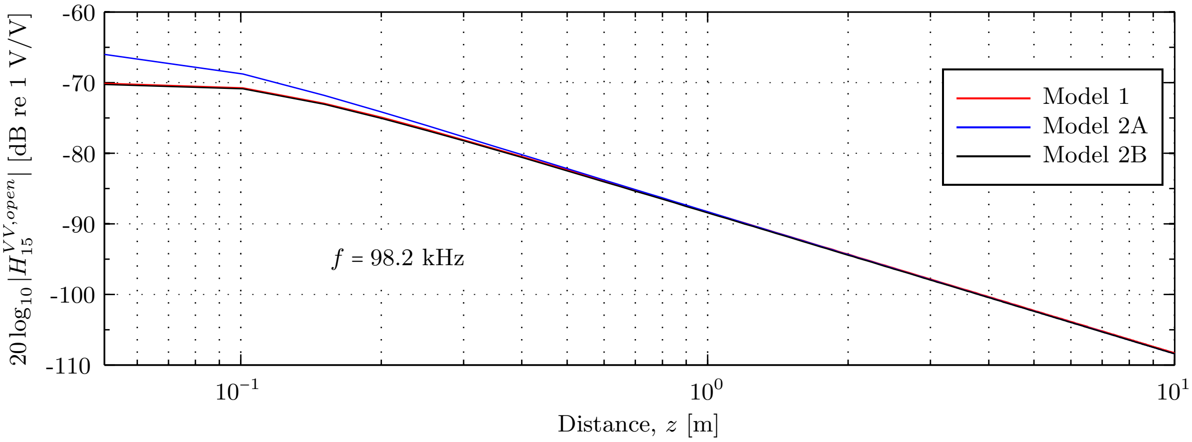

Figure 7.20: Comparison between $|H_{15}^{VV,open}|$ plotted against distance z for Model 1, 2A and 2B.

In Fig. 7.20 it is seen that for small distances z, Model 2A is larger than the other two, while the models show a better agreement between them for larger z. The deviation is approximately 4 dB at z = 0.05 m, 2 dB at z = 0.1 m and 0.1 dB at z = 10 m.

Through the rest of this chapter, *Model 1A* is used when calculating $|H_{15}^{VV,open}|$ for use in the system model.

7.6 Element to microphone

Measurements are done using a piezoelectric element as transmitter and the microphone as receiver, cf. Table 7.1. This measurement case is less complex than the element to element transducer to microphone and transducer to transducer cases, as the piezoelectric element is relatively simple as a structure, compared to a full transducer construction, and the microphone is calibrated up to 200 kHz (cf. 3.5.1), with a relatively flat M_V response.

Fig. 7.21 shows magnitude comparison between measured and simulated $H_{0m6,\alpha}^{VV}$. Two measurements are compared to the simulation; measurement (1), using 2 volts peak-to-peak driving voltage to the transmitting transducer (V$_{pp}$), and measurement (2), using V$_{pp}$ = 20 V. The measurement setup for the two measurements shown in Fig. 7.21, is given in Table 7.1. Both blue curves in Fig. 7.21 is measurement (1), where the solid line is extracted from the measurment using the Fourier method post-process routine (cf. Section 3.7.2), and the dashed line is extracted using the direct method for calculating V_{pp}^{rec} (cf. Section 3.7.3). The same goes for measurement (2), using red lines.

Table 7.1: Measurement setup overview for Figs. 7.21 - 7.26.

Transmitting transducer:	Element # 16
Receiving transducer:	B&K 4138 pressure condenser microphone
Generator output voltage:	(1) V_{pp} = 2 V and (2) V_{pp} = 20 V (cf. legend Fig. 7.21)

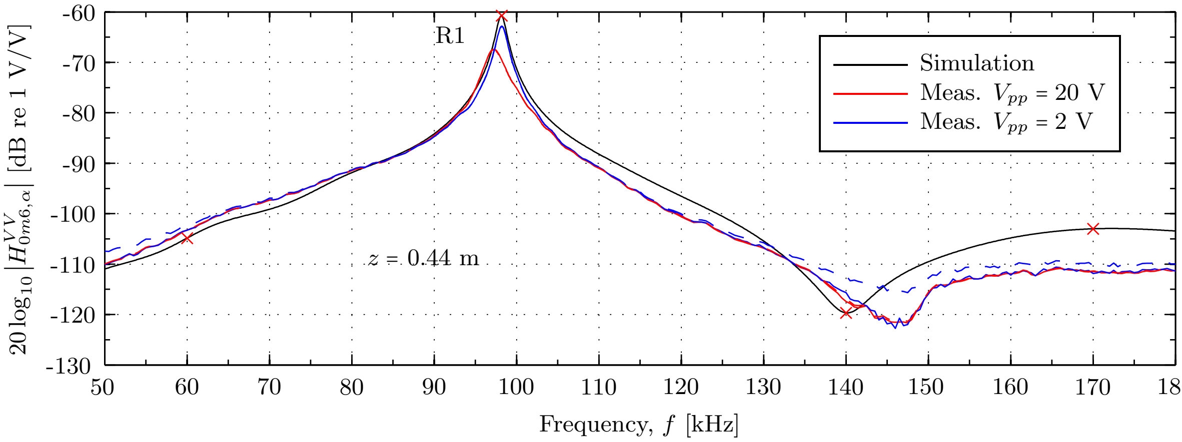

Figure 7.21: Measurements and FEMP simulation of $\left|H^{VV}_{0m6,\alpha}\right|$. V_{pp} is calculated using both the Fourier (solid line) and direct (dashed line) method (cf. Section 3.7). The "×" indicates which frequencies are used for plotting the time responses in Figs. 7.23 - 7.26.

In Fig. 7.21 it is seen that the biggest disagreement between measurement (1) and (2) is found at the R1 resonance frequency, where measurement (2) is shifted down in both frequency and magnitude level, compared to both measurement (1) and the simulation. A qualitative agreement is seen below and above R1, up to the dip at approximately 140 kHz. The measured dip is shifted upwards in frequency compared to the simulation.

In Fig. 7.22, the measured $|S_{V,\alpha}|$ is compared to the simulated. The measured $|S_{V,\alpha}|$ is calculated in Section 2.9, while the simulated $|S_{V,\alpha}|$ is calculated using Eq. (2.51), together with Section 4.2 (for calculation of S_V).

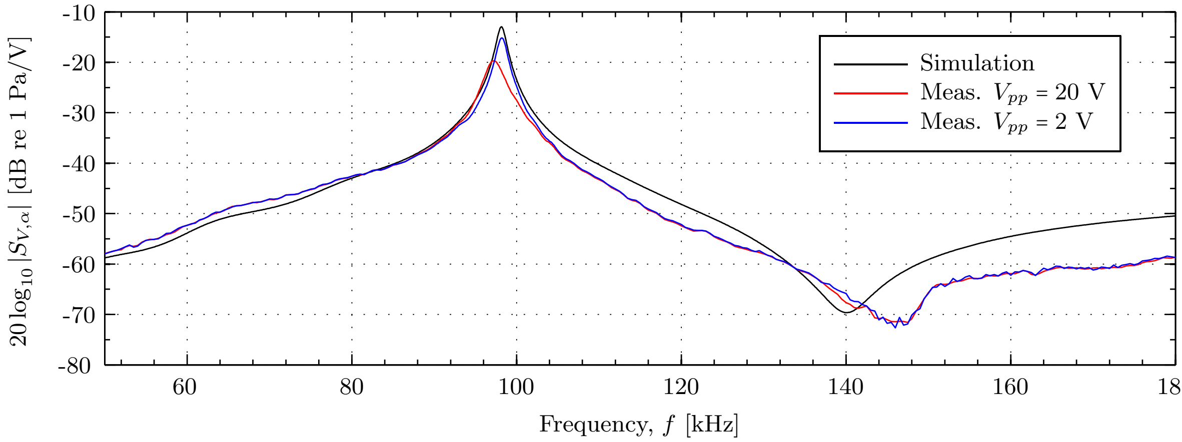

Figure 7.22: Measurements and FEMP simulation of $|S_{V,\alpha}|$.

From Fig. 7.22, it is seen that when using a microphone receiver, $|S_{V,\alpha}|$ has roughly the same shape as $\left|H^{VV}_{0m6,\alpha}\right|$, while $|S_{V,\alpha}|$ is almost 50 dB larger than $\left|H^{VV}_{0m6,\alpha}\right|$ at R1. This can also be seen from Eq. (2.135), where $|M_V|$ for the microphone, and a distance scaling factor is what differ $|S_{V,\alpha}|$ from $\left|H^{VV}_{0m6,\alpha}\right|$. In Fig. 3.23, $|M_V|$ for the B&K pressure condenser microphones used in this work is seen to have a smooth variation over the measured frequency range.

The recorded waveforms of V_{0m} and $V_{6,\alpha}$ are compared to time response simulations, see Section 2.8. In Figs. 7.23 - 7.26, comparisons are done for frequencies 60, 98.2, 140 and 170 kHz, respectively. The measured waveforms are extracted from measurement (2). The measurement represented by Table 7.1 are conducted with a temporal range which includes the onset, transient and steady-state of the waveform, but not the transient decay, due to the measurement settings for the measurements using a microphone receiver.

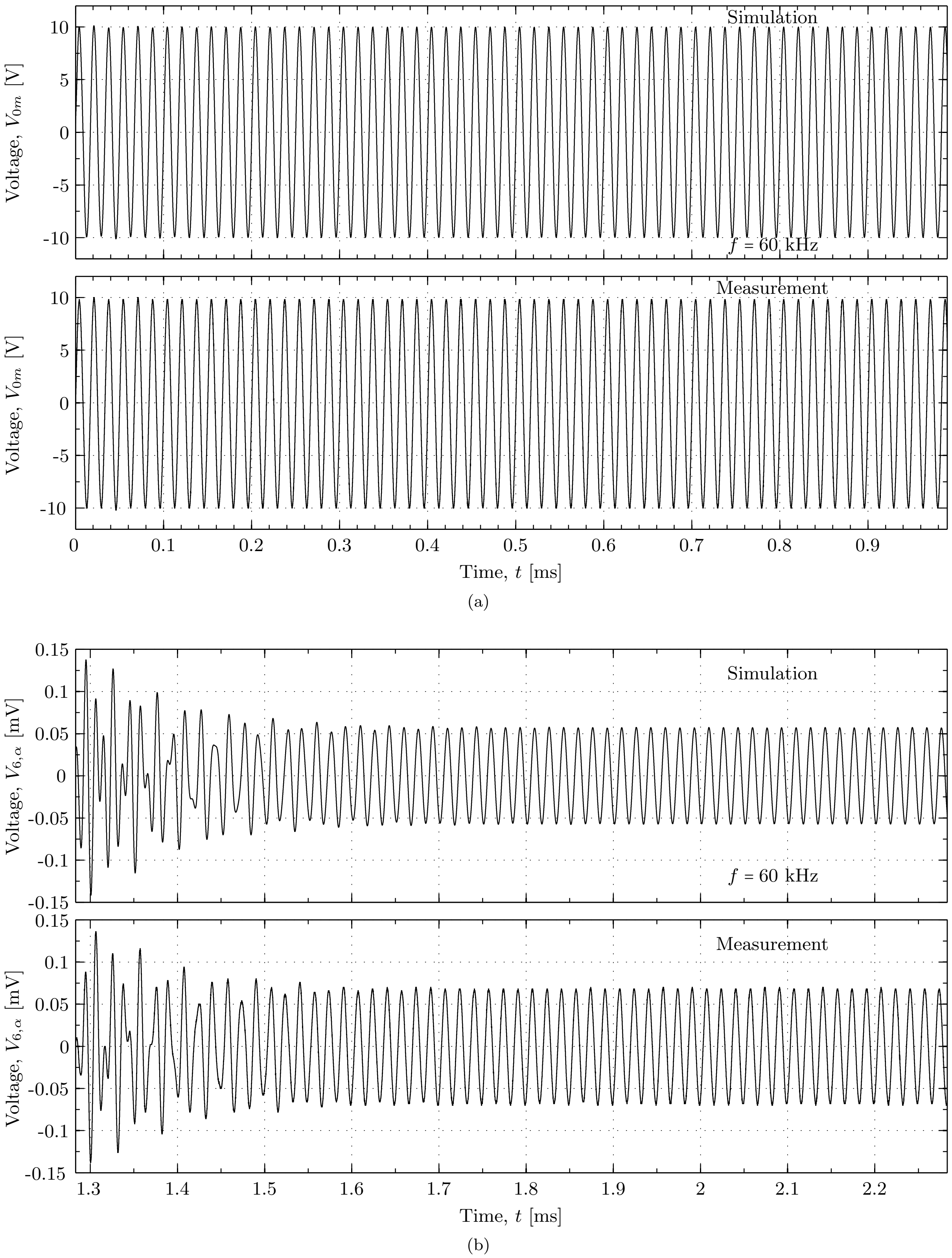

(a)

(b)

Figure 7.23: The simulated and measured waveform (V_{pp} = 20 V) of (a) V_{0m} and (b) $V_{6,\alpha}$. The measurement frequency is 60 kHz.

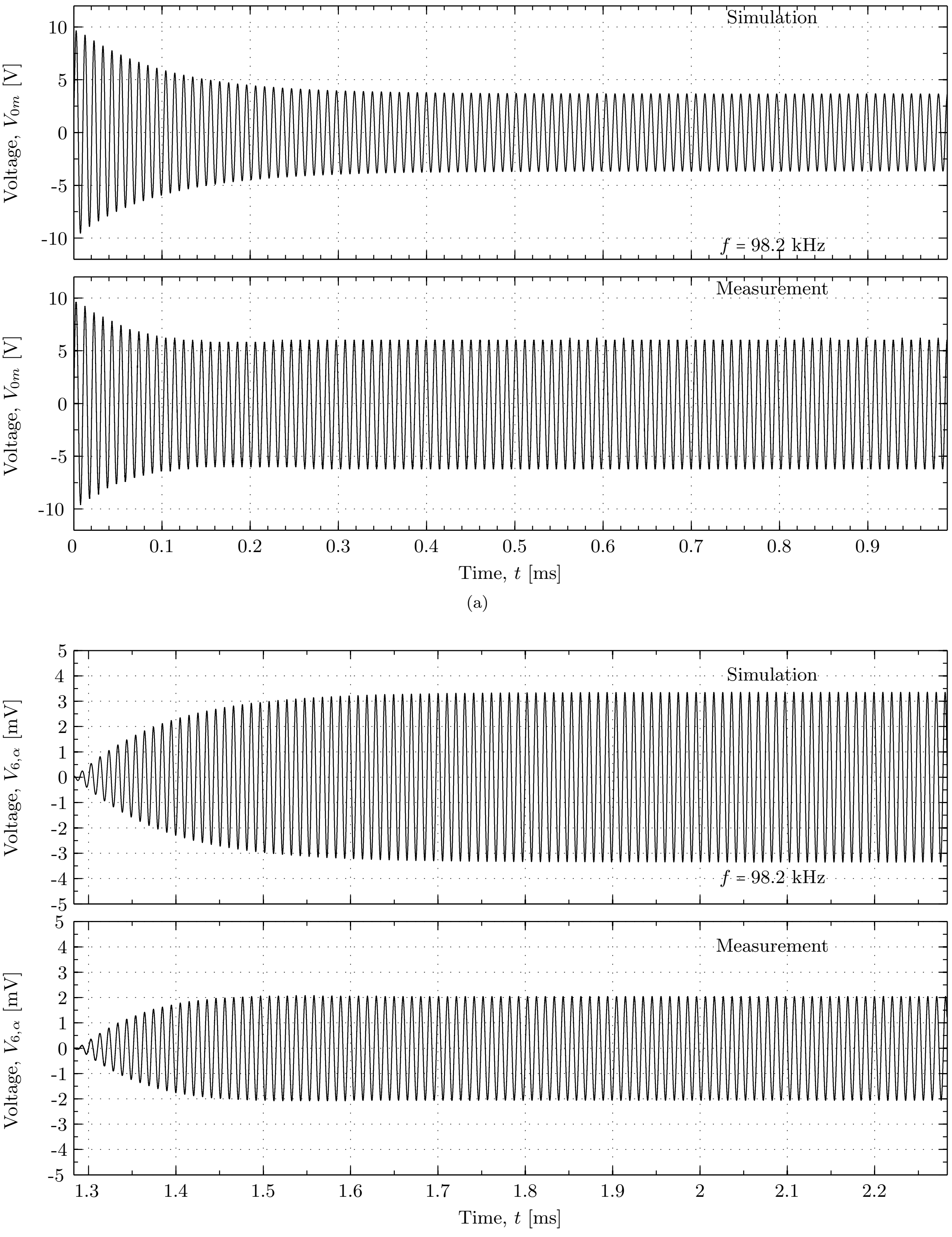

(a)

(b)

Figure 7.24: As for Fig. 7.23, but for a measurement frequency of 98.2 kHz.

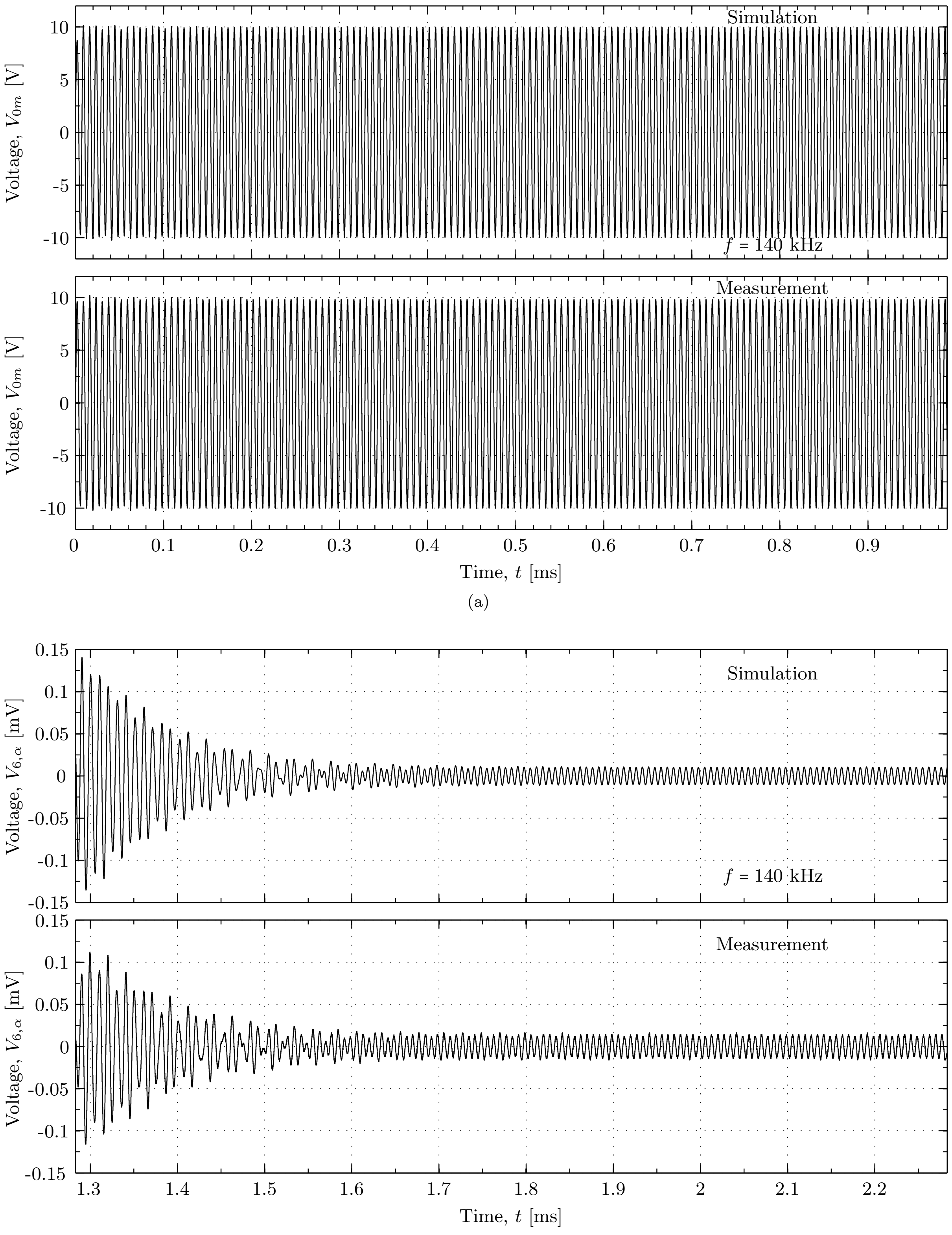

(a)

(b)

Figure 7.25: As for Fig. 7.23, but for a measurement frequency of 140 kHz.

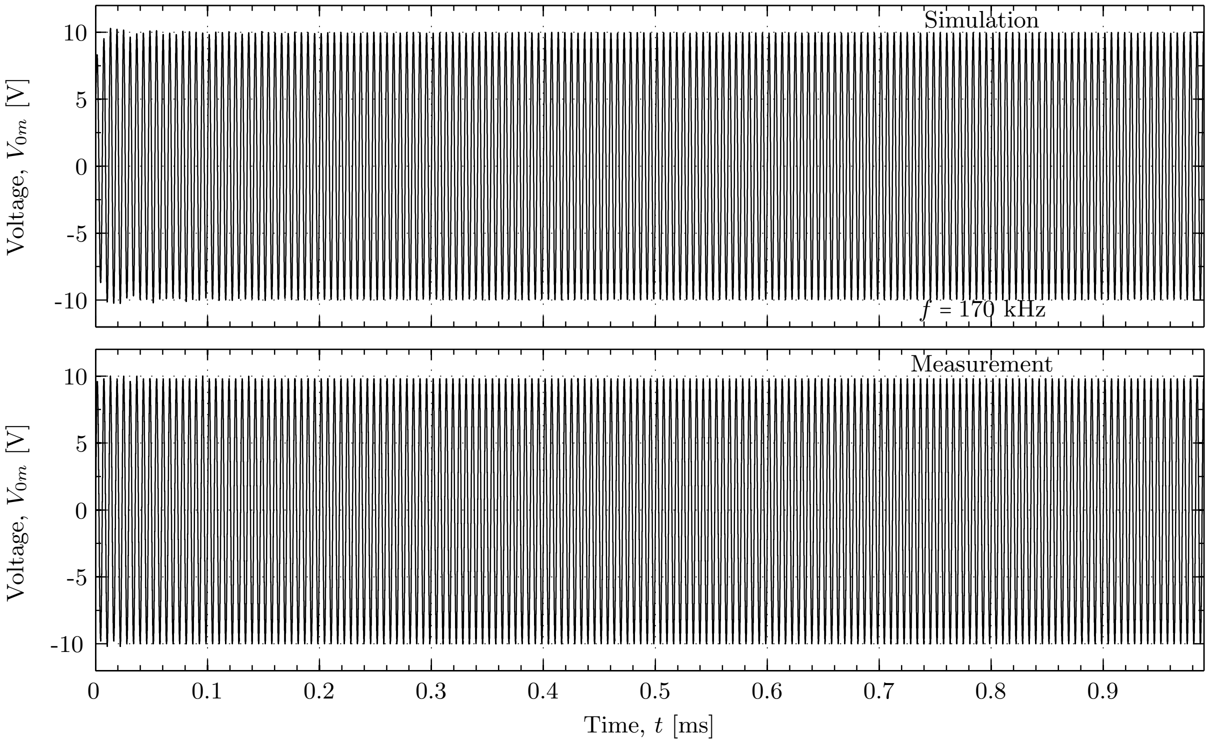

(a)

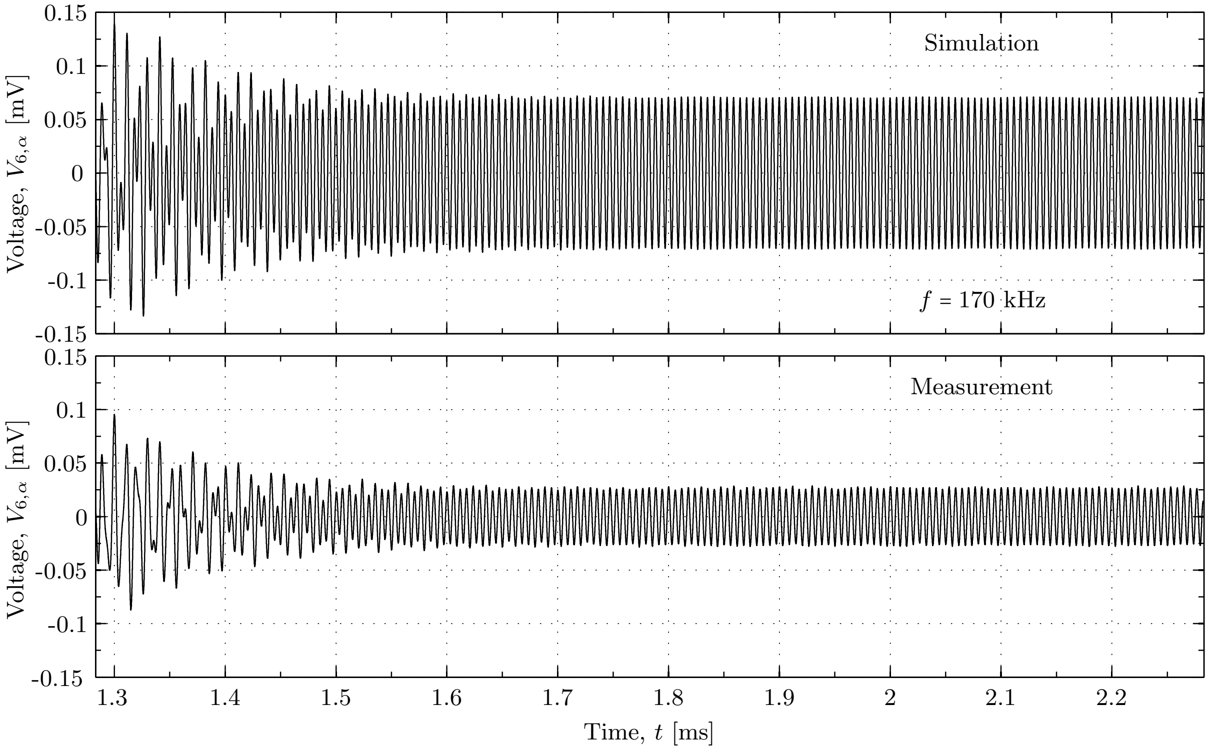

(b)

Figure 7.26: As for Fig. 7.23, but for a measurement frequency of 170 kHz.

From Figs. 7.23 - 7.26 it is seen that there are a qualitative good agreement between the simulated and measured waveforms. The agreement between the measured and simulated $V_{6,\alpha}$ in Figs. 7.23 - 7.26 are seen to correspond to the agreement between measured and simulated $|H_{0m6,\alpha}^{VV}|$ in Fig. 7.21. For instance, at 170 kHz, the $|H_{0m6,\alpha}^{VV}|$ magnitude level is higher for the simulation than the measurement, which is also seen in Fig. 7.26b.

7.7 Element to element

In this section, piezoelectric elements are used both as transmitter and receiver. The piezoelectric elements are from the same batch as the elements used in the transducer construction, see Chapter 6.

In Fig. 7.27, two measurements are compared to the simulation; measurement (1) using $V_{pp} = 2$ V, and measurement (2), using $V_{pp} = 20$ V. Both blue curves in Fig. 7.27 is measurement (1), where the solid line is extracted from the measurment using the Fourier method post-process routine (cf. Section 3.7.2), and the dashed line is extracted using the direct method for calculating V_{pp}^{rec} (cf. Section 3.7.3). The same goes for measurement (2), using red lines.

The measurement setup is given in Table 7.2, and the simulations are conducted using the `piezodiskfluid` structure (cf. Section 4.3).

Table 7.2: Measurement setup overview for Figs. 7.27 - 7.31.

Transmitting transducer:	Element # 16
Receiving transducer:	Element # 10
Generator output voltage:	(1) V_{pp} = 2 V and (2) V_{pp} = 20 V (cf. legend Fig. 7.27)

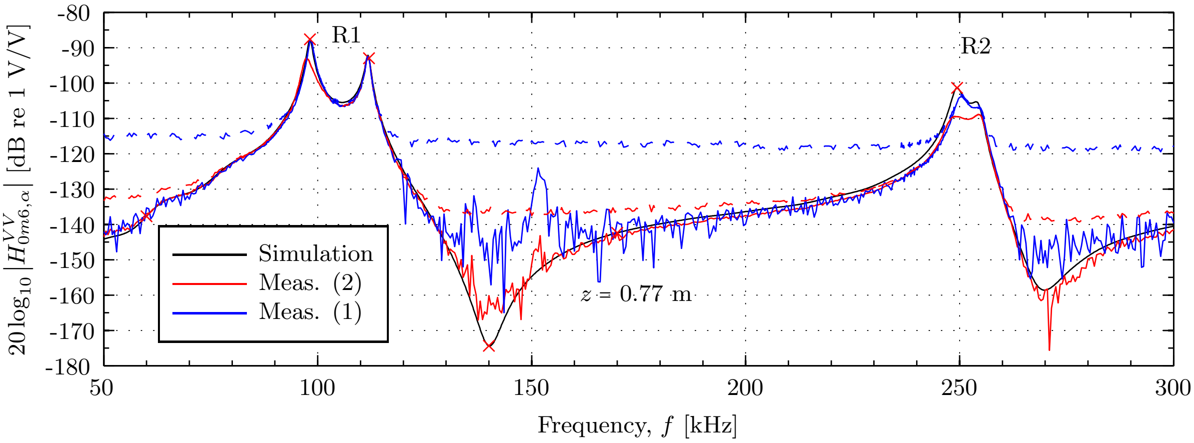

Figure 7.27: Comparison of measured and simulated $|H^{VV}_{0m6,\alpha}|$, plotted against frequency. The "×" indicates which frequencies are used for plotting the time responses below.

In Fig. 7.27, when comparing the measured $|H^{VV}_{0m6,\alpha}|$ extracted by either the Fourier or the direct method, it is seen that outside the radial modes, R1 and R2, there is much more information available in the transfer function measured using the Fourier post-process method.

It is seen that measurement (2) has good qualitative agreement with the simulation. It is shifted downwards in magnitude and frequency at the first resonance frequency at R1 (as in Fig. 7.21), and it has rapid oscillations in the dips following R1 and R2. At R2, measurement (2) is approximately 7 dB lower than the simulation. Measurement (1) has closer agreement at the resonance frequencies at R1 and R2, but has rapid oscillations and poor agreement at the dips following R1 and R2.

The recorded waveforms of V_{0m} and $V_{6,\alpha}$ are compared to time response simulations, see Section 2.8. In Figs. 7.28 - 7.31, comparisons are done for frequencies 98.2, 112, 140 and 249.4 kHz, respectively. The measured waveforms are extracted from measurement (2) of Table 7.2.

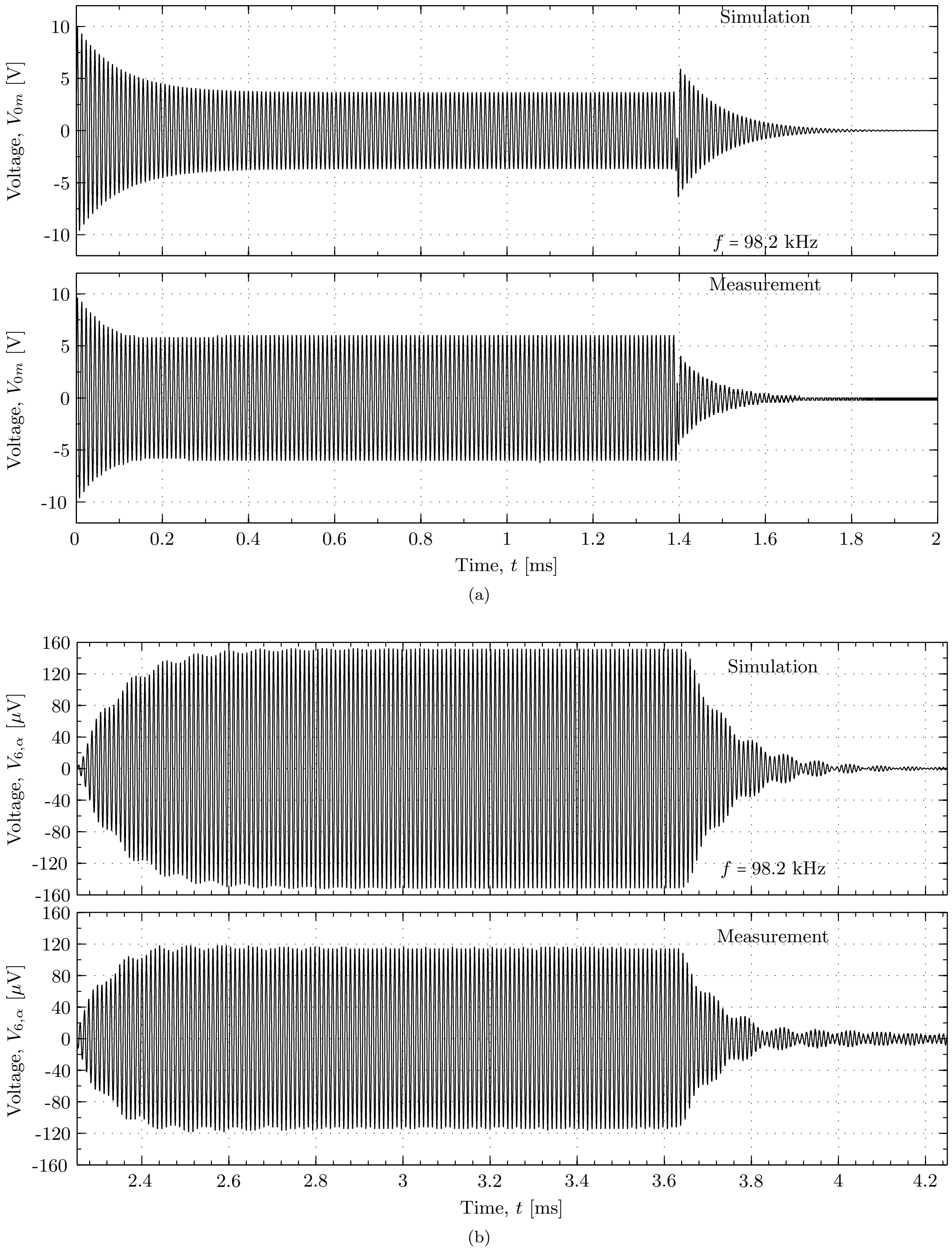

Figure 7.28: The simulated and measured waveform (V_{pp} = 20 V) of (a) V_{0m} and (b) $V_{6,\alpha}$. The measurement frequency is 60 kHz.

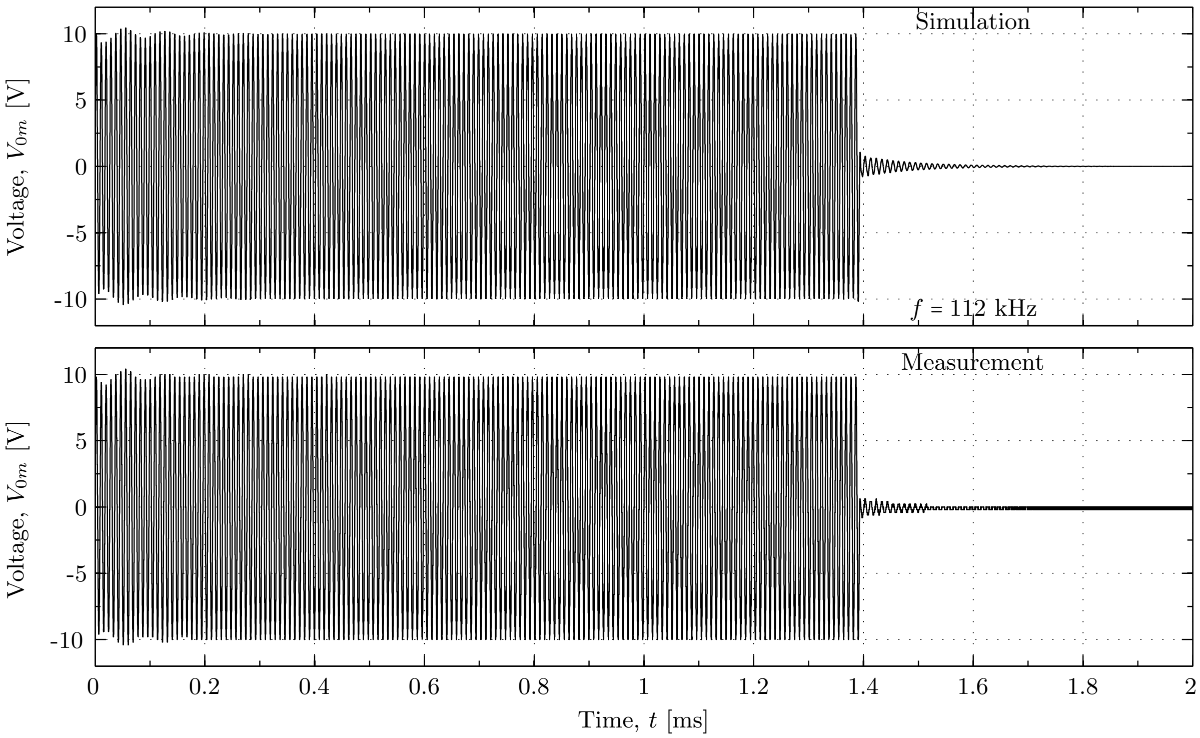

(a)

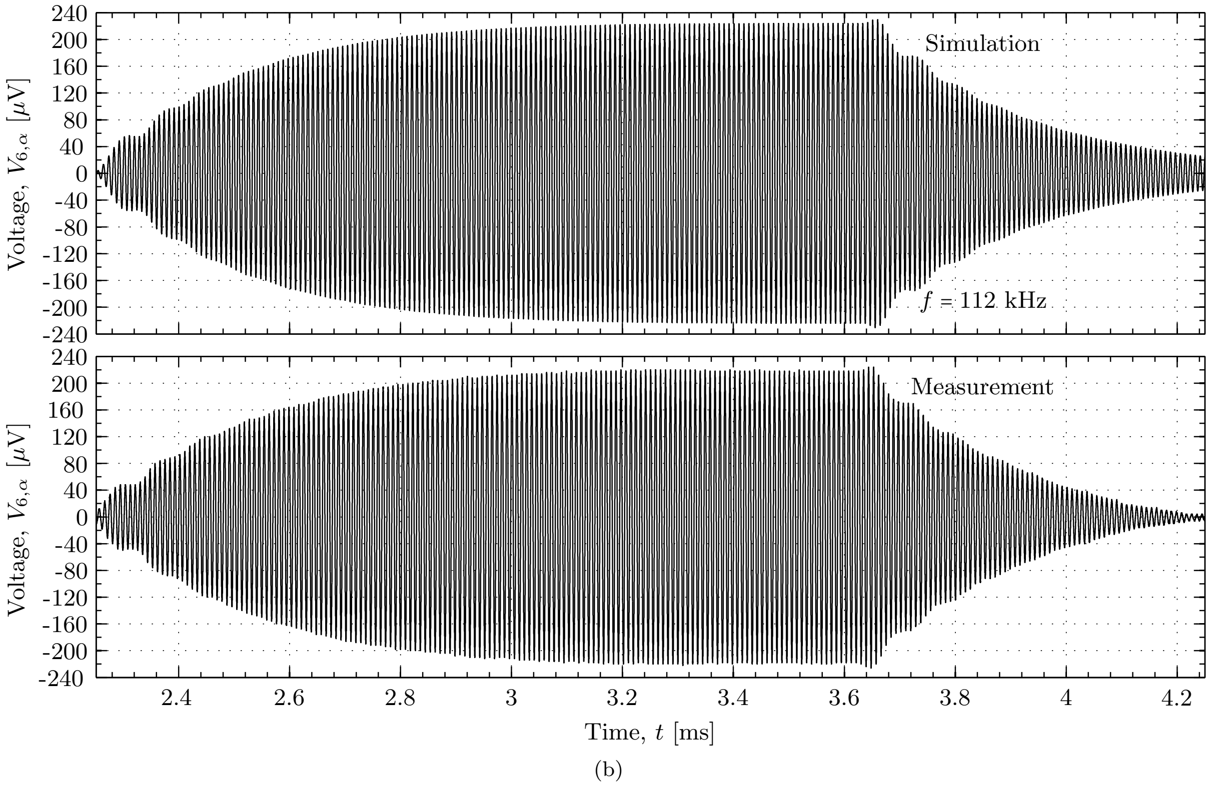

(b)

Figure 7.29: As for Fig. 7.28, but for a measurement frequency of 112 kHz.

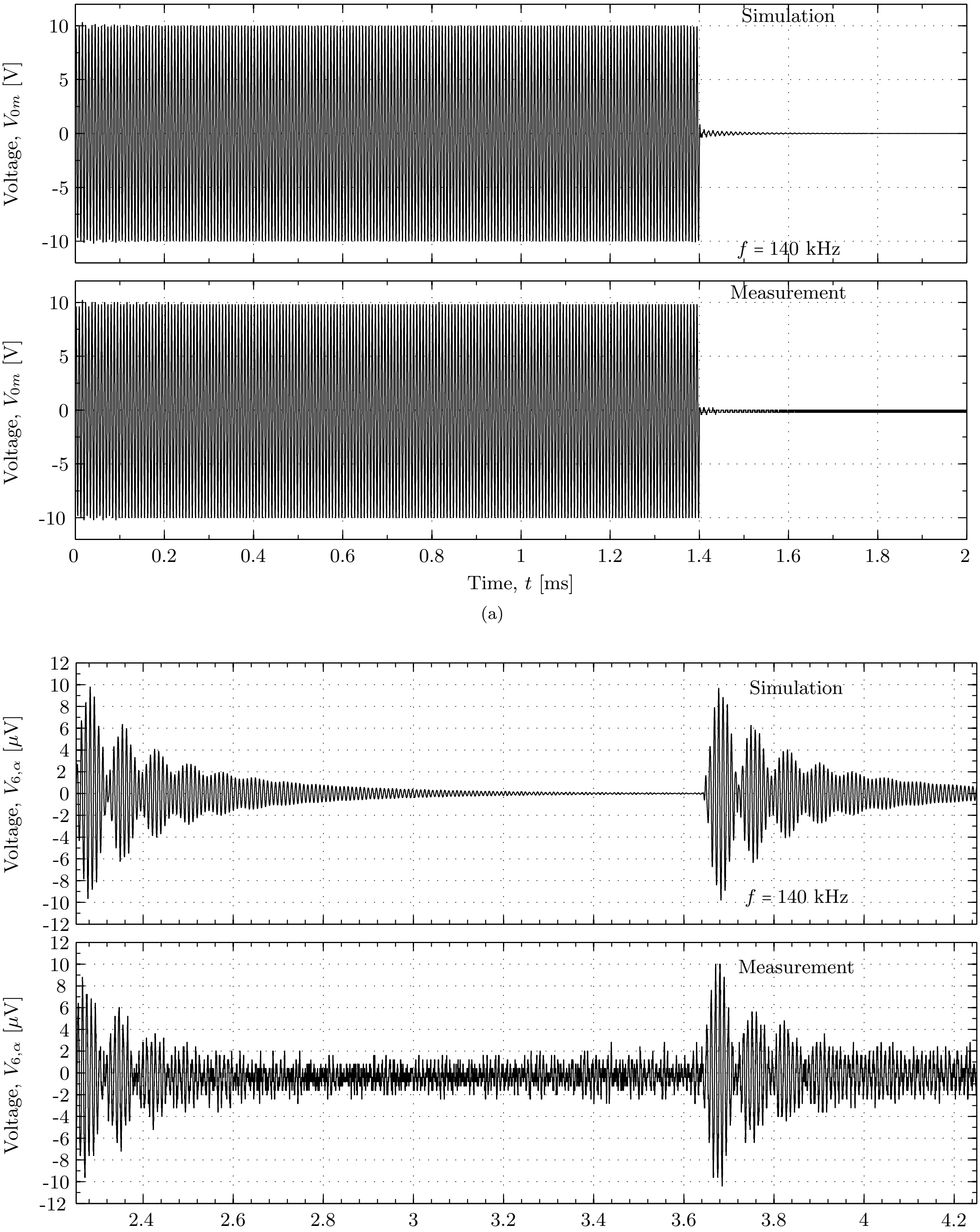

(a)

(b)

Figure 7.30: As for Fig. 7.28, but for a measurement frequency of 140 kHz.

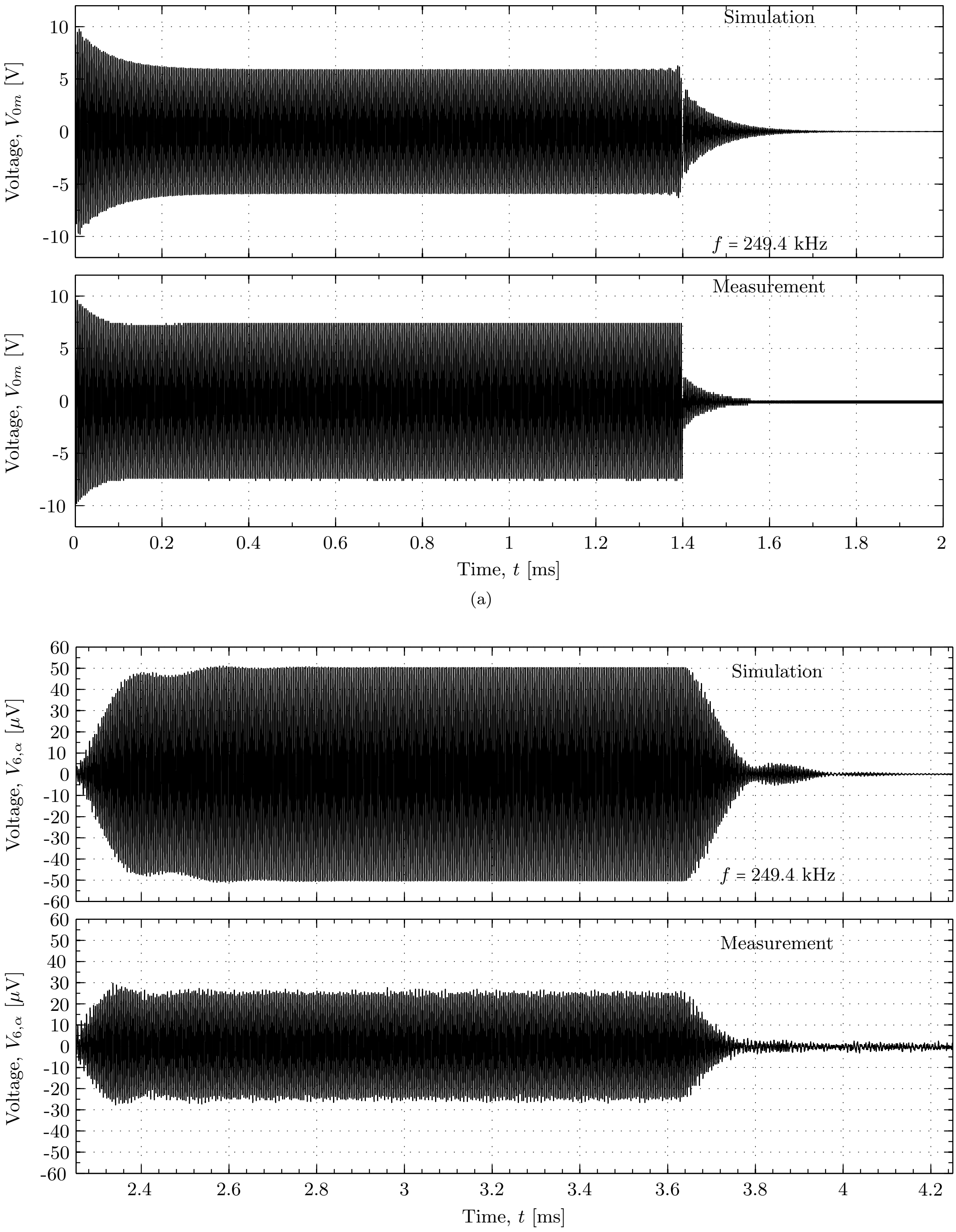

(a)

(b)

Figure 7.31: As for Fig. 7.28, but for a measurement frequency of 249,4 kHz.

For all Figs. 7.28 - 7.31, a qualitative agreement is seen, as the shape of the measured waveforms resemble the simulated waveforms. The effect of measurement noise is seen in Fig. 7.30b, which is at a $|H_{0m6,\alpha}^{VV}|$ dip (seen in Fig. 7.27). In Figs. 7.28a, and 7.31a, it can be seen that the measured V_{0m} is larger than the simulated. A close agreement between measured and simulated V_{0m} is seen in Figs. 7.29a and 7.30a.

The simulated $|S_{V,\alpha}|$ (cf. Eq. (2.51)) and $|M_V|$ (cf. Eq. (2.65)) for the transmitting piezoelectric element used in the measurement in Table 7.2, are shown in Figs. 7.32 and 7.33, respectively.

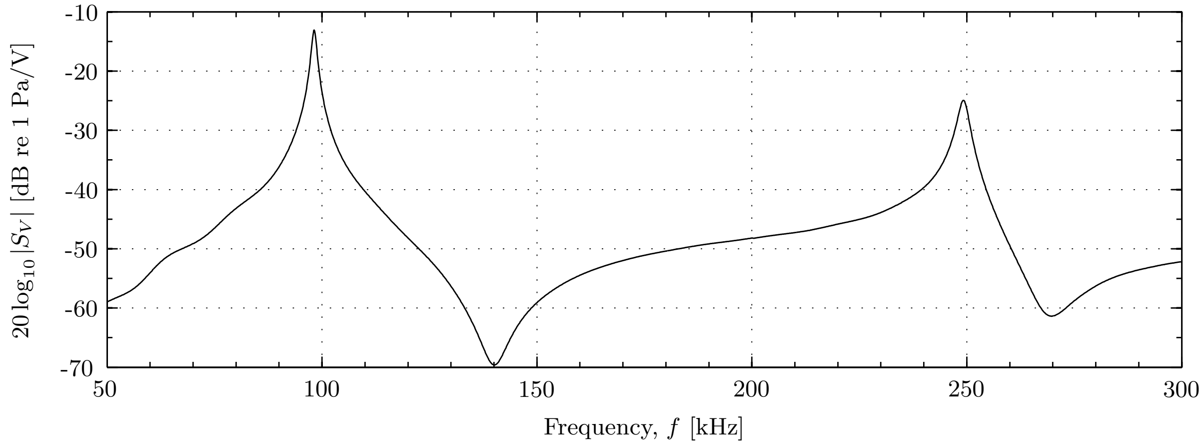

Figure 7.32: Simulated $|S_{V,\alpha}|$ for the piezoelectric ceramic disk # 16.

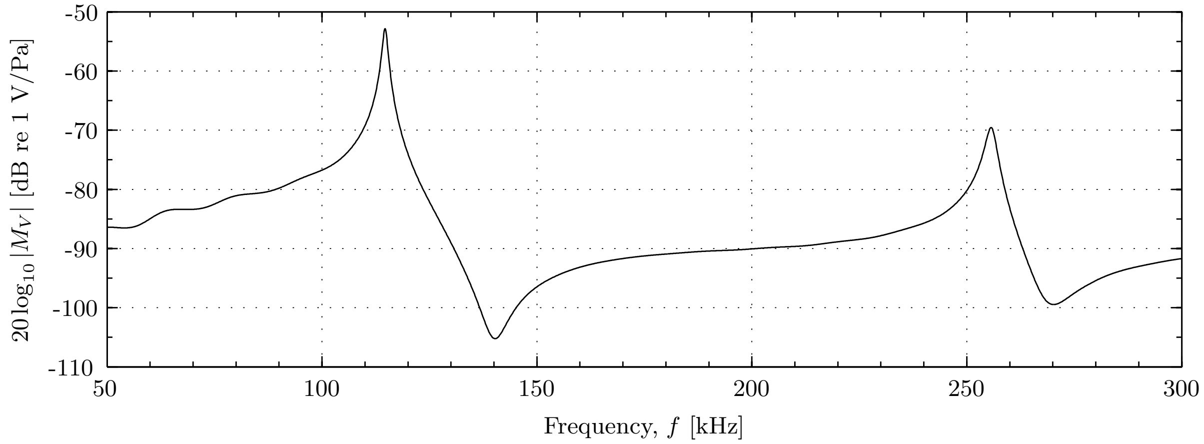

Figure 7.33: Simulated $|M_V|$ for the piezoelectric ceramic disk # 16.

It is seen that $|S_{V,\alpha}|$ has its R1 resonance frequency at 98.2 kHz, while the R1 resonance frequency for $|S_{V,\alpha}|$ is at 114.7 kHz.

In Fig. 7.34, the two measurements in Fig. 7.27 are combined. Measurement (1) is used from 90 to 119 kHz, and from 230 to 258 kHz. Measurement (2) is used from 50 to 90 kHz, from 119 to 230 kHz and from 258 to 300 kHz.

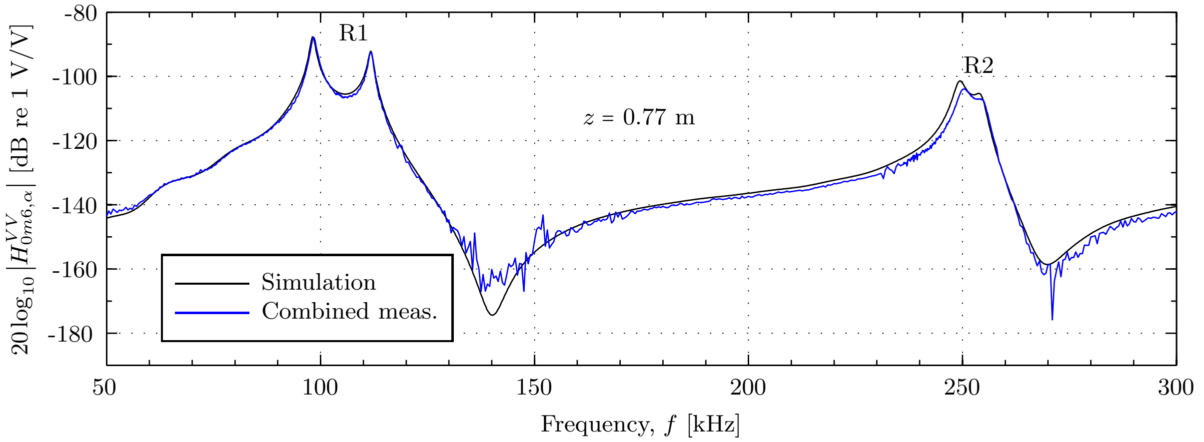

Figure 7.34: Comparison of measured and simulated $|H^{VV}_{0m6,\alpha}|$, plotted against frequency. The measurement is combined from the two measurements shown in Fig. 7.27.

In Fig. 7.34, a fair agreement is seen between the simulation and the combined measurement. Some deviation is seen in the dips at approximately 140 kHz and 270 kHz.

In the following Fig. 7.34 is used to visualize the effects of the transmitting and receiving electronics, in addition to the effect of absorption.

7.7.1 Correction effects

In Figs. 7.35 - 7.37, the effects of the cables in the transmitting and receiving electronics, i.e. Module B and F, respectively, on the voltage-to-voltage transfer function $|H^{VV}_{0m6,\alpha}|$, are shown. Fig. 7.35 shows $|H^{VV}_{0m6,\alpha}|$ calculated without including Module B or F, i.e. $|H^{VV}_{0m1}| = |H^{VV}_{5open6}| = 1$, compared to the simulated $|H^{VV}_{0m6,\alpha}|$ (simulated with all modules present). Fig. 7.36 shows $|H^{VV}_{0m6,\alpha}|$ calculated using $|H^{VV}_{0m1} = 1|$, i.e. not including Module B, and Fig. 7.37 shows $|H^{VV}_{0m6,\alpha}|$ calculated using $|H^{VV}_{5open6} = 1|$, i.e. not including Module F.

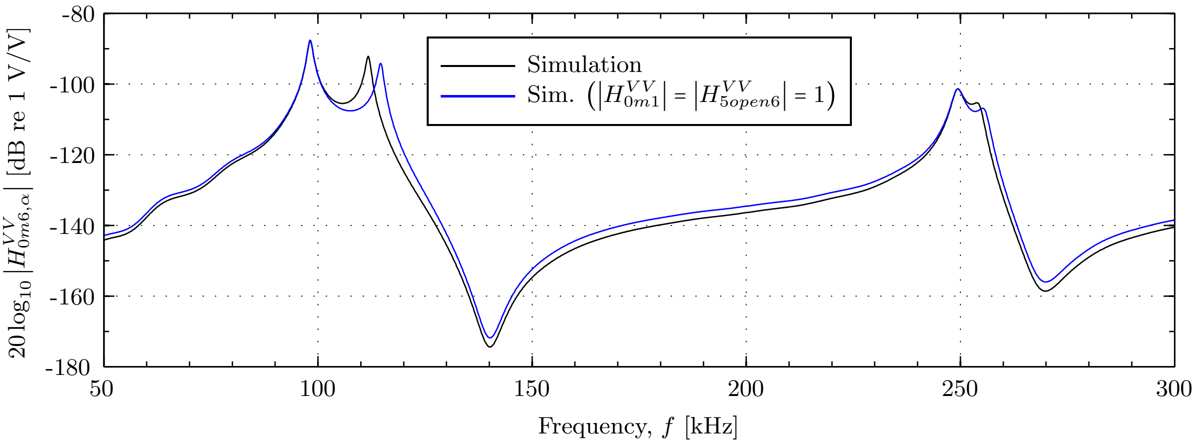

Figure 7.35: Comparison of $|H^{VV}_{0m6,\alpha}|$, calculated with and without Modules B and F.

Note that $|H^{VV}_{0m6,\alpha}|$ calculated in Fig. 7.35, using $|H^{VV}_{0m1}| = |H^{VV}_{5open6}| = 1$, has its first R1 resonance frequency at 98.2 kHz, equal to $|S_{V,\alpha}|$ (see Fig. 7.32), and the second R1 resonance frequency is at 114.7 kHz, which is equal to $|M_V|$ (see Fig. 7.33).

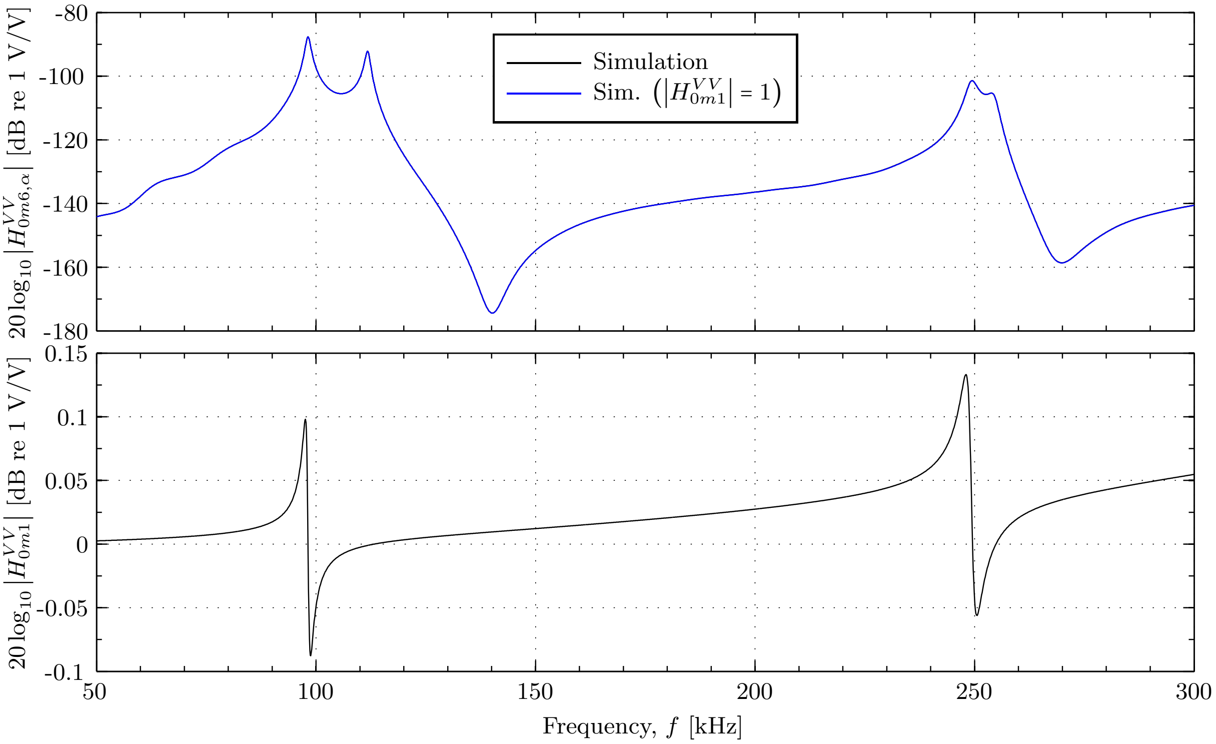

Figure 7.36: (Upper:) Comparison of $|H_{0m6,\alpha}^{VV}|$, calculated with and without Modules B, and (lower:) $|H_{0m1}^{VV}|$ plotted against frequency (as Fig. 7.1, included for visibility purposes).

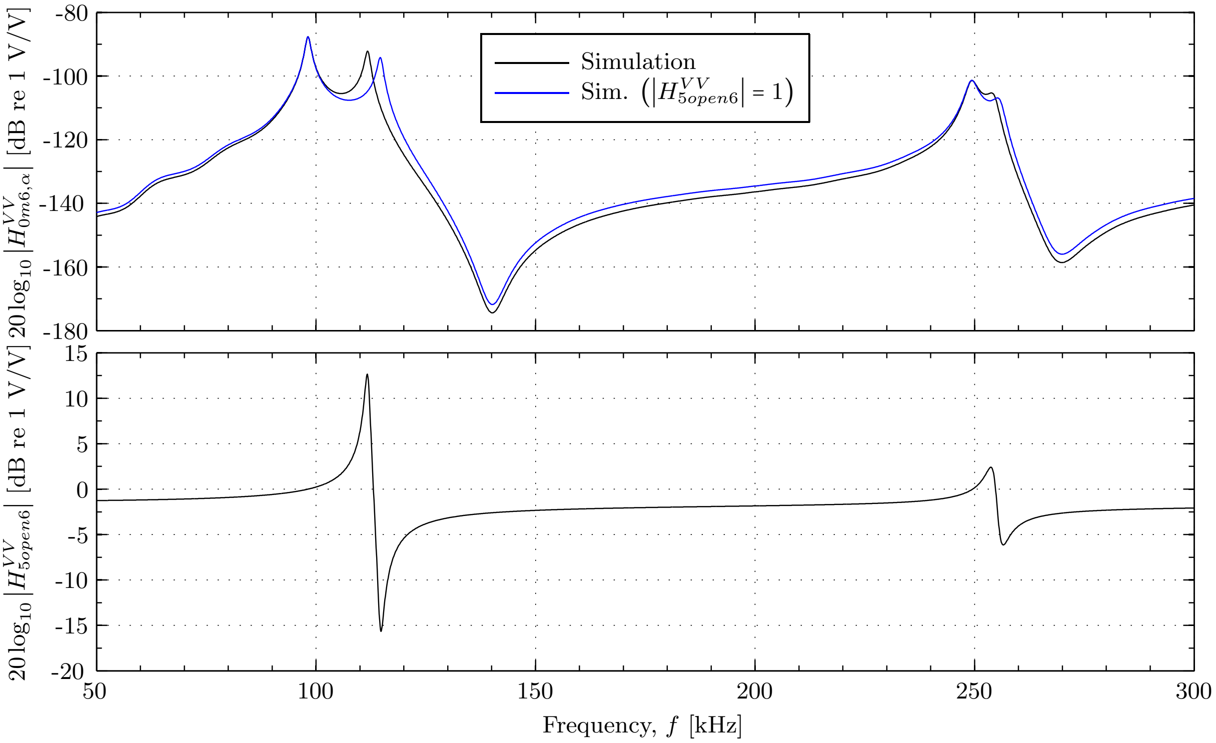

Figure 7.37: (Upper:) Comparison of $|H_{0m6,\alpha}^{VV}|$, calculated with and without Modules F, and (lower:) $|H_{5open6}^{VV}|$ plotted against frequency.

From Figs. 7.35 - 7.37, it is seen that Module F has a much larger impact on the calculated $|H_{0m6,\alpha}^{VV}|$ than Module B. The effect when omitting the Module B from the calculation is negligible. In Fig. 7.37, it is seen that when not accounting for the receiving electronics, the second peak at R1 in $|H_{0m6,\alpha}^{VV}|$ is shifted upwards in frequency. From Figs. 7.2 - 7.3, it is seen that $|H^{VV}_{5open5'}|$ is by far the largest contributor to the effect seen introduced by the receiving electronics (Module F).

Fig. 7.38 show the effect of the air absorption on the calculated $|H^{VV}_{0m6,\alpha}|$. The absorption is calculated from the environmental parameters measured in measurement (2) in Fig. 7.27.

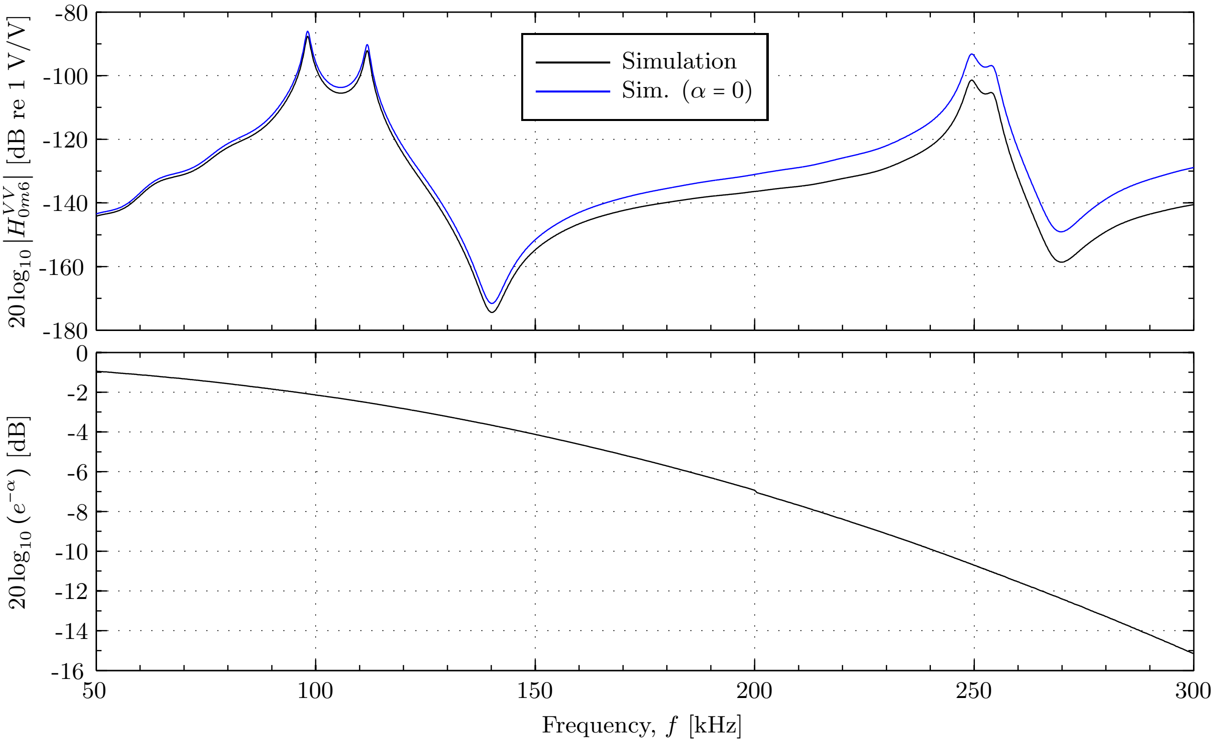

Figure 7.38: (Upper:) Comparison of $|H^{VV}_{0m6,\alpha}|$, calculated with and without the medium absorption effect, and (lower:) $e^{-\alpha}$ plotted against frequency.

In Fig. 7.38, it is seen that the air absorption increases for increasing frequency, causing $|H^{VV}_{0m6,\alpha}|$ calculated in a lossless medium to be approximately 10 dB larger at R2 than for the same function calculated with absorption effects. At R1, the effect is less than 2 dB.

7.8 Transducer to microphone

Three transducers are built in the current work; Transducer No. 1, No. 2 and No. 3, cf. Chapter 6. In this section, measurements and simulations are presented, where the constructed transducers are used as transmitters, with the B&K 4138-A-15 microphone used as receiver.

In Fig. 7.39, measurements using each of the constructed transducers as transmitter are shown. The measurement details for Fig. 7.39, is given in Table 7.3.

Table 7.3: Measurement setup overview for Fig. 7.39.

Transmitting transducer:	Transducer No. 1, No. 2 and No. 3 (cf. legend Fig. 7.39)
Receiving transducer:	B&K 4138-A-015 pressure condenser microphone
Generator output voltage:	$V_{pp} = 2$ V

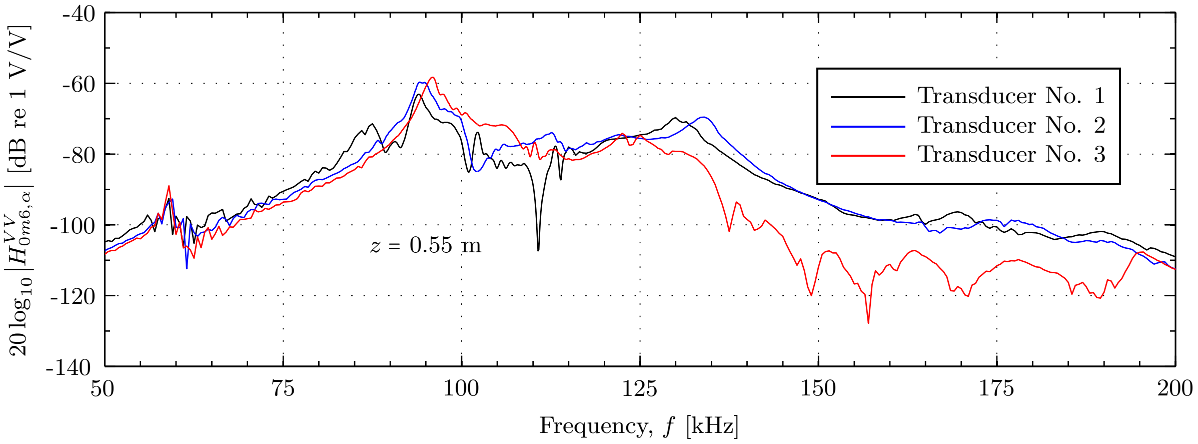

Figure 7.39: Measured $|H^{VV}_{0m6,\alpha}|$, using each of the presently constructed transducers as transmitters, and microphone receiver.

Fig. 7.39 shows that Transducer No. 1 has a narrow dip approximately at 110 kHz and 20 dB deep, which is not seen for Transducers No. 2 and No. 3. For frequencies above 125 kHz, Transducer No. 3 has a lower magnitude level than No. 1 and 2. Apart from the aforementioned differences, a qualitative agreement is seen.

Fig. 7.40 shows the simulated $|H^{VV}_{0m6,\alpha}|$ for the three transducers, using the structure `transducerfluid`, see Section 4.3.

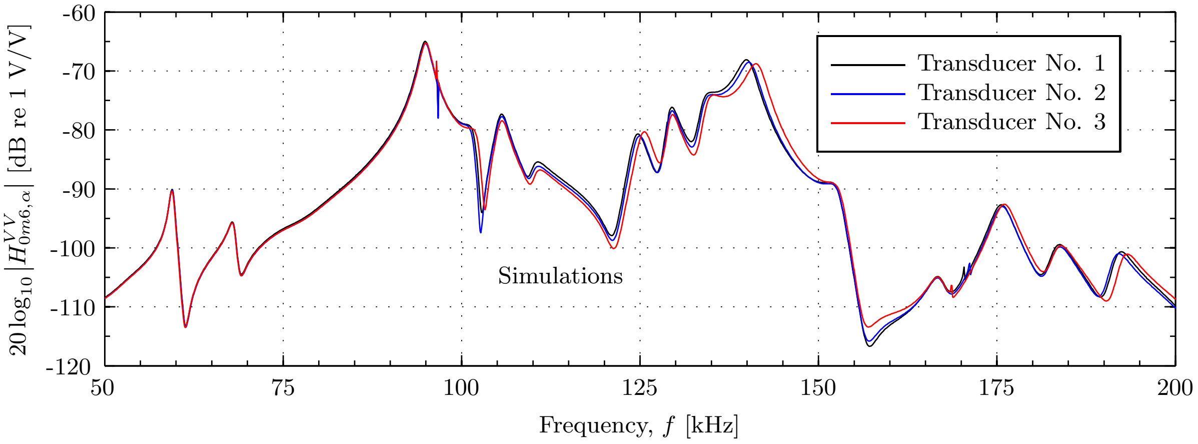

Figure 7.40: Simulated $|H^{VV}_{0m6,\alpha}|$, for each of the presently constructed transducers as transmitters, and microphone receiver.

In Fig. 7.40, it can be seen that the difference in $|H^{VV}_{0m6,\alpha}|$ expected from the simulations are quite small compared to the difference in the acoustical measurements seen in Fig. 7.39. From 50 to 100 kHz, the three simulations coincide, whereas the largest frequency shift is seen at the resonance frequency at approximately 140 kHz, where the simulation of Transducer No. 3 is shifted upwards in frequency. In general, $|H^{VV}_{0m6,\alpha}|$ for Transducer No. 3, deviates from the other two in both frequency and magnitude level, for frequencies above 100 kHz.

Figs. 7.41 - 7.43 show comparison between simulated and measured $|S_{V,\alpha}|$, for each of the three transducers, calculated from the same simulation as used in Fig. 7.40.

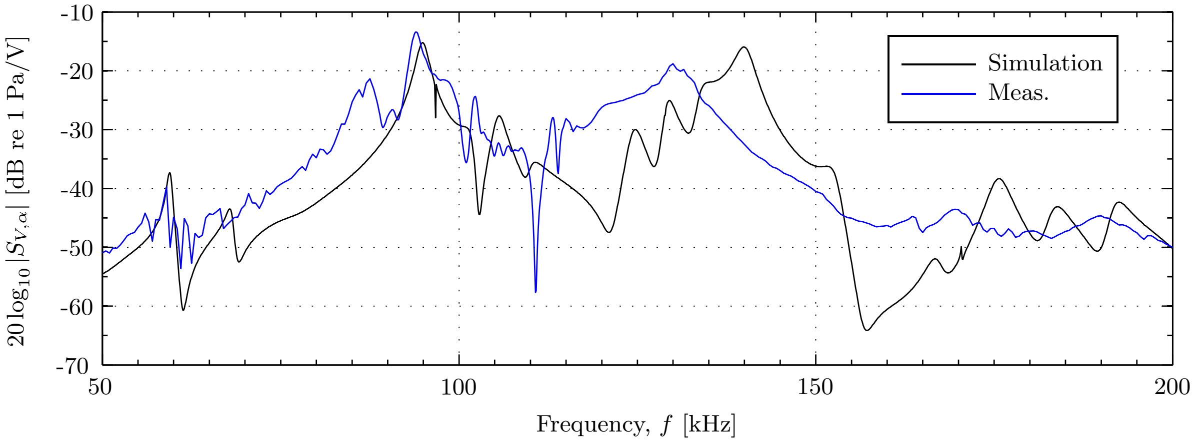

Figure 7.41: Measured and simulated $|S_{V,\alpha}|$, for Transducer No. 1 acting as transmitter, and the B&K microphone as receiver.

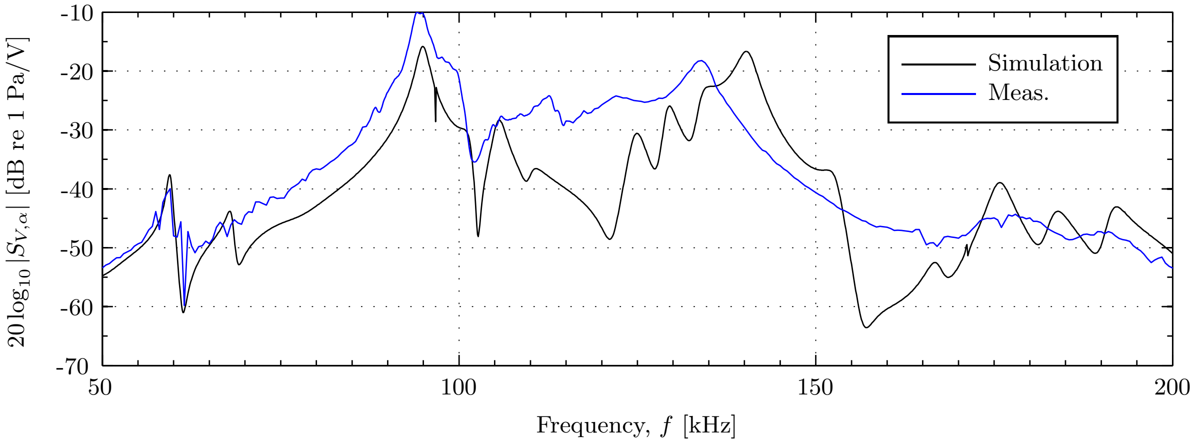

Figure 7.42: As Fig. 7.41, but for Transducer No. 2 acting as transmitter.

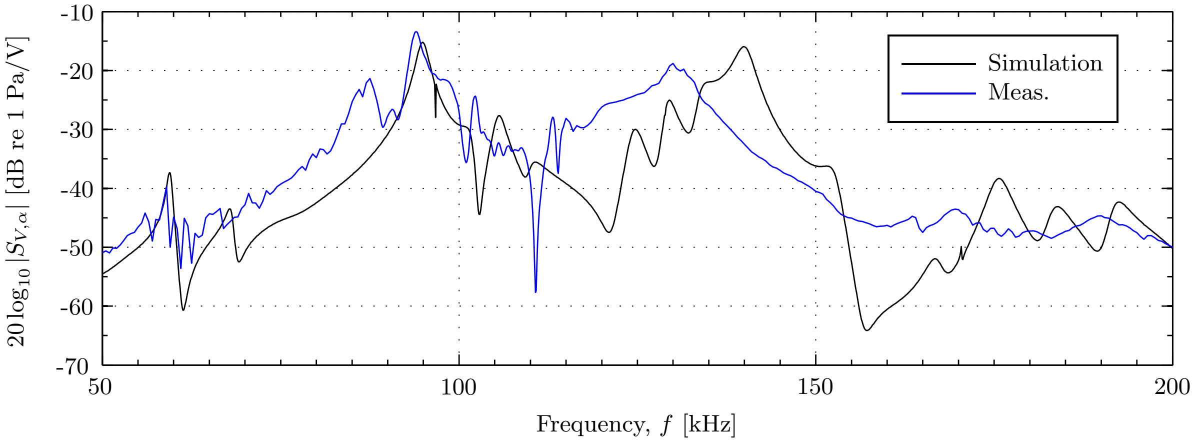

Figure 7.43: As Fig. 7.41, but for Transducer No. 3 acting as transmitter.

In Figs. 7.41 - 7.43, it is seen that there is a qualitative agreement between the measurements and simulations for the resonance peak at approx. 60 kHz. In Fig. 7.41 and 7.43, a decent agreement is seen for the resonance frequency at approx. 90 kHz. In Fig. 7.42, the shape of the resonance peak at 90 kHz is seen, but there is a disagreement in magnitude of over 5 dB. The shape of the second simulated resonance frequency in R1 (at approx. 140 kHz) is seen in the measurements for all transducers, but there is a mismatch in both frequency and magnitude.

7.9 Transducer to transducer

In this section, simulations are compared to measurements where Transducer No. 1 and No. 2 are used both as transmitter and receiver; Transducer No. 1 transmits to No. 2 in Fig. 7.44, and vice versa in Fig. 7.45. The transducers are simulated using the `transducerfluid` structure.

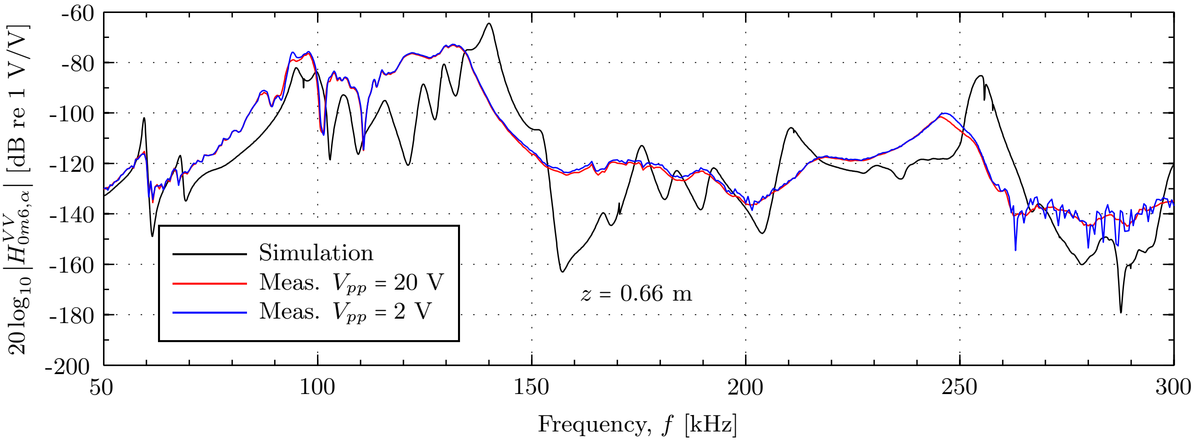

Figure 7.44: Comparison of measured and simulated $|H^{VV}_{0m6,\alpha}|$, where Transducer No. 1 is used as transmitter and Transducer No. 2 as receiver.

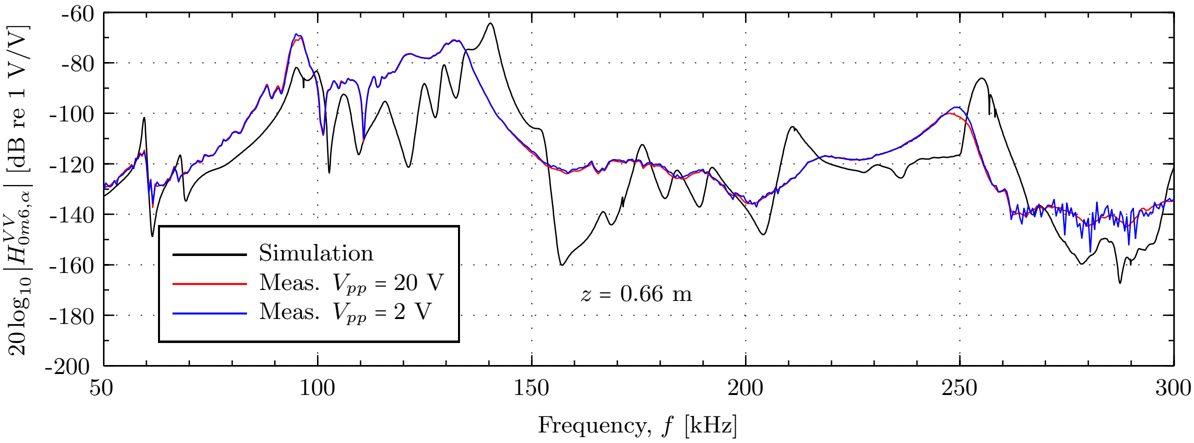

Figure 7.45: Comparison of measured and simulated $|H^{VV}_{0m6,\alpha}|$, where Transducer No. 2 is used as transmitter and Transducer No. 1 as receiver.

As in Figs. 7.41 - 7.43, the transducer to transducer cases in Figs. 7.44 - 7.45 show a somewhat qualitative agreement over the measured frequency range. The biggest disagreements are found where the simulated $|H^{VV}_{0m6,\alpha}|$ has a dip at approx. 160 kHz, and at approx. 120 kHz in the R1 mode. In general, many of the simulated peaks are also observed in the measurements, but the measured $|H^{VV}_{0m6,\alpha}|$ appears to be more "dampened" than the simulations.

Some deviations between the measurement using V_{pp} = 20 V and V_{pp} = 2 V is seen at the resonance frequencies at approx 95 and 245 kHz. Here the higher voltage measurement has a slightly lower mangitude than the lower voltage measurement.

The recorded waveforms of V_{0m} and $V_{6,\alpha}$ are compared to time response simulations, see Section 2.8. In Figs. 7.46 - 7.47, comparisons are done between the V_{pp} = 20 V measurement and simulation in Fig. 7.44, for frequencies 95 and 245.5 kHz, respectively.

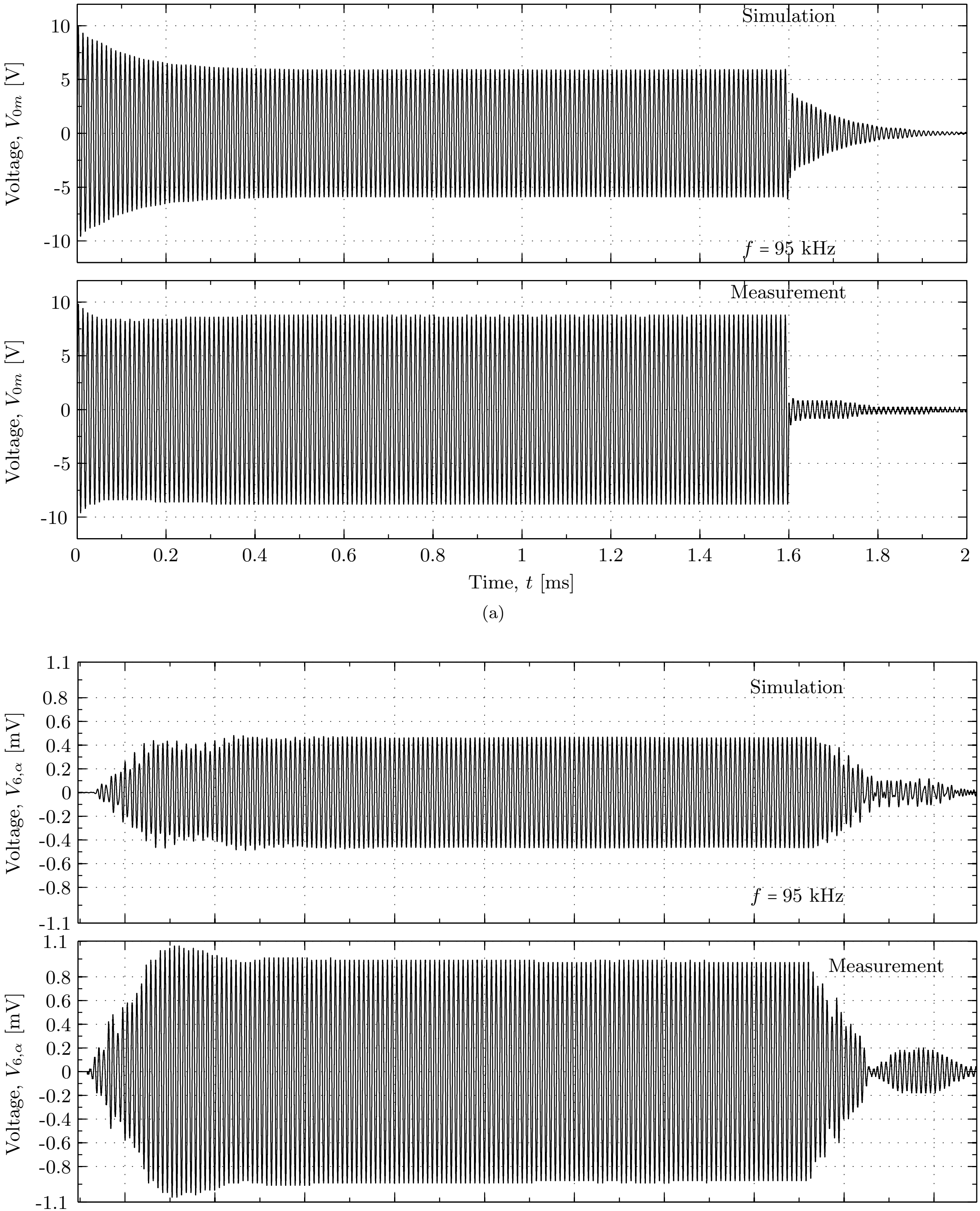

(a)

(b)

Figure 7.46: The simulated and measured waveform (V_{pp} = 20 V) of (a) V_{0m} and (b) $V_{6,\alpha}$. The measurement frequency is 95 kHz.

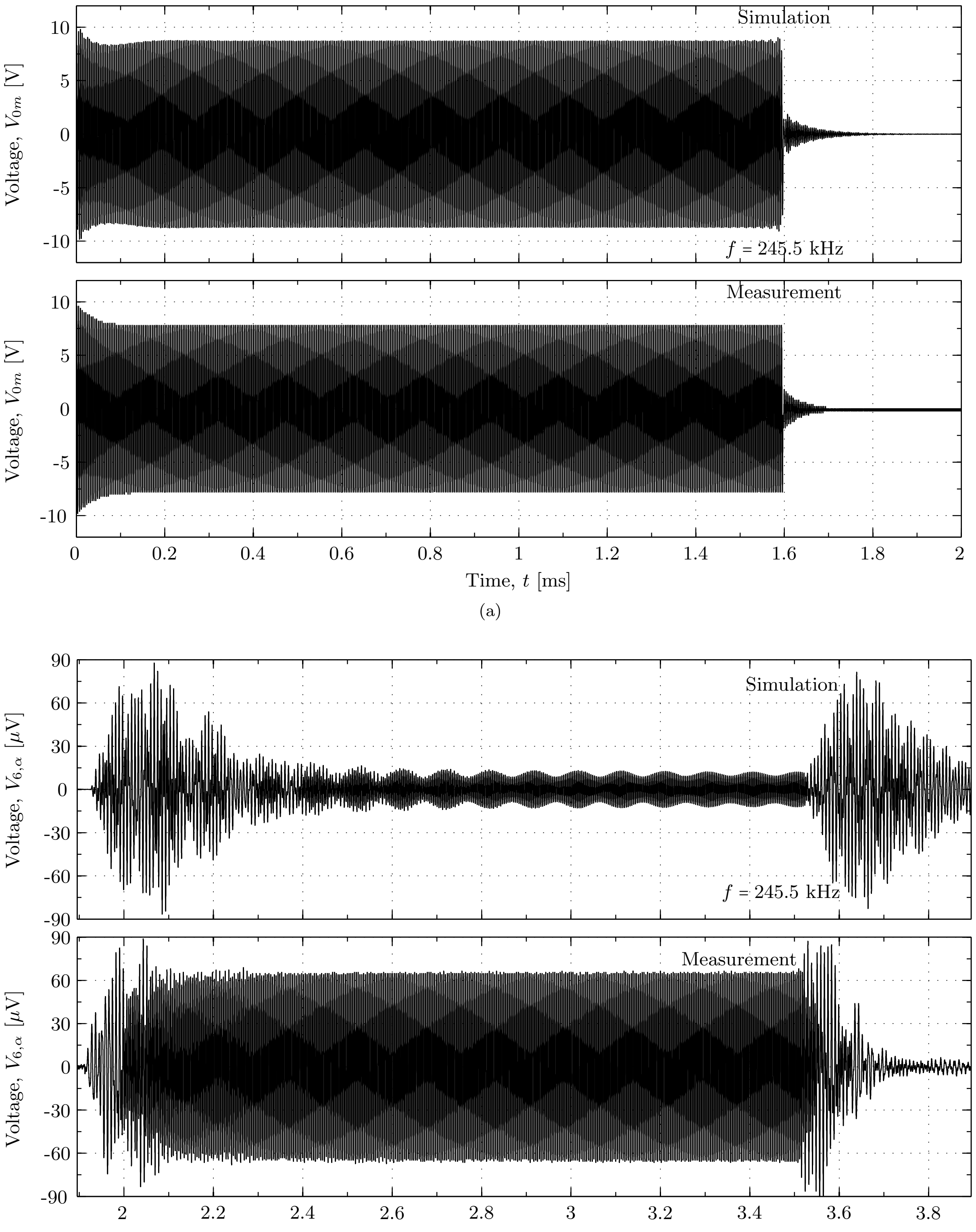

(a)

(b)

Figure 7.47: As for Fig. 7.46, but for a measurement frequency of 245.5 kHz.

In Fig. 7.46, a amplitude difference and a slight change in shape is seen between the simulated and measured V_{0m} and $V_{6,\alpha}$. The measured $V_{6,\alpha}$ has a higher amplitude than the simulated, which also can be seen at 95 kHz in Fig. 7.44

In Fig. 7.47, a qualitative agreement is seen for the shape and amplitude between the measured and simulated V_{0m}. However, a substantial difference is seen between the measured and simulated $V_{6,\alpha}$. The measured $V_{6,\alpha}$ has significantly larger amplitude than the simulated. It can also be noted that steady-state is reached shortly after the onset of the measured $V_{6,\alpha}$.

There is a time shift between the simulated and measured onset for $V_{6,\alpha}$, seen in both Figs. 7.46 and 7.47. The simulated onset is approx. 14 μs later than the measured.

Chapter 8

Discussion

In this chapter, the experimental and simulation results given in this thesis are discussed, using the theoretical background given in Chapter 2.

8.1 Measurement setup and experimental methods

Several aspects affect the acoustical and electrical measurements, e.g. positioning and aligning of the transmitter/receiver, the separation distance z, measurement noise, non-linearity and reflections. In this work, the measurement uncertainties for the acoustical and electrical measurement setups are not quantified, as it is outside the scope of this thesis.

8.1.1 Positioning

A coaxial alignment of the transmitter and receiver are assumed when calculating $H_{15}^{VV,open}$. Therefore, such an alignment is sought achieved in the measurement setup, using the methods for alignment described in Section 3.3.3. In the following, the positioning and alignment of the different types of transducers used in the current measurement setup are discussed.

Alignment

The alignment of the receiver using the two linear position stages are conducted by acoustic measurements, where the waveforms steady-state V_{pp} is manually read from the oscilloscope. Depending on the SNR for the transmit-receive combination, see Section 8.1.2, the recorded waveform varies. Accurate determination of the correct alignment is thus difficult.

As seen in Fig. 3.12, the B&K microphone are fixed in the aluminum rod by a screw. The microphones is thus steadily fastened, and moved only by the linear position stages, seen in Fig. 3.11, which alleviates the coaxial alignment of the microphone receiver.

The rotational alignment and tilting of the piezoelectric disks are done by hand, and visual inspection, aided by a laser cross leveler. This makes alignment of the elements difficult, as there is no fixed reference points for this alignment.

For transducers developed in the current work, as for the piezoelectric disks, tilting and rotational alignment are done by hand and visual inspection, aided by a laser cross leveler.

Measuring the distance z

Measurement of the measurement distance z, is done by hand, using a folding rule. This results in a increased measurement uncertainty of z, which can be reduced in further work by using e.g. a fixed ruler or laser range finder. An accuracy measurement of z is of great importance during phase measurements, and the accuracy is increasingly important for higher frequencies phase measurements.

The estimated total uncertainty in the present z measurements is ± 2 mm, which translates to a magnitude difference for $|H_{15}^{VV,open}|$ of ± 0.2 dB at R1. For a phase measurement[1] in air at 100 kHz, the uncertainty in z results in a phase measurement uncertainty of approximately ± 210°.

---

[1] Not conducted in this thesis.

8.1.2 Noise

For measurements using piezoelectric ceramic disks in air at 1 atm., with no acoustic matching to the gas, SNR is relatively low. This can be seen in Figs. 7.5 - 7.6, where for the element to microphone and element to element measurement cases, respectively. The SNR is smaller when measuring element to element, than element to microphone, as the microphone receiver is designed for use in air. This is illustrated by Figs. 7.25b and 7.30b, where measurement noise is seen affecting the latter measurement.

In Fig. 7.9, the element to microphone configuration is compared to transducer to microphone. There it is seen that the SNR magnitude is quite similar at R1, but the transducer R1 mode has a larger frequency area.

For the transducer to transducer case, a relatively high SNR is seen for a larger frequency area at R1 than for element to element.

To improve the SNR, a frequency filter is applied to the received voltage signal, and the recorded signal is averaged in the oscilloscope using 128 recorded waveforms. The SNR is also improved by increasing the driving voltage to the transmitting transducer, as seen in Figs. 7.5 - 7.8, where the SNR is increased between 15 and 20 dB, when increasing V_{pp} from 2 to 20 V, depending of the transmitter/receiver case.

The post-process routine for extracting the received peak-to-peak voltage, V_{pp}^{rec}, is also seen to be important. This is illustrated well in Fig. 7.27, where the Fourier method (cf. Section 3.7.2) yields much more information in areas where the direct method (cf. Section 3.7.3) is buried in noise.

8.1.3 Non-linearity

The system models derived in Chapter 2 are assumed to be linear. However, most physical systems are inherently non-linear in nature. Observation of an effect in the measurements, not seen in the simulations, which is caused by non-linearity, is thus expected. The non-linear effect is expected to be greater for higher excitation values of the physical system, i.e. higher excitation voltage.

In Fig. 7.21, an effect is visible for the piezoelectric disk acting as transmitter, and the B&K microphone as receiver. At R1, it is seen that the higher excitation voltage (V_{pp} = 20 V) measurement deviates from the lower voltage (V_{pp} = 2 V) measurement and the FE simulation. This is probably due to the inherent non-linear effects in the piezoelectric disk transmitter.

In Fig. 7.27 the difference between the higher voltage and lower voltage measurement is visible at the first resonance peak at R1, and at the R2 resonance frequencies, but not at the second resonance frequency at R1. The first R1 resonance frequency in $|H_{0m6,\alpha}^{VV}|$ is associated with the radiation of the transmitting transducer, and the second resonance frequency with the reception of the signal. The reason can be seen when the transmitting and receiving electronics are omitted from the calculation of $|H_{0m6,\alpha}^{VV}|$ (see. Fig. 7.35), where it is seen that the first and second R1 resonance frequencies coincides with the R1 resonance frequencies of $|S_{V,\alpha}|$ (see Fig. 7.32) and $|M_V|$ (see Fig. 7.33), respectively.

Thus, it appears that the non-linear effects seen in $|H_{0m6,\alpha}^{VV}|$ at the first resonance frequency of R1, is associated with non-linear effects in the transmitting transducer, due to the voltage it is excited with. The lack of visible non-linear effects for the second peak in R1 is probably due to the relative low excitation[2] of the receiving transducer, which causes non-linear effects which is not observable with the current accuracy.

For the transducer to transducer case, i.e. the constructed piezoelectric transducer acting both as transmitter and receiver, experimental results are given in Figs. 7.44 - 7.45. An effect similar as in the element to element case is seen at R1 and R2, approx. 95 and 245 kHz, where the higher voltage measurement is deviating from the lower voltage measurement. The magnitude of this effect is approx. half of that seen for the element to element, i.e. it appears that there is less non-linear effects when the constructed transducers are utilized.

8.1.4 Cables and electronics

In Fig. 7.2, it is seen that cable #3, connecting the receiver to the amplifier, is expected to have the largest impact on the propagating signal through the system. $|H_{5open5'}^{VV}|$ is several orders of magnitude larger than $|H_{0m1}^{VV}|$. For both $|H_{5open5'}^{VV}|$ and $|H_{0m1}^{VV}|$, it is seen that when using a constructed transducer as transmitter/receiver, the cable effect is smaller than when using elements. This is due to the difference in Z_T between the constructed transducers and the elements, since Z_T is the quantity representing the transmitting/receiving transducer when calculating $|H_{5open5'}^{VV}|$ and $|H_{0m1}^{VV}|$, as seen in Section 2.6.

---

[2] The receiver has an output voltage at the second resonance peak in R1 of about 120 μV in the calculation area, see Fig. 7.29b.

The transfer function $|H^{VV}_{gen1}|$ is shown in Fig. 7.4. Around R1 and R2, the transmitting transducers electrical impedance decreases, thus decreasing V_1. The effect is seen to be larger when using elements as transmitter, than when using the constructed transducer.

8.1.5 Distance/reflections

The measurement distance z influences the measurements in several ways; an increase in z will e.g. (1) decrease SNR, (2) enable for longer bursts without standing waves occurring between the transmitter and receiver, and (3) make an accurate alignment of the transmitter and receiver harder to accomplish.

The measurement distances chosen for the different transmit-receive combinations, are sought to balance these factors. However, physical limitations in the measurement setup might interfere, e.g. for the element to element transmit-receive case, where long transients is observed before steady-state is reached. To enable for longer bursts, the distance is set to 77 cm, which is the maximum distance available in the present measurement setup. If the measurement setup had the possibility of higher z, better steady-state areas could have been reached for more frequencies, at the expense of SNR.

8.2 FE modeling

In this work, the FE modeling tool FEMP is used for modeling of the piezoelectric transmitting transducer and the sound field.

Stationary signals are calculated in the current implementation of FEMP , i.e. the transients of a signal can not be modeled. This introduces a simplification compared to the experiments, where a burst with both transients and steady-state is measured.

Infinite elements are used in the present work, and no physical receiver is used, which means that no reflecting or standing waves are modeled. Precautions are taken in the measurement setup to reduce standing waves and reflections from other surfaces, but some reflected waves are assumed to be measured.

The accuracy of the FE simulations is limited by the uncertainty in the complex elastic, dielectric and piezoelectric material data of the piezoelectric ceramic, and different elastic materials used. In several cases, not all the material data needed in order to simulate a material are given, and estimates have to be made. An adjusted data set for the material Pz27 is used in this work, which is determined experimentally to fit with a certain batch of Pz27 elements.

In addition, the accuracy is dependent on the number of elements per wavelength in the mesh. The number of elements per wavelength is here chosen as a compromise between calculation time and accuracy [46].

8.3 Transducer construction

Piezoelectric transducer structures are built (cf. Chapter 6), in order to presumably increase the bandwidth and sensitivity, compared to using a single piezoelectric ceramic disk transducer.

Three transducers are built, in order to conduct the three-transducer reciprocity calibration in [2]. In Figs. 7.39 and 7.40, it is seen that the measured $|H^{VV}_{0m6,\alpha}|$ for the transducer to microphone case, shows a significantly greater difference between the three transducers than the simulated. The difference in response for each transducer is mainly due to the assembly process, as the same materials and dimensions are used for all transducers. Effort has been made to ensure a similar assembly process for each transducer, but practical difficulties during the process has probably resulted in differences in the transducers, affects their performance in an acoustical measurement situation. Above all, it was hard to obtain an even thickness of the conductive epoxy glue, attaching the piezoelectric element to the matching layer, and the matching layer to the transducer housing

Since the backing layer is not attached to the piezoelectric element in the transducer, it is possible that there is a small gap between the backing and element on some transducers, which might effect the response of the transducer.

8.4 System models

Two equivalent system models are derived in Chapter 2; *Model 1*, *Model 2A* and *Model 2B*. These are based on the same assumptions, but might differ due to the differences in implementation of each model. This is seen in Figs. 7.19 and 7.20, where a disagreement between the models is seen in the dips in Fig. 7.19, and for small z in Fig. 7.20.

One reason for the deviation between the models is the different implementations of the diffraction correction. *Model 1* uses Khimunin's diffraction correction, where a piston source is assumed, whereas *Model 2A* uses the relative diffraction correction $R^{dif}(z)$ *formulation A*, where the averaged free-field sound pressure over the receiver, calculated in FEMP is used. *Model 2B* utilizes $R^{dif}(z)$ *formulation B*, which is Khimunin's diffraction correction at distance z relative to the diffraction correction at distance z_∞. Thus, it is expected that *Model 2A* is the most accurate for small z, as near-field effects from a full transmitting transducer are modeled in FEMP.

In Fig. 7.12 it is seen that the largest deviation between $R^{dif}(z)$ *formulation A* and *formulation B* is at the frequencies corresponding to the dips in Fig. 7.19. But the model which deviates the most from the others in the dips is *Model 2B*, which is unexpected since both *Model 2B* and *Model 1* utilizes Khimunin's diffraction correction.

Different assumptions have been made about M_V in *Model 1* and *Model 2A* and *2B*. In *Model 1*, M_V is assumed to be independent of the axial distance z, both for the relatively general and the plane waves propagation model. In *Model 2A* and *2B*, it is assumed that M_V is independent of the axial distance z, for near-field and far-field, where it is assumed that $\langle p_4(z_\infty)\rangle \approx p_4(z_\infty)$.

In this work, M_V is calculated using the spherical reciprocity factor, J, see Section 2.5. When using J, the transmitting and receiving transducer are assumed to be equal, linear, passive and reversible, in addition to fulfilling certain reciprocity factors. The electrical measurements in Figs. 7.13 - 7.18 show that although the electrical characteristics of the elements are similar, they are not equal. The electrical and acoustical comparisons between the constructed transducers also show an internal difference between them. Hence, the assumption of the transmitter/receiver being equal is a simplification. As discussed in Section 8.1.3, non-linear effects are observed when using both the piezoelectric elements and the constructed transducers, thus the assumption of the transducers being linear is also a simplification.

Comparison with measurements

The agreement between the simulations and experiments is seen to depend on which transmitter/receiver configuration is used.

For the element to microphone case, see Fig. 7.21, a qualitative agreement is seen up to 140 kHz. At R1, a fair agreement is seen between the lower voltage measurement and the simulation, where the non-linear effect is small. After 130 kHz, some deviations are seen, which might be caused by the calibrated M_V for the microphone, where frequency response data are given up to 200 kHz, but the stated frequency range from the manufacturer is up to 140 kHz. Bear in mind that the microphone transducer is not modeled in the system model, but represented by the calibrated M_V (cf. Section 3.5.1). The measured and simulated time-domain waveforms of V_{0m} and $V_{6,\alpha}$ for the element to microphone configuration is seen in Figs. 7.23 - 7.26. Here, a qualitative agreement is seen for the waveforms at 98,2 and 170 kHz, whereas a good agreement is seen for frequencies 60 and 140 kHz.

For the element to element configuration, the two measurements in Fig. 7.27, extracted using the FFT post-process routine (the solid lines), is seen to have a fair agreement when compared to the simulation. However, non-linear effects are seen at the two R modes for the V_{pp} = 20 V measurement, and the V_{pp} = 2 V measurement is distorted by the low SNR at the dips (approx. 140 and 270 kHz). A cleaner view of the agreement between simulation and measurements for $|H^{VV}_{0m6,\alpha}|$ is seen in Fig. 7.34, where the two measurements displayed in Fig. 7.27 are combined. The effect of a relatively low SNR are still seen in the dips at approx. 140 kHz and 270 kHz, but a fair agreement is seen elsewhere.

Time domain plots of V_{0m} and $V_{6,\alpha}$, for the element to element configuration are shown in Figs. 7.28 - 7.31. It is seen that the shape of the measured signals are simulated reasonably well for the chosen frequencies, while the amplitude agreement of $V_{6,\alpha}$ depends on the agreement between measured and simulated $|H^{VV}_{0m6,\alpha}|$ at the respective frequencies.

In Figs. 7.13 - 7.18, a good agreement is seen between the measurements and simulations of G_T and B_T, for the element to element case.

The magnitude of the measured transmitting voltage response $|S_{V,\alpha}|$, is in Figs. 7.41 - 7.43 compared to simulations using the transducer to microphone configuration. A qualitative agreement between measurements and simulations is seen at best. Some of the simulated resonance peaks are also visible in the measurements, with some agreement in frequency area and magnitude of the peak.

In Figs. 7.44 - 7.45, measured $|H^{VV}_{0m6,\alpha}|$ using either Transducer No. 1 or No. 2 as transmitter/receiver is compared to simulated $|H^{VV}_{0m6,\alpha}|$. As for the transducer to microphone case, a qualitative agreement are seen in some frequency areas, and the measured $|H^{VV}_{0m6,\alpha}|$ appears to be more "dampened" than the simulated.

Electrical measurements and simulations of the constructed transducers are compared in Figs. 6.13 - 6.15, where a qualitative/decent agreement is seen at the first radial mode and a even better agreement at the second radial mode. The simulations are performed without fluid loading (vacuum), and without backing layer and housing lid. It is evident that the electrical characteristics of the constructed transducer are simulated more accurately when comparing to measurements, than $|H_{0m6,\alpha}^{VV}|$, measured in the acoustical measurement setup. This might be caused by the implementation of the transmitter/receiver modules, using the constructed transducer, into the system model, which might introduce errors in the modeled $|H_{0m6,\alpha}^{VV}|$.

Chapter 9

Conclusions

A model for a linear and axisymmetric ultrasonic transmit-receive measurement system is developed, based on 3D FE modeling of the piezoelectric transmitting transducer and sound propagation in the fluid medium, combined with spherical reciprocity for description of the receiving transducer. The medium is air at 1 atm. and room temperature. Transmission-line modeling is used to model the cables connecting the transmitting and receiving electronics, where a significant effect for some cables are observed. Simulation of signal propagation in time and frequency domain is enabled, and near-field and diffraction effects are accounted for.

Comparison between experiments and simulations are conducted in an experimental setup for acoustical measurements. The measurement setup is further developed in this work.

The FE modeling tool FEMP 5.0 is used for modeling of the transmitting transducers radiation, and the resulting sound field in a fluid medium. Piezoelectric ceramic disks and transducer structures are both modeled, and utilized in the experimental setup.

To presumably increase the sensitivity and bandwidth of a piezoelectric element radiating into air, two types of matching layer materials are acquired. Due to lack of material data for one of the materials, sound speed and density measurements are conducted for both. The measurements are compared to the values given/suggested by the manufacturer, where an inconsistency larger than the given uncertainty is seen.

Piezoelectric transducer structures are built to presumably increase the sensitivity and bandwidth compared to a single piezoelectric ceramic disk. FE modeling was used in the design process, to optimize the transducers for use at the first radial mode. Three transducer are constructed, in order to conduct the three transducer reciprocity calibration in [2]. Although the same assembly process method was used on the three, comparison between electrical and acoustical measurements showed considerable differences. The agreement between electrical simulations and measurement was better than for the simulations and measurements conducted in the acoustical measurement setup.

Results for simulations and measurements of the magnitude of the voltage-to-voltage transfer function, $|H^{VV}_{0m6,\alpha}|$, are compared, for frequencies up to 300 kHz, covering the two lowest radial modes of the transmitters used. A fair agreement is seen when using the piezoelectric ceramic disks as transmitter and receiver. The agreement between the constructed transducers is seen to be qualitative at best.

Suggestions for further work

The measurement distance z between the transmitter and receiver is in this work measured by hand. A fixed holder would decrease the measurement uncertainty of this measurement. In addition, a rigid holder for the piezoelectric elements in the acoustical measurement system, with a fixed reference point for alignment, would simplify the alignment procedure of the elements, and increase its accuracy.

The assembly process might be further developed to ensured a more consistent result for the acoustical measurements done with each of the transducers. Different dimensions, design, and materials for the backing- and matching layers and housing, might prove beneficial both in the assembly process and for the consistency and performance of the transducers.

Improving the SNR in the measurement setup, either by reducing the measurement noise, or by increasing the signal strength, could enable for phase measurements. If the signal onset of the transmitted and received signal can be determined, and the distance between the transmitter and receiver is known, the phase can be calculated. This can be done e.g. by examining corresponding steady-state periods in the transmitted and received signal, extracting a time-difference which can be related to the expected time difference by knowledge of the sound speed in the medium.

The system models can be calulated using SFDC, rather than Khimunin's diffraction correction, thus accounting for the radiation of a full transmitting transducer. In this thesis, $\langle p_4(z) \rangle$ is simplified as the free-field sound pressure averaged over the front of a receiver, without the receiver present. In future works, this might be calculated by averaging the sound pressure over the whole surface of the receiver, and with the receiver present, giving a more general solution.

The accuracy of FEMP can be improved by use of more accurate material data. In addition, modeling of the complete transducer structure in a fluid medium is desirable in order to account for the fluid loading effects on the transducer.

Bibliography

[1] E. Storheim, PhD thesis, Department of Physics and Technology, University of Bergen, Bergen, Norway (in preparation, 2013).

[2] E. Mosland, “Reciprocity calibration method for ultrasonic piezoelectric transducers in air.”, Master’s thesis, Department of Physics and Technology, University of Bergen, Bergen, Norway (2013).

[3] ”Regulations relating to measurement of petroleum for fiscal purposes and for calculation of CO2 tax”, Norwegian Petroleum Directorate, Stavanger, Norway (2001).

[4] ”AGA Report no. 9. Measurement of gas by ultrasonic meters. 2nd revision”, American Gas Association, Transmission Measurement Committee, Washington DC, U.S.A. (2007).

[5] ”Measurement of fluid flow in closed conduits - Ultrasonic meters for gas - Part 1: meters for custody transfer and allocation measurement. ISO 17089-1:2010”, International Organization for Standardization, Geneva, Switzerland (2010).

[6] ”GERG project on ultrasonic gas flow meters, Phase II. GERG Technical Monograph TM11 2000.” Lunde, P., Frøysa, K.-E., Vestrheim, M., editors. Groupe Européen de Recherches Gazières (GERG). Düsseldorf: VDI Verlag (2000).

[7] K.-E. Frøysa and P. Lunde, “Density and calorific value measurement in natural gas using ultrasonic flow meters”, in *Proceedings of the 23rd International North Sea Flow Measurement Workshop, Tønsberg, Norway, 18-21 October 2005* (2005).

[8] K.-E. Frøysa, P. Lunde, A. Paulsen, and E. Jacobsen, “Density and calorific value measurement of natural gas using ultrasonic flow meters. Results from testing on various North Sea gas field data”, in *Proceedings of the 24th International North Sea Flow Measurement Workshop, St. Andrews, Scotland, 24-27 October 2006* (2006).

[9] P. Norli and P. Lunde, “A three-way pulse method for a precision sound velocity measurement cell”, in *Proceedings of the 2006 IEEE Ultrasonics Symposium, Vancouver, Canada, 3-6 October, 2006*, 888–893 (2006).

[10] P. Lunde, P. Norli, M. Vestrheim, and R. A. Kippersund, “Precision sound velocity cell as reference for gas quality measurement in ultrasonic flow meters. Preliminary results using two candidate methods with argon at low pressure”, in *Proceedings of the 30th Scandinavian Symposium on Physical Acoustics, Geilo, Norway, January 28-31, 2007* (2007).

[11] E. Storheim, P. Lunde, and M. Vestrheim, “Diffraction Correction in Ultrasonic Fields for Measurements of Sound Velocity in Gas. Conventional and Alternative Methods”, in *Proceedings of the 34th Scandinavian Symposium on Physical Acoustics - Geilo 30th January - 2nd February* (2011).

[12] E. Storheim, P. Lunde, and M. Vestrheim, “Diffraction correction for precision measurements of sound velocity in gas. use of an alternative method for non-uniform piezoelectric transmitting transducer vibration”, Poster presented at 2011 IEEE International Ultrasonics Symposium, orlando, USA, 18-21 October 2011.

[13] R. Ludwig and W. Lord, “A finite-element formulation for the study of ultrasonic NDT systems”, IEEE Transactions on Ultrasonics, Ferroelectrics and Frequency Control **35**, 809–820 (1988).

[14] L. Schmerr and S. Song, *Ultrasonic nondestructive evaluation systems: models and measurements* (Springer London, Limited) (2007).

[15] Belanger, P. ’Feasibility of Thickness Mapping Usinig Ultrasonic Guided Waves’, Mechanical Engineering Department, Imperial College London, 2009.

[16] Wilcox, P. D., 'Lamb wave inspection of large structu res using permanently attached transducers', Mechanical Engineering, Imperial College London, 1998.

[17] A. Lygre, M. Vestrheim, P. Lunde, and V. Berge, "Numerical simulation of ultrasonic flowmeters", in *Ultrasonics International 1987 (UI'87)*, 196–201 (Butterworth Scientific Ltd., Guildford, UK) (1987).

[18] S. Vervik, "Transitt-tidsbestemmelse for ultralyd strømningsmetre. nullstrømningsforhold", Master thesis, University of Bergen, Department of Physics and Technology, Bergen, Norway (1995).

[19] S. Vervik, "Methods for characterization of gas-coupled ultrasonic sender-receiver measurement systems", PhD-thesis, Department of Physics and Technology, University of Bergen, Bergen, Norway (2000).

[20] C. Dang, L. W. Schmerr, and A. Sedov, "Modeling and measuring al the elements of an ultrasonic nondestructive evaluation system I: modeling foundations", Research in Nondestructive Evaluation **14**(3), 141–176 (2002).

[21] C. Dang, L. W. Schmerr, and A. Sedov, "Modeling and measuring all the elements of an ultrasonic nondestructive evaluation system II: model-based measurements", Research in Nondestructive Evaluation **14**(4), 177–201 (2002).

[22] P. Lunde, R. A. Kippersund, and M. Vestrheim, "Signal modelling using the FLOSIM system model in ultrasonic instrumentation for industrial applications", in *Proc. of NORSIG 2003, Norwegian Symposium on Signal Processing 2003, Bergen, October 2004* (2003).

[23] C. D. Reid, "Some investigations into the velocity of sound at ultra-sonic frequencies using quartz oscillators", Physical Review **35**, 814–831 (1930).

[24] C. D. Reid, "Notes on the effect of distance from the source on the velocity of sound at ultrasonic frequencies", Physical Review **37**, 1147–1148 (1931).

[25] M. Grabau, "A Study of the Velocity of Sound in Air", J. Acoust. Soc. Am. **5**(1), 1–9 (1933).

[26] W. J. Fry, "The Double Crystal Acoustic Interferometer", J. Acoust. Soc. Am. **21**(1), 17–28 (1949).

[27] H. Seki, A. Granato, and R. Truell, "Diffraction Effects in the Ultrasonic Field of a Piston Source and Their Importance in the Accurate Measurement of Attenuation", J. Acoust. Soc. Am. **28**(2), 230–238 (1956).

[28] G. Hayward, C. J. MacLeod, and T. S. Durrani, "A systems model of the thickness mode piezoelectric transducer", J. Acoust. Soc. Am. **76**(2), 369–382 (1984).

[29] P. Wilcox, R. Monkhouse, P. Cawley, M. Lowe, and B. Auld, "Development of a computer model for an ultrasonic polymer film transducer system", NDT & E International **31**(1), 51 – 64 (1998).

[30] Van Deventer, J. and Lofqvist, T. and Delsing, J., "PSpice simulation of ultrasonic systems", Ultrasonics, Ferroelectrics and Frequency Control, IEEE Transactions on **47**, 1014–1024 (2000).

[31] P. Lunde, "Modellar for beskrivelse av elektroakustisk sender-mottakar målesystem, inkl. diffraksjonseffektar/diffraksjonskorreksjon", Unpublished note, Department of Physics and Technology, University of Bergen, Bergen, Norway (2013).

[32] P. Lunde, K.-E. Frøysa, and M. Vestrheim, "Transient diffraction effects on ultrasonic flow meters for gas and liquid", in *Proceedings of the 26th Scandinavian Symposium on Physical Acoustics, Ustaoset, Norway, 26-29 January 2003* (2003).

[33] P. Lunde, K.-E. Frøysa, R. Kippersund, and M. Vestrheim, "Transient diffraction effects in ultrasonic meters for volumetric, mass and energy flow measurement of natural gas", in *Proceedings of the 21st North Sea Flow Measurement Workshop, Tønsberg, Norway, 28-31 October 2003* (2003).

[34] P. Lunde, R. A. Kippersund, M. Vestrheim, and K.-E. Frøysa, "Transient diffraction effects in piezoelectric ultrasonic transducers using finite element modelling", in *Proceedings of the 27th Scandinavian Symposium on Physical Acoustics, 25-28 January, 2004, Ustaoset, Norway* (2004).

[35] R. Hauge, E. Mosland, E. Storheim, P. Lunde, M. Vestrheim, and J. Kocbach, "Finite element modeling of ultrasound measurement systems for gas. comparison with experiments in air.", in *Proceedings of the 36th Scandinavian Symposium on Physical Acoustics - Geilo 3rd February - 6th February* (2013).

[36] M. Vestrheim, “PHYS 373 - Akustiske Målesystem”, Lecture notes, University of Bergen, Bergen (2008).

[37] ANSI, “ANSI S1.1-1994 (R2004) - Acoustical terminology”, American Institute of Physics (2004).

[38] A. S. Khimunin, “Numerical calculation of the diffraction corrections for the precise measurement of ultrasound absorption”, Acustica **27**, 173–181 (1972).

[39] A. O. Williams Jr., “The Piston Source at High Frequencies”, J. Acoust. Soc. Am. **23**(1), 1–6 (1951).

[40] A. S. Khimunin, “Numerical Calculation of the Diffraction Corrections for the Precise Measurement of Ultrasound Phase Velocity”, Acustica **32**, 192–200 (1975).

[41] H. Hobæk, “On the acoustical near field of a circular piston source. results from a numerical investigation”, Scientific/Technical Report No. 32, Department of Physics, University of Bergen, Norway (1970).

[42] ANSI, “ANSI S1.26-1995 (R2009) - Method for calculation of the absorption of sound by the atmosphere”, American Institute of Physics (1995).

[43] L. L. Foldy and H. Primakoff, “A general theory of passive linear electroacoustic transducers and the electroacoustic reciprocity theorem”, J. Acoust. Soc. Am. **17**(2), 109–120 (1945).

[44] M. Vestrheim, “PHYS 272 - Akustiske Transdusere”, Lecture notes, University of Bergen, Bergen (2007).

[45] R. W. King, H. R. Mimno, and A. H. Wing, *Transmission lines, antennas and wave guides* (Dover Publications, Inc, New York) (1965).

[46] J. Kocbach, “Finite element modeling of ultrasonic piezoelectric transducers”, PhD thesis, Department of Physics, University of Bergen, Bergen, Norway (2000).

[47] J. Kocbach, P. Lunde, M. Vestrheim, and R. Kippersund, “Finite element modeling of ultrasonic piezoelectric transducers: Extension of FEMP to 3D analysis.”, CMR Report no. CMR-06-A10046-RA-01, Christian Michelsen Research AS, Bergen, Norway (December 2006).

[48] L. E. Kinsler, A. R. Frey, A. B. Coppens, and J. V. Sanders, *Fundamentals of Acoustics*, 4th edition (John Wiley & Sons, New York) (2000).

[49] Hewlett Packard, *Operation and service manual: 4192 LF impedance analyzer* (1982).

[50] Vaisala, “Data sheet: HMI41 indicator and HMP42/HMP46 probes”, (2013).

[51] Brüel & Kjær, “Product data: Pistonphone - Type 4228”, (1996).

[52] O. S. Amundsen, “Material constants determination for piezoelectric disks, and influence on source sensitivity. Measurements and simulations.”, Master’s thesis, Department of Physics and Technology, University of Bergen, Bergen, Norway (2011).

[53] Agilent, “Product Data: Type 33220A signal generator”, (2007).

[54] Tektronix, “Product Data: Type DPO3012 digital oscilloscope”, (2010).

[55] Brüel & Kjær, “Product data: 1/8″ pressure-field microphone - Type 4138”, (2008).

[56] Brüel & Kjær, “Product data: Microphone preamplifiers - Types 2633, 2639, 2645, 2660”, (1993).

[57] Brüel & Kjær, “Product data: Falcon Range 1/4-inch microphone preamplifier - Type 2670”, (2004).

[58] Physik Instrumenet GmbH, “Operating manual MS 45E: C-842 DC-motor controllers”, (1996).

[59] Physik Instrumente GmbH, “Product data - PI C-852 signal processor”, (2012).

[60] Physik Instrumente GmbH, “Product data - PI M-531 linear stage”, (2010).

[61] Physik Instrument GmBH, “Product data - PI M-535 linear stage”, (2010).

[62] Physik Instrumente GmbH, “Product data - PI M-037 rotational stage”, (2010).

[63] Bruel & Kjær, "Product Data: Wide Range Measuring Amplifiers - Types 2610 and 2636", (1996).

[64] Krohn-Hite, "Product Data: Type 3940A bandpass filter", (2012).

[65] Vaisala, "Product data - Vaisala HMT310 series", (2010).

[66] Vaisala, "Calibration certificate: Humidity and temperature transmitter HMT313, serial no. F4850018", (2010).

[67] Mitutoyo, "Product data - Mitutoyo MDH-25H digital micrometer", (2012).

[68] Tesa, "Product data - Tesa digital caliper", (2012).

[69] A. Erdal, *Elementær innføring i sannsynlighetsregning og problemløsninger ved analyse av måleresultater* (Alma Mater, Bergen, Norway) (1972).

[70] A&D, "GF Series precision balance - Instruction manual", A&D Company, Limited, Tokyo, Japan (2008).

[71] Bruel & Kjær, "Calibration data for 4138-A-015 microphone system serial no. 2795107", (2012).

[72] Brüel & Kjær, "Calibration data for Type 4138 microphone serial no. 1832479", (1995).

[73] Brüel & Kjær, "Calibration data for Type 4138 microphone serial no. 2784915", (2012).

[74] Brüel & Kjær, "Certificate of calibration No. C1201771 for B&K 4138-A-015 microphone system serial no. 2795107", (2012).

[75] Brüel & Kjær, *Condenser microphones and microphone preamplifiers for acoustic measurements - Data handbook* (1982).

[76] Brüel & Kjær, "Calibration data for Type 4228 pistonphone serial no. 1918465", (1996).

[77] M. Aanes, "Undersøkelser av piezokeramiske skiver . Målinger og endelig element analyser .", Master's thesis, Department of Physics and Technology, University of Bergen, Bergen, Norway (2009).

[78] Ferroperm Piezoceramics A/S (now a member of Meggitt's Sensing Systems division), "High quality components and materials for the electronic industry", DK-3490 Kvistgård (2012).

[79] "The fundamentals of FFT-based signal analysis and measurement in LabVIEW and LabWindows/CVI", Available at URL http://www.ni.com/white-paper/4278/en (last viewed 21.05.2013) (2009).

[80] M.-A. Parseval, "Memoire sur les series et sur l'integration complete d'une equation aux differences partielle lineaires du second ordre, a coefficiens constans", Academie des Sciences (1806).

[81] H. Hobæk, "Private communication", Department of Physics and Technology, University of Bergen, Bergen, Norway (2013).

[82] J. P. Bentley, *Principles of measurement systems - 4th ed.* (Pearson Education Limited, England) (2005).

[83] J. Kocbach, "Femp version 3.5 - documentation", (N/A).

[84] E. Storheim, "Private communication", Department of Physics and Technology, University of Bergen, Bergen, Norway.

[85] V. Knappskog, "Radiellmode svingninger i piezoelektriske ultralydstransdusere for luft. målinger og endelig element analyser.", Master's thesis, Department of Physics and Technology, University of Bergen, Bergen, Norway (2007).

[86] K. D. Lohne, "Undersøkelse og utnyttelse av svingemoder i ultralyd transduserkonstruksjoner", Master thesis, Department of Physics and Technology, University of Bergen, Bergen, Norway (2005), (in Norwegian).

[87] R. Fardal, "Endelig element analyse av elektriske egenskaper til piezoelektriske skiver", Master thesis, Department of Physics, University of Bergen, Bergen, Norway (2002), (in Norwegian).

[88] Andrew Hurrel, BSc (Hons), PhD, "Correspondence", Precision Acoustics Ltd, Dorset, UK (2012).

[89] Precision Acoustics, "Syntactic foam, http://www.acoustics.co.uk/products/syntactic-foam", (Last reviewed 05.05.2013).

[90] MG Chemicals, "Silver conductive epoxy adhesive 8331 - Technical data sheet", (2012).

[91] Onda Corporation, "Acoustic properties of solids", Data sheet (2003).

[92] Atlas Steels, "Grade data sheet: 316, 316l, 316h", (2011).

[93] M. Grujicic and H. Zhao, "Optimization of 316 stainless steel/alumina functionally graded material for reduction of damage induced by thermal residual stresses", Materials Science and Engineering: A **252**, 117–132 (1998).

[94] P. Norli, "Sound velocity cell for gas characterization", PhD thesis, Department of Physics and Technology, University of Bergen, Bergen, Norway (2007).

[95] DIAB, "Divinycell h, technical data", (2012).

[96] H. Fosså, "Ultrasound Phantom for Myocardium", Master thesis, University of Bergen (2011).

[97] N. Bilaniuk and G. S. K. Wong, "Speed of sound in pure water as a function of temperature", The Journal of the Acoustical Society of America **93**(3), 1609–1612 (1993).

[98] N. Bilaniuk and G. S. K. Wong, "Erratum: Speed of sound in pure water as a function of temperature [j. acoust. soc. am. [bold 93], 1609–1612 (1993)]", The Journal of the Acoustical Society of America **99**(5), 3257–3257 (1996).

[99] Olympus NDT Inc., Waltham, USA, "Olympus Immersion Transducers - V309-SU", URL adress: "http://www.olympus-ims.com/en/ultrasonic-transducers/immersion/", Last viewed: 04.06.2013.

[100] Hanna Instruments, "HI 98509 - Checktemp 1", URL adress: http://www.hannainst.com/manuals/manHI_98509_98510.pdf, Last viewed: 04.06.2013.

Appendix A

MATLAB-scripts

Here the Matlab-scripts used for electrical measurements, acoustical measurements, and signal processing are included.

A.1 Electrical measurements

The acoustical measurements are performed with the Matlab-script `impanal.m`, based on a similarly named script found in [77].

A.1.1 `impanal.m`

```
%%%%%%%%%%%%%%%%%%%%%%%%%%%%%%%%%%%%%%%%%%%%%%%%%%%%%%%%%%%%%%%%%%%%%%%%
% impanal.m
%
% Performs admittance measurements.
% Based on work by Magne Aanes.
%
% Rune Hauge and Eivind Mosland, 2012/2013
%%%%%%%%%%%%%%%%%%%%%%%%%%%%%%%%%%%%%%%%%%%%%%%%%%%%%%%%%%%%%%%%%%%%%%%%

% Find a GPIB object.
% Computer EXP 2
%obj1 = instrfind(’Type’, ’gpib’, ’BoardIndex’, 0, ’PrimaryAddress’, 17, ’Tag’, ’’);
% Computer EXP 3
obj1 = instrfind(’Type’, ’gpib’, ’BoardIndex’, 1, ’PrimaryAddress’, 17, ’Tag’, ’’);

% Create the GPIB object if it does not exist
% otherwise use the object that was found.
if isempty(obj1)
    % Computer EXP 2
    %obj1 = gpib(’NI’, 0, 17);
    % Computer EXP 3
    obj1 = gpib(’NI’, 1, 17);
else
    fclose(obj1);
    obj1 = obj1(1);
end

% Connect to instrument object, obj1.
fopen(obj1);

tic

% Enables parametric measurements, with respect to
% impedance analyzer drive voltage.
for amplitudes = 0.3;

    %%%%%%%%%%%%%%%%%%%%%%%%%%%%%%%%%%%%%%%%%%%%%%%%
    % Specify object, environmental parameters and
    % frequency
    elnr = ’TransducerNo1’;
    dimensjon = ’20x2mm’;
    temp = ’24,7’;
    hr = ’29,5’; %luftfuktighet [%]
    p = ’1013’; % lufttrykk [hPa]
```

```

    % Osc. level [V]
    amplitude = amplitudes;

    % Frequency vector 5, corresponding to
    % acoustical measurements.
    f = [50e3:500:88e3,...
    88.1e3:100:114.9e3,...
    115e3:500:200e3,...
    200.5e3:500:236e3,...
    236.1e3:100:255.9e3,...
    256e3:500:300e3]./1e3;

    %%%%%%%%%%%%%%%%%%%%%%%%%%%%%%%%%%%%%%%%%%%%%%%%
    ol = sprintf(’%3.3f’,amplitude);
    % Set impedance analyzer to admittance mode
    fprintf(obj1, [’A2C3F1OL’,ol,’EN’]);

    % Timestring on the format yyyymmddHHMMSS
    time = datestr(now, ’yyyymmddHHMMSS’);
    % Filename
    title = [elnr,’_’,dimensjon,’_freq_frekvensoppsett5’,...
        ’_’,temp,’_’,hr,’_’,p,’_’,time,’_’,num2str(amplitudes*10)];

    i = 1;
    ii = 1;
    antal = length(f);
    g = ones(1,antal);
    b = ones(1,antal);
    fr = ones(1,antal);
    disp([num2str(antal),’␣frequencies.’])
    disp(’Starting␣measurement...’)
    for freq = f
        percent = i/antal*100;
        if percent >= ii*10
            disp([num2str(ii*10),’␣%’])
            ii = ii + 1;
        end

        s = sprintf(’%3.3f’,freq);
        fprintf(obj1, [’FR’,s,’ENEX’]);
        pause(0.25)
        data1 = fscanf(obj1);
        d=sscanf(data1,’%4c%f,%4c%f,%2c%f’);
        g(i)=d(5);b(i)=d(10);fr(i)=d(13);
        i = i + 1;
    end
    disp(’Measurement␣finished.’)
    disp(’Saving...’)
    save(title,’g’,’b’,’fr’)
    disp(’Done!’)
    stoptime = datestr(now, ’yyyymmddHHMMSS’);

end

toc
```

A.2 Acoustical measurements

The acoustical measurements are performed with the MATLAB-script `main.m`, which loads `measurement_parameters.m` and calls several subscripts.

A.2.1 `main.m`

```
%%%%%%%%%%%%%%%%%%%%%%%%%%%%%%%%%%%%%%%%%%%%%%%%%%%%%%%%%%%%%%%%%%%%%%%%
% main.m
% Main software for acoustic measurements in air.
% Espen Storheim, 2011 (v1.0)
% Based on work by Vidar Knappskog and Magne Aanes.
%
% Rune Hauge and Eivind Mosland, 2012/2013 (v2.0)
%%%%%%%%%%%%%%%%%%%%%%%%%%%%%%%%%%%%%%%%%%%%%%%%%%%%%%%%%%%%%%%%%%%%%%%%

%% Version number.
```

```
airversion = ’2.0’;

%% Add the subfolders to MATLABs path, just in case.
% Change folder names to exclude spaces.
if (isunix || ismac)
    addpath([pwd ’/User␣input’])
    addpath([pwd ’/Kernel’])
    addpath([pwd ’/Instrument␣control␣etc’]);
else
    addpath([pwd ’\User␣input’])
    addpath([pwd ’\Kernel’])
    addpath([pwd ’\Instrument␣control␣etc’]);
end

% Load information about the measurement about to be performed.
measurement_parameters

% Initialization of the instruments prior to measurements.
init_instruments

% Read the electrical signal.
ch = 2;

% Adjust scaling according to input voltage.
voltage_scaling = [0.02 0.05 0.1 0.2 0.5 1 2 5 10];
for ii = 1:(length(voltage_scaling));
    if (4*voltage_scaling(ii) >= meas.voltage_in)
        fprintf(instrument.scope,[’CH2:SCA␣’ num2str(voltage_scaling(ii))]);
        break;
    end
end

disp(’Starting␣measurements␣of␣the␣electrical␣pulses.’)
for ii = 1:length(meas.f)

    % Adjust the burst length to ensure temporal resolution.
    t = 16*100e-6;
    %     t = 14*100e-6;
    %     t = 10*100e-6;

    % Number if cycles is adjusted according to the given frequency so that
    % the burst length equals 1.4 ms.
    disp([num2str(meas.f(ii)/1000) ’␣kHz’])
    fprintf(instrument.generator,[’BM:NCYC␣’, num2str(floor(meas.f(ii)*t))]);
    fprintf(instrument.generator,[’FREQ␣’, num2str(meas.f(ii))]);

    % Record environmental data.
    [Temp RH] = VaisalaHMT313(instrument.humidity);
    results.temp_electric(ii) = Temp;
    results.humidity_electric(ii) = RH;
    results.electric_time(ii,:) = clock;
    clear Temp RH

    % Adjust time window.
    adjustTime(’electric’,instrument,meas)

    % Stop aquisition.
    fprintf(instrument.scope,’ACQ:STATE␣STOP’);
    % Wait to ensure that the scope wipes its memory.
    pause(1)
    % Start aquisition.
    fprintf(instrument.scope,’ACQ:STATE␣RUN’);
    % Wait for averaging.
    pause(meas.wait_scaling)

    % Read and save.
    [dum1 dum2 dum3] = DPO_les(ch,instrument.scope);
    results.electric_t(ii,:) = dum1;
    results.electric(ii,:) = dum2;
    results.electric_timescale(ii) = dum3;
    results.electric_Vscale(ii) = ...
    str2num(query(instrument.scope,[’CH’,num2str(ch),’:SCA?’]));
    results.electric_Termination(ii) = ...
    str2num(query(instrument.scope,[’CH’,num2str(ch),’:TER?’]));
    clear dum1 dum2 dum3

```

```
end

disp('␣')
disp('Finished␣reading␣the␣electrical␣signal.)
disp('Now readjusting the scope and continuing to acoustic...')

% Read the acoustic pulses.
ch = 1;

disp('Starting␣measurements␣of␣the␣acoustical␣pulses.')
for ii = 1:length(meas.f);

    % Adjust the bandwidth of the KH-filter
    pause(0.1)
    % Set the cutoff frequency for channel 1. (Not working properly)
    fprintf(instrument.filter,['F' num2str((meas.f(ii)/1000)/2) 'K']);
    pause(0.1)
    % Set the cutoff frequency for channel 2.
    fprintf(instrument.filter,['F' num2str((meas.f(ii)/1000)*2) 'K']);

    % Adjust the burst length to ensure temporal resolution.
    t = 16*100e-6;
    %      t = 14*100e-6;
    %      t = 10*100e-6;

    % Number if cycles is adjusted according to the given frequency so that
    % the burst length equals 1.4 ms.
    disp([num2str(meas.f(ii)/1000) '␣kHz'])
    fprintf(instrument.generator,['BM:NCYC␣', num2str(floor(meas.f(ii)*t))]);
    fprintf(instrument.generator,['FREQ␣', num2str(meas.f(ii))]);

    % Record environmental data.
    [Temp RH] = VaisalaHMT313(instrument.humidity);
    results.temp_acoustic(ii) = Temp;
    results.humidity_acoustic(ii) = RH;
    results.acoustic_time(ii,:) = clock;
    clear Temp RH

    % Adjust time window.
    adjustTime('acoustic',instrument,meas)

    % Adjust amplitude scaling and read out signal.
    [dum1 dum2 dum3] = adjustAmplitude(1,instrument,meas);

    results.acoustic_t(ii,:) = dum1;
    results.acoustic(ii,:) = dum2';
    results.acoustic_timescale(ii) = dum3;
    results.acoustic_Vscale(ii) = ...
    str2num(query(instrument.scope,['CH',num2str(ch),':SCA?']));
    results.acoustic_Termination(ii) = ...
    str2num(query(instrument.scope,['CH',num2str(ch),':TER?']));
    clear dum1 dum2 dum3

end

%% Storing data

results.electric_f = meas.f;
results.acoustic_f = meas.f;

xx = strcat(meas.name,'_',datestr(now,'yyyymmddHHMMSS'));
save(xx,'results', 'meas', 'instrument');

%% Finishing touches.
% Close the instrument ports and clear device handles.
instrument_shutdown
```

A.2.2 measurement_parameters.m

```
%%%%%%%%%%%%%%%%%%%%%%%%%%%%%%%%%%%%%%%%%%%%%%%%%%%%%%%%%%%%%%%%%%%%%%%%%%
% measurement_parameters.m
% Information about the calibration of the measurement microphone.
% Part of the software for acoustic measurements in air.
% Espen Storheim, 2011
% Based on work by Vidar Knappskog and Magne Aanes.
%
```

```
% Modified by Rune Hauge and Eivind Mosland, 2012/2013
%%%%%%%%%%%%%%%%%%%%%%%%%%%%%%%%%%%%%%%%%%%%%%%%%%%%%%%%%%%%%%%%%%%%%%%%%

% This file is designed to be tampered with prior to each measurement.

%% Define initial bandpass filter low and high cutoff frequency
meas.cutoff_1 = 20; % kHz
meas.cutoff_2 = 300; % kHz
% At present, cutoff_2 is adjusted for each measurement frequency in
% main.m. This is currently not done for cutoff_1.

%% General measurement info.
% Version of this software which was used to make the measurements.
% Should be taken from elsewhere.
% meas.version = 'Updated 20/7-2011.';

% Name of the person performing the measurement and date.
meas.name = '200,5kHzto300kHz_2Vpp';
TT = clock;
meas.date = [date ',␣' num2str(TT(4)) ':' num2str(TT(5))];
clear TT

% Information about the transmitting transducer.
meas.source = 'Pz27␣disk,␣D␣=␣20.0␣mm,␣T␣=␣2.0␣mm,␣Element␣No.␣16␣in␣batch␣9/12.';

% Information about the receiving transducer.
meas.receiver = 'Pz27␣disk,␣D␣=␣20.0␣mm,␣T␣=␣2.0␣mm,␣Element␣No.␣6␣in␣batch␣9/12.';

% Additional notes regarding the specific simulation.
meas.notes = 'Elm␣16␣til␣elm␣6.';

%% Distance from transmitter.
meas.distance = 0.77;
%meas.z

%% Frequency information [Hz]

% Frekvensoppsett 50-200 kHz elm 16 til elm 10.
meas.f = [50e3 100e3];

% meas.f = frequencies;

% meas.f = [50e3:500:88e3,...
%      88.1e3:100:114.9e3,...
%      115e3:500:236e3,...
%      236.1e3:100:255.9e3,...
%      256e3:500:300e3];

%% Input waveform data.
% Peak voltage out from the signal generator [V]
meas.voltage_in = 1;
% Number of periods in each burst [-]
% Only used in initialization of the generator. In main.m the number of
% cycles is adjusted to fit a certain burst length [ms] specified therein.
meas.cycles = 40;
meas.burst_cycles = meas.cycles;
% Burst repetition rate [Hz]
meas.burst_period = 40e-3;
meas.burst_rate = 1/meas.burst_period;

% Approximate time before the signal is steady after a voltage scaling change.
 meas.wait_scaling = 7;

% A note on the input voltage: The signal generator claims that the voltage
% specified above is the peak to peak voltage. This is the case when the
% generator is connected to a 50 Ohm load. However, the transmitting
% transducer typically has an electrical impedance in the kilo Ohm range and
% is connected directly to the generator. This causes a voltage division which
% depends of the impedance of the transducer, and hence an impedance mismatch.

%% Oscilloscope parameters.
% Number of pulses which the signal is averaged.
meas.average = 128;
% Number of data points recorded by the scope.
meas.samples = 1e5;
% Channel used for measurements.
```

```
%meas.channel = 1;

% Channel number where the signal generator is connected.
meas.channel_electrical = 1;
% Channel number where the oscilloscope is connected.
meas.channel_acoustical = 2;

%% Distance from transmitter to receiver [m].
%meas.distance = meas.z;

%% Total input gain in the B&K 2636 measurement amplifier [dB].
% Only recorded for later reference. Must be set manually.
meas.gain_in = 40;
meas.gain_out = 20;
meas.gain = meas.gain_in + meas.gain_out;
```

A.2.3 init_instruments.m

```
%%%%%%%%%%%%%%%%%%%%%%%%%%%%%%%%%%%%%%%%%%%%%%%%%%%%%%%%%%%%%%%%%%%%%%%%
% init_instruments.m
% Initialize the instruments according to measurement_parameters
% Part of the software for acoustic measurements in air.
% Espen Storheim, 2011
% Based on work by Vidar Knappskog and Magne Aanes.
%%%%%%%%%%%%%%%%%%%%%%%%%%%%%%%%%%%%%%%%%%%%%%%%%%%%%%%%%%%%%%%%%%%%%%%%

% This script is used to initialize the instruments to the proper settings.
% Most of the values are taken from the "meas" structure specified by the
% user in the m-file "measurement_parameters.m".

instruments;

%% Initialize the oscilloscope.
% Code for the Tektronix DPO3012.
if strcmp(instrument.scope_name, 'Tektronix␣DPO3012.␣S/N:␣')
    % Set the acquisition mode to averaging.
    fprintf(instrument.scope,'ACQ:MOD␣AVE');
    % Set the number of cycles to average.
    fprintf(instrument.scope,['ACQ:NUMAV␣' num2str(meas.average)]);
    % Number of points which shall be read from the scope.
    fprintf(instrument.scope,['HOR:RECO␣' num2str(meas.samples)]);
    % Start point for the recorded signal
    fprintf(instrument.scope,'DAT:START␣1');
    % Stop point for the recorded signal
    fprintf(instrument.scope,['DAT:STOP␣' num2str(meas.samples)]);
    % Trigger specifications. Set to edge detection from external source.
    fprintf(instrument.scope,'TRIG:A:EDGE:SOU␣EXT');
    % Set the trigger type to positive edge.
    fprintf(instrument.scope,'TRIG:A:TYP␣EDG');
    % 2012.11.19 EM: Added additional initialization.
    % CH1
    % Set Offset to zero.
    fprintf(instrument.scope,'CH1:OFFS␣0');
    % Set position to zero.
    fprintf(instrument.scope,'CH1:POS␣0');
    % Set coupling to AC.
    fprintf(instrument.scope,'CH1:COUP␣AC');
    % CH2
    % Set Offset to zero.
    fprintf(instrument.scope,'CH2:OFFS␣0');
    % Set position to zero.
    fprintf(instrument.scope,'CH2:POS␣0');
    % Set coupling to AC.
    fprintf(instrument.scope,'CH2:COUP␣AC');
end

%% Initialize the bandpass filter.
% Code for Krohn-Hite 3940A filter.
if strcmp(instrument.filter_name, 'Krohn-Hite␣3940A.␣S/N:␣AM2626')
    % There seems to be an overflow when the commands are combined, so they
    % have been separated and a pause of 100 ms is set between each
    % command.
    %
    % Set the input and output gain on both channels to 0 dB.
    pause(0.1)
    fprintf(instrument.filter,'AL;0IG;0OG;B');
```

```
    pause(0.1)
    % Set channel 1 to high pass mode.
    fprintf(instrument.filter,'CH1.1;M2');
    pause(0.1)
    % Set the cutoff frequency for channel 1.
    fprintf(instrument.filter,['F' num2str(meas.cutoff_1) 'K']);
    pause(0.1)
    % Set channel 2 to low pass mode.
    fprintf(instrument.filter,'CH1.2;M1');
    pause(0.1)
    % Set the cutoff frequency for channel 2.
    fprintf(instrument.filter,['F' num2str(meas.cutoff_2) 'K']);
end

%% Initialize the signal generator.
% This code is for the Agilent 33*** series signal generators
if strcmp(instrument.generator_name, 'Agilent␣33220A.␣S/N:␣')
    fprintf(instrument.generator,'OUTP␣OFF');
    fprintf(instrument.generator,['APPL:SIN␣' num2str(meas.f(1)) ...
    '␣HZ,␣' num2str(meas.voltage_in) '␣VPP']);
    % Set the trigger to internal and positive slope.
    fprintf(instrument.generator,'TRIG:SOUR␣IMM');
    fprintf(instrument.generator,'TRIG:SLOP␣POS');
    % Set the number of periods in one burst.
    fprintf(instrument.generator,['BURS:NCYC␣' num2str(meas.burst_cycles)]);
    fprintf(instrument.generator,'BURS:STAT␣ON');
    % Set the burst rate, i.e. the frequency of the bursts.
    fprintf(instrument.generator,['BM:INT:RATE␣' num2str(meas.burst_rate)]);
    % Set the peak voltage.
    fprintf(instrument.generator,['VOLT␣' num2str(meas.voltage_in(1))]);
    % Activate the output.
    fprintf(instrument.generator,'TRIG:SLOP␣POS');
    fprintf(instrument.generator,'OUTP␣ON');
end
```

A.2.4 instruments.m

```
%%%%%%%%%%%%%%%%%%%%%%%%%%%%%%%%%%%%%%%%%%%%%%%%%%%%%%%%%%%%%%%%%%%%%%%%
% Instruments.m
% Part of the software for acoustic measurements in air.
% Espen Storheim, 2011
% Based on work by Vidar Knappskog and Magne Aanes.
%%%%%%%%%%%%%%%%%%%%%%%%%%%%%%%%%%%%%%%%%%%%%%%%%%%%%%%%%%%%%%%%%%%%%%%%

% Initialization of the instrumens used in the measurement setup for air.
% Contains MATLAB-handles for the instruments used in the setup, both GPIB,
% serial, and the special functions used by the PI positioning equipment.
%
% This file contains information about many devices in the laboratory, many
% that are not in use on the setup for measurements in air. These are by
% default commented out in the code.
%
% Comment out instruments not in use!
%
% Notes about future updates.
% - Include a test to check for acoustic or impedance measurements.
% - Remove the _idn parameter since there is no common response.

instrument = {};

%% Signal generators.

% Signal Generator: Agilent 33220A. S/N:
%instrument.generator = gpib('find','DEV10');

instrument.generator = gpib('ni',0,10);
% fopen(instrument.generator)

% 14.09.2012 Rune Hauge: Include 'instrfind' for locating a GPIB object
% instrument.generator = instrfind('Type', 'gpib', 'BoardIndex', 0, ...
% 'PrimaryAddress', 10, 'Tag', '');

% if isempty(instrument.generator)
%     instrument.generator = gpib('NI', 0, 10);
% else
%     fclose(instrument.generator);
```

```
%     instrument.generator = instrument.generator(1):
% end

fopen(instrument.generator);

instrument.generator_name = 'Agilent␣33220A.␣S/N:␣';
instrument.generator_idn = query(instrument.generator,'*IDN?');

% Test the connection. Should be a command where the response can be
% verified.
if isempty(instrument.generator_idn)
    disp('Warning:␣The␣signal␣generator␣is␣not␣connected␣or␣configured␣properly.')
else
    disp('The␣signal␣generator␣is␣connected␣and␣appears␣to␣be␣working.')
end

%% Oscilloscopes.

% Digital oscilloscope: Tektronix DPO3012. S/N:
%instrument.scope =  gpib('ni',0,2);

% 14.09.2012 Rune Hauge: Include 'instrfind' for locating a GPIB object
instrument.scope = instrfind('Type', 'visa-usb', 'RsrcName', ...
'USB0::0x0699::0x0410::C010246::0::INSTR', 'Tag', '');

if isempty(instrument.scope)
    % Our oscilloscope
    instrument.scope = visa('NI', 'USB0::0x0699::0x0410::C010246::0::INSTR');
    % Magne Aanes's oscilloscope
    % instrument.scope = visa('NI', 'USB0::0x0699::0x0410::C011044::0::INSTR');
else
    fclose(instrument.scope);
    instrument.scope = instrument.scope(1);
end
% 20.09.2012 Rune Hauge: Set scope InputBufferSize to high enough value.
% Trying 1000000.
instrument.scope.InputBufferSize = 2000000;

fopen(instrument.scope)
instrument.scope_name = 'Tektronix␣DPO3012.␣S/N:␣';
instrument.scope_idn = query(instrument.scope,'*IDN?');

% Old oscilloscope: LeCroy ###. S/N:

% Test the connection. Should be a command where the response can be
% verified.
if isempty(instrument.scope_idn)
    disp('Warning:␣The␣oscilloscope␣is␣not␣connected␣or␣configured␣properly.')
else
    disp('The␣oscilloscope␣is␣connected␣and␣appears␣to␣be␣working.')
end

%% Environmental parameters.

% % Temperature sensor: ASL F250. S/N:
% %instrument.temperature = gpib('ni',0,3);
% % 14.09.2012 Rune Hauge: Include 'instrfind' for locating a GPIB object
% instrument.temperature = instrfind('Type', 'gpib', 'BoardIndex', 0, ...
% 'PrimaryAddress', 3, 'Tag', '');
%
% if isempty(instrument.temperature)
%     instrument.temperature = gpib('NI', 0, 3);
% else
%     fclose(instrument.temperature);
%     instrument.temperature = instrument.temperature(1);
% end
% fopen(instrument.temperature)
% set(instrument.temperature,'EOSmode','read&write');
% set(instrument.temperature,'EOSCharCode',10); % Set terminator to LF.
% instrument.temperature_name = 'ASL F250 mk II. S/N: ';
% fprintf(instrument.temperature,'A0');
% instrument.temperature_idn = fscanf(instrument.temperature);

% % Test the connection. Should be a command where the response can be
% % verified.
% if isempty(instrument.temperature_idn)
```

```
%     disp('Warning: The thermometer is not connected or configured properly.')
% else
%     disp('The thermometer is connected and appears to be working.')
% end

% Pressure sensor: Paroscientific DigiQuartz 740. S/N:
%instrument.pressure = serial('COM2','Baudrate',4800,'Terminator', ...
%'cr','Databit',7,'Parity','even');;
instrument.pressure_name = 'Paroscientific␣DigiQuartz␣740.␣S/N:';

% Relative humidity and temperature sensor: Vaisala HMT313. S/N:
instrument.humidity = serial('COM5','Baudrate',4800,'Terminator','cr',...
'Databit',7,'Parity','even');
instrument.humidity_name = 'Vaisala␣HMT313.␣S/N:';
fopen(instrument.humidity);


%% Signal processing.

% Bandpass filter: Krohn-Hite 3940A. S/N: AM2626.
%instrument.filter = gpib('ni',0,25);
% 14.09.2012 Rune Hauge: Include 'instrfind' for locating a GPIB object
instrument.filter = instrfind('Type', 'gpib', 'BoardIndex', 0, ...
'PrimaryAddress', 25, 'Tag', '');

if isempty(instrument.filter)
    instrument.filter = gpib('NI', 0, 25);
else
    fclose(instrument.filter);
    instrument.filter = instrument.filter(1);
end
fopen(instrument.filter)
instrument.filter_name = 'Krohn-Hite␣3940A.␣S/N:␣AM2626';
instrument.filter_idn = query(instrument.filter,'*IDN?');


%% Impedance analyzer.

% Impedance analyzer: HP 4192 LF. S/N:
%instrument.impedance = gpib('find','DEV17');
%instrument.impedance_name = 'HP 4192 LF. S/N:';

% Impedance analyzer: Agilent 4294A. S/N:
%instrument.impedance2 = gpib('find','DEV17');
%instrument.impedance2_name = 'Agilent 4194A. S/N:';


%% Positioning equipment.
% Controlling the stages with MATLAB is not possible at present.

% Rotational stage: PI M-037

% Linear stage, horizontal: PI M-531

% Linear stage, vertical: PI M-535
```

A.2.5 adjustAmplitude.m

```
%%%%%%%%%%%%%%%%%%%%%%%%%%%%%%%%%%%%%%%%%%%%%%%%%%%%%%%%%%%%%%%%%%%%%%%%%%%%
% adjustAmplitude.m
%
% [x wf timeDiv] = adjustAmplitude(ch,instrument,meas)
%
% Adjusts voltage scaling and records acoustic data.
%
% Rune Hauge & Eivind Mosland, 2012
%%%%%%%%%%%%%%%%%%%%%%%%%%%%%%%%%%%%%%%%%%%%%%%%%%%%%%%%%%%%%%%%%%%%%%%%%%%%

function [x wf timeDiv] = adjustAmplitude(ch,instrument,meas)

% Stop aquisition.
fprintf(instrument.scope,'ACQ:STATE␣STOP');
% Wait to ensure that the scope wipes its memory.
pause(1)
% Start aquisition.
fprintf(instrument.scope,'ACQ:STATE␣RUN');
```

```
% Wait for averaging.
pause(meas.wait_scaling)

% Read waveform.
[x wf timeDiv] = DPO_les(ch,instrument.scope);
maxV = max(wf);

% Get current scaling.
Scaling = str2num(query(instrument.scope,['CH',num2str(ch),':SCA?']));

% A minimum scaling of 10 mV/div is used to ensure that the noise prior to
% averaging is within the voltage range.
verticalScalings = [10e-3, 20e-3, 50e-3, 100e-3, 200e-3, 500e-3 1 2];
ind = find(Scaling==verticalScalings);
if isempty(ind)
    disp('ind␣er␣tom!')
    ind = 1;
    fprintf(instrument.scope,['CH',num2str(ch),':SCA␣',num2str(verticalScalings(ind))]);

    [x wf timeDiv] = DPO_les(ch,instrument.scope);
    maxV = max(wf);
end

% Half the number of vertical division. 8 visible divisons on the screen
% and one additional above and below.
scrnRows = 5;

% Adjust vertical scaling and measure until no clipping.
finished = 0;
while ~finished
    %disp(['Current volt/div: ',num2str(verticalScalings(ind))])
    if maxV >= scrnRows*verticalScalings(ind)
        Scaling = verticalScalings(ind+1);
        fprintf(instrument.scope,['CH',num2str(ch),':SCA␣',num2str(Scaling)]);
        ind = ind +1;

        % Wait for averaging to finish.
        pause(meas.wait_scaling)

        %disp('Measuring')
        [x wf timeDiv] = DPO_les(ch,instrument.scope);
        maxV = max(wf);

    elseif ind ~= 1 && maxV < scrnRows*verticalScalings(ind-1)
        %disp('Decreasing scaling')
        Scaling = verticalScalings(ind-1);
        fprintf(instrument.scope,['CH',num2str(ch),':SCA␣',num2str(Scaling)]);
        ind = ind -1;

        % Wait for averaging to finish.
        pause(meas.wait_scaling)

        %disp('Measuring')
        [x wf timeDiv] = DPO_les(ch,instrument.scope);
        maxV = max(wf);
    else
        finished = 1;
    end
end

end
```

A.2.6 adjustTime.m

```
%%%%%%%%%%%%%%%%%%%%%%%%%%%%%%%%%%%%%%%%%%%%%%%%%%%%%%%%%%%%%%%%%%%%%%%%%%%%%%%%%%%%%%%%%%%%%%%%%%%%%%%%
% adjustTime.m
%
% adjustTime(type,instrument,meas)
%
% Sets time scaling and adjusts window position.
%
% Rune Hauge & Eivind Mosland, 2012/2013
%%%%%%%%%%%%%%%%%%%%%%%%%%%%%%%%%%%%%%%%%%%%%%%%%%%%%%%%%%%%%%%%%%%%%%%%%%%%%%%%%%%%%%%%%%%%%%%%%%%%%%%%

function adjustTime(type,instrument,meas)
    import instrument
```

```

    % Set scaling.
    if ~strcmp(type,'noise')

        % Get frequeny and number of cycles.
        freq = query(instrument.generator,'FREQ?');
        cycles = query(instrument.generator,'BURS:NCYC?');
        % Compute appropriate scaling.
        SignalLength = 1/str2num(freq)*str2num(cycles);
        minScaling = SignalLength/10;

        if minScaling <= 40e-6
            Scaling = 40e-6;
        elseif minScaling <= 100e-6
            Scaling = 100e-6;
        elseif minScaling <= 200e-6
            Scaling = 200e-6;
        elseif minScaling <= 400e-6
            Scaling = 400e-6;
        elseif minScaling <= 1e-3
            Scaling = 1e-3;
        end

        % disp(['Desired scaling found to be ',num2str(Scaling),...
        % ' Adjusting scope...'])
        fprintf(instrument.scope,['HOR:SCA␣',num2str(Scaling)]);
    else
        noise_Scaling = 40e-6;
        fprintf(instrument.scope,['HOR:SCA␣',num2str(noise_Scaling)]);
    end

    % Set window position.
    if strcmp(type,'electric')
        triggerDelay = Scaling*5;
    elseif strcmp(type,'acoustic')
        % Ensures that the onset of the acoustic signal is recorded.
        triggerDelay = Scaling*5 + (meas.distance-0.01)/343;
    elseif strcmp(type,'noise')
        triggerDelay = (meas.distance+0.002)/343 - noise_Scaling*5;
    end
    fprintf(instrument.scope,['HOR:DEL:TIM␣',num2str(triggerDelay)]);
end
```

A.2.7 DPO_les.m

```
%%%%%%%%%%%%%%%%%%%%%%%%%%%%%%%%%%%%%%%%%%%%%%%%%%%%%%%%%%%%%%%%%%%%%%%%
% DPO_les.m
%
% function [x,wf,tidsskala] = DPO_les(ch,scope)
% Script that communicates with Tektronix DPO3012
% 8-bit unsigned characters. Windows version.
%
% Espen Storheim
%%%%%%%%%%%%%%%%%%%%%%%%%%%%%%%%%%%%%%%%%%%%%%%%%%%%%%%%%%%%%%%%%%%%%%%%

function [x,wf,tidsskala] = DPO_les(ch,scope)

    fprintf(scope,'HOR:RECO␣100000');

    fprintf(scope,'DAT:SOUR␣CH1');
    fprintf(scope,'DAT:START␣1');
    fprintf(scope,['DAT:STOP␣' num2str(100000)]);

    % Gating mode {SCREEN | CURSOR | NON}. Horizontal.
    fprintf(scope,'SAV:WAVE:GATI␣NON');
    fprintf(scope,['DAT:SOUR␣REF1']);
    fprintf(scope,['SAV:WAVE␣CH' num2str(ch) ',REF1']);
    pause(5);
    fprintf(scope,['DAT:SOUR␣CH' num2str(ch)]);

    fprintf(scope,'WFMO:XZE?');
    xze = fscanf(scope,'%f');

    fprintf(scope,'WFMO:XIN?');
    xin = fscanf(scope,'%f');

```

```
    fprintf(scope,'WFMO:YOF?');
    YOF = fscanf(scope,'%f');

    fprintf(scope,'WFMO:YMU?');
    YMU = fscanf(scope,'%f');

    fprintf(scope,'WFMO:YZE?');
    YZE = fscanf(scope,'%f');

    fprintf(scope,['DAT:SOUR␣REF1']);

    fprintf(scope,'CURV?');

    b = fread(scope,100000,'int8');
    %disp('Finished reading')
    %%%wf = b(8:end-1);
    %x = xze:xin:(xze+9999*xin);
    %x = linspace(xze,100000*xze,length(wf));
    %wf = ((wf-YOF)*YMU) + YZE;

    fprintf(scope,'HOR:SCA?');
    tidsskala = fscanf(scope,'%f');

    wf = b(9:end-1);
    x = xze:xin:(xze+(length(wf)-1)*xin);

    wf = ((wf-YOF)*YMU) + YZE;
end
```

A.2.8 instrument_shutdown.m

```
%%%%%%%%%%%%%%%%%%%%%%%%%%%%%%%%%%%%%%%%%%%%%%%%%%%%%%%%%%%%%%%%%%%%%%%%%%%%%%
% instrument_shutdown.m
%
% Shut down the instruments and clean up.
% Part of the software for the new measurement setup in air.
%
% Espen Storheim, 11/09-2012.
%%%%%%%%%%%%%%%%%%%%%%%%%%%%%%%%%%%%%%%%%%%%%%%%%%%%%%%%%%%%%%%%%%%%%%%%%%%%%%

% Close all the handles used for communication with the various
% instruments.

fclose(instrument.humidity)
%fclose(instrument.temperature)
%fclose(instrument.pressure)
fclose(instrument.generator)
fclose(instrument.scope)
fclose(instrument.filter)

delete(instrfindall)
```

A.2.9 VaisalaHMT313.m

```
% VaisalaHMT313.m
% Script which reads the temperature and relative humidity from the Vaisala
% HMT313 temperature/humidity sensor. It uses serial communication.
% Warning! This script only works on Windows at present.
% There are two different operational modes:
% - 'single', used to do a spot reading. Warning: The command
% delete(instrfindall) is executed every time to delete existing instrument
% handles and prevent overflow.
% - 'cont', used for continuous reading. This requires the port handle s to
% be initialized in an external script.
%
% Espen Storheim, 18/05-2011
% function [T,RH] = VaisalaHMT313

function [T, RH] = VaisalaHMT313(handle)
    fprintf(handle,'send');
    a = fscanf(handle,'%f%f');
    %a = fscanf(handle);
    %a = strread(a,'%s',2);
    T = a(2);
    RH = a(1);
end
```

A.2.10 `findpeakToPeak.m`

```matlab
% findPeakToPeak
%
% function peakToPeak = findPeakToPeak(signal,signal_f,sample_rate,l_lim,u_lim)

function peakToPeak = findPeakToPeak(signal,signal_f,sample_rate,l_lim,u_lim)
    %% Acquire peak-to-peak values of the steady-state intervals
    signal = signal(:,l_lim:u_lim);

    for nn = 1:length(signal(:,1))
        %disp(['Freq: ',num2str(signal_f(nn))])
        zero = mean(signal(nn,:));
        cross = zero-signal(nn,:);
        found = find((sign(cross(2:end))-sign(cross(1:end-1)))==2 | ...
         (sign(cross(2:end))-sign(cross(1:end-1)))==-2);
        samples = found(1);
        % Found first zero-cross, now continuing find the voltage peak-to-peak
        % on each periode

        step = round(1/signal_f(nn)*sample_rate(nn));

        i = 1;
        while samples+step<length(signal(nn,:))
            maximum = max(signal(nn,samples:samples+step));
            minimum = min(signal(nn,samples:samples+step));
            peakToPeak_freq(i) = (maximum-minimum);
            i = i + 1;
            samples = samples + step;
        end


%          Plotter den siste perioden for ein gitt frekvens dersom ein vil sjaa
%          om inndelinga er fornuftig.
%              plot(signal(found(1):found(2)))
%              pause(2)

        peakToPeak(nn) = mean(peakToPeak_freq);
        %disp(['pp: ',num2str(peakToPeak(nn))])

    end
end
```

A.2.11 `findPeakToPeak_FFT.m`

```matlab
% findpeakToPeak_FFT

function pp_FFT = findPeakToPeak_FFT(V_out,V_out_f,sample_rate,l_lim_ac,u_lim_ac)

    % Voltage out (acoustical signal) FFT
    signal = V_out(:,l_lim_ac:u_lim_ac);

    for nn = 1:length(signal(:,1))
        N = 2e5;
        Fs = sample_rate;
        sigL = length(signal(nn,:));
        sig_spect = fft(signal(nn,:),N)*2/sigL;
        sig_spect = fftshift(sig_spect);
        ff = -Fs/2:Fs/N:Fs/2-Fs/N;
        % Interpolate the measured frequencies upon the FFT spectra
        start = find(ff==0);
        stop = find(ff==V_out_f(end));
        spect_meas = interp1(ff(start:stop),sig_spect(start:stop),V_out_f);
        pp_FFT(nn) = 2*abs(spect_meas(nn));
    end

end
```

A.3 Other

A.3.1 `Khimunin_diffractioncorrection.m`

```matlab
% Khimunin_diffractioncorrection.
%
% Calculate the diffraction correction for uniformly vibrating piston in a
```

```
% rigid baffle of infinite extent according to the expression given by Khimunin in
% A. S. Khimunin, "Numerical calculation of the diffraction corrections
% for the precise measurement of ultrasound absorption", Acustica 27(4),
% 173-181 (1972).
%
% There is a slight modification in the present script compared to the
% article. The output here is K = |p/p0| = A + iB, while the "output" in
% the article is |p/p0| = sqrt(A^2 + B^2). This allows the user to
% calculate both the magnitude and phase.
%
% Note: This version is limited to a fixed axial distance, z.
%
% Input variables:
% k : The wavenumber.
% a : The radius of the piston.
% z : The axial distance.
% N : Number of trapezoids in the numerical integration. 1000 is typically OK.
%
% Output variables:
% K : The complex diffraction correction.
%
% Espen Storheim (2009-2012).

function K = Khimunin_diffractioncorrection(k,a,z,N)

theta = pi*[0:1:N]/(2*N);    % Khimunins integration variable.
S = z/a^2*2*pi./k;           % Scaled axial distance.
ka = k*a;                    % ka number.

% Calculate the diffraction correction for the frequencies specified.
for ii = 1:length(ka)

    % Calculate the integrand for C and D in Eq. (3).
    CC = cos(sqrt(S(ii)^2*ka(ii)^4/(2*pi)^2 + 4*ka(ii)^2.*(cos(theta)).^2)).*(sin(theta)).^2;
    DD = sin(sqrt(S(ii)^2*ka(ii)^4/(2*pi)^2 + 4*ka(ii)^2.*(cos(theta)).^2)).*(sin(theta)).^2;

    % Numerical integration of C and D with the trapezoidal rule.
    C = theta(2)*(sum(CC(1:end)) - 0.5*(CC(1) + CC(end)));
    D = theta(2)*(sum(DD(1:end)) - 0.5*(DD(1) + DD(end)));

    % Calculate the real and imaginary part of the diffraction
    % correction.
    A = 1 - C*4/pi*cos(ka(ii)^2*S(ii)/(2*pi)) - D*4/pi*sin(ka(ii)^2*S(ii)/(2*pi));
    B = D*4/pi*cos(ka(ii)^2*S(ii)/(2*pi)) - C*4/pi*sin(ka(ii)^2*S(ii)/(2*pi));
    KK = A + 1i*B;

    % Store the complex diffraction correction for each ka number.
    K(ii) = KK;

    % Clear temp variables.
    clear CC DD C D A B

end


end
```

A.3.2 absorpsjonluft.m

Calculate the absorption coefficient in air [42].

```
function korr_trykk = absorbsjonluft(frekvens,trykk,fukt,temp )

%Vidar Knappskog 2007
%Programmet regner ut absorbsjonskoeffisienten for hver frekvens
f=frekvens;
p=trykk;
h_rel=fukt;
T=temp;

%f=10000;                %Frekvens
%p=101.325;             %Atmosfaeretrykket
%h_rel=50;               %Relativ luftfuktighet
%T=253.15;              %Temperatur i Kelvin


T_01=273.16;    %Trippelpunkts isotermisk temperatur(0.01C)
```

```
p_ref=101.325;  % Referansetrykket i kPa( 1atm)
T_ref=293.15;   %Referanse temperatur Kelvin.(20 deg C)

%Finner foerst den molare konsentrasjonen av vann i luften
V=10.79586*(1-(T_01/T))-5.02808.*log10(T/T_01)+1.50474*(10^-4)*(1-10^(-8.29692*(T/T_01-1)))+0.4
h=h_rel*(10^V)*(p/p_ref)^-1;    %Molare luftfuktighet

%Relaksasjons frekvens for Oksygen
f_rO=(p/p_ref)*(24 + ((4.04*(10^4)*h)*(0.02+h)/(0.391+h)));

%Relaksasjonsfrekvensen for Nitrogen
f_rN=(p/p_ref)*(T/T_ref)^(-0.5)*(9+280*h*exp(-4.170*((T/T_ref)^(-1/3)-1)));

%Dempningskoeffisient
alfa=8.686*f^2*( (1.84*(10^-11)*(p/p_ref)^-1*(T/T_ref)^(0.5)) + (T/T_ref)^(-5/2)*(0.01275*(exp

% Absorbsjon i dB/km
korr_trykk=alfa*1000;
```

Appendix B

FEMP-structures

The FEMP -structures used in this work and not included in FEMP 5.0. Described in Section 4.3.

B.1 piezodiskwidefrontglue

```
%! Piezoceramic disk with a wider front layer and a
%! glue layer, vibrating in vacuum.
%!
%! Based on work by Espen Storheim
%!
%! Eivind Mosland 2013

function [read]=read_inn_project(read,commands);

%%%%%%%%%%%%%%%%%%%%%%%%%%%%%%%%%%%%%%%%%%%%%%%%%%%%%%%%%%%%%%%%%%%%%%%%%%%
% read_inn_project.m which should be in the working directory
%
% Part of FEMP (Finite Element Modeling of Piezoelectric structures)
% Programmed by Jan Kocbach (jan@kocbach.net)
% (C) 2000 Jan Kocbach. This file is free software;  you can redistribute
% it and/or modify it only under the the terms of the GNU GENERAL PUBLIC
% LICENSE which should be included along with this file.
% (C) 2000-2010 Christian Michelsen Research AS
%%%%%%%%%%%%%%%%%%%%%%%%%%%%%%%%%%%%%%%%%%%%%%%%%%%%%%%%%%%%%%%%%%%%%%%%%%%

% Put a file read_inn_project.m in your project directory to define local
% FEMP input commands. Also include init_const_project.m in this directory
% and define the commands there.

global glob;
read = read;


if ~isempty(read.piezodiskwidefrontglue)
    read.points=[]; read.areas=[]; read.materials=[]; read.dof=[]; read.restraints=[];

    %! Read parameters from the inn-file.
    r = read.piezodiskwidefrontglue(1,1,:); %! Radius of the piezoceramic element.
    t = read.piezodiskwidefrontglue(1,2,:); %! Thickness of the piezoceramic element.
    elr = read.piezodiskwidefrontglue(1,3,:); %! Number of elements/wavelength in the
    % radial direction in the piezoceramic element.
    elt = read.piezodiskwidefrontglue(1,4,:); %! Number of elements/wavelength in the
    % thickness direction in the piezoceramic element.
    matnum = read.piezodiskwidefrontglue(1,5,:); %! Piezo materialnumber.
    rfront = read.piezodiskwidefrontglue(1,6,:); %! Radius frontlayer.
    tfront = read.piezodiskwidefrontglue(1,7,:); %! Thickness frontlayer.
    matnumfront = read.piezodiskwidefrontglue(1,8,:); %! Frontlayer materialnumber.
    tglue = read.piezodiskwidefrontglue(1,9,:); %! Thickness glue.
    matnumglue = read.piezodiskwidefrontglue(1,10,:); %! Glue materialnumber.

    for s=1:size(r,3)

        T(s) = t(s)+tglue(s)+tfront(s);

        %! Specify the points in the model.
        read.points(:,:,s) = [  1, 0, -T(s)/2;
                                2, r(s), -T(s)/2;
```

```
                                3, 0, -T(s)/2+t(s);
                                4, r(s), -T(s)/2+t(s);
                                5, rfront(s), -T(s)/2+t(s);
                                6, 0, -T(s)/2+t(s)+tglue(s);
                                7, r(s), -T(s)/2+t(s)+tglue(s);
                                8, rfront(s), -T(s)/2+t(s)+tglue(s);
                                9, 0, T(s)/2;
                                10, r(s), T(s)/2;
                                11, rfront(s), T(s)/2;
                                ];

        %! Set up the different areas in the model.
        read.areas(:,:,s) = [   %! Piezoceramic element.
                                1, 3, 1, 2, 4, elr(s), elt(s), 0, 0;
                                %! Glue layer.
                                3, 6, 3, 4, 7, elr(s), elt(s), 0, 0;
                                3, 7, 4, 5, 8, elr(s), elt(s), 0, 0;
                                %! Matching layer.
                                2, 9, 6, 7, 10, elr(s), elt(s), 0, 0;
                                2, 10, 7, 8, 11, elr(s), elt(s), 0, 0;
                                ];

        %! Define the various materials.
        read.materials(:,:,s) = [   1 glob.globvariables.piezo matnum(s);
                                    2 glob.globvariables.mechanic matnumfront(s);
                                    3 glob.globvariables.mechanic matnumglue(s);
                                ];

        %! "Ground" the front electrode of the transmitter.
        read.dof(:,:,s) = [-1e-9, r(s)+1e-9, -T(s)/2+t(s)-1e-9, ...
                              T(s)/2+t(s)+1e-9, glob.free.ep];

        %! Impose a 1 V electrical potential at the rear surface of the transmitter.
        read.restraints(:,:,s) = [-1e-9, r(s)+1e-9, -T(s)/2-1e-9, ...
                                     -T(s)/2+1e-9, glob.free.ep, 1];

    end
end
```

B.2 transducervacuum

```
%! Set up the structure for the piezoelectric transducer developed during
%! this work, radiating in vacuum.
%!
%! Eivind Mosland 2013

function [read]=read_inn_project(read,commands);

%%%%%%%%%%%%%%%%%%%%%%%%%%%%%%%%%%%%%%%%%%%%%%%%%%%%%%%%%%%%%%%%%%%%%%%%
% read_inn_project.m which should be in the working directory
%
% Part of FEMP (Finite Element Modeling of Piezoelectric structures)
% Programmed by Jan Kocbach (jan@kocbach.net)
% (C) 2000 Jan Kocbach. This file is free software;  you can redistribute
% it and/or modify it only under the the terms of the GNU GENERAL PUBLIC
% LICENSE which should be included along with this file.
% (C) 2000-2010 Christian Michelsen Research AS
%%%%%%%%%%%%%%%%%%%%%%%%%%%%%%%%%%%%%%%%%%%%%%%%%%%%%%%%%%%%%%%%%%%%%%%%

% Put a file read_inn_project.m in your project directory to define local
% FEMP input commands. Also include init_const_project.m in this directory
% and define the commands there.

global glob;
read = read;

if ~isempty(read.transducervacuum)
    read.points=[]; read.areas=[]; read.materials=[]; read.dof=[]; read.restraints=[];

    %! Read parameters from the inn-file.
    r = read.transducervacuum(1,1,:); %! Radius of the piezoceramic element.
    t = read.transducervacuum(1,2,:); %! Thickness of the piezoceramic element.
    elr = read.transducervacuum(1,3,:); %! Number of elements/wavelength in
    % the radial direction in the piezoceramic element.
    elt = read.transducervacuum(1,4,:); %! Number of elements/wavelength in
    % the thickness direction in the piezoceramic element.
```

```
    matnum = read.transducervacuum(1,5,:); %! Piezo materialnumber.
    rfront = read.transducervacuum(1,6,:); %! Radius frontlayer.
    tfront = read.transducervacuum(1,7,:); %! Thickness frontlayer.
    matnumfront = read.transducervacuum(1,8,:); %! Frontlayer materialnumber.
    rglue = read.transducervacuum(1,9,:); %! Radius glue.
    tglue = read.transducervacuum(1,9,:); %! Thickness glue.
    matnumglue = read.transducervacuum(1,10,:); %! Glue materialnumber.
    lcasing = read.transducervacuum(1,11,:); %! Length of the casing.
    tcasing = read.transducervacuum(1,12,:); %! Thickness of the casing.
    matnumcasing = read.transducervacuum(1,13,:); %! Casing material number.
    matnumbacking = read.transducervacuum(1,14,:); %! Backing material number.

    for s=1:size(r,3)

        T(s) = lcasing(s);

        %! Specify the points in the model.
        read.points(:,:,s) = [  1, rfront(s) + rglue(s), -T(s)/2;
                                2, rfront(s) + rglue(s) + tcasing(s), -T(s)/2;
                                3, 0, T(s)/2 - tfront(s) - tglue(s) - t(s);
                                4, r(s), T(s)/2 - tfront(s) - tglue(s) - t(s);
                                5, 0, T(s)/2 - tfront(s) - tglue(s);
                                6, r(s), T(s)/2 - tfront(s) - tglue(s);
                                7, rfront(s), T(s)/2 - tfront(s) - tglue(s);
                                8, rfront(s) + rglue(s), ...
                                   T(s)/2 - tfront(s) - tglue(s);
                                9, rfront(s) + rglue(s) + tcasing(s), ...
                                   T(s)/2 - tfront(s) - tglue(s);

                                10, 0, T(s)/2 - tfront(s);
                                11, r(s), T(s)/2 - tfront(s);
                                12, rfront(s), T(s)/2 - tfront(s);
                                13, rfront(s) + rglue(s), T(s)/2 - tfront(s);
                                14, rfront(s) + rglue(s) + tcasing(s), ...
                                    T(s)/2 - tfront(s);

                                15, 0, T(s)/2;
                                16, r(s), T(s)/2;
                                17, rfront(s), T(s)/2;
                                18, rfront(s) + rglue(s), T(s)/2;
                                19, rfront(s) + rglue(s) + tcasing(s), T(s)/2;

                                20, 0, -T(s)/2;
                                21, r(s), -T(s)/2;
                                22, rfront(s) + rglue(s), ...
                                    T(s)/2 - tfront(s) - tglue(s) - t(s);
                                23, rfront(s) + rglue(s) + tcasing(s), ...
                                    T(s)/2 - tfront(s) - tglue(s) - t(s);
                                ];

        %! Set up the different areas in the model.
        read.areas(:,:,s) = [   %! Piezoceramic element.
                                1, 5, 3, 4, 6, elr(s), elt(s), 0, 0;
                                %! Glue layer.
                                3, 10, 5, 6, 11, elr(s), elt(s), 0, 0;
                                3, 11, 6, 7, 12, elr(s), elt(s), 0, 0;
                                3, 12, 7, 8, 13, elr(s), elt(s), 0, 0;
                                3, 17, 12, 13, 18, elr(s), elt(s), 0, 0;
                                %! Matching layer.
                                2, 16, 11, 12, 17, elr(s), elt(s), 0, 0;
                                2, 15, 10, 11, 16, elr(s), elt(s), 0, 0;
                                %! Backing layer.
                                5, 3, 20, 21, 4, elr(s), elt(s), 0, 0;
                                5, 4, 21, 1, 22, elr(s), elt(s), 0, 0;
                                %! Casing wall.
                                4, 18, 13, 14, 19, elr(s), elt(s), 0, 0;
                                4, 13, 8, 9, 14, elr(s), elt(s), 0, 0;
                                4, 8, 22, 23, 9, elr(s), elt(s), 0, 0;
                                4, 22, 1, 2, 23, elr(s), elt(s), 0, 0;
                                ];

        %! Define the various materials.
        read.materials(:,:,s) = [   1 glob.globvariables.piezo matnum(s);
                                    2 glob.globvariables.mechanic matnumfront(s);
                                    3 glob.globvariables.mechanic matnumglue(s);
                                    4 glob.globvariables.mechanic matnumcasing(s);
```

```
                                    5 glob.globvariables.mechanic matnumbacking(s);
                                ];

        %! "Ground" the front electrode of the transmitter.
        read.dof(:,:,s) = [-1e-9, r(s)+1e-9, T(s)/2-tfront(s)-tglue(s)-1e-9, ...
                              T(s)/2-tfront(s)-tglue(s)+1e-9, glob.free.ep];

        %! Impose a 1 V electrical potential at the rear surface of the transmitter.
        read.restraints(:,:,s) = [-1e-9, r(s)+1e-9, T(s)/2-tfront(s)-tglue(s)-t(s)-1e-9, ...
                                     T(s)/2-tfront(s)-tglue(s)-t(s)+1e-9, glob.free.ep, 1];
    end
end
```

B.3 piezodiskwidefrontfluid

```
%! Piezoceramic disk with a wider matching layer, in a medium.
%! Espen Storheim, February 2013.
%! Updated 13/02-2013: Included support for parametric analysis.
%! Updated 12/02-2013: Fixed problem with the infinite elements.
%! Updated 2013 by RH & EM: Fixed meshing order.


function [read]=read_inn_project(read,commands);

%%%%%%%%%%%%%%%%%%%%%%%%%%%%%%%%%%%%%%%%%%%%%%%%%%%%%%%%%%%%%%%%%%%%
% read_inn_project.m which should be in the working directory
%
% Part of FEMP (Finite Element Modeling of Piezoelectric structures)
% Programmed by Jan Kocbach (jan@kocbach.net)
% (C) 2000 Jan Kocbach. This file is free software;  you can redistribute
% it and/or modify it only under the the terms of the GNU GENERAL PUBLIC
% LICENSE which should be included along with this file.
% (C) 2000-2010 Christian Michelsen Research AS
%%%%%%%%%%%%%%%%%%%%%%%%%%%%%%%%%%%%%%%%%%%%%%%%%%%%%%%%%%%%%%%%%%%%

% Put a file read_inn_project.m in your project directory to define local
% FEMP input commands. Also include init_const_project.m in this directory
% and define the commands there.

global glob;
read = read;


if ~isempty(read.piezodiskwidefrontfluid)
    read.points=[]; read.areas=[]; read.materials=[]; read.dof=[]; read.restraints=[];

    %! Read parameters from the inn-file.
    r = read.piezodiskwidefrontfluid(1,1,:); %! Radius of the piezoceramic element.
    t = read.piezodiskwidefrontfluid(1,2,:); %! Thickness of the piezoceramic element.
    elr = read.piezodiskwidefrontfluid(1,3,:); %! Number of elements/wavelength in the
    % radial direction in the piezoceramic element.
    elt = read.piezodiskwidefrontfluid(1,4,:); %! Number of elements/wavelength in the
    % radial direction in the piezoceramic element.
    matnum = read.piezodiskwidefrontfluid(1,5,:); %! Piezo materialnumber.
    rfront = read.piezodiskwidefrontfluid(1,6,:); %! Radius frontlayer.
    tfront = read.piezodiskwidefrontfluid(1,7,:); %! Thickness frontlayer.
    matnumfront = read.piezodiskwidefrontfluid(1,8,:); %! Frontlayer materialnumber.
    elfluid = read.piezodiskwidefrontfluid(1,9,:); %! Elements/wavelength in the fluid.
    rf = read.piezodiskwidefrontfluid(1,10,:); %! Rinf, i.e. radius of the finite elements.
    matnumfluid = read.piezodiskwidefrontfluid(1,11,:); %! Medium materialnumber.
    rinf = 2*rf; %! Radius of the infinite elements.
    zf = 0.6*rf; %! Square fluid region in front and to the rear.

    for s=1:size(r,3)
        %! Angles used to generate the curved finite and infinite areas.
        theta1 = atan(tfront(s)/rfront(s));
        theta2 = atan((tfront(s)+zf(s))/rfront(s));
        theta3 = atan((tfront(s)+zf(s))/r(s));
        theta4 = atan(t(s)/rfront(s));
        theta5 = atan((t(s)+zf(s))/rfront(s));
        theta6 = atan((t(s)+zf(s))/r(s));

        %! Specify the points in the model.
        read.points(:,:,s) = [  1, 0, -t(s);
                                2, r(s), -t(s);
```

```
                                3, 0, 0;
                                4, r(s), 0;
                                5, rfront(s), 0;
                                6, 0, tfront(s);
                                7, r(s), tfront(s);
                                8, rfront(s), tfront(s);
                                9, rfront(s), -t(s);
                                10, 0, -rf(s);
                                11, rf(s)*cos(theta5), -rf(s)*sin(theta5);
                                12, rf(s)*cos(theta4), -rf(s)*sin(theta4);
                                13, rf(s), 0;
                                14, rf(s)*cos(theta1), rf(s)*sin(theta1);
                                15, rf(s)*cos(theta2), rf(s)*sin(theta2);
                                16, rf(s)*cos(theta3), rf(s)*sin(theta3);
                                17, 0, rf(s);
                                18, 0, tfront(s)+zf(s);
                                19, r(s), tfront(s)+zf(s);
                                20, rfront(s), tfront(s)+zf(s);
                                21, 0, -rinf(s);
                                22, rinf(s)*cos(theta5), -rinf(s)*sin(theta5);
                                23, rinf(s)*cos(theta4), -rinf(s)*sin(theta4);
                                24, rinf(s), 0;
                                25, rinf(s)*cos(theta1), rinf(s)*sin(theta1);
                                26, rinf(s)*cos(theta2), rinf(s)*sin(theta2);
                                27, rinf(s)*cos(theta3), rinf(s)*sin(theta3);
                                28, 0, rinf(s);
                                29, 0, -t(s)-zf(s);
                                30, r(s), -t(s)-zf(s);
                                31, rfront(s), -t(s)-zf(s);
                                32, rf(s)*cos(theta6), -rf(s)*sin(theta6);
                                33, rinf(s)*cos(theta6), -rinf(s)*sin(theta6);
                                ];

        %! Set up the different areas in the model.
        read.areas(:,:,s) = [   %! Piezoceramic element.
                                1, 3, 1, 2, 4, elr(s), elt(s), 0, 0;
                                %! Matching layer.
                                2, 6, 3, 4, 7, elr(s), elt(s), 0, 0;
                                2, 7, 4, 5, 8, elr(s), elt(s), 0, 0;
                                %! Square fluid reqion.
                                3, 4, 2, 9, 5, elr(s), elt(s), 0, 0;
                                3, 18, 6, 7, 19, elr(s), elt(s), 0, 0;
                                3, 19, 7, 8, 20, elr(s), elt(s), 0, 0;
                                3, 2, 1, 29, 30, elr(s),elt(s), 0, 0;
                                3, 2, 30, 31, 9, elr(s), elt(s), 0, 0;
                                %! Finite fluid elements with a curvature.
                                3, 18, 19, 16, 17, elfluid(s), elfluid(s), 0, 3;
                                3, 19, 20, 15, 16, elfluid(s), elfluid(s), 0, 3;
                                3, 20, 8, 14, 15, elfluid(s), elfluid(s), 0, 3;
                                3, 8, 5, 13, 14, elfluid(s), elfluid(s), 0, 3;
                                3, 5, 9, 12, 13, elfluid(s), elfluid(s), 0, 3;
                                3, 9, 31, 11, 12, elfluid(s), elfluid(s),  0, 3;
                                3, 31, 30, 32, 11, elfluid(s),elfluid(s), 0, 3;
                                3, 30, 29, 10, 32, elfluid(s), elfluid(s), 0, 3;
                                %! Infinite elements.
                                4, 32, 10, 21, 33, elfluid(s), 1, 3, 3;
                                4, 11, 32, 33, 22, elfluid(s), 1, 3, 3;
                                4, 12, 11, 22, 23, elfluid(s), 1, 3, 3;
                                4, 13, 12, 23, 24, elfluid(s), 1, 3, 3;
                                4, 14, 13, 24, 25, elfluid(s), 1, 3, 3;
                                4, 15, 14, 25, 26, elfluid(s), 1, 3, 3;
                                4, 16, 15, 26, 27, elfluid(s), 1, 3, 3;
                                4, 17, 16, 27, 28, elfluid(s), 1, 3, 3;
                                ];

        %! Define the various materials.
        read.materials(:,:,s) = [   1 glob.globvariables.piezo matnum(s);
                                    2 glob.globvariables.mechanic matnumfront(s);
                                    3 glob.globvariables.fluid matnumfluid(s)
                                    4 glob.globvariables.infinitefluid matnumfluid(s)
                                ];

        %! "Ground" the front electrode of the transmitter.
        read.dof(:,:,s) = [-1e-9, r(s)+1e-9, 0-1e-9, 0+1e-9, glob.free.ep];

        %! Impose a 1 V electrical potential at the rear surface of the transmitter.
```

```
        read.restraints(:,:,s) = [-1e-9, r(s)+1e-9, -t(s)-1e-9,-t(s)+1e-9, glob.free.ep, 1];

    end
end
```

B.4 transducerfluid

```
%! Transducer with piezoelectric element, matching layer, housing cylinder
%! and backing layer, radiating in a fluid.
%!
%! Based on a FEMP model of a Massa E188/220 transducer, as presented in
%! Norli (2007), with some minor adjustments, implemented by Espen Storheim.
%!
%! Some modifications performed by Rune Hauge, 2013

function [read]=read_inn_project(read,commands);

%%%%%%%%%%%%%%%%%%%%%%%%%%%%%%%%%%%%%%%%%%%%%%%%%%%%%%%%%%%%%%%%%%%%%
% read_inn_project.m which should be in the working directory
%
% Part of FEMP (Finite Element Modeling of Piezoelectric structures)
% Programmed by Jan Kocbach (jan@kocbach.net)
% (C) 2000 Jan Kocbach. This file is free software;  you can redistribute
% it and/or modify it only under the the terms of the GNU GENERAL PUBLIC
% LICENSE which should be included along with this file.
% (C) 2000-2010 Christian Michelsen Research AS
%%%%%%%%%%%%%%%%%%%%%%%%%%%%%%%%%%%%%%%%%%%%%%%%%%%%%%%%%%%%%%%%%%%%%

% Put a file read_inn_project.m in your project directory to define local
% FEMP input commands. Also include init_const_project.m in this directory
% and define the commands there.

global glob;
read = read;

if ~isempty(read.transducerfluid)
    read.points=[]; read.areas=[]; read.materials=[]; read.dof=[]; read.restraints=[];
    tb = read.transducerfluid(1,1,:); %! Not used.
    td = read.transducerfluid(1,2,:); %! Not used.
    elr = read.transducerfluid(1,3,:); %! El/lambda, radial dir. in piezoelectric element.
    elt = read.transducerfluid(1,4,:); %! El/lambda, thickness dir. in piezoelectric element.
    matnum = read.transducerfluid(1,5,:); %! Material number of the piezoelectric element.
    tfr = read.transducerfluid(1,6,:);
    tw1 = read.transducerfluid(1,7,:);
    tw2 = read.transducerfluid(1,8,:);
    afr = read.transducerfluid(1,9,:);
    ad = read.transducerfluid(1,10,:);
    elfluid = read.transducerfluid(1,11,:);
    matnumfront = read.transducerfluid(1,12,:);
    matnumfluid = read.transducerfluid(1,13,:);
    matnumcasing = read.transducerfluid(1,14,:);
    matnumside = read.transducerfluid(1,15,:);
    matnumback = read.transducerfluid(1,16,:);
    rf = read.transducerfluid(1,17,:);

    rinff = 2*rf;
    r1 = ad;
    r2 = afr;
    r3 = r2 + tw1;
    r4 = r2 + tw2;
    T = tb + td + tfr;
    t1 = T/2;
    t2 = T/2 - tfr;
    t3 = t2 - td;
    t4 = -T/2;

for s = 1:size(tb,3)
    theta1 = atan(t1(s)/r1(s));
    theta2 = atan(t1(s)/r2(s));
    theta3 = atan(t1(s)/r3(s));
    theta4 = atan(t1(s)/r4(s));
    theta5 = atan(t2(s)/r4(s));
    theta6 = atan(t3(s)/r4(s));
    theta7 = atan(t4(s)/r4(s));
    theta8 = atan(t4(s)/r3(s));
    theta9 = atan(t4(s)/r2(s));
```

```
    theta10 = atan(t4(s)/r1(s));

    %! Specify the points in the model.
        read.points(:,:,s) = [  1 0 t1(s);
                2 r1(s) t1(s);
                3 r2(s) t1(s);
                5 r4(s) t1(s);
                6 0 t2(s);
                7 r1(s) t2(s);
                8 r2(s) t2(s);
                10 r4(s) t2(s);
                11 0 t3(s);
                12 r1(s) t3(s);
                13 r2(s) t3(s);
                15 r4(s) t3(s);
                16 0 0;
                17 0 t4(s);
                18 r1(s) t4(s);
                19 r2(s) t4(s);
                21 r4(s) t4(s);
                22 0 rf(s);
                23 rf(s)*cos(theta1) rf(s)*sin(theta1);
                24 rf(s)*cos(theta2) rf(s)*sin(theta2);
                26 rf(s)*cos(theta4) rf(s)*sin(theta4);
                27 rf(s)*cos(theta5) rf(s)*sin(theta5);
                28 rf(s)*cos(theta6) rf(s)*sin(theta6);
                29 rf(s)*cos(theta7) rf(s)*sin(theta7);
                31 rf(s)*cos(theta9) rf(s)*sin(theta9);
                32 rf(s)*cos(theta10) rf(s)*sin(theta10);
                33 0 -rf(s);
                34 0 rinff(s);
                35 rinff(s)*cos(theta1) rinff(s)*sin(theta1);
                36 rinff(s)*cos(theta2) rinff(s)*sin(theta2);
                38 rinff(s)*cos(theta4) rinff(s)*sin(theta4);
                39 rinff(s)*cos(theta5) rinff(s)*sin(theta5);
                40 rinff(s)*cos(theta6) rinff(s)*sin(theta6);
                41 rinff(s)*cos(theta7) rinff(s)*sin(theta7);
                43 rinff(s)*cos(theta9) rinff(s)*sin(theta9);
                44 rinff(s)*cos(theta10) rinff(s)*sin(theta10);
                45 0 -rinff(s);
                ];

    %! Set up the different areas in the model.
        read.areas(:,:,s) = [
                                %! Matching layer.
                                2, 2,7,8,3, elr(s), elt(s), 0, 0;
                                2, 1,6,7,2, elr(s), elt(s), 0, 0;
                                %! Piezoceramic element.
                                1, 6, 11, 12, 7, elr(s), elt(s), 0, 0;
                                %! Side layer.
                                4, 7, 12, 13, 8, elr(s), elt(s), 0, 0;
                                %! Backing layer.
                                3, 11, 17, 18, 12,elr(s), elt(s), 0, 0;
                                3, 12, 18, 19, 13,elr(s), elt(s), 0, 0;
                                %! Casing.
                                5, 3, 8, 10, 5, elr(s), elt(s), 0, 0;
                                5, 8, 13, 15, 10, elr(s), elt(s), 0, 0;
                                5, 13, 19, 21, 15, elr(s), elt(s), 0, 0;
                                %! Curved fluid regions.
                                6, 1, 2, 23, 22, elr(s), elt(s), 0, 16;
                                6, 2, 3, 24, 23, elr(s), elt(s), 0, 16;
                                6, 3, 5, 26, 24, elr(s), elt(s), 0, 16;
                                6, 5, 10, 27, 26, elr(s), elt(s), 0, 16;
                                6, 10, 15, 28, 27, elr(s), elt(s), 0, 16;
                                6, 15, 21, 29, 28, elr(s), elt(s), 0, 16;
                                6, 21, 19, 31, 29, elr(s), elt(s), 0, 16;
                                6, 19, 18, 32, 31, elr(s), elt(s), 0, 16;
                                6, 18, 17, 33, 32, elr(s), elt(s), 0, 16;
                                %! Infinite elements.
                                7, 22, 23, 35, 34, elfluid(s), 1, 16, 16;
                                7, 23, 24, 36, 35, elfluid(s), 1, 16, 16;
                                7, 24, 26, 38, 36, elfluid(s), 1, 16, 16;
                                7, 26, 27, 39, 38, elfluid(s), 1, 16, 16;
                                7, 27, 28, 40, 39, elfluid(s), 1, 16, 16;
                                7, 28, 29, 41, 40, elfluid(s), 1, 16, 16;
                                7, 29, 31, 43, 41, elfluid(s), 1, 16, 16;
```

```
                                    7, 31, 32, 44, 43, elfluid(s), 1, 16, 16;
                                    7, 32, 33, 45, 44, elfluid(s), 1, 16, 16;
                                    ];

    %! Define the various materials.
        read.materials(:,:,s) = [   1 glob.globvariables.piezo matnum(s);
                                    2 glob.globvariables.mechanic matnumfront(s);
                                    3 glob.globvariables.mechanic matnumback(s)
                                    4 glob.globvariables.fluid matnumside(s)
                                    5 glob.globvariables.mechanic matnumcasing(s)
                                    6 glob.globvariables.fluid matnumfluid(s)
                                    7 glob.globvariables.infinitefluid matnumfluid(s)
                                    ];

    %! "Ground" the front electrodes (transmitter and receiver), and set the velocity
    %! potential at the edge of of the PML regions to zero.

        read.dof(:,:,s) = [-1e-9, r1(s)+1e-9, t3(s)-1e-9, t3(s)+1e-9, glob.free.ep;
                            ];

    %! Impose a 1 V electrical potential at the rear surface of the transmitter.
        read.restraints(:,:,s) = [-1e-9, r1(s)+1e-9, t2(s)-1e-9,t2(s)+1e-9, glob.free.ep, 1];

    glob.tfront(s) = T(s)/2;
    end
end
```

Appendix C

Paper submitted for the proceedings of the 36$^{\text{th}}$ Scandinavian Symposium on Physical Acoustics, Geilo 3$^{\text{rd}}$ - 6$^{\text{th}}$ February 2013

36^{th} *Scandinavian Symposium on Physical Acoustics, Geilo, Norway, 3-6 February 2013*

Finite element modeling of ultrasound measurement systems for gas. Comparison with experiments in air.

Rune Hauge[a,b,*], Eivind Mosland[a,b], Espen Storheim[a,b], Per Lunde[a,c,b], Magne Vestrheim[a,b], and Jan Kocbach[c,b]

[a] *University of Bergen, Department of Physics and Technology, P.O. Box 7803, N-5020 Bergen, Norway*
[b] *The Michelsen Centre for Industrial Measurement Science and Technology, P.O. Box 6031, N-5892 Bergen, Norway*
[c] *Christian Michelsen Research AS (CMR), P.O. Box 6031, N-5892 Bergen, Norway*

Abstract

System modeling can be of considerable value for many applications involving ultrasound measurement systems. The objective of the present work is (a) to develop a system model based on finite element (FE) modeling of the transmitting and receiving transducers and sound propagation in the fluid medium, combined with transmission line modeling of the transmitting and receiving electronics and cables, and (b) to compare the system model with measurements. Signal propagation can be modeled in time and frequency domains (signal waveforms and frequency spectra), including description of nearfield diffraction effects. Simulations are compared with measurements for the transmit-receive voltage-to-voltage transfer function of two piezoelectric ceramic disk transducers vibrating in air at 1 atm., over the frequency range of the first two radial modes of the disks.

1. Introduction

Accurate simulation tools for ultrasonic measurement systems are important for design and optimization of ultrasonic measurement instruments, quality assurance in construction of transducers, analysis of measurement data, etc. Applications include e.g. fiscal measurement of oil and gas [1, 2], calorific value measurements and gas characterization [3], accurate measurements of sound speed and absorption in gases and liquids [4, 5], and non-destructive testing and evaluation.

System models in use today include models based on the Mason model (or similar one-dimensional descriptions) for the transmitting and receiving transducers, combined e.g. with uniform piston type of radiation models for the wave propagation in the medium [6–10]; simplified electrical transmission line descriptions [11]; an electroacoustic measurement model [12–14], to more advanced FE based descriptions [15, 16].

In the present work a comprehensive model of an axisymmetric ultrasonic transmit-receive measurement system is developed [17], which combines models for the electrical components (signal generator, receiver and cables), piezoelectric transmit and receive transducers, and sound propagation in a fluid medium. Under assumptions of the system to be linear, a frequency domain transfer function description is used for the various electrical/acoustical/electroacoustical components of the system. Fourier synthesis methods are used for description of signal propagation in time domain. Wave propagation in the transducers and the fluid medium is described using three-dimensional FE modeling, including description of nearfield diffraction effects. Simulations are compared with experimental measurements for the transmit-receive voltage-to-voltage transfer function of two piezoelectric ceramic circular disk transducers vibrating in air at 1 atm., over the frequency range of their first two radial modes, from the input voltage of the transmitting transducer to the received voltage recorded by the oscilloscope.

2. Theory

The electroacoustic measurement system is modeled by representing the key parts of the system as modules, see Fig. 1.

---

[*] Corresponding author. Email adress: `rune.oyerhamn@gmail.com`.

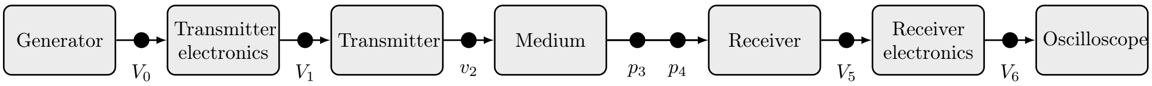

Figure 1: The electroacoustic system model with key parts represented by modules.

In Fig. 1, V_0 is the output voltage from the signal generator, V_1 is the input voltage to the transmitting transducer, v_2 is the particle velocity at the center of the transmitting transducers front, and $p_3(d_0)$ is the free-field axial sound pressure in the medium at the reference distance $z = d_0$, where z is the axial distance from the transmitters front. $p_4(z)$ is the axial free-field sound pressure in the medium at z, which is the center of the receiving transducers front face, in absence of the receiver. V_5 is the output voltage from the receiving transducer, and V_6 is the voltage recorded by the oscilloscope. By use of transfer functions, the signal propagation through each module or the complete system can be calculated. By combining the transfer functions for each module, the output voltage of the measurement system, V_6, can be calculated based on the input voltage to the system, V_0.

Calculation of the transfer function H_{1m6}^{VV}, from the measured node 1 voltage to the measured node 6 voltage
Some assumptions are applied to the system model illustrated in Fig. 1: (1) infinite termination of the receiver[1], (2) the transmitter and receiver are coaxially aligned, and (3) the signal generator is modeled using a Thévenin circuit. The electromotive force of the generator is termed V_{gen}, the output impedance of the generator is termed Z_{gen}. In Fig. 2, the system model from Fig. 1 is represented in greater detail and with open-circuit conditions for the receiver.

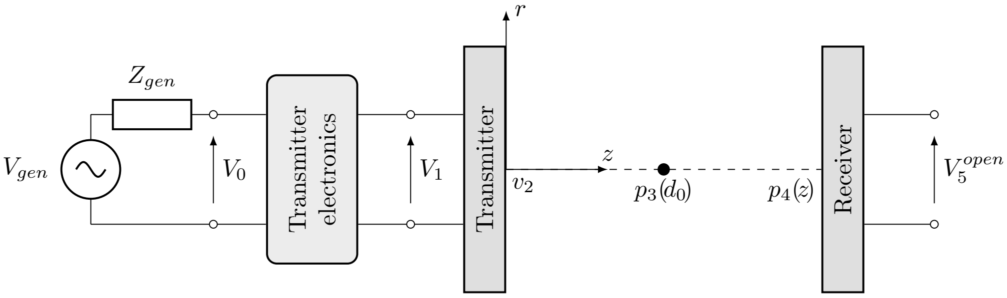

Figure 2: The electroacoustic system model with infinite impedance termination of the receiving transducer.

In Fig. 2 V_5^{open} is the open-circuit output voltage from the receiver. The voltage-to-voltage transfer function from node 1 to node 5 with open-circuit conditions, $H_{15}^{VV,open}$, is expressed as [18]

$$H_{15}^{VV,open} = \frac{V_5^{open}}{V_1} = \frac{c}{i\pi a^2 f V_1} p_4(z_\infty) z_\infty M_V H^{dif}(z) e^{ik(z_\infty - z)}. \tag{1}$$

In Eq. (1) c is the sound speed in the medium, a is the radius of the transmitting transducer, f is the frequency, $k = \omega/c$ is the wavenumber, $p_4(z_\infty)$ is the free-field axial sound pressure at the far-field distance z_∞, M_V is the open-circuit receiving voltage sensitivity [19], $H^{dif}(z)$ is the diffraction correction [20] and z is the axial distance from the transmitter to the receiver.

M_V is expressed by assuming that the transmitting and receiving transducers are equal, linear, passive, reversible and reciprocal, using the complex spherical reciprocity parameter, J, the transmitting voltage response, S_V, and the electrical impedance of the transmitting transducer, Z_T i.e. $M_V = JS_V Z_T$ [21].

The diffraction correction at distance z, $H^{dif}(z)$ is formulated by Khimunin [20]. Khimunins diffraction correction is valid for a uniformly vibrating piston source and an acoustical transparent measurement area of equal radius as the source. The use of a plane piston as source is a simplification in the system model represented in Fig. 2, where the source is modeled using FE modeling.

---

[1] For deriving Eq. (1). $H_{15}^{VV,open}$ is later expanded to include finite termination of the receiver, details given in [17].

The oscilloscope measures the input voltage of the transmitter in addition to the voltage received by the receiver. The cables connecting the signal generator to the transmitting transducer and the oscilloscope are modeled using the distributed element model [22]. The cables are in the model assumed to be lossless transmission lines. Due to these cables the recorded input voltage of the transmitter is not equal to V_1. The recorded voltage is termed $V_{1,m}$.

The receiving electronics consists of a measurement amplifier, a frequency filter, the oscilloscope, and the coaxial cables connecting them. The transfer function from V_5^{open} to V_6 is calculated by treating the cables as lossless transmission lines and model them using the distributed element model. The gain in the amplifier is accounted for as the data is collected from the oscilloscope, and in this preliminary implementation of the system model, the frequency filter is assumed not to affect the voltage at the measurement frequency, and the measurement amplifier is assumed not to affect the voltage other than the gain it applies to the magnitude of the measured voltage. For more details regarding the implementation of the measurement instruments in the system model, cf. [17].

$H_{15}^{VV,open}$ is expanded to include the transmitting and receiving electronics and cables (with some limitations, as mentioned above). The new transfer function is termed $H_{1m6}^{VV} = V_6/V_{1,m}$. This function corresponds to the transfer function found from the experiments.

The absorption in the medium is accounted for in the system model by introducing a complex wavenumber[2], $\kappa = k - i\alpha$, where k is the real wavenumber and α is the absorption coefficient in the medium, calculated using [23]. A harmonic time dependency of $e^{i\omega t}$ is assumed.

3. Experiments and simulations

3.1. Experimental setup

Electrical measurements have been done using a Hp 4192A impedance analyzer for determining the admittance of the piezoelectric elements.

A picture of the experimental setup used for the acoustical measurements is shown in Fig. 3.

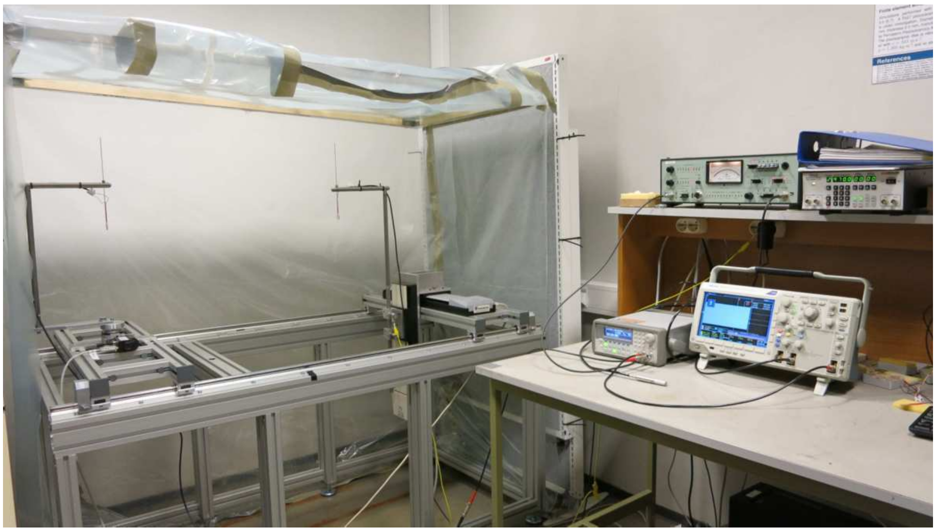

Figure 3: A picture of the experimental setup used for the acoustical measurements.

In the acoustical measurements the transmitting transducer is driven by an Agilent 33220A signal generator. The generator applies a sinusoidal single frequency burst to the transmitter. The receiving transducer is coaxially aligned with the transmitter. The output voltage from the receiver is amplified using a Brüel &

---

[2] The implementation of the complex wavenumber κ in the system model is given in [17].

Kjær 2636 measurement amplifier and filtered in the frequency domain (Butterworth filter) using a Krohn-Hite 3940 filter. The received voltage is then recorded by a Tektronix DPO3012 oscilloscope. The recorded voltage is termed V_6, see Fig. 1.

3.2. FE modeling setup

The FE simulation tool Femp 5.0 [24, 25], is used for calculating the propagation of the acoustical signal through the medium. The simulations used here includes the transmitting transducer and medium. The received signal is calculated using spherical reciprocity. The piezoelectric elements used in the experiments and simulations are Pz27 [26] circular piezoelectric ceramic disks with diameter of approximately 20 mm and thickness of approximately 2 mm. An adjusted material data set for Pz27 [27] is used when modeling the piezoelectric transducers. See Appendix A for an overview of the simulation parameters used, and cf. [17] for more details about the simulation setup.

4. Preliminary results

The modeled transfer function H_{1m6}^{VV} is compared to the transfer function found in the experiments, see Fig. 4. The separation distance between the transmitting and receiving transducer in the measurements and simulations is 77 cm. The frequency range is 50 to 300 kHz. The medium is air at 1 atm. and room temperature. Two measurements are used for comparison; (1) using 2 volts peak-to-peak (V_{pp}) driving voltage to the transmitting transducer and (2) using 20 V_{pp} driving voltage to the transmitting transducer.

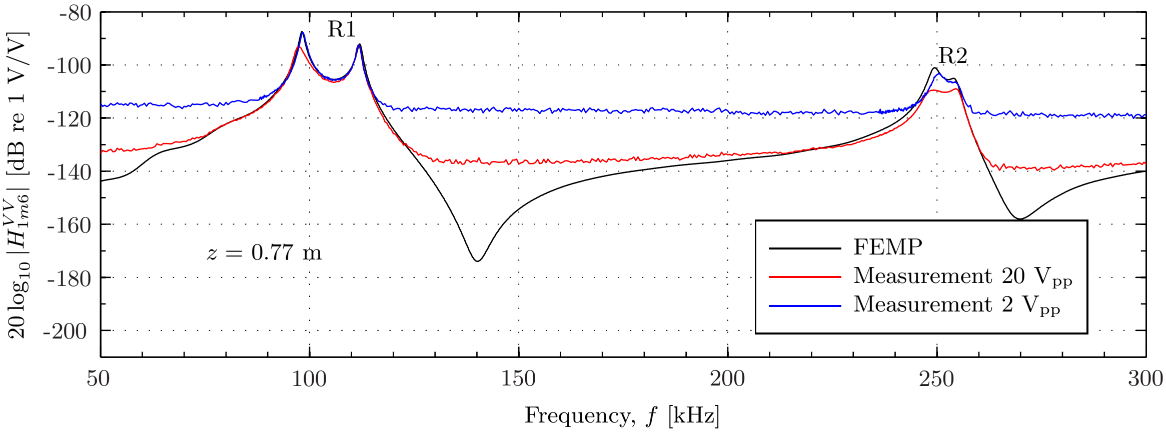

Figure 4: The magnitude of the voltage-to-voltage transfer function, H_{1m6}^{VV}. Measurements compared to calculations.

In the frequency range presented in Fig. 4 the first and second radial modes (R1 and R2 respectively) are visible.

The agreement between measurements (1) and (2) and the simulation is greater at R1 than in the frequency area above and below, but inverse for R2, where the agreement is closer in the vicinity of, than at R2. At the first peak in R1 measurement (1) is approximately 0.3 dB lower in magnitude than the simulation and is shifted 200 Hz upwards in frequency. Measurement (2) is approximately 5.5 dB lower in magnitude and 900 Hz shifted down in frequency. At the second peak in R1 both measurement (1) and (2) is approximately 0.4 dB lower in magnitude and 200 Hz shifted down in frequency compared to the simulation. At R2 both measurements show less agreement with the simulation. At R2 the difference in magnitude between measurement (2) and the simulation is approximately 8 dB.

5. Discussion

5.1. Experiments

The main factors affecting the measurements is the measurement noise, non-linearity, distance between the transducers, cables and instruments, and positioning/aligning.

For measurements using piezoelectric ceramic disks in air at 1 atm., with no acoustic matching to the gas, the signal-to-noise ratio[3] (SNR) is relatively low. To improve the SNR, a frequency filter is applied to the received voltage signal, and the recorded signal is averaged in the oscilloscope using 128 recorded waveforms. The SNR is also improved by increasing the driving voltage to the transmitting transducer, as illustrated by the two measurement curves in Fig. 4, for 2 and 20 V_{pp} input voltage. However the higher driving voltage is seen to cause non-linear effects at the first peak in R1. The SNR could also be improved significantly by reducing the separation distance, z, between the transducers. The relatively long separation distance of 77 cm is used to minimize the occurrence of standing waves between the transducers, and the resulting interference. Due to the limited bandwidth of the system, relatively long burst lengths are required to reach steady-state, used for the measurements.

As the cables were modeled and included in the system model they greatly improved the agreement between measurements and simulations. Before the cables were included there was a frequency shift between the measurements and simulations at the second peak in R1, of about 3 kHz. The importance of the cables and measurement instruments is discussed further in [17]. The uncertainty in the positioning and coaxial aligning of the transmitter and receiver increases with higher separation distance, z.

5.2. Simulations

As spherical reciprocity is used here for calculating M_V from FE simulations of S_V and Z_T, the transmitting and receiving transducers are inherently assumed to be linear, passive, reversible, reciprocal, and equal. Electrical impedance measurements not included here show that the two piezoelectric disks are relatively equal, but not equal. This approach thus represents a simplification, which may be overcome in future work by more fully accounting for the receiving transducer.

For the diffraction correction of the transducers, H^{dif}, a simplified model is used here, based on radiation from a uniformly vibrating planar and circular piston mounted in a rigid baffle of infinite extent. This approach represents a simplification, which may be overcome in future work by accounting for the diffraction correction of the real transducer sound field (cf. e.g. [1]).

The accuracy of the FE simulations is limited by the uncertainty in the complex elastic, dielectric and piezoelectric material data of the piezoelectric ceramic material used, and is expected to improve as improved material data become available.

Non-linear effects as observed in the measurements are not described by the linear system model used here.

6. Conclusions

A model for a linear and axisymmetric ultrasonic transmit-receive measurement system is developed, based on 3D FE modeling of the piezoelectric transmitting and receiving transducers and sound propagation in the fluid medium, combined with transmission-line modeling of the transmitting and receiving electronics and cables. Simulation of signal propagation in the time and frequency domain is enabled, and nearfield diffraction effects are accounted for. Preliminary results for simulations and measurements of the transmit-receive voltage-to-voltage transfer function H_{1m6}^{VV} are compared, for two piezoelectric ceramic disk transducers vibrating in air at 1 atm. The frequency range up to 300 kHz covers the two lowest radial modes of the disks, R1 and R2.

Acknowledgements

This work is done as part of the master thesis of the first author [17]. The work is supported by The Michelsen Centre for Industrial Measurement Science and Tecnology.

---

[3] $\mathrm{SNR} = 20 \log_{10}(V_{\mathrm{signal}}/V_{\mathrm{noise}})$.

References

[1] P. Lunde, K.-E. Frøysa, R. Kippersund, and M. Vestrheim, "Transient diffraction effects in ultrasonic meters for volumetric, mass and energy flow measurement of natural gas", in *Proceedings of the 21st North Sea Flow Measurement Workshop, Tønsberg, Norway, 28-31 October 2003* (2003).

[2] P. Lunde, M. Vestrheim, S. Smorgrav, and A. K. Abrahamsen, "Reciprocal operation of ultrasonic flow meters: Criteria and applications", in *Proceedings of the 2007 IEEE Ultrasonics Symposium, 28-31 October, 2007, New York, USA*, 381–386 (2007).

[3] K.-E. Frøysa, P. Lunde, A. Paulsen, and E. Jacobsen, "Density and calorific value measurement of natural gas using ultrasonic flow meters. Results from testing on various North Sea gas field data", in *Proceedings of the 24th International North Sea Flow Measurement Workshop, St. Andrews, Scotland, 24-27 October 2006* (2006).

[4] P. Norli and P. Lunde, "A three-way pulse method for a precision sound velocity measurement cell", in *Proceedings of the 2006 IEEE Ultrasonics Symposium, Vancouver, Canada, 3-6 October, 2006*, 888–893 (2006).

[5] P. Lunde, P. Norli, M. Vestrheim, and R. A. Kippersund, "Precision sound velocity cell as reference for gas quality measurement in ultrasonic flow meters. Preliminary results using two candidate methods with argon at low pressure", in *Proceedings of the 30th Scandinavian Symposium on Physical Acoustics, Geilo, Norway, January 28-31, 2007* (2007).

[6] G. Hayward, C. J. MacLeod, and T. S. Durrani, "A systems model of the thickness mode piezoelectric transducer", J. Acoust. Soc. Am. **76**(2), 369–382 (1984).

[7] A. Lygre, M. Vestrheim, P. Lunde, and V. Berge, "Numerical simulation of ultrasonic flowmeters", in *Ultrasonics International 1987 (UI'87)*, 196–201 (Butterworth Scientific Ltd., Guildford, UK) (1987).

[8] S. Vervik, "Transitt-tidsbestemmelse for ultralyd strømningsmetre. nullstrømningsforhold", Master thesis, University of Bergen, Department of Physics and Technology, Bergen, Norway (1995).

[9] P. Wilcox, R. Monkhouse, P. Cawley, M. Lowe, and B. Auld, "Development of a computer model for an ultrasonic polymer film transducer system", NDT & E International **31**(1), 51 – 64 (1998).

[10] S. Vervik, "Methods for characterization of gas-coupled ultrasonic sender-receiver measurement systems", PhD-thesis, Department of Physics and Technology, University of Bergen, Bergen, Norway (2000).

[11] Van Deventer, J. and Lofqvist, T. and Delsing, J., "PSpice simulation of ultrasonic systems", Ultrasonics, Ferroelectrics and Frequency Control, IEEE Transactions on **47**, 1014–1024 (2000).

[12] C. Dang, L. W. Schmerr, and A. Sedov, "Modeling and measuring al the elements of an ultrasonic nondestructive evaluation system I: modeling foundations", Research in Nondestructive Evaluation **14**(3), 141–176 (2002).

[13] C. Dang, L. W. Schmerr, and A. Sedov, "Modeling and measuring all the elements of an ultrasonic nondestructive evaluation system II: model-based measurements", Research in Nondestructive Evaluation **14**(4), 177–201 (2002).

[14] L. Schmerr and S. Song, *Ultrasonic nondestructive evaluation systems: models and measurements* (Springer London, Limited) (2007).

[15] R. Ludwig and W. Lord, "A finite-element formulation for the study of ultrasonic NDT systems", IEEE Transactions on Ultrasonics, Ferroelectrics and Frequency Control **35**, 809–820 (1988).

[16] P. Lunde, R. A. Kippersund, and M. Vestrheim, "Signal modelling using the FLOSIM system model in ultrasonic instrumentation for industrial applications", in *Proc. of NORSIG 2003, Norwegian Symposium on Signal Processing 2003, Bergen, October 2004* (2003).

[17] R. Hauge, Master thesis, Department of Physics and Technology, University of Bergen, Bergen, Norway (in preparation, 2013).

[18] P. Lunde, "Modeller for beskrivelse av elektroakustisk sender-mottaker målesystem, inkl. diffraksjonseffekter/diffraksjonskorreksjon", Unpublished note, Department of Physics and Technology, University of Bergen, Bergen, Norway (2013).

[19] ANSI, "ANSI S1.1-1994 (R2004) - Acoustical terminology", American Institute of Physics (2004).

[20] A. S. Khimunin, "Numerical calculation of the diffraction corrections for the precise measurement of ultrasound absorption", Acustica **27**, 173–181 (1972).

[21] L. L. Foldy and H. Primakoff, "A general theory of passive linear electroacoustic transducers and the electroacoustic reciprocity theorem", J. Acoust. Soc. Am. **17**(2), 109–120 (1945).

[22] R. W. King, H. R. Mimno, and A. H. Wing, *Transmission lines, antennas and wave guides* (Dover Publications, Inc, New York) (1965).

[23] ANSI, "ANSI S1.26-1995 (R2009) - Method for calculation of the absorption of sound by the atmosphere", American Institute of Physics (1995).

[24] J. Kocbach, "Finite element modeling of ultrasonic piezoelectric transducers", PhD thesis, Department of Physics, University of Bergen, Bergen, Norway (2000).

[25] J. Kocbach, P. Lunde, M. Vestrheim, and R. Kippersund, "Finite element modeling of ultrasonic piezoelectric transducers: Extension of FEMP to 3D analysis.", CMR Report no. CMR-06-A10046-RA-01, Christian Michelsen Research AS, Bergen, Norway (December 2006).

[26] Ferroperm Piezoceramics A/S (now a member of Meggitt's Sensing Systems division), "High quality components and materials for the electronic industry", DK-3490 Kvistgård (2012).

[27] V. Knappskog, "Radiellmode svingninger i piezoelektriske ultralydstransdusere for luft. målinger og endelig element analyser.", Master's thesis, Department of Physics and Technology, University of Bergen, Bergen, Norway (2007).

Appendix A. Simulation parameters

Table A.1: Simulation parameters.

Transmitter material:	Pz27 [26] piezoelectric ceramic disk.
Transmitter dimensions:	D = 20.24 mm, T = 2.035 mm (cf. Fig. A.5).
Calculation distance:	$z_\infty = 1000$ m.
Frequency range:	$f = 0$ to 300 kHz.
Medium:	Air: $c = 343$ m/s, $\rho = 1.21$ kg/m^3.
Finite elements:	8 nodes, isoparametric.
Elements per wavelength	5 elements/wavelength specified at $f = 300$ kHz.
Radius to the infinite elements:	$R_{inf} = 2.74$ cm
Infinite elements order:	12. order

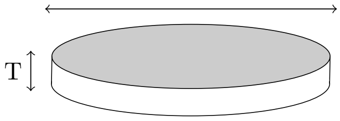

Figure A.5: Illustration of the Pz27 piezoelectric ceramic disk.